A Search For High-Redshift Radio Galaxies Within The Epoch of Reinization

By

Hanifa Teimourian

A thesis submitted to University of Hertfordshire
for the degree of
Doctor of Philosophy
School of Physics, Astronomy and Mathematics
May 2013

Typeset in LaTeX 2_ε.

Dedication

To ...

Busha and Mamani

Acknowledgements

My deepest thanks goes to my supervisor Matt Jarvis, not only for his scientific oversight of my reaserch project but also for the friendly manner in which he would resolve all my problems and for sparing time for me even during his holidays. I also remain indebted to him for his understanding and support during the times when I was really down and depressed. It is because of Matt that I will miss the UK.

I would like to thank my mother for all the books that she bought for me and read to me during my chilhood, for her unconditional love towards me, for installing in me a love of astronomy and for keeping me motivated from thousands of miles away through skype.

I am indebted to my father for all of the trips into the wilderness and instilling in me a love of nature, for understanding me and even my most stupid thoughts, for giving me faith in myself and for his unconditional support.

I am grateful to Amir for being my best flat mate, for all the times he would listen to my every word as we walked in the snow far far way from home, and for all the times in which he suffered to make me happy.

Dear Mehri and Ahmad thank you for supporting and encouraging me to pursue my dream. A big thanks also goes to Tara for her kindly motivation.

It would have been impossible to write this thesis without all the crazy political discussions and all the Mafia games that I have enjoyed with Roberto. Thanks also to my office mates over the last four years for all their IRAF help and their funny jokes.

Dear *my old Greek enemy*, I am forced to thank you by Alexander for your frequent company in front of the Innovation centre and for all the late night drinks we have enjoyed at crazy Jully's house.

Finally I would like to thank Ata, Pejman, Sara, Ehsan, Ali, Vahid and Amir for starting me on the path of astronomy with an old fashioned and small 8 inch Telescope.

To hamid:


وقتی که پیمان بدن با دست خالقت می بست
وقتی ابد پیشه تر از پیش از ازل می آمد
وقتی زمین ناز تر از آسمانها می شد
وقتی عطش نام تر از الکل مایه می پیشید
من عاشق پیشست شدم نه عقل بر در نه دلی
چیزی نمی دانم از این حیرانکی و عاقلی
پاک آن شد این عاشق شدن جنها و انسان پاک لقا بود
آن دم که پیشانت مرا از عشق پیشانم ربود
وقتی که من عاشق شدم شیطان به نامم سجده کرد
آدم ز هیبت تر شد و عالم به آدم سجده کرد
من بر دم و پیشان تر نه آتشی و نه گلی
چیزی نمی دانم از این حیرانکی و عاقلی

Abstract

In this thesis I used a sample of radio galaxies with 1.4 GHz radio luminosity, $S_{1.4} > 10$mJy, with the aim of finding high-redshift radio galaxies in the Lockman Hole, ELAIS-N1, ELAIS-N2, XMM-LSS and CDFS using near-infrared data from the *Spitzer Space Telescope*, and in the VIMOS4/SSA22 field using near-infrared data from the UKIRT Infrared Deep Sky Survey Deep Extragalactic Survey (UKIDSS-DXS). I used these near-infrared data to filter out low redshift ($z < 2$) radio galaxies by only including sources with either a very faint identification or non-detection in the $K-$band or at 3.6μm. I then applied a radio selection criteria based on the compactness of the radio structure in the FIRST survey, to ensure that it was possible to correctly associate a near-infrared identification if detected.

Using these filtering critera I reduced the sample from 498 to 220, and I obtained spectroscopic observations for 46 of these. I successfully measured redshifts for 22 of these. Four of these sources were found to have redshifts at $z > 3$, thus proving the efficiency of the selection. Using these spectroscopically identified sources I investigated the correlation between radio luminosity and Lyα emission line luminosity and showed that these radio sources lie on the same correlations as their more radio-luminous counterparts, suggesting that accretion rate on to the central supermassive black hole determines the power of the AGN, both in terms of photoionizing radiation and radio power. I also investigated the near infrared properties of the host galaxy for these sources. Studying the 3.6μm magnitude versus redshift, I found that many of the radio galaxies in our sample lie on a similar relation as other powerful radio sources studied by different methods, although in my selection there is a bias to the fainter end of the distribution, likely due to the selection bias that I impose.

The selection criteria has led us to report on the discovery of the highest redshift radio galaxy ever found, however the robustness of the redshift should be confirmed by follow up spectroscopy as the source has K_{AB} magnitude of ~ 20.7 which is in an area of the $K - z$ diagram which makes it consistent with both z~ 1 (in the case of [OII]) and $z \sim 5$ (in the case of Lyα).

Finally I determined the number density of high-redshift sources in my sample at different epochs and show that the SKADS simulation is consistent with our observed radio galaxy sample. Using this knowledge I go on to predict the number of sources for current and future near-infrared surveys, where the future appears very bright for this kind of work.

Contents

Dedication iii

Acknowledgements v

Abstract vii

List of Figures xi

List of Tables xix

1 Introduction 1
- 1.1 The AGN Zoo . . . 1
  - 1.1.1 Seyfert galaxies . . . 1
  - 1.1.2 Quasars and Quasi-Stellar Objects . . . 3
  - 1.1.3 Obscured or Type II Quasars . . . 4
  - 1.1.4 Blazars . . . 5
  - 1.1.5 Radio galaxies . . . 6
- 1.2 Unification schemes . . . 7
  - 1.2.1 Orientation-based Unification of AGN . . . 7
  - 1.2.2 Modifications to Orientation-based Unification of AGN . . . 8
  - 1.2.3 Evolutionary-based Unification of AGN . . . 10
- 1.3 Triggering of AGN activity . . . 11
- 1.4 A brief history of the Universe and the Epoch of Reionization . . . 12
- 1.5 High redshift radio galaxies as probes of the EoR . . . 13
  - 1.5.1 Ionized Gas . . . 14
  - 1.5.2 Molecular Gas . . . 16
  - 1.5.3 Dust emission . . . 17
  - 1.5.4 Stellar masses of radio galaxy hosts . . . 17
  - 1.5.5 Finding high-redshift radio galaxies . . . 18
  - 1.5.6 High redshift radio galaxy hosts . . . 19
  - 1.5.7 Evolution of the Radio Luminosity Function . . . 20
- 1.6 The SKA Design Study Semi-empirical Extragalactic Simulation . . . 25
- 1.7 This thesis . . . 25

2 Sample definition **27**
2.1 Sample Selection . . . 27
2.2 Infrared Surveys . . . 28
2.3 The Radio Surveys . . . 31
2.4 The Sample . . . 34

3 Spectroscopy and Redshift estimation **57**
3.1 Target selection . . . 57
3.2 Spectroscopic Observations . . . 58
3.2.1 WHT Data reduction . . . 60
3.2.2 GEMINI Observations & Data Reduction . . . 64
3.3 Notes on Individual Sources . . . 65
3.4 Lyα luminosity versus radio luminosity . . . 78
3.5 3.6μm magnitude–redshift relation . . . 82

4 A Radio galaxy at z=5.33? **87**
4.1 Introduction . . . 87
4.1.1 The Epoch Of Reionisation . . . 87
4.1.2 High redshift radio galaxies . . . 88
4.2 Finding the highest redshift radio sources . . . 89
4.3 A RADIO GALAXY at z=5.33? . . . 89
4.3.1 Spectroscopy . . . 91
4.3.2 Radio properties . . . 93
4.3.3 Host galaxy properties . . . 94
4.4 Conclusion . . . 94

5 The Comoving Space Density of Radio Sources at $z > 2$ **97**
5.1 SKADS simulations . . . 97
5.2 Comparison of results . . . 101
5.3 Predictions for current and future near-infrared surveys . . . 103
5.3.1 The Visible and Infrared Survey Telescope for Astronomy (VISTA) . . . 103
5.3.2 High-redshift radio galaxies in the VISTA surveys . . . 105

6 Conclusion & Future Work **109**
6.1 Conclusions . . . 109
6.2 Future Work . . . 111

A Radio source candidates **113**

B Overlays **119**

C The discovery of a typical radio galaxy at $z = 4.88$ **179**

References **189**

List of Figures

1.1 Spectra showing the difference between Seyfert galaxies 1, 1.5 and 2. The hydrogen and helium lines are much broader in the spectra of type 1, while in type 2 the emission lines are much narrower Osterbrock (1984). 2

1.2 Cartoon taken from Roy et al. (1994) showing how our line of sight effects the classification of Seyfert galaxies. If we look along the axis of the torus we can see the BLR and the accretion disk while if we look along the edge, the torus blocks the view of the BLR and we can only see the NLR. 4

1.3 Composite quasar spectrum of quasars from the Sloan Digital Sky Survey with $0.044 \leq z \leq 4.789$.(Vanden Berk et al., 2001). 5

1.4 Radio wavelength image of the radio galaxy, Cygnus A. The central point is the galaxy nucleus, which feeds the jets and lobes of radio emitting plasma.(Carilli & Barthel, 1996) 6

1.5 Example of a Fanaroff-Riley type I and type II galaxies. (a) shows a radio map of the 3C 272.1(M84) based on VLA 4.9 GHz data (Laing et al., 1983), and (b) shows a radio map of the 3C 175, as observed with the VLA at 4.9 GHz. 7

1.6 A conceptual AGN unification scheme which shows how the orientation along the line of sight leads to different AGN classifications. Taken from Urry & Padovani (1995). 9

1.7 Cartoon representation of the history of the universe. Taken from http://www.astro.caltech.edu/∼geo

1.8 Simulated spectrum of a high redshift radio galaxy from Carilli et al. (2002) with S=20 mJy at z=10. HI 21cm absorption by the neutral IGM is seen above 129 MHz (corresponding to $z = 10$ for 21 cm radiation) due to the neutral hydrogen abundance at $6 < z < 10$, with $z = 6$ corresponding to a redshifted 21 cm line at ~ 200 MHz, beyond the extent of the figure. 14

1.9 Radio continuum contours overlaid on a rest-frame U/B-band image of 3C368 at z = 1.13 (Best et al., 1996). The X and Y axis present the RA and DEC respectively. 16

1.10 The radio spectrum of the radio galaxy Cygnus A at $z = 0.05$, showing spectral curvature. Taken from Kellermann et al. (1969). 19

1.11 Correlation between redshift and spectral index of 3CR radio galaxies from van Breugel et al. (1998). 20

1.12 The radio luminosity function determined by Dunlop & Peacock (1990) using the pure luminosity evolution model between redshift $0 < z < 4$. 21

1.13 The change in peak redshift with radio luminosity from Rigby et al. (2011). The error bars show the uncertainty in the polynomial fits, and the shaded region represents the range in results which come from repeating this process for the additional grids. 24

2.1 K-z diagram for radio galaxies 7CRS, 6CE, 6C and 3CRR samples ((Willott et al., 2003)). One can see the tight correlation between $K-$magnitude and redshift to isolate high-redshift radio galaxies, because if $K > 20$ the redshift is likely to be at $z > 2$. 29
2.2 The sky coverage of the UKIDSS survey. Cross-hatch : Large Area Survey. Dark Grey : Galactic Plane Survey. Light Grey : Galactic Clusters Survey. Open rectangles : Deep Extragalactic Survey. Note that the Ultra Deep Survey lies just to the west of the DXS field at 02h18m -05°10'. The dashed line marks the Galactic plane. Taken from Lawrence et al. (2007). 30
2.3 The 3.6μm magnitude versus redshift diagram for radio galaxies from Seymour et al. (2007). 31
2.4 The redshift distribution of simulated radio galaxies as a function of redshift from the SKADS simulation, over 34 deg^2 33
2.5 The IRAC-3.6μm images from SWIRE in the ELAIS-N1 field, overlaid with the radio image from FIRST survey. Images of all the ELAIS-N1 targets are presented in Appendix A 52
2.6 The IRAC-3.6μm images from SWIRE in the ELAIS-N2 field, overlaid with the radio image from FIRST survey. Images of all the ELAIS-N2 targets are presented in Appendix A 53
2.7 The IRAC-3.6μm images from SWIRE in the Lockman Hole field, overlaid with the radio image from FIRST survey. Images of all the Lockman Hole targets are presented in Appendix A 54
2.8 The IRAC-3.6μm images from SWIRE in the XMM-LSS field, overlaid with the radio image from GMRT data. For the full image of all the XMM-LSS targets see Appendix A 55
2.9 The K-band images from DXS in the VIMOS field, overlaid with the radio image from FIRST data. For the full image of all the VIMOS targets see Appendix A . 56

3.1 Throughput of the 5300Å dichroic. It is better than that of the other dichroic units available (>95 per cent) in the red arm, and also in the blue. Ripples, in particular in the blue arm, are much less pronounced than other available dichroics. The cut-off region is also narrower, with the throughput in both arms below 70 per cent in the 5200-5400Å region. (Figure taken from the ING web page: http://www.ing.iac.es/astronomy/instruments/isis/isis_dich.html) 58
3.2 Bias subtracted 2D spectrum of EN2_45 in both the blue (left) and red arm (right). 61
3.3 Flat fielded 2D spectrum of EN2_45 in both blue (left) and red (right) arms. . . 63
3.4 Final reduced 2D spectra of EN2_45 in both blue (left) and red (right) arms. The wavelength (in Angstroms) is given along the y-axis of both the blue and red arms. 64

3.5 2D spectra of EN2-45. The two green circles in the image at the top and the bottom highlight the position of a cosmic ray and a real line at 7146Å, respectively. As one can see the spatial and spectral extent of the emission line are larger than the cosmic ray. 65
3.6 The 1D spectra of the our sources in ELAIS-N1 field with the emission-line identifications. 71
3.7 The 1D spectra of the our sources in ELAIS-N2 field with the emission-line identifications. 72
3.8 The 1D spectra of the our sources in ELAIS-N2 and Lockman Hole fields with the emission-line identifications. 73
3.9 The 1D spectra of the our sources in Lockman Hole field with the emission-line identifications. 74
3.10 The 1D spectra of the our sources in Lockman Hole field with the emission-line identifications. 75
3.11 The 1D spectra of the our sources in Lockman Hole field with the emission-line identifications. 76
3.12 The 1D spectra of the our sources in XMM-LSS field with the emission-line identifications. An example sky spectrum in both blue and red arms is also shown. 77
3.13 2D spectra of the radio galaxy EN2-45 in the red part, showing the Lyα line at 7146Å and redshift of $z = 4.8$ 78
3.14 Lyα emission line luminosity against rest-frame 151-MHz radio luminosity for radio galaxies at z > 1.75 from the 3CRR (circles), 7CRS (squares), 6CE (triangles) and 6C* (stars) radio samples. The filled circles are the high-redshift sources from De Breuck et al. (2000a) while the solid line shows the best fit. (Jarvis et al. (2001b)) 80
3.15 Lyα emission line luminosity against rest-frame 151-MHz radio luminosity for radio galaxies at z > 1.75. The red squares and triangles present the Jarvis et al. (2001b) and De Breuck et al. (2000a) sources. The black diamond symbols represent our sources from Lockman Hole, Elais-N1 and Elais-N2 fields and the black symbols are for the XMM field. 81
3.16 The 3.6μm magnitude against redshift diagram for the sample of high redshift radio galaxies from Seymour et al. (2007), overplotted with the radio galaxies from this thesis. The black symbols represent my observed radio galaxies which are biased due to the selection effect and the red symbols represent the Seymour et al. (2007) galaxies. 84
3.17 The $K - z$ Hubble diagram for radio galaxies from the 3CRR (circles), 6CE (triangles), 6C* (stars) and 7C-III (squares) samples, for a Ω_M=0.3, Ω_Λ=0.7 cosmology with H_0=70 km s^{-1} Mpc^{-1}. The two vertical lines show the redshift above which the alignment effect begins to be seen ($z = 0.6$). The solid lines are the fits to the 3CRR data points at z< 0.6 and 0.6 < z < 1.8. The dashed line is the fit to the 6CE and 6C* sources at 0.6 < z < 1.8 and z > 1.8. The filled stars represent five of the six objects in 6C* which do not have secure redshifts. From Jarvis et al. (2001a). 86

4.1 The number of sources with the flux density > 10 mJy as a function of redshift, using the semi-empirical method (Wilman et al. 2008). The decline is caused by the lack of radio source population beyond redshift 6. 90
4.2 The IRAC-3.6μm image from SWIRE, which is overlaid with the radio image from GMRT survey. The faint point in the centre is the host galaxy. Contour levels are 2,4,8,16,32 and 32 mJy/beam. 90
4.3 1D spectra of the radio galaxy J022200.34-033934.6 which shows a strong emission line at 7700Å which we tentatively identify as Lyα at $z = 5.33$. 91
4.4 2D spectrum of the radio galaxy J022200.34-033934.6 at PA 170°, showing the emission line from two objects. The line on the left hand side is the line associated with the targeted radio galaxy, J022200.34-033934.6. 92
4.5 IRAC 4-bands and MIPS 2-band images from SWIRE of the J022200.34-033934.6. 93

5.1 The normalised differential source counts at 1.4 GHz. Note that the filled diamonds show the counts of AGNs only, while all the other symbols refer to total counts. A straightforward extrapolation of evolutionary models fitting the far-IR to mm counts of populations of star-forming (normal late-type (spirals or sp), starburst (sb), and proto-spheroidal) galaxies, exploiting the well-established far-IR/radio correlation, naturally accounts for the observed counts below $\sim 30\mu$Jy. At higher flux densities, the counts are dominated by radio-loud AGNs. Taken from de Zotti et al. (2010). 98
5.2 The radio luminosity function derived for model C for $\Omega_{\rm M} = 1$ (top panel) and $\Omega_{\rm M}0$ (bottom panel). Dashed lines show the low-luminosity population at $z = 0$; $z = 0.5$ and $z = 0.7$ (bottom to top). The dotted lines are the high-luminosity RLF at $z = 0, 0.5, 1, 3$ and 2 (bottom to top). Solid lines show the sum of both components. Taken from Willott et al. (2001). 100
5.3 The number of sources with the flux density > 10 mJy as a function of redshift for both SKADS targets and our sample. The SKADS source distribution has been corrected for the spectroscopic incompleteness of our observed sample, just by scaling of the successful redshift measurement compared to the fraction observed. 102
5.4 The VISTA focal plance with 16 near-infrared detectors which together provide an instantaneous field of view of ~ 0.6 degress^2. Image taken from www.vista.ac.uk. 103
5.5 A schematic representation of the sky coverage of the various VISTA surveys. Taken from Arnaboldi et al. (2007). 104
5.6 Redshift distribution for radio sources with $S_{1.4} > 10$ mJy for the VHS (top left), VIKING (top right), VIDEO (bottom left) and UltraVISTA (bottom right) surveys. 106

B.1 The IRAC-3.6μm images from SWIRE in the Elais-N1 field, overlaid with the radio image from FIRST. 120
B.2 The IRAC-3.6μm images from SWIRE in the Elais-N1 field, overlaid with the radio image from FIRST. 121
B.3 The IRAC-3.6μm images from SWIRE in the Elais-N1 field, overlaid with the radio image from FIRST. 122

B.4 The IRAC-3.6μm images from SWIRE in the Elais-N1 field, overlaid with the radio image from FIRST. . . . 123
B.5 The IRAC-3.6μm images from SWIRE in the Elais-N1 field, overlaid with the radio image from FIRST. . . . 124
B.6 The IRAC-3.6μm images from SWIRE in the Elais-N1 field, overlaid with the radio image from FIRST. . . . 125
B.7 The IRAC-3.6μm images from SWIRE in the Elais-N1 field, overlaid with the radio image from FIRST. . . . 126
B.8 The IRAC-3.6μm images from SWIRE in the Elais-N1 field, overlaid with the radio image from FIRST. . . . 127
B.9 The IRAC-3.6μm images from SWIRE in the Elais-N1 field, overlaid with the radio image from FIRST. . . . 128
B.10 The IRAC-3.6μm images from SWIRE in the Elais-N1 field, overlaid with the radio image from FIRST. . . . 129
B.11 The IRAC-3.6μm images from SWIRE in the Elais-N1 field, overlaid with the radio image from FIRST. . . . 130
B.12 The IRAC-3.6μm images from SWIRE in the Elais-N1 field, overlaid with the radio image from FIRST. . . . 131
B.13 The IRAC-3.6μm images from SWIRE in the Elais-N2 field, overlaid with the radio image from FIRST. . . . 132
B.14 The IRAC-3.6μm images from SWIRE in the Elais-N2 field, overlaid with the radio image from FIRST. . . . 133
B.15 The IRAC-3.6μm images from SWIRE in the Elais-N2 field, overlaid with the radio image from FIRST. . . . 134
B.16 The IRAC-3.6μm images from SWIRE in the Elais-N2 field, overlaid with the radio image from FIRST. . . . 135
B.17 The IRAC-3.6μm images from SWIRE in the Elais-N2 field, overlaid with the radio image from FIRST. . . . 136
B.18 The IRAC-3.6μm images from SWIRE in the Elais-N2 field, overlaid with the radio image from FIRST. . . . 137
B.19 The IRAC-3.6μm images from SWIRE in the Elais-S1 field, overlaid with the radio image from ATLAS. . . . 138
B.20 The IRAC-3.6μm images from SWIRE in the Elais-S1 field, overlaid with the radio image from ATLAS. . . . 139
B.21 The IRAC-3.6μm images from SWIRE in the Elais-S1 field, overlaid with the radio image from ATLAS. . . . 140
B.22 The IRAC-3.6μm images from SWIRE in the Elais-S1 field, overlaid with the radio image from ATLAS. . . . 141
B.23 The IRAC-3.6μm images from SWIRE in the Lockman Hole field, overlaid with the radio image from FIRST. . . . 142
B.24 The IRAC-3.6μm images from SWIRE in the Lockman Hole field, overlaid with the radio image from FIRST. . . . 143
B.25 The IRAC-3.6μm images from SWIRE in the Lockman Hole field, overlaid with the radio image from FIRST. . . . 144

B.26 The IRAC-3.6μm images from SWIRE in the Lockman Hole field, overlaid with the radio image from FIRST. . . . 145
B.27 The IRAC-3.6μm images from SWIRE in the Lockman Hole field, overlaid with the radio image from FIRST. . . . 146
B.28 The IRAC-3.6μm images from SWIRE in the Lockman Hole field, overlaid with the radio image from FIRST. . . . 147
B.29 The IRAC-3.6μm images from SWIRE in the Lockman Hole field, overlaid with the radio image from FIRST. . . . 148
B.30 The IRAC-3.6μm images from SWIRE in the Lockman Hole field, overlaid with the radio image from FIRST. . . . 149
B.31 The IRAC-3.6μm images from SWIRE in the Lockman Hole field, overlaid with the radio image from FIRST. . . . 150
B.32 The IRAC-3.6μm images from SWIRE in the Lockman Hole field, overlaid with the radio image from FIRST. . . . 151
B.33 The IRAC-3.6μm images from SWIRE in the Lockman Hole field, overlaid with the radio image from FIRST. . . . 152
B.34 The IRAC-3.6μm images from SWIRE in the Lockman Hole field, overlaid with the radio image from FIRST. . . . 153
B.35 The IRAC-3.6μm images from SWIRE in the Lockman Hole field, overlaid with the radio image from FIRST. . . . 154
B.36 The IRAC-3.6μm images from SWIRE in the Lockman Hole field, overlaid with the radio image from FIRST. . . . 155
B.37 The IRAC-3.6μm images from SWIRE in the Lockman Hole field, overlaid with the radio image from FIRST. . . . 156
B.38 The IRAC-3.6μm images from SWIRE in the XMM-LSS field, overlaid with the radio image from GMRT data. . . . 157
B.39 The IRAC-3.6μm images from SWIRE in the XMM-LSS field, overlaid with the radio image from GMRT data. . . . 158
B.40 The IRAC-3.6μm images from SWIRE in the XMM-LSS field, overlaid with the radio image from GMRT data. . . . 159
B.41 The IRAC-3.6μm images from SWIRE in the XMM-LSS field, overlaid with the radio image from GMRT data. . . . 160
B.42 The IRAC-3.6μm images from SWIRE in the XMM-LSS field, overlaid with the radio image from GMRT data. . . . 161
B.43 The IRAC-3.6μm images from SWIRE in the XMM-LSS field, overlaid with the radio image from GMRT data. . . . 162
B.44 The IRAC-3.6μm images from SWIRE in the XMM-LSS field, overlaid with the radio image from GMRT data. . . . 163
B.45 The IRAC-3.6μm images from SWIRE in the XMM-LSS field, overlaid with the radio image from GMRT data. . . . 164
B.46 The IRAC-3.6μm images from SWIRE in the XMM-LSS field, overlaid with the radio image from GMRT data. . . . 165
B.47 The IRAC-3.6μm images from SWIRE in the CDFS field, overlaid with the radio image from ATLAS. . . . 166

B.48 The IRAC-3.6μm images from SWIRE in the CDFS field, overlaid with the radio image from ATLAS. . . . 167
B.49 The IRAC-3.6μm images from SWIRE in the CDFS field, overlaid with the radio image from ATLAS. . . . 168
B.50 The IRAC-3.6μm images from SWIRE in the CDFS field, overlaid with the radio image from ATLAS. . . . 169
B.51 The IRAC-3.6μm images from SWIRE in the CDFS field, overlaid with the radio image from ATLAS. . . . 170
B.52 The IRAC-3.6μm images from SWIRE in the CDFS field, overlaid with the radio image from ATLAS. . . . 171
B.53 The IRAC-3.6μm images from SWIRE in the CDFS field, overlaid with the radio image from ATLAS. . . . 172
B.54 The K-band images from DXS in the VIMOS field, overlaid with the radio image from FIRST data. . . . 173
B.55 The K-band images from DXS in the VIMOS field, overlaid with the radio image from FIRST data. . . . 174
B.56 The K-band images from DXS in the VIMOS field, overlaid with the radio image from FIRST data. . . . 175
B.57 The K-band images from DXS in the VIMOS field, overlaid with the radio image from FIRST data. . . . 176
B.58 The K-band images from DXS in the VIMOS field, overlaid with the radio image from FIRST data. . . . 177
B.59 The K-band images from DXS in the VIMOS field, overlaid with the radio image from FIRST data. . . . 178

C.1 Expected number of radio sources above 10 mJy as a function of redshift per square degree. The dark solid line is the expected number of low-luminosity radio sources which would have low-luminosity emission lines and be very difficult to obtain redshifts for. The grey banded area shows the degree of uncertainty in the high-redshift evolution of the more powerful, typically FRII sources, from a constant comoving space density and one with a steady decline [see Jarvis & Rawlings (2000) for more details]. The dashed line is the best-fit model C from Willott et al. (2001). . . . 182
C.2 The *Spitzer*-3.6μm image (greyscale) overlaid with radio contours from the FIRST survey. Contour levels are 0.8, 1.6, 3.2, 6.4 and 12.8 mJy/beam. One can see the faint source at the centre of the radio emission at 16 39 12.11 +40 52 36.5 which we identify as the host galaxy. . . . 183
C.3 1-dimensional spectrum of the radio galaxy J163912.11+405236.5. One can see the bright Lyman-α emission line at $\lambda = 7149$Å, which corresponds to a redshift of $z = 4.88$. . . . 185

List of Tables

2.1 Summary of the fields that were targeted as part of the SWIRE survey. Positions given are the central coordinates of the fields. Information taken from the SWIRE web page (http://swire.ipac.caltech.edu/swire/public/overview.html). . 30

2.2 This table shows the number of sources after the various cuts. The second column presents the number of sources with $S_{1.4} > 10$mJy, the third column presents the number of compact sources with $S_{1.4} > 10$mJy and the last column presents the number of compact sources with $S_{1.4} > 10$mJy and $S_{3.6} < 50\mu$Jy. 36

2.3 FIRST radio sources in the ELAIS-N1 field with radio flux $S_{1.4} > 10$mJy cross-matched with the SWIRE survey. $S_{3.6}$ is the flux-density measurement at 3.6 μm. The separation between the radio position and the near-infrared counterpart is also given (Sep) in arcsec, if the separation value is not shown the sources are not detected in the SWIRE catalogues. The structure of the radio sources are given for the compact (c) and not compact (nc). For the undetected sources in the SWIRE catalogues at 3.6μm, the lower limit of 7.3 μJy is shown. The rms of the FIRST survey is 0.147mJy. The $\star$ sign marks those which are not covered in the IRAC imaging and the $\wr$ sign denotes two possible identifications and we provide the fluxes for all possible IDs. 36

2.4 FIRST radio sources in the Elais-N2 field with radio flux > 10mJy cross-matched with the SWIRE survey 40

2.5 FIRST radio sources in the Lockman Hole field with radio flux > 10mJy cross-matched with the SWIRE survey 42

2.6 GMRT data at 610 MHz radio sources in the XMM-LSS field with radio flux > 19mJy cross-matched with the SWIRE survey 46

2.7 FIRST radio sources in the VIMOS field with radio flux > 10mJy cross-matched with the DXS survey 49

3.1 our candidates for observation 59

3.2 The candidates in the XMMLSS field for which we obtained optical spectroscopy observations, including the telescope on which the spectra were taken, the date of the observation and the exposure time used for both the blue (B) and red (R) arms. 60

3.3 The candidates in the VIMOS field for which we obtained optical spectroscopy observations, including the telescope on which the spectra were taken, the date of the observation and the exposure time. 61

3.4 our candidates for observation 69

3.5 Emission line measurements obtained from the spectra of sources. The '?' denotes an uncertain line identification. The typical uncertainty on the line fluxes is 20-30 per cent due to both sky noise and possible slit losses. 79

5.1 The number of radio galaxies with $S_{1.4} > 10$mJy in 34 deg^2 both for SKADS simulation and the real observed data sample, above several redshift limits. . . . 102
5.2 Summary of the key VISTA Surveys that could be used to find high-redshift radio galaxies. Also shown is the expected number of radio galaxies with $S_{1.4} > 10$ mJy in the given survey area from the S^3-SEX simulation. The † denotes that we only consider the 1.5 degree^2 part of the UltraVISTA survey which reaches a shallower depth than the full deep survey which covers only half of this area. 105
5.3 The total and fraction of $S_{1.4} > 10$ mJy radio galaxies that a given VISTA Survey could isolate above a given redshift based on the S^3-SEX simulation and the limits shown. 107

A.1 ATLAS radio sources in the CDFS field with radio flux > 10mJy cross-matched with the SWIRE survey with $S_{3.6} < 50\mu$m 113
A.2 ATLAS radio sources in the ES1 field with radio flux > 10mJy cross-matched with the SWIRE survey 116

C.1 Photometric data for the radio galaxy. The quoted limits are 3σ limits for a 2 arcsec diameter aperture for the INT data, 4 arcsec diameter aperture for the channels 1-4 IRAC data and a 10.5 arcsec diameter aperture for the 24μm limit. All are in the AB magnitude system. The radio galaxy is unresolved in both the FIRST and WENSS survey data and as such the radio flux densities are integrated flux over the synthesized beam area. 186

Chapter 1

Introduction

Active Galactic Nuclei (AGN) are among the most luminous and energetic objects in the universe. Carl Seyfert (Seyfert, 1943) was the first to describe them as a class in 1943 but the physical processes occurring in these phenomena were first suggested by Woltjer (1959), where it was noted the nuclei must be compact ($\sim 100\,\mathrm{pc}$) and "extremely massive" ($> 10^8\,\mathrm{M}_\odot$).

Many theories tried to explain the extreme power of the AGN (Hoyle & Fowler, 1963) but the common explanation today is that AGN must be powered by accretion onto super massive black holes (Lynden-Bell, 1969). AGN emission covers all wavebands, from X-ray through the optical and radio, while powerful AGN are very luminous and can be found at the highest redshifts. Another property of AGN is the high variability of their emission observed at all frequencies on short time scales, which can be explained by a very compact structure of the emission region.

In the following, I describe the current view of what AGN are within a unification scenario.

1.1 The AGN Zoo

Based on observational properties, AGN are divided into various classifications, with most AGN classified as Seyfert galaxies, quasars, blazars and radio galaxies.

1.1.1 Seyfert galaxies

Seyfert galaxies were first discovered by Carl Seyfert in 1943 (Seyfert, 1943). These objects exhibit bright nuclei and their spectra show strong emission lines and very little radio emission. Seyfert galaxies show an intermediate level of nuclear activity compared to the other types of AGN. The luminosity of their nuclei typically range from $10^{36} - 10^{38}\,\mathrm{W}$ but they are defined as low luminosity AGN. The hosts of Seyferts are usually spiral galaxies and tend to be observed at low redshift (Weedman, 1977).

Seyfert galaxies have traditionally been classified as Type I and Type II based on the width of their emission lines (Khachikian & Weedman, 1974). As one can see in Fig. 1.1, Type II Seyferts have narrow forbidden emission lines ($< 2000\,\mathrm{km\,s^{-1}}$) while type I Seyfert galaxies have an additional broader ($> 2000\,\mathrm{km\,s^{-1}}$) component from permitted lines which are either absent in type II or stronger and more dominant in type I. It is believed that these two types

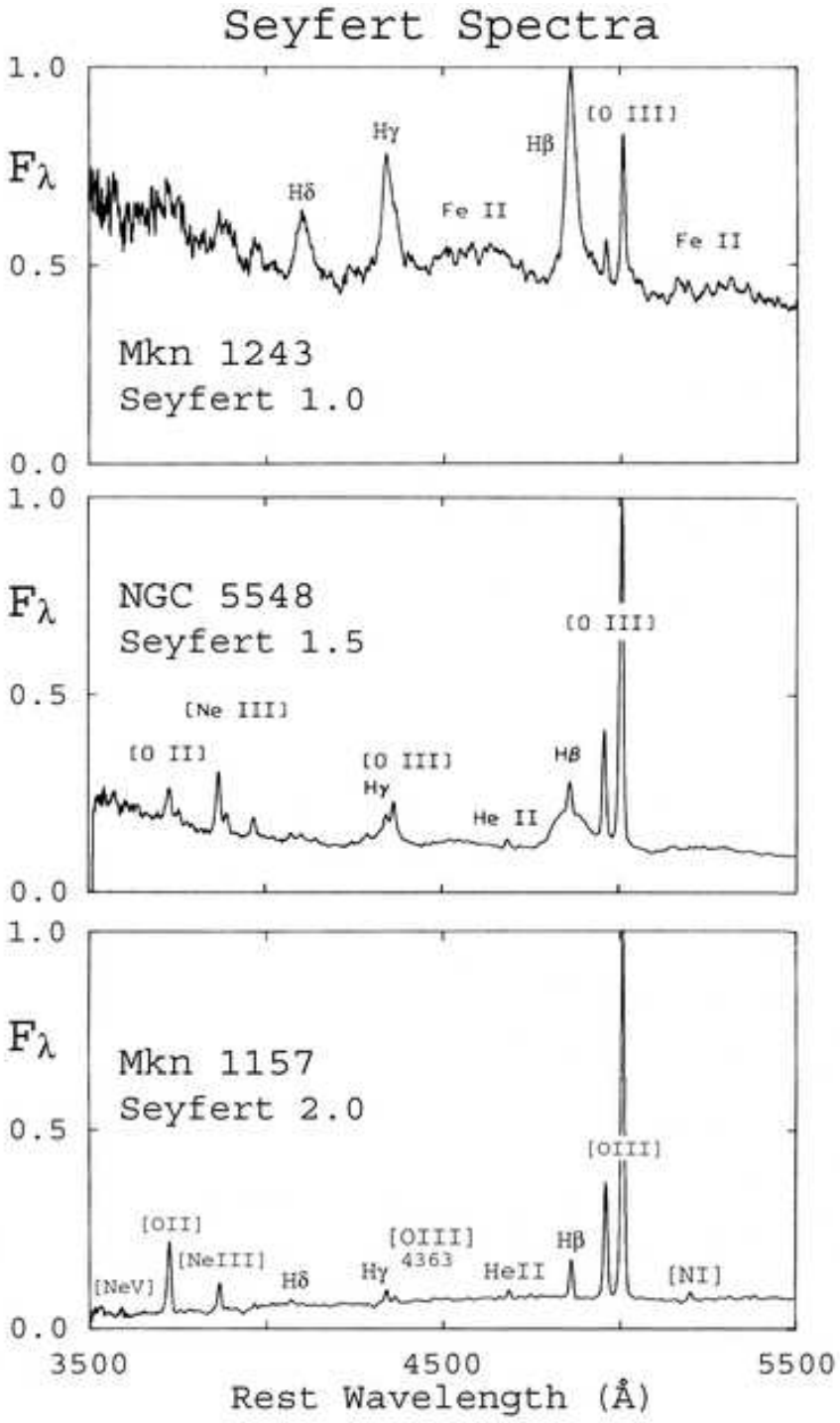

Figure 1.1: Spectra showing the difference between Seyfert galaxies 1, 1.5 and 2. The hydrogen and helium lines are much broader in the spectra of type 1, while in type 2 the emission lines are much narrower Osterbrock (1984).

of object are basically the same, but our line of sight is obscured by dust toward the central region in type II Seyfert galaxies, either by a toroidal structure or a more clumpy cloud-like structure. Thus type II Seyferts might be the same type of objects as type I Seyfert galaxies but observed at a different orientation with respect to our line of sight.

In 1981, Osterbrock classified Seyfert galaxies by adding intermediate classifications, 1.2,1.5 and 1.8 as better data showed the gradual change in the broad and narrow emission lines strength (Osterbrock, 1981). Another common feature in Seyfert galaxies is the white light continuum emission from the nucleus. This feature is stronger in type I than type II galaxies (Mas-Hesse et al., 1994; Kinney et al., 1991).

It is believed that the source of energy, which drives nuclear activity in Seyfert galaxies, lies in the gravitational field due to the central super massive black hole (Rees, 1984). The gas that is falling towards the black hole, via the accretion disk, radiates over most of the electromagnetic spectrum. The X-ray emission comes from the hottest, inner part of the disk, and the UV and optical emission comes from the outer parts. This radiation is then able to flood out into the galaxy and ionize surrounding gas, leading to emission line radiation.

The ionised gas that is located close to the accretion disk should be rotating quickly around the central supermassive black hole due to its proximity to the central mass concentration. Thus this gas emits with broad lines, with the increased velocity width caused by Doppler broadening due to the motion of the gas, and hence this region is called the Broad Line Region (BLR). To provide the obscuration along certain lines of site, dense gas and dust are situated outside the BLR in a form of torus that does not let the radiation escape from the regions around the black hole, except along the poles along the torus axis (Antonucci, 1993). This reasonably well collimated radiation field is then able to ionize gas in the outer region where the gas is less dense and with lower velocities than the BLR, causing narrow emission lines, and is named the Narrow Line Region (NLR). The collimated radiation field usually forces the NLR to have a biconical shape.

1.1.2 Quasars and Quasi-Stellar Objects

Quasi-Stellar Radio Sources (quasars) were discovered in the late 1950s. They were recorded as radio sources with no optical detection, with many discovered in the Third Cambridge Catalogue of radio sources (Bennett, 1962). The visible counterparts to some of these radio sources were discovered later (Schmidt, 1962; Matthews & Sandage, 1963), which enabled the first optical spectrum to be obtained showing that the quasar 3C273 had a spectrum where the Hydrogen Balmer lines were redshifted ($z = 0.158$) with respect to the rest frame (Schmidt, 1963).

Over the following decades many more quasars were discovered and and it became clear that the vast majority did not emit strongly at radio wavelengths, thus the term Quasi-Stellar Object (QSO) was introduced to describe all source with bright nuclear emission regions. Nowadays, these objects are divided into radio-loud and radio-quiet classes although the term “quasar” is used more generally for both QSOs and quasars. Their emission across the spectrum covers the range from X-ray to the far-infrared while some are strong sources in radio and gamma rays.

Quasars and QSOs are bright and can be found at high redshift, and the combination of having very broad lines and bright narrow forbidden lines are some of their spectral characteristics (Greenstein & Schmidt, 1964). It is now widely believed that QSOs are distant and

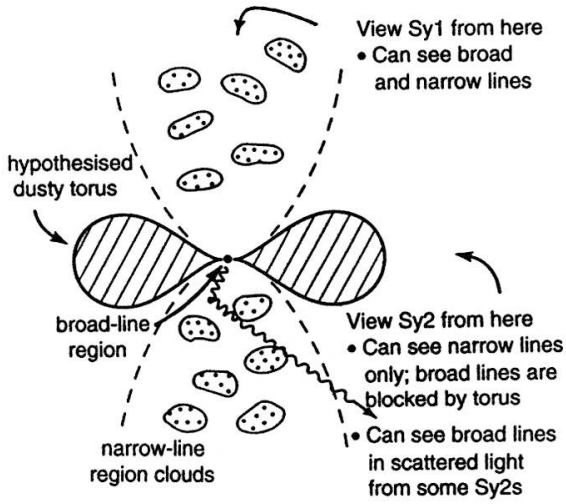

Figure 1.2: Cartoon taken from Roy et al. (1994) showing how our line of sight effects the classification of Seyfert galaxies. If we look along the axis of the torus we can see the BLR and the accretion disk while if we look along the edge, the torus blocks the view of the BLR and we can only see the NLR.

powerful active galactic nuclei with a huge luminosity, that is the result of the accretion disc around a central supermassive black hole, in other words, more powerful counterparts of the Seyfert galaxies.

QSOs are a particular type of AGN like Seyfert 1, but with higher luminosity, which is possibly related to the higher mass of the black hole. Fig. 1.3 shows a composite quasar spectrum, produced by combining quasar spectra from the Sloan Digital Sky Survey (Vanden Berk et al., 2001), showing that the broad permitted and narrow forbidden emission lines can be seen in much the same way as for Seyfert 1 galaxies but with higher luminosities.

1.1.3 Obscured or Type II Quasars

In addition to the quasars described above, there also exists a population of obscured quasars (e.g. Norman et al., 2002; Zakamska et al., 2003). Obscured quasars do not exhibit the blue continua or broad lines seen in unobscured quasars, and their nuclear radiation does not outshine host galaxies. In imaging data they therefore resemble normal, inactive galaxies (Jarvis et al., 2005; Martínez-Sansigre et al., 2005, 2006) and due to this fact are more difficult to identify than the unobscured quasars.

Most studies have concentrated on using X-ray observations to select hard-spectrum sources, i.e. those with an excess of emission at higher energies (e.g. Almaini et al., 1995; Ohta et al., 1996; Akiyama et al., 2002), to find these obscured AGN. However, the *Spitzer Space Telescope* revolutionised this field, since a quasar obscured by dust would heat up the obscuring dust which would then emit thermal radiation at a wavelength dictated by the temperature of the dust. As quasars emit at both X-ray and UV wavelengths, the dust should be relatively hot but still below the sublimation temperature of approximately 1500 K for graphite and approximately 1000 K for silicate grains (e.g. Granato et al., 1997).

We would also expect the majority of the dust to lie in a torus, invoked by unified models

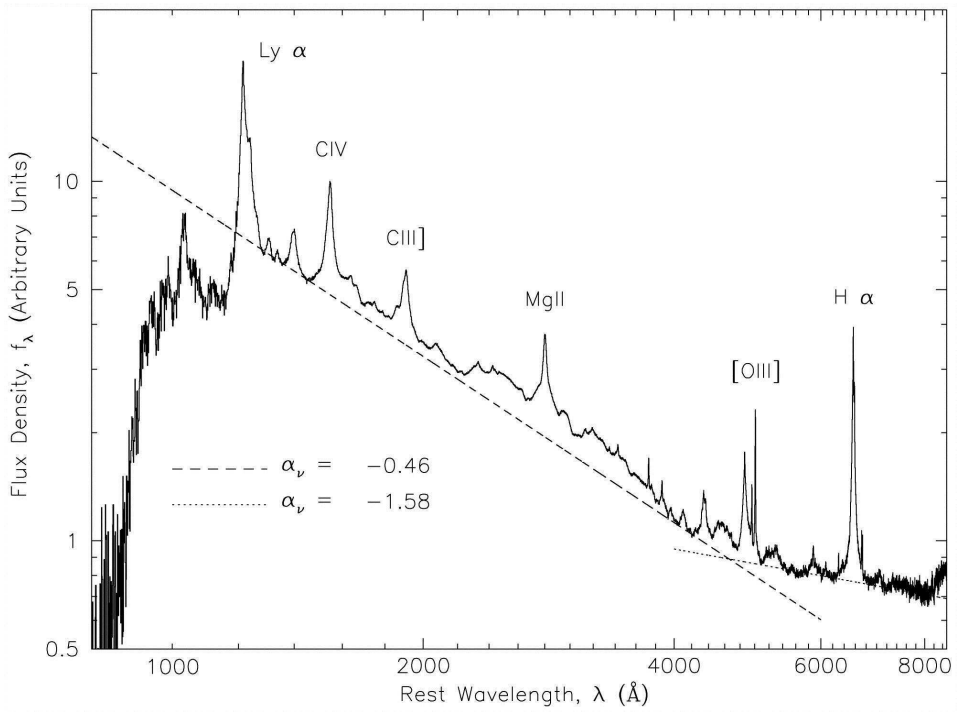

Figure 1.3: Composite quasar spectrum of quasars from the Sloan Digital Sky Survey with $0.044 \leq z \leq 4.789$.(Vanden Berk et al., 2001).

(Section 1.2), to be at a lower temperature than the sublimation temperature (since we expect the outer regions of the torus to be cooler than the inner regions). Using Wien's law we find that the peak of the thermal black body radiation occurs at $2 - 30\,\mu$m for temperatures spanning 100–1500 K. Therefore targeting objects that peak at mid-infrared wavelengths, where *Spitzer* was very sensitive, allows the identification of large samples of obscured AGN (e.g. Lacy et al., 2004; Stern et al., 2005; Martínez-Sansigre et al., 2005, 2006; Polletta et al., 2006; Villar-Martín et al., 2011). Obscured quasars are sometimes referred to as type 2 quasars in accordance with the naming convention of Seyfert galaxies.

1.1.4 Blazars

The blazar category of AGN is a combination of optically violent quasars (OVVs) and BL Lac objects (Angel & Stockman, 1980). BL Lac objects are characterised by flat spectra, variable optical flux and highly variable optical polarisation (Miller et al., 1978). They do not show emission or absorption lines in their spectra. OVVs have all the properties of BL Lac objects but they also exhibit luminous broad lines in their spectra (Miller et al., 1978).

Blazars can be explained by powerful relativistic jets, which are presumably related to the accretion of matter towards the central super massive black hole, which are pointed along our line of sight and tend to show apparent superluminal velocity. At all frequencies, they have rapid variability as well as having high polarisation and also in some cases there is a lack of strong optical emission lines.

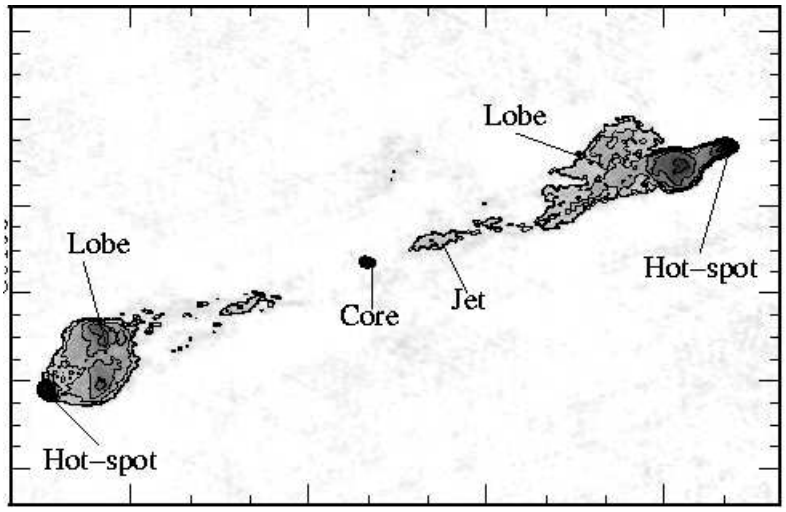

Figure 1.4: Radio wavelength image of the radio galaxy, Cygnus A. The central point is the galaxy nucleus, which feeds the jets and lobes of radio emitting plasma.(Carilli & Barthel, 1996)

1.1.5 Radio galaxies

Radio galaxies are radio loud AGN with luminosities up to 10^{39} W, they derive their energy from gravitational potential energy on galactic scales due to their central super massive black hole and their radio emission is due to the synchrotron emission. Their main observed structural components are radio core, radio jets, radio lobes and hotspots as shown in Fig. 1.4. The radio core is located in the centre of the host galaxy and associated with the nucleus. This component usually has a flat spectrum and a linear size of less than ~ 0.2 pc. Radio jets link the core to the outermost part of the radio structure and may be visible over all their path or just part of it. They are collimated by the magnetic fields and constitute a small part of the total radio flux density of the radio galaxy. Their spectral index is usually between $-0.8 < \alpha < -0.5$, where we define $S_\nu \propto \nu^\alpha$. The lobes are double symmetrical structures located on either side of the nucleus and describe the extended region of radio emitting plasma. They also have steep radio spectra similar to the jets. Hotspots are bright components on the outermost part of the radio lobes with a linear size of $\leq$1 kpc. When the jet interacts with the intergalactic medium it can create a shock which converts part of the kinetic energy to relativistic particles which then emerge as hotspots.

Fanaroff & Riley (1974) divided radio galaxies into two classes based on their morphology, and called them FRI and FRII radio sources. The FRI sources have bright cores and dark lobes while the FR II sources have bright lobes and hotspots located up to large (Mpc) distances. Fanaroff & Riley (1974) found a divide in luminosity between these two classes at $L_{178} = 2 \times 10^{26}$ W Hz^{-1}, with FRII sources being more luminous than FRIs. Most FRI objects exhibit jets and have steep spectra, which become steeper towards the outer part of the structure. The jets are wide, complicated and distorted while the FRII jets are faint, narrow, smooth and bright hotspots at the end of the lobes.

Radio galaxies are also classified into two other groups based on their optical emission lines, Broad Line Radio Galaxies (BLRGs) that have broad line spectra similar to Seyfert 1 galaxies but no discernible nuclear continuum emission, while the Narrow Line Radio Galaxies exhibit

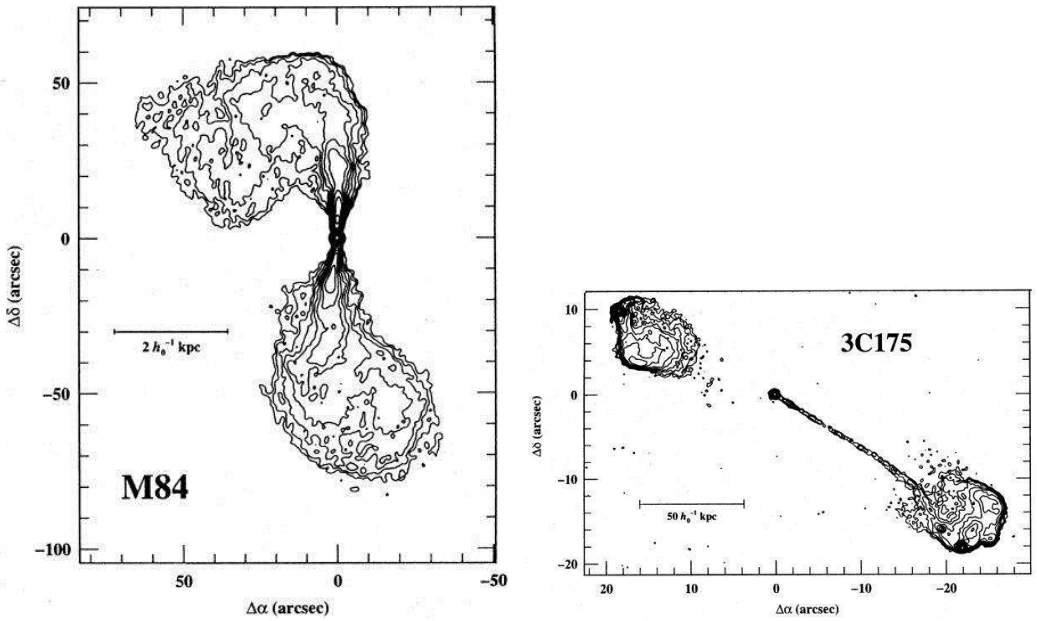

(a) FRI (b) FRII

Figure 1.5: Example of a Fanaroff-Riley type I and type II galaxies. (a) shows a radio map of the 3C 272.1(M84) based on VLA 4.9 GHz data (Laing et al., 1983), and (b) shows a radio map of the 3C 175, as observed with the VLA at 4.9 GHz.

only narrow lines for both permitted and forbidden transitions (McCarthy, 1993).

1.2 Unification schemes

Observational evidence suggests that different types of AGN may be unified into a single paradigm where the difference between the various AGN classifications is just based on orientation (Antonucci, 1993; Urry & Padovani, 1995), although alternatives based on an evolutionary picture (e.g. Sanders et al., 1988) also warrant discussion.

1.2.1 Orientation-based Unification of AGN

In the orientation-based unified scheme, the central part of the AGN is comprised of a supermassive black hole, of mass 10^7–10^{10} $M_\odot$. Surrounding this is an accretion disc composed of gas, where viscosity of the gas removes angular momentum and thus heats it up. The accretion disc is extremely hot, with an approximate temperature of 10^5–10^6 K (e.g. Bonning et al., 2007). It is exceedingly luminous from optical to X-ray wavelengths (particularly its inner region) and is the source of the radiation which originates in the centre of the AGN.

As discussed in Section 1.1.1, the accretion disc is surrounded by dense, fast-moving dust clouds that make up the broad line region (BLR). Their density means only permitted emission lines are seen, whilst the high velocity (typically ~ 5000 km s^{-1}) gives rise to the width of the lines.

The key component of the orientation-based unification model is that beyond the central regions of the black hole and BLR there is a dusty torus composed of graphite and silicate particles. The dust in the torus is able to absorb UV and X-ray radiation from the central engine and re-emits it in the infrared. The toroidal shape of this component is important since it permits a view of the central engine to some observers but not to others, depending on their viewing angle, which is key for the orientation-based unification model (Fig. 1.6) .

Beyond the torus (and thus visible to all observational lines of sight) is the narrow line region (NLR), comprised of slower moving (200–900 km s^{-1}) gas clouds with a lower density than those in the BLR. This lower density means that both permitted and forbidden emission lines are seen in the spectra from these regions.

The foundations of the orientation-based unified scheme were established with the detection of broad emission lines in the polarised spectrum of the Seyfert 2 galaxies (Miller et al., 1991). This was interpreted as the polarised broad emission lines emanating from the BLR, where photons are scattered off the inner regions of the dusty torus to produce the polarised signal. These observations therefore suggest that the Seyfert 1 and 2 galaxies are basically the same type of object, but the orientation with respect to our line of sight determines what we see (Osterbrock, 1978). In all types we are able to see the NLR as these clouds reside outside the dusty torus, whereas we only see the BLR (and the bright nuclear emission) if we are looking along the axis of the dusty torus.

One of the issues with the simple orientation-based unification scheme is that there is no explanation for the radio loud and quiet subsets. Barvainis et al. (2005) argue that in radio-quiet AGN the jets become entangled with the inter-stellar medium (ISM), thus the powerful extended radio structures, that are used to define the radio loudness, cannot be formed. Begelman et al. (1984) and Ye & Wang (2005) suggested another model based on the spin of the black hole which shows the black holes with higher spin rate produce more jets. (See also Martínez-Sansigre & Rawlings (2011a,b).)

In the case of radio-loud AGN, two parameters are needed to apply the orientation-based unification scheme. The first one is common with the radio-quiet objects, which is their observed visible-wavelength properties depend on the orientation of the AGN, while the other is the angle that the jet makes to the line of sight, since relativistic beaming needs to be accounted for. As Fig. 1.6 shows FRI radio galaxies can be interpreted as counterparts to BL Lac objects, where the jets are misaligned with our line of sight in FRIs but along the line of sight in BL Lacs. The narrow line FRII radio galaxies can also be explained as the misaligned parent population of radio-loud quasars while the jet and the line of sight are aligned close for the OVV sources (Barthel, 1989).

1.2.2 Modifications to Orientation-based Unification of AGN

Although the traditional Unified Scheme described above provides a good description of most of the observed properties of AGN, there have also been attempts to explain some of the more subtle properties of AGN via modifications to the simple orientation picture. One of the most popular modification is the so-called "receding torus model", first suggested by Lawrence (1991).

This idea stems from the fact that the spectral energy distributions of quasars longward of 1μm appear almost identical (e.g. Elvis et al., 1994). This consistency of spectral shapes into

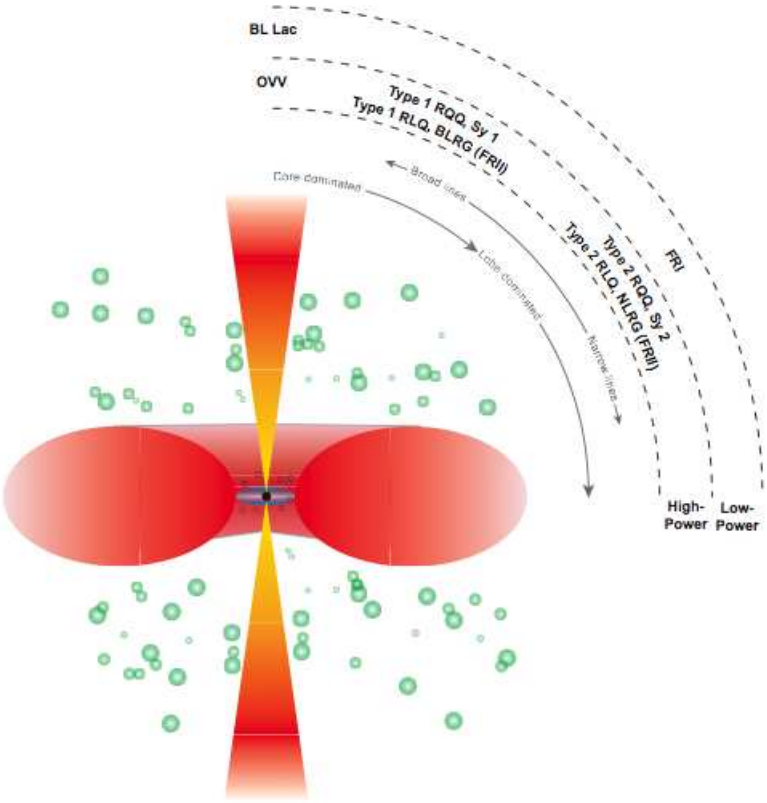

Figure 1.6: A conceptual AGN unification scheme which shows how the orientation along the line of sight leads to different AGN classifications. Taken from Urry & Padovani (1995).

the near-infrared waveband implies that the location of the inner surface of the dusty torus (see Figure 1.6) is determined by the distance at which dust can survive without sublimating due to the heat emitted from the accretion disc. This idea is also reinforced by time-delay experiments in the optical and near-infrared wavebands (e.g. Clavel et al., 1989), where more luminous objects exhibit longer time delays between the optical and the near-infrared continua. The result of a receding torus model is that more luminous AGN have larger torus opening angles, which in turn leads to the observed fraction of Type 1 AGN increasing with quasar luminosity.

Low-frequency radio surveys have provided some of the strongest evidence in support of the receding torus model where the low radio frequency selection provides an effective way of creating a sample free of orientation biases, as the selection is based on the optically-thin extended lobe emission which should be the same in pole-on and edge-on radio sources. Many studies have found evidence for a higher fraction of quasars with respect to the obscured Type 2 radio galaxies in these samples, (e.g. Hill et al., 1996; Simpson et al., 1999; Simpson & Rawlings, 2000; Willott et al., 2000; Grimes et al., 2004). In addition to radio based surveys, X-ray surveys which are also less influenced by orientation than optical surveys (e.g. Luo et al., 2011), have found similar evidence (e.g. Steffen et al., 2003; Hasinger, 2004).

Furthermore, using narrow-emission lines as a tracer of the orientation of the AGN, Simpson

(2005) determined the luminosity function for the [OIII] emission line for both broad- and narrow-line AGN (or type 1 and type 2 AGN) line. He found that the fraction of broad-line AGN increases with luminosity of the [OIII] line, consistent with the receding torus model. However, this study does assume that [OIII] is an isotropic tracer of the intrinsic AGN luminosity and this has recently been called into question (Fine et al., 2011). More recent work using the *Spitzer Space Telescope* has also found evidence that the receding torus model may be correct. Treister et al. (2008) used 24μm observations to show that the level of hot-dust emission appears to decrease with increasing bolometric luminosity.

However, a critical review of the receding torus hypothesis was undertaken by Lawrence & Elvis (2010) where they suggest that the evidence of an increasing fraction of Type 1 objects may be due to selection effects and misclassification of genuine Type II objects. Thus, it is still unclear whether some of this evidence may be due to obscuration in the host galaxy, leading to the picture of an evolutionary unified scheme (e.g. Section 1.2.3; Sanders et al., 1988).

1.2.3 Evolutionary-based Unification of AGN

Although the orientation-based unified scheme, along with modifications along the lines of the receding torus model, explain many properties of the AGN phenomenon, they do not explain everything. Evolution in the properties of AGN should play some role, as we know that AGN have lifetimes much shorter than the Hubble time (e.g. Martini & Schneider, 2003). Thus an alternative to the simple orientation-based unified scheme is one in which the galaxy hosting the AGN moves from an obscured system to an unobscured system over a period of time. An evolutionary scenario was proposed by Sanders et al. (1988) who found strong evidence of AGN activity in infrared-luminous galaxies which are thought to be undergoing a major episode of obscured star formation. Since this early work, other groups have also found evidence that an evolutionary scheme, in which galaxy mergers play a key role, may be needed to understand AGN in the Universe (Sanders & Mirabel, 1996; Surace et al., 1998; Surace & Sanders, 1999; Canalizo & Stockton, 2000, 2001a). More recent detailed studies of AGN host galaxies however, find mixed evidence of merger triggered AGN activity (e.g. Bahcall et al., 1997; Dunlop et al., 2003).

In the high redshift Universe, where the bulk of the AGN activity occurs (see Section 1.5.7), work with (sub-)mm telescopes has paved the way to studying "host-obscured" AGN. Alexander et al. (2005) used deep X-ray observations to determine the AGN component in far-infrared/sub-millimetre bright high-redshift galaxies, presumably undergoing a major burst of star formation, and find evidence for continual growth of the supermassive black hole during this intense star-burst phase. Later the same group suggested that the black holes in these obscured systems had an order of magnitude less mass than their unobscured counterparts (Alexander et al., 2008).

More recently, Rafferty et al. (2011) studied a large sample of AGN at $0.3 < z < 3$ at 70μm, to investigate how AGN activity may be linked to the strength of the star-burst. They find evidence that the most intense bursts of star formation in galaxies is accompanied by an increasing probability of AGN activity, with around 30% of these far-infrared bright galaxies exhibiting X-ray emission due to an AGN. This is very similar to that found in the higher redshift sub-mm galaxies and suggests that the mergers which cause the most intense star-burst events in high-redshift galaxies may also trigger the AGN activity.

From these studies, and many others, it is clear that an evolutionary unification is probably needed to account for some of the properties of the whole AGN population. However, we still do not have a clear understanding of when and how the evolutionary unification dominates our selection of AGN at various wavelengths over the more traditional orientation-based unification. Deep imaging studies underway with the *Hubble Space Telescope* (e.g. Kocevski et al., 2012) combined with some of the deepest observations at X-ray and far-infrared wavelengths using *Chandra* (e.g. Brandt & Alexander, 2010), *Herschel* (e.g. Mullaney et al., 2012) and now ALMA (see e.g. Simpson et al., 2012, for a precursor to the work that will be possible with ALMA) should elucidate this connection in the near future.

1.3 Triggering of AGN activity

A broad range of triggering processes of AGN have been suggested to explain how gas is supplied to the AGN nucleus, where it can then trigger an active phase of the supermassive black hole. The disturbance of the galaxy potential is one of the possibilities to supply the gas to the central region. Tidal interaction in mergers and satellite accretion makes the gas funnel towards the nucleus and supply the black hole (Lin et al., 1988). Various studies have found evidence of disturbance and interactions including tails, fans, bridges, shells and dust lanes in radio galaxies (for example Heckman et al. (1986); Canalizo & Stockton (2001b); Canalizo et al. (2007); Bennert et al. (2008); Tasse et al. (2008)). Heckman et al. (1986) and Roche & Eales (2000) found that $> 85\%$ of radio galaxies show signs of disturbance while the morphological disturbance that FRI sources show is less than FRII radio galaxies (Heckman et al., 1986; Baum et al., 1992).

Hierarchical galaxy evolution models also suggest that the gas-rich mergers cause AGN activity (Di Matteo et al., 2005; Hopkins et al., 2008). Although the interaction of gas-rich objects may trigger AGN activity, several observations have detected large amounts of gas in early type galaxies which do not harbour an AGN (Morganti et al., 2006; Combes et al., 2007). Thus gas rich galaxy mergers are not a sufficient condition to activate the black hole, and even accretion of small companion galaxies may provide the required masses. Since only a small amount of gas ($10^3 < M_{gas} < 10^5 M_\odot$) is required to trigger the black hole (van Gorkom et al., 1989), the accretion of the cold gas from the intergalactic medium (IGM) could be another possibility to cause the nuclear activity (Kaufmann et al., 2006; Dekel & Birnboim, 2008; Brooks et al., 2009).

The accretion onto a super massive black hole can also be driven by a stellar bar on the kpc scale, resulting in a gaseous disk with radius of 100 pc. Instabilities of the disk allows the material to flow inward and trigger a nuclear starburst (Shlosman et al., 1989; Schinnerer et al., 2007); most studies of this subject have been done on nearby late type objects.

On the other hand, Dunlop et al. (2003) used HST imaging of the host galaxies of low redshift radio-loud quasars, radio-quiet quasars and radio galaxies and conclude that AGN hosts lie in the most massive and old population of ellipticals, with very few signs of merger activity. Their result also showed that quasars in their sample have a central black hole with a mass of $5 \times 10^8 M_\odot$, with the radio-loud subset containing black holes with mass $> 10^9 M_\odot$.

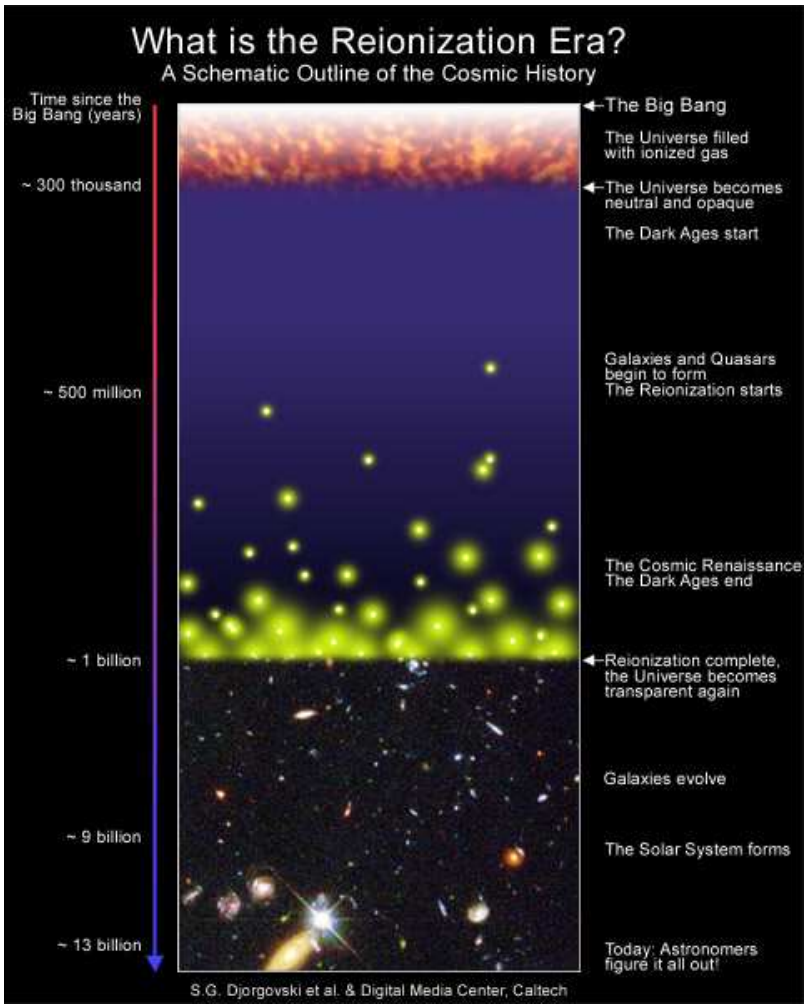

Figure 1.7: Cartoon representation of the history of the universe. Taken from http://www.astro.caltech.edu/∼george/reion/.

1.4 A brief history of the Universe and the Epoch of Reionization

The formation of the first galaxies played a crucial role in the evolution of structure in the universe but they also transformed the neutral intergalactic medium to ionised plasma, this period in the Universe is called the Epoch of Reionization. At redshift 1100 (∼ 350,000 years after the Big Bang) the density of the Universe has decreased and cooled enough to allow photons to decouple from baryons and make the universe transparent, and it is at this point that we are able to see the first radiation permeating throughout the Universe in the form of the cosmic microwave background (CMB) radiation. After this time the universe entered the dark ages, where the first stars and galaxies had yet to form and there was essentially no source of high-energy photons in the Universe. After about 400 million years the first galaxies began to form and start to emit radiation (see e.g. Abel et al., 2002; Jeon et al., 2012). This period marks the start of the Epoch of Reionization (EoR). At the beginning of the EoR the intergalactic

medium was predominantly neutral except the regions close to the first objects. After enough UV-radiation has been emitted from these first objects the temperature and ionised fraction of the gas increases until the neutral gas is reduced to a small fraction of the density of the Universe, allowing photons to traverse through the Universe without being absorbed by the neutral gas (Barkana & Loeb, 2001; Bromm & Larson, 2004; Morales & Wyithe, 2010).

Some of the key aims of current and future facilities are to determine which sources are responsible for reionising the Universe, how quickly this occurred, and when it ended. To measure the speed at which reionization occurs, one needs to trace the evolution in the abundance of neutral hydrogen at these early epochs.

The first direct measurement that established that we are beginning to see the EoR at $z > 6$ came from observations of the highest-redshift quasars found by the SDSS (Fan et al., 1999, 2000, 2001). Becker et al. (2001) and Fan et al. (2002) both found evidence for a Gunn-Peterson trough (Gunn & Peterson, 1965), i.e. the complete absorption of Lyα photons resulting in a trough of zero flux shortward of the Lyα emission line in the high-redshift quasars due to a high neutral fraction. From these observations it is now clear that the EoR was coming to an end around $z \sim 6.3$.

However, the Gunn-Peterson trough does not provide the complete picture. This is because neutral hydrogen is too good at absorbing Lyα photons, therefore information about the rate of evolution of the neutral fraction within the EoR is difficult to determine and relies on assumptions about the intrinsic line profile of the Lyα emission line in distant quasars (e.g. Mortlock et al., 2011; Bolton et al., 2011).

An alternative method of tracing the neutral hydrogen abundance at these early epochs is to use the hyperfine transition of neutral hydrogen at a rest-frame wavelength of 21 cm, i.e. in the radio waveband. At $z > 6$ this line is redshifted to low frequencies ($\nu < 200$ MHz). It is only now becoming possible to observe these frequencies to sufficient depth where we may detect the signature of reionization through the 21 cm line with the imminent commissioning of the Low-Frequency Array (LOFAR; Heald et al., 2011) and the Murchison Widefield Array (MWA; Williams et al., 2012), both of which lead towards the much larger Square Kilometre Array (SKA; Carilli & Rawlings, 2004). The evolution of neutral hydrogen within the EoR can be investigated broadly by two methods. The first utilizes the power spectrum variations in the intensity of the 21 cm radiation (Iliev et al., 2008; Harker et al., 2010) and is where the majority of current work is concentrated. However, an alternative method would be to measure the 21 cm forest against background powerful radio sources (e.g. Carilli et al., 2002), in much the same way that the Lyman-α forest is used to probe the intergalactic medium at lower redshifts (Péroux et al., 2001). The key missing ingredient for this method to be successful is the discovery of powerful radio sources at sufficiently high redshift with which to observe the 21 cm forest.

1.5 High redshift radio galaxies as probes of the EoR

Obvious targets to enable the measurement of the 21-cm forest in the EoR are high-redshift radio-loud AGN. Although searches for quasars at $z > 6$ may yield some radio-loud sources suitable for measuring the 21-cm forest, a large fraction of radio-loud AGN would be omitted from such a strategy as only around 15 per cent of quasars tend to be radio loud (Ivezić et al.,

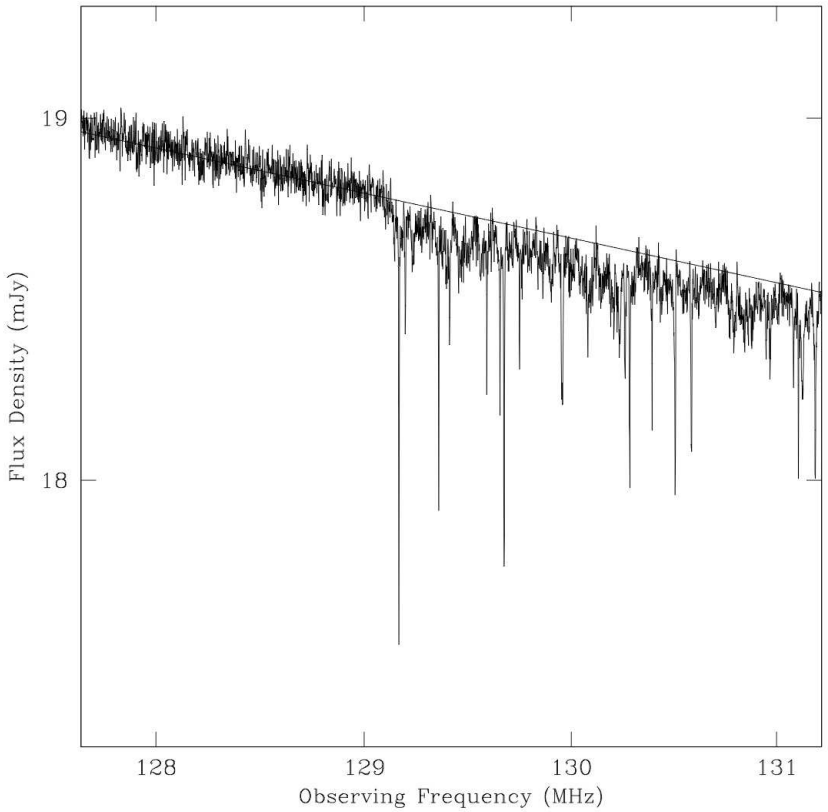

Figure 1.8: Simulated spectrum of a high redshift radio galaxy from Carilli et al. (2002) with S=20 mJy at z=10. HI 21cm absorption by the neutral IGM is seen above 129 MHz (corresponding to $z = 10$ for 21 cm radiation) due to the neutral hydrogen abundance at $6 < z < 10$, with $z = 6$ corresponding to a redshifted 21 cm line at ~ 200 MHz, beyond the extent of the figure.

2002). However, if we are able to find other types of high-redshift radio-loud AGN, i.e. radio galaxies, then this provides us with a complementary strategy for answering the key question on the evolution of the EoR. In this section I describe the key observational properties of high-redshift radio galaxies and then go on to highlight how we can use these properties to search for radio galaxies at very high redshift.

1.5.1 Ionized Gas

Bright emission lines in radio galaxies are a tool that enables us to determine their redshift in relatively short spectroscopic observations, and therefore play a crucial role in making them useful cosmological probes. The composite emission line spectrum for high redshift radio galaxies, given by McCarthy (1993) demonstrates that the key emission lines are the Balmer series of Hydrogen and the Lyα λ1216Å line which can be observed to $z > 6$ with optical spectrographs. Lyα is also usually highly extended in powerful radio galaxies. These emission-line haloes can be extended up to $\sim$200 kpc and they may be tracing the gas from which the galaxy forms (e.g.

Dekel et al., 2009). These ionised gas halos have Lyα luminosities up to $\sim 10^{37}$ W and line widths between a few hundred km s^{-1} in their outer parts to > 1000 km s^{-1}, near the centre of galaxy nucleus (e.g. McCarthy, 1993; Jarvis et al., 2003). The morphology of the Lyα halos is clumpy and usually aligned with the radio axes. The inner region has a relatively high velocity dispersion, which may be induced by hydrodynamical interactions of the radio jets with the gas, while the low velocity dispersion of the outer part could be due to rotation of a protogalactic gas cloud (e.g. van Ojik et al., 1997). Although the Lyα line is spectacular in high redshift radio galaxies, other emission lines such as CIV, [OII], [OIII] are also detected in their spectra. The chemical abundance of the halo gas is close to solar (Vernet et al., 2001; Humphrey et al., 2006) consistent with the high redshift radio galaxies having undergone prodigious star formation at earlier epochs. The higher ratio of Lyα/HeII beyond redshift 3 shows that the star formation rate in high redshift radio galaxies may have been higher in the past Villar-Martín et al. (2007a), since the difference in ionisation parameter between HeII and Lyα means that the Lyα radiation is enhanced in a softer ionisation field, such as stellar photospheres, whereas a harder radiation field would not lead to such an enhancement, although we also note that metallicity can also play an important role.

Different scenarios have been suggested to explain how the gas is excited including photoionisation from an AGN, photoionisation from stars, photoionisation by X-rays emitted by shocked hot gas and collisional ionisation from shocks (for a review see Miley & De Breuck, 2008). Various studies have shown that in the case of nearby radio galaxies, both jet powered shocks and photoionisation by the central AGN can be responsible (e.g. Villar-Martin et al., 1997; Bicknell et al., 2000; Groves et al., 2004). In the case of high redshift radio galaxies, the interpretation of emission line ratios are however influenced by dust and viewing angles (Sec. 1.2; Villar-Martin & Binette, 1996) and most of these sources are spatially extended over regions of 10 or more kiloparsec thus the interpretation of the source of excitation becomes more complicated. However, photoionisation from an AGN is thought to be the dominant source of excitation in these distant sources (Humphrey et al., 2006) but not the only one. Variations in relative emission line strength within individual high-redshift radio galaxies shows that collisional excitation from shocks particularly close to radio jets could be another possibility (Bicknell et al., 2000; Best et al., 2000).

For distant radio galaxies the optical and UV emission from the host galaxy can be aligned with the axis of their relativistic plasma jet (Fig 1.9; McCarthy et al., 1987; Chambers et al., 1987; van Breugel et al., 1998; Pentericci et al., 1999; Bicknell et al., 2000). This alignment effect can be seen in radio galaxies at redshifts above 0.7. Studies show that the alignment effect increases at z > 2.5 and display more clumpy structure than their low redshift counterparts (Pentericci et al., 1999, 2001).

The infrared structure of radio galaxies in the 6C sample at $z \sim 1$ is less aligned with the radio structure than the radio sources in the 3C sample at the same given redshift which shows the radio luminosity dependency of the alignment effect (Eales et al., 1997). Although the optical polarisation in high redshift radio galaxies provides evidence of dust scattering, it cannot explain the alignment effect alone, and a combination of star formation induced by the jets and scattering of hidden quasar light may be responsible for this effect. Studies of 4C41.17 at z= 3.8 showed the interaction between a powerful jet and dense clouds in its halo produce shock-excited emission lines and induced star formation (Bicknell et al., 2000), while many studies of low redshift radio galaxies also presented evidence of jet-induced star formation (van

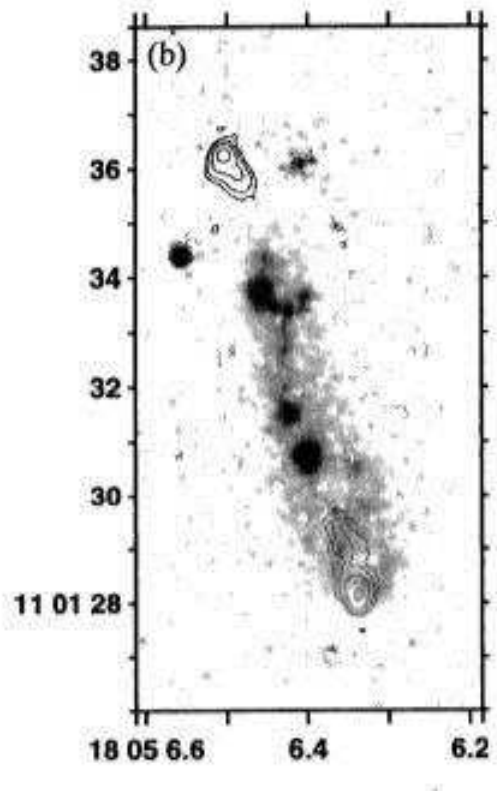

Figure 1.9: Radio continuum contours overlaid on a rest-frame U/B-band image of 3C368 at z = 1.13 (Best et al., 1996). The X and Y axis present the RA and DEC respectively.

Breugel & Dey, 1993; Graham, 1998; Croft et al., 2006).

1.5.2 Molecular Gas

Star formation occurs in molecular clouds. Unfortunately H_2 emission is not easy to detect and thus CO, which is the next abundant molecule and also a good tracer for molecular hydrogen has been used (Evans et al., 1996; van Ojik et al., 1997; Solomon & Vanden Bout, 2005; Omont, 2007). In the case of nearby galaxies, the mass conversion factor between CO and H_2 is derived based on ultra-luminous infrared galaxies (ULIRGS) observations (Downes et al., 1993). If one assumes that this value is applicable to high redshift radio galaxies, the mass of the molecular gas also can be derived. The calculated mass of H_2 in radio galaxies with CO detections is $\sim 10^{10} - 10^{11}$ $M_\odot$, which demonstrates that there are large amounts of molecular gas which could be a resource for future star formation (Miley & De Breuck, 2008).

High-redshift radio galaxies have in the past been prime targets for detecting CO due to their bright and extreme nature. In many high-redshift radio galaxies, the CO is spatially resolved (Papadopoulos et al., 2000; Greve et al., 2004; De Breuck et al., 2005) and extended up to 20 kpc, with some studies showing the existence of the alignments between the molecular gas and radio morphologies (e.g. Klamer et al., 2004). Many searches for CO at high redshifts indicate that the ratio between the gas and dust in such sources could be systematically underestimated due to a bias in favour of dusty targets (Scoville et al., 1997; Alloin et al., 2000; Klamer et al.,

2004). To explore the evolution of the molecular gas, deeper observations will be required on well-defined samples of high redshift radio galaxies. The CO lines are faint which means that a large amount of observing time and more sensitive facilities are required. The Atacama Large Millimeter Array (ALMA) and The Jansky Very Large Array (JVLA) will be helpful in these research areas in next decades.

1.5.3 Dust emission

From extensive studies at far-infrared and millimetre wavelengths, we now know that dust obscures around 50 per cent of the star light in the Universe (Murphy et al., 2011). Therefore it is probably not surprising that high-redshift radio galaxies also contain significant amounts of dust (Dunlop et al., 1994; Ivison, 1995; Archibald et al., 2001; Reuland et al., 2004).

Reuland et al. (2004) observed a sample of 69 radio galaxies between $1 < z < 5$ at 850 and 450μm and found typical dust masses of $\sim 10^8$ M$_\odot$. There are two explanations for the heating source of the dust, from an AGN or from young stars. Since both processes are able to heat dust to partially overlapping temperatures at around 20-100μm, it is difficult to distinguish whether the source of heating is the AGN or young stars. Some studies show that since the dust temperature is relatively cool $\sim$ 50K it could be due to heating from young stars (Archibald et al., 2001; Stevens et al., 2003; Reuland et al., 2004) while there is also evidence for warmer dust temperatures in radio galaxies which shows the AGN as a source of heating (Rocca-Volmerange & Remazeilles, 2005).

Recently, observations with the *Herschel Space Observatory* have shown that the amount of dust emission may also be related to the radio emission and/or the accretion rate of the central AGN (Hardcastle et al., 2010; Seymour et al., 2010) and that the temperature of the dust is the key governing factor in this rather than the dust mass (Hardcastle et al., 2012).

1.5.4 Stellar masses of radio galaxy hosts

There have been many studies on characterising the stellar populations in distant radio galaxies (Dey et al., 1997; van Breugel et al., 1998; Simpson & Eisenhardt, 1999; Pentericci et al., 2001; Zirm et al., 2005), as they provide a clear view of the host galaxies of AGN, unlike quasars where the quasar light outshines the host. Spectral energy distributions (SEDs) are a powerful tool to explore the stellar populations and galaxy evolution while the UV and 4000Å break provide information about the young and old stellar population respectively. The SEDs of old (> 1 Gyr) stellar populations peak in the near-IR and high redshift radio galaxies have very bright $K-$band luminosities in the early universe compared to normal galaxies (e.g. De Breuck et al., 2002). Therefore the brightness of the observed $K-$band emission has been used to argue that distant radio galaxies are very massive ($\sim 10^{12}$M$_\odot$; Rocca-Volmerange et al., 2004; Seymour et al., 2007) and at least for the most powerful ones occupy the most massive galaxies at all cosmic epochs. Most of the reasoning behind this has come from a wealth of previous studies of high redshift radio galaxies that have shown a tight correlation in the Hubble $K-z$ diagram for powerful radio sources (e.g. Lilly & Longair, 1984; Eales & Rawlings, 1996; Jarvis et al., 2001a; De Breuck et al., 2002; Willott et al., 2003; Bryant et al., 2009).

Jarvis et al. (2001a) demonstrate that there is a remarkably small scatter in the $K-z$ relation for high redshift radio galaxies, with a dispersion of $\delta K \sim 0.6$. It is now clear that

some of this scatter is due to a correlation between stellar mass and radio luminosity (Best et al., 1998; Willott et al., 2003; McLure et al., 2004; Best et al., 2005). This can be understood in the context of the radio luminosity of the radio sources depending on their accretion luminosity and thus the central black hole mass (Rawlings & Saunders, 1991; Magorrian et al., 1998).

There are also other factors that one should consider in using the $K-z$ diagram to infer galaxy mass. The first one is the difficulty of distinguishing the stellar component from the warm dust component of the $K-$band flux, as the tail of the blackbody distribution would still be present at around $1-2\mu$m in the rest frame. The second factor is the contribution of the bright emission lines to the K-band emission which may result in overestimating the mass and age (Eales & Rawlings, 1996; Jarvis et al., 2001a; Rocca-Volmerange et al., 2004), and finally the uncertainties in the stellar population models on which the masses are based (e.g. Bruzual & Charlot, 2003). A comprehensive study by Seymour et al. (2007), using data from the *Spitzer Space Telescope* investigated 69 radio galaxies between $1 < z < 5.2$ and found the stellar mass in these galaxies was between 10^{11} and 10^{12} M$\odot$ with no redshift dependence and no significant correlation between stellar mass and radio power, although their sample was generally dominated by the most luminous radio sources at all epochs, thus detecting a luminosity dependence would be very difficult.

1.5.5 Finding high-redshift radio galaxies

High redshift ($z > 2$) radio galaxies are a small subset of all radio sources. There have been many surveys to find such sources (De Breuck, 2000; De Breuck et al., 2002; Jarvis et al., 2001b,a; Best et al., 2003; Jarvis et al., 2004; Cruz et al., 2006; Brookes et al., 2008).

For the powerful nearby radio galaxy Cygnus A, at higher frequency the spectrum is steeper as shown in Fig 1.10. If we assume that all powerful radio galaxies exhibit similar spectra, due to synchrotron or inverse Compton losses, we will see the steeper part of the spectra as the redshift increases. van Breugel & McCarthy (1990) showed that in the 3CR sample the spectral index and redshift ($\alpha - z$) correlation leads support to such a hypothesis (Fig 1.11). Other surveys have also shown that radio sources with ultra steep spectral index $\alpha > 1$ tend to be fainter and reside at higher redshift than the less steep spectral-index radio sources (Tielens et al., 1979; Blumenthal & Miley, 1979; Chambers et al., 1996; De Breuck et al., 2002; Cohen et al., 2004; Cruz et al., 2006).

One physical interpretation of the $\alpha - z$ correlation is basically the relation between the band shifting and redshift, i.e. by increasing the redshift we could see the steeper part of the spectra. However, there is evidence that the spectra of at least some high-redshift radio sources are not curved, thus resulting in an absence of a steeper spectrum at high frequencies (e.g. Klamer et al., 2006; Ker et al., 2012). Another interpretation for the steeper radio spectra is needed and this could be that the high redshift radio galaxies reside in dense environments, as this is observed at low redshift (e.g Athreya & Kapahi, 1998). Since radio emission is more pressure confined in higher gas density environments, as a consequence radio lobes in rich galaxy clusters will expand adiabatically and lose energy via synchrotron and inverse Compton losses, resulting in a steeper radio spectra.

One of the first ultra-steep spectrum searches to find high redshift radio galaxies by Chambers et al. (1990) resulted in the discovery of the $z = 3.8$ radio galaxy 4C41.17 which remained

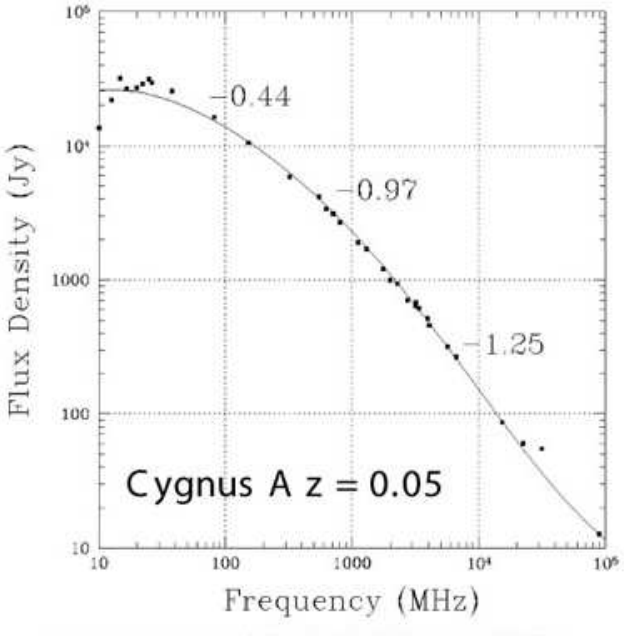

Figure 1.10: The radio spectrum of the radio galaxy Cygnus A at $z = 0.05$, showing spectral curvature. Taken from Kellermann et al. (1969).

the highest redshift radio galaxy for many years. Rawlings et al. (1996), based on the 6C* sample of radio sources (Blundell et al., 1998; Jarvis et al., 2001b,a) combined the steep-spectrum technique with a constraint on the maximum angular size of the radio galaxy to further refine the search for high-redshift radio galaxies, and discovered the most distant radio galaxy at the time, 6C0140+326 at $z = 4.41$. Two years later this was overtaken again by another ultra-steep spectrum search which found a radio galaxy at $z = 5.19$ (van Breugel et al., 1998). No radio galaxy at higher redshift than this has since been found.

However, it is clear that methods such as steep-spectral index and angular size filtering are not 100 per cent efficient and a large number of radio sources at $z > 5$ may also be filtered out (e.g. Jarvis et al., 2001c; Cruz et al., 2007). This is crucially important when the space density of the $z > 5$ radio source population is extremely low to start with.

1.5.6 High redshift radio galaxy hosts

These luminous radio galaxies have accreting super massive black holes, which emit at UV, optical, and soft X-ray energies but the bulk of the UV and optical emission is absorbed by dust, and allowing us a clear view of the host galaxy.

We have mentioned that the near infrared luminosity of high redshift radio galaxies makes them some of the most massive galaxies in the early universe, and the clumpy morphology of high redshift radio galaxies hosts is consistent with mergers and hierarchical models of galaxy evolution (Dubinski, 1998; Gao et al., 2004; Springel et al., 2005). These distant sources may also be the progenitors of the most massive galaxies, brightest cluster galaxies and cD galaxies (e.g. McLure et al., 2004).

As described in Section 1.5.4, studies of high redshift radio galaxies have shown a tight

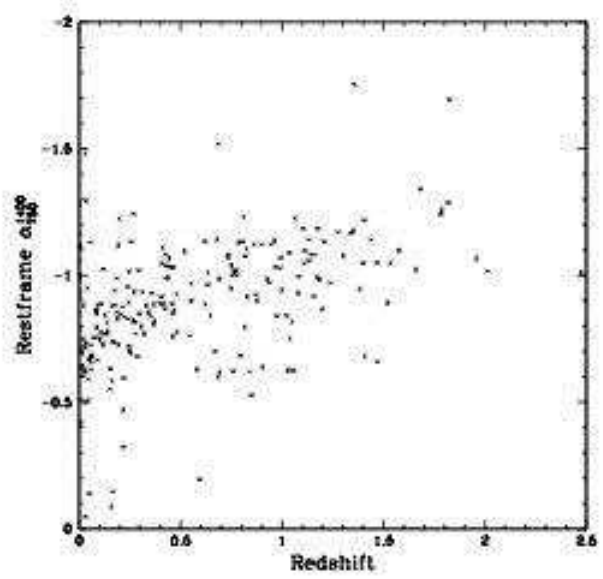

Figure 1.11: Correlation between redshift and spectral index of 3CR radio galaxies from van Breugel et al. (1998).

correlation in the Hubble K -z diagram for powerful radio sources ((Eales & Rawlings, 1996; Jarvis et al., 2001a; Willott et al., 2003; Bryant et al., 2009)). Willott et al. (2003) investigated the $K-z$ relation using various complete radio samples such as 3CRR (Laing et al., 1983), 6CE (Eales et al., 1997; Rawlings et al., 2001), 6C* (Jarvis et al., 2001a) and the 7CRS (Lacy et al., 2000; Willott et al., 2003) at different flux-density limits and concluded that 3CRR and 7CRS radio galaxies were offset by ~ 0.55 in the $K-$magnitude over all redshifts, while the 6C radio galaxies were offset by ~ 0.3 mag. They also presented the best fit for the 3CRR, 6C, 7CRS sample as,

$$K(z) = 17.37 + 4.53 \log_{10} z - 0.31(\log_{10} z)^2. \tag{1.1}$$

The $K-$band magnitude has also been used to find high redshift radio galaxies. Lilly (1988) discovered the first radio galaxy at $z > 3$ by using a flux limited sample of 70 objects based on faint $K-$band magnitude ($K \sim 18.5$). McCarthy et al. (1996) used the same technique on a larger sample which was no more successful than the Lilly one, and they only found one source with redshift above 3. De Breuck et al. (2000b) defined a sample of 669 radio sources with ultra steep spectral index over several radio surveys and selected 15% of these sources for near-infrared observations, which led them to find the highest redshift radio galaxy TN 50924-2201 at $z = 5.19$ (van Breugel et al., 1999).

1.5.7 Evolution of the Radio Luminosity Function

The radio luminosity function (RLF) describes the space density per unit comoving volume of radio sources as a function of the radio luminosity. The evolution of the RLF plays a crucial role to understand the cosmic evolution of radio sources. Longair (1966) was the first to investigate

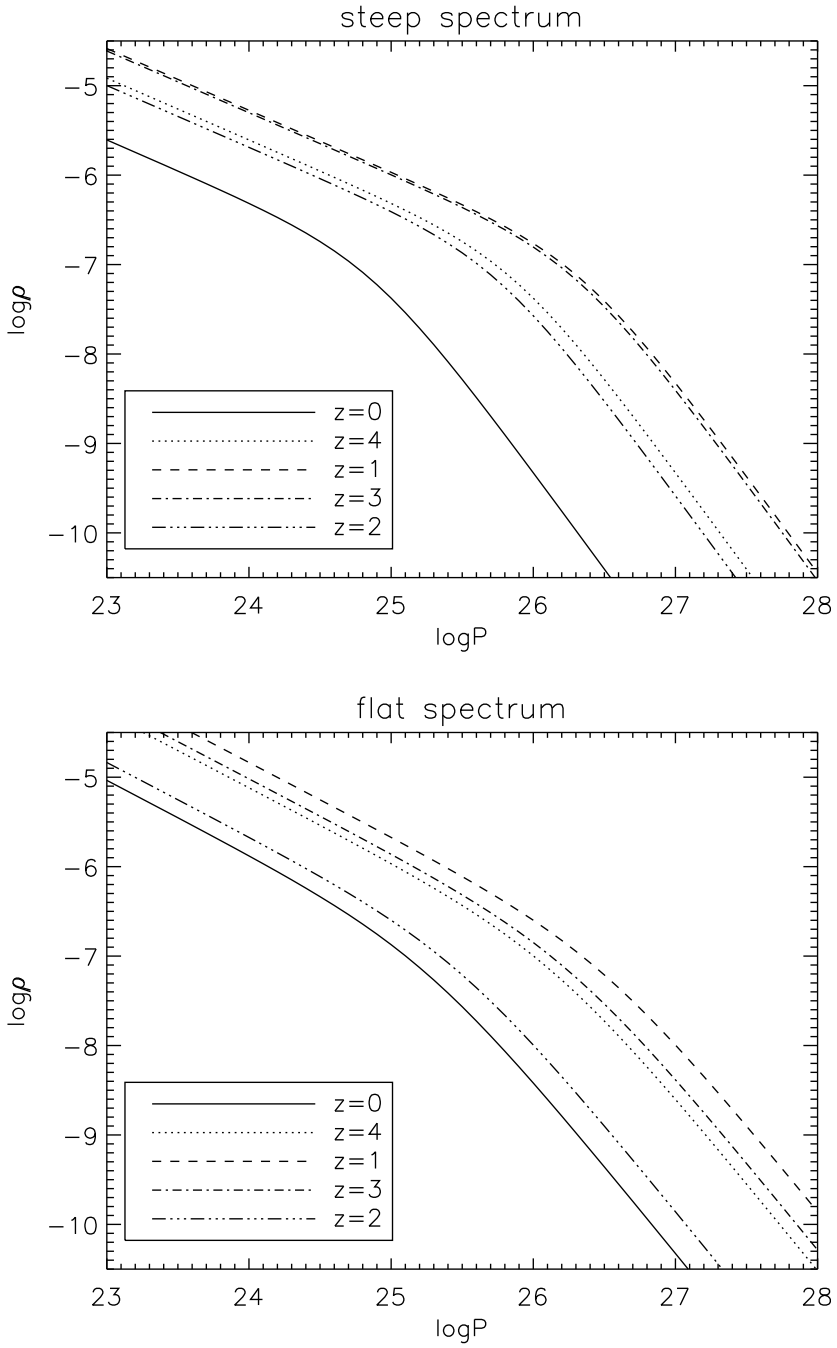

Figure 1.12: The radio luminosity function determined by Dunlop & Peacock (1990) using the pure luminosity evolution model between redshift $0 < z < 4$.

how the population of radio sources evolves, using a model based on low-frequency source counts. They found that the evolution in co-moving space density is greater in powerful radio sources. Using 3CRR (Laing et al., 1983) complete samples, Riley & Longair (1983) conclude that quasars and powerful radio galaxies have a similar evolution. Dunlop & Peacock (1990) used several complete samples at 2.7 GHz for flat and steep spectrum radio sources separately and presented the RLF for each population (Fig 1.12). They conclude that the co-moving number density increases steeply to $z \sim 2$ but decreases beyond this redshift for both steep and flat spectrum radio sources, for which they used the term "redshift cut off". However, their results were limited by the lack of spectroscopic redshifts from their faintest radio-selected sample, where they relied on the $K - z$ diagram to estimate redshifts, so they were not able to quantify the decline very strongly. Later, Shaver et al. (1996) used a sample of flat-spectrum radio sources, which are predominantly quasars and therefore easier to obtain spectroscopic redshifts for, and found evidence for a sharp cut-off in space density of these sources at $z > 2$. Jarvis & Rawlings (2000) reassessed the evidence for such a steep cut off in the space density of flat-spectrum radio sources at $z > 2$ using the Parkes Half-Jansky Sample (Drinkwater et al., 1997) and showed that the sharp cut-off found by Shaver et al. (1996) may have been caused by not considering any spectral curvature of the radio sources, i.e. Shaver et al. (1996) assumed all sources to have a flat power-law spectral slope. Jarvis & Rawlings (2000) demonstrated that by considering the presence of spectral curvature, then the 7σ evidence for a decline in the space density decreased to $\sim 2\sigma$ and that the space density was consistent with being constant with redshift. Using the same sample of radio-loud quasars as Shaver et al. (1996), albeit with more complete redshifts and multi-frequency radio observations, Wall et al. (2005) again reassessed the claim of Shaver et al. (1996) and Jarvis & Rawlings (2000). Wall et al. (2005) incorporated all spectral information, including spectral curvature, and also possible time variability in the radio continuum emission as a function of radio luminosity and frequency. They again found evidence for a decrease in the number density of flat-spectrum sources at $z \geq 3$ at the level of $\geq 4\sigma$.

The study of flat-spectrum radio sources by the various groups above, does not tell the whole picture, as the flat-spectrum population only makes up a small fraction (~ 2 per cent) of the whole radio source population (e.g. Jarvis & McLure, 2002). It is therefore useful to study the steeper-spectrum radio source population, as this is where the bulk of the population reside. Jarvis et al. (2001c) used the combined radio samples from the 3CRR (Laing et al., 1983), 6CE (Eales et al., 1997), 7CRS (Willott et al., 2003) and 6C* (Blundell et al., 1998), which had very high spectroscopic completeness to investigate the space density of radio sources at $z > 2$. They found a shallow decline in the space density of radio sources between $2.5 < z < 4.5$ in this sample of low-frequency selected sources, consistent with the decline found for the flat-spectrum population in Jarvis & Rawlings (2000), but also consistent with a constant comoving space density to high redshift. Cruz et al. (2006, 2007) extended this work to a larger sample of radio sources 6C**, selected in a similar way to the 6C* sample to filter out low-redshift radio sources using their spectral index and angular size. They also find no evidence for a decline in the comoving space density of distant radio sources.

These studies of the steep-spectrum population concentrated on the most powerful radio sources at high-redshift, and may not be comparable to the studies of Shaver et al. (1996) and Wall et al. (2005), as Doppler boosting of the flat-spectrum sources may mean that the flat-spectrum samples are dominated by intrinsically less-luminous radio sources, which in turn

may evolve differently to their more powerful counterparts.

Indeed, using a deeper radio survey, Waddington et al. (2001) found that, by comparing with brighter flux-density limited samples, the turnover for lower luminosity sources occurs at lower redshift, however the lack of volume in their survey did not allow them to make a conclusive measurement of the evolution in the comoving space density of powerful radio sources. More recently, Rigby et al. (2011) undertook an extensive investigation of the evolution of radio sources as a function of their radio luminosity. Using a range of radio surveys with varying flux-density limits, they were able to determine the redshift at which sources of varying radio power peaked. They found clear evidence ($> 3\sigma$) of declines in the comoving space density, but that this is heavily dependent on the radio luminosity. For example, radio sources with $L = 10^{25} - 10^{26}$ W Hz^{-1} appear to peak at $z \sim 0.7$, whereas for sources with $L > 10^{27}$ W Hz^{-1}, the peak moves to $z > 3$ (See Fig. 1.13). This behaviour of a luminosity-dependent redshift cut-off is also seen in samples of optical and X-ray selected AGN (Ueda et al., 2003; Hasinger et al., 2005; Richards et al., 2005; Babić et al., 2007; Wall, 2008). This property of AGN evolution therefore appears to mirror the "cosmic downsizing" scenario found for normal (non-AGN) galaxies (e.g. Cowie et al., 1996)

Although the evolution of FRII radio sources is now well established, there are still open debates on how the lower luminosity sources evolve with redshift. Due to the increased difficulty in detecting the low-power radio sources over comparable distances the low redshift evolution of low-luminosity radio sources is considerably less well constrained, but early studies of the radio source counts indicated that they could not be evolving as strongly as their high luminosity counterparts (Longair, 1966; Doroshkevich et al., 1970).

Jackson & Wall (1999) found evidence for possible negative evolution from $z = 0$ to $z \sim 1$, while Laing et al. (1983), using the complete 3CRR sample suggested no evolution for these sources. Waddington et al. (2001) found evidence of evolution in the space density between $0 < z < 1$, and Snellen & Best (2001) also found evidence for positive evolution, albeit based on only 2 objects.

Using the large amount of data available from the Sloan Digital Sky Survey cross-matched to large-scale radio surveys such as the Westerbork Northern Sky Survey (WENSS; Rengelink et al., 1997), the Faint Images of the Radio Sky at Twenty-one centimetres (FIRST; Becker et al., 1995) and the National Radio Astronomy Observatory (NRAO), Very Large Array (VLA) Sky Survey (NVSS; Condon et al., 1998), Clewley & Jarvis (2004), found evidence for a constant comoving space density over the redshift range $0 < z < 0.8$ for the lower luminosity ($L_{325} < 10^{25}$ W Hz sr^{-1}) population. Sadler et al. (2007) find evidence of mild evolution out to $z \sim 0.7$ in their comparison of the radio luminosity function of sources in the 2dF-SDSS Luminous Red Galaxy and QSO (2SLAQ; Cannon et al. 2006) survey with that of sources in the 6-degree Field Galaxy survey (6dFGS; Jones et al. 2004). Their study appears to rule out the no-evolution scenario. They find evidence of more rapid evolution towards higher luminosities, consistent with the results of Clewley & Jarvis (2004). Donoso et al. (2009) also find evidence of mild positive evolution in the $0.1 < z < 0.55$ redshift range. These three studies make use of radio sources detected in the wide-area NVSS and FIRST surveys whose flux density limits (≥ 1 mJy) are high enough to ensure that contamination from star-forming galaxies and radio-quiet AGN is low.

Smaller, deeper radio surveys have also been used to study the low-luminosity sources out to higher redshifts. These include studies in the Very Large Array (VLA) Cosmic Evolution

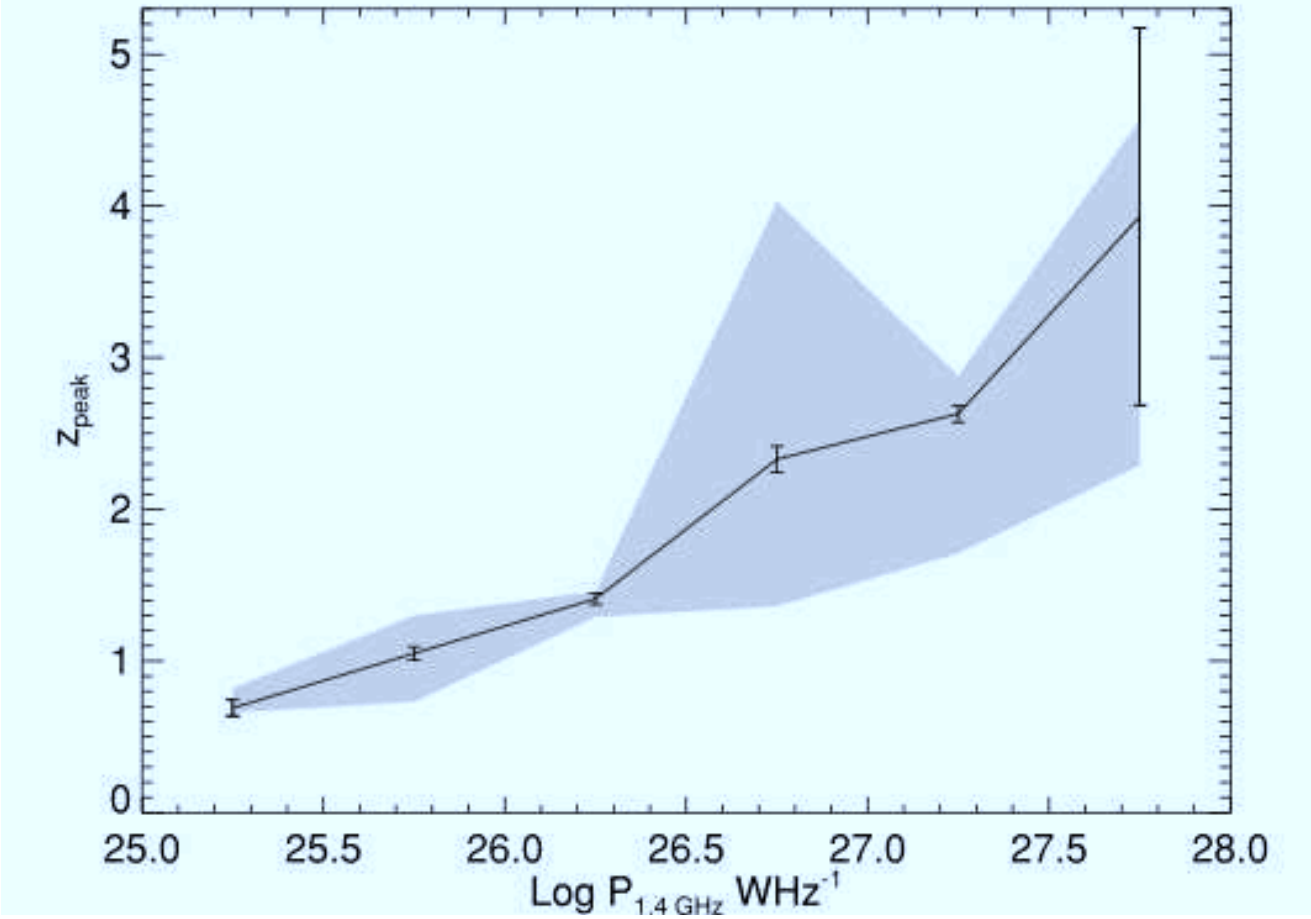

Figure 1.13: The change in peak redshift with radio luminosity from Rigby et al. (2011). The error bars show the uncertainty in the polynomial fits, and the shaded region represents the range in results which come from repeating this process for the additional grids.

Survey (VLA-COSMOS) field by Smolčić et al. (2009), in the Lockman Hole Spitzer Wide-area Extragalactic legacy survey (SWIRE) field by Strazzullo et al. (2010), the Chandra Deep Field South by Padovani et al. (2011) and the Suburu/XMM-Newton Deep field by Simpson et al. (2012) all of whom find evidence of positive evolution of their low-luminosity AGN sources consistent with density enhancements ranging between $2-10$ over the redshift range $0 < z < 1.3$. These studies use different criteria to identify the AGN contribution in their sub-mJy samples which may contribute to small differences in their exact determinations of the strength of evolution taking place in these sources. Furthermore the survey sizes in all these studies are all small, ranging from 2 to 0.1 degrees^2, thus sample variance is likely to contribute to variations in their findings. All of these studies imply that the level of evolution in the low power AGN is significantly less than that taking place in the high luminosity AGN. Two possible explanations of this observed separation in evolutionary behaviour have been put forward, the first being that evolution in the entire radio source population is luminosity dependent or that the radio source population is divided into two independently evolving components, a rapidly evolving high luminosity component and a lower luminosity component with much weaker evolution.

As both the morphological and accretion mode classification schemes divide the radio AGN population roughly according to their luminosities both the low luminosity FRIs (Jackson & Wall, 1999) and low-excitation radio galaxies (Smolčić et al., 2009; Best & Heckman, 2012a) have been suggested as candidates for the slowly evolving component of the radio population. As the fundamentally different nature of the accretion taking place in low-excitation and high-excitation radio galaxies has only recently been clarified earlier work focused on determining whether the evolutionary behaviour of the FRI populations is significantly different to that taking place in the FRIIs. Rigby et al. (2007) found evidence that high luminosity FRI sources evolve as rapidly as FRII sources of comparable radio power. Furthermore, Gendre et al. (2010) performed a detailed comparison of the radio luminosity function of FRI and FRII sources at a number of redshifts and revealed that both populations experience luminosity dependent number density enhancements at higher redshifts, $z \approx 0.8 - 2.5$, and that there were no significant differences between the enhancements measured for these two populations. These results would seem to suggest that both types of FR sources experience a common evolutionary history and thus cannot fully account for the observed dichotomy in cosmic evolution.

1.6 The SKA Design Study Semi-empirical Extragalactic Simulation

Wilman et al. (2008) developed a semi-empirical simulation for modelling the cosmological distribution of radio galaxies which brings together our understanding of the evolution of the radio source population and extrapolates it out to very high redshift ($z = 20$) and to 10-nJy flux-density limits in preparation for the continuum surveys possible with the Square Kilometre Array (SKA) and its pathfinder facilities. I only give a brief overview of this simulation here and the reader is referred to Wilman et al. (2008) for full details.

The simulation randomly draws its sources from the observed radio continuum luminosity function of the extragalactic populations, covering a sky area of $20 \times 20\text{deg}^2$ at 151, 610, 1400, 4860 and 18000 MHz. The simulation starts at z=0, using a dark matter density field $\delta\rho/\rho$ defined on a cuboid grid of 5h^{-1}Mpc comoving cells which makes a $550 \times 550 \times 1550$ array. Radio sources are then distributed on this underlying dark matter distribution according to a prescription of how the various sub-populations of radio source (FRIIs, FRIs, radio-quiet quasars, star-forming galaxies and starburst galaxies) relate to their typical dark-halo mass. I will use this simulation to compare my results on the space density of high-redshift radio galaxies in this thesis to the best available models of the expected evolution of high redshift radio sources.

1.7 This thesis

In this thesis I present a project with the aim of finding high-redshift radio sources within the epoch of reionization, and to be subsequently used to study the evolution of neutral hydrogen at this important epoch in the Universe through 21-cm absorption line studies. However, as a by-product of this work I also address the question of what do the typical radio galaxies look like at very high redshift, i.e. do they share similar properties to their lower redshift counterparts?

The structure of the thesis is as follows; in Chapter 2.4 I describe a new technique for targeting high-redshift radio sources, whereby the dominant lower-redshift population is filtered out according to their near-infrared magnitude, rather than repeat the previous techniques of using steep-radio-spectral index and/or small angular size. I then present the parent sample of high-redshift radio source candidates that were targeted for follow-up spectroscopy. In Chapter 3.5 I present the follow-up spectroscopic observations and the reduction steps that were necessary to find the redshifts of distant radio galaxies using optical spectroscopy. This is followed by an investigation of whether these radio sources lie on the same correlations as their lower-redshift counterparts and with radio sources selected by alternative methods. These include investigating the correlation between radio luminosity and Lyα emission line luminosity, and also whether their host galaxies are similar by placing them on the radio galaxy $K-z$ diagram. In Chapter 4.4 I undertake an in-depth study of a candidate $z = 5.33$ radio galaxy, and propose a possible way to confirm the redshift of this object. In Chapter 5.3.2 I compare the space density of $z > 2$ radio sources found in this thesis with prediction from the SKADS continuum simulation of Wilman et al. (2008) and subsequently predict how current and future surveys will perform in finding high-redshift radio galaxies. In Chapter 6 I summarise the results of the thesis and give an indication of what I believe to be the best way to find radio sources in the epoch of reionization in the future.

Chapter 2

Sample definition

There have been many surveys hunting high redshift radio galaxies (Tielens et al., 1979; Blumenthal & Miley, 1979; Chambers et al., 1996; Blundell et al., 1998; Jarvis et al., 2001b; Cohen et al., 2004; Cruz et al., 2006), however the highest redshift radio galaxy ever found is at z=5.19 (van Breugel et al. (1999)). The relatively small number of high redshift radio galaxies that have been discovered is due to the fact that they comprise << 1% of the total radio source population in large radio surveys (e.g. Wilman et al., 2008). Because of this small fraction of radio galaxies at high redshift, in order to find the highest redshift radio galaxies we need to efficiently filter out the low redshift radio sources. Many filtering criteria have been used to overcome this problem in the past, such as spectral index and radio size, although such techniques are not completely efficient and a significant fraction of high-redshift ($z > 3$) radio galaxies may also be filtered out (Jarvis et al., 2001c).

In this chapter I outline my filtering criteria to find high-redshift radio galaxies, which differs from those traditionally used based on the radio-wavelength properties of radio galaxies.

2.1 Sample Selection

As outlined in Chapter 1, radio galaxies exhibit a relatively tight relationship between their observed $K-$band magnitude and their redshift. Although such a relationship is not a surprise, as objects further away are inevitably fainter than similar objects closer to us, the tightness of the relation implies that powerful radio galaxies tend to reside in the most massive galaxies at all cosmic epochs (e.g. Jarvis et al., 2001a; Willott et al., 2003).

In the past, obtaining the near-infrared imaging data to construct such a $K - z$ diagram required large amounts of observing time, where the individual radio galaxies were targeted one at a time. This was primarily due to the relatively small near-infrared detectors that were available. However, over the past decade near-infrared astronomy has moved from "single-object" work, towards large-scale surveys. This has been due to the commissioning of the wide-field camera (WFCAM) on the United Kingdom Infrared Telescope (UKIRT) in Hawaii, and the launch of the *Spitzer Space Telescope* (I discuss the surveys conducted with these facilities in Section 2.2).

Given this large increase in the availability of near-infrared imaging data it is now worth considering whether these data can be used to efficiently filter out low-redshift radio galaxies

from the larger radio surveys, in order to find the highest-redshift radio galaxies in the Universe. This would follow a similar to the technique investigated by Best et al. (2003), who used optical $I-$band imaging from the ESO Imaging Survey to obtain identifications for the radio sources selected from the Northern VLA Sky Survey (NVSS; Condon et al., 1998), in order to follow them up with optical spectroscopy to obtain redshifts. However, this survey still required additional near-infrared data to identify the faintest, highest-redshift radio galaxies (Brookes et al., 2006).

Rather than using relatively shallow optical imaging, we are now in a position to use relatively deep near-infrared data. If we inspect the $K-z$ diagram for radio galaxies (Fig. 2.1; Willott et al., 2003) we see that if we use $K-$band imaging data over a field with radio continuum data, we could in principal estimate the redshift of the radio source using the $K-z$ diagram. For example, if there was a near-infrared survey that had a depth reaching $K \sim 17$ (Vega), then anything detected with $K < 17$ would have a high probability of lying at $z < 1$. If the survey reached $K \sim 19$ (Vega) then the majority of detected sources would lie at $z < 2$. Such a technique is not new, and actually played a large part in establishing the evidence for a decline in the space density of powerful radio sources at high redshift (Dunlop & Peacock, 1990). As described in the following sections, surveys such as UKIDSS and those carried out by the *Spitzer Space Telescope* are deep enough to efficiently filter out low-redshift radio galaxies from radio surveys.

2.2 Infrared Surveys

The UKIRT Infrared Deep Sky Survey

UK astronomers have been carrying out several near-infrared surveys using WFCAM on UKIRT over the past decade, under the umbrella of the UKIRT Infrared Deep Sky Survey (UKIDSS; Lawrence et al., 2007). UKIDSS extends at least three magnitudes deeper than the 2 micron all-sky survey (2MASS; Skrutskie et al., 2006) and is therefore a good infrared counterpart to the visible Sloan Digital Sky Survey (SDSS; Abazajian et al., 2009). UKIDSS is comprised of five sub-surveys (see Fig. 2.2 for the UKIDSS sky coverage) covering a total of 7500 square degrees of the Northern hemisphere. The five sub-surveys are structured in a 'wedding cake' format moving from relatively shallow depths over the largest area of the sky (Large Area Survey) to ultra deep exposures over a relatively small area (Ultra Deep Survey). The five sub-surveys are; the Large Area Survey (LAS), Galactic Plane Survey (GPS), Galactic Clusters Survey (GCS), Deep Extragalactic Survey (DXS) and Ultra Deep Survey (UDS) which together have the aim of finding the coolest and nearest brown dwarfs, high redshift starburst galaxies, ellipticals and galaxy clusters between $1 < z < 2$ and high redshift quasars.

Of particular relevance to the goals of this thesis is the UKIDSS Deep eXtragalactic Survey (DXS) which has both $K-$ and $J-$band data with a 5σ point source depth of $J = 22.3$ and $K = 20.8$ (Vega Magnitudes) eventually covering 35 deg^2. The DXS was designed to measure the abundance of galaxy clusters between redshift $1 < z < 2$ to obtain constraints on cosmological parameters, to measure galaxy clustering and bias at z > 1 to test hierarchical models and to provide multi-wavelength census of the luminosity density in star formation and active galactic nuclei (Lawrence et al., 2007). As I will show in Section 2.4, at a depth of

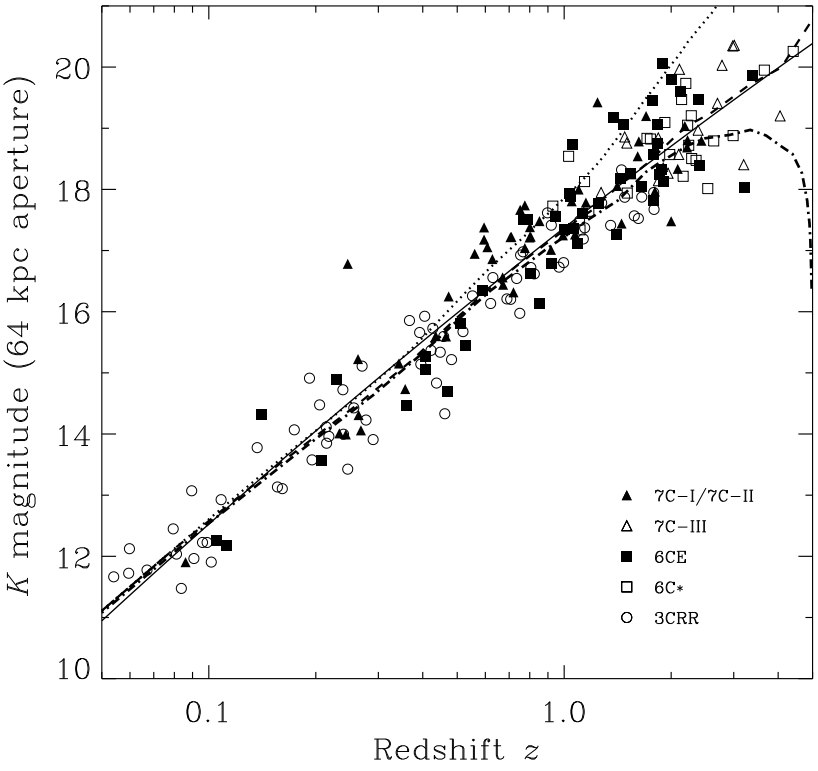

Figure 2.1: K-z diagram for radio galaxies 7CRS, 6CE, 6C and 3CRR samples ((Willott et al., 2003)). One can see the tight correlation between $K-$magnitude and redshift to isolate high-redshift radio galaxies, because if $K > 20$ the redshift is likely to be at $z > 2$.

$K = 20.8$ in the Vega magnitude system, this survey may also be very efficient at filtering out low-redshift ($z < 2$) radio galaxies, with those powerful radio sources that are undetected at $K-$band in the DXS being likely to reside at $z > 2$.

The Spitzer Wide-Area Infrared Extragalactic Survey

The Spitzer Wide-Area Infrared Extragalactic Survey (SWIRE; Lonsdale et al., 2003) is the largest Legacy program of *Spitzer Space Telescope* with the aim of tracing the evolution of dusty star-forming galaxies, evolved stellar populations and AGNs as a function of environment. SWIRE covers 60-65 deg^2 with all *Spitzer* bands, including the Infrared Array Camera (IRAC) at 3.6, 4.5, 5.6 and 8 μm and Multiband Imaging Photometer for *Spitzer* (MIPS) at 24, 70 and 160 μm in six different fields ELAIS-N1, ELAIS-N2, the Lockman hole, ELAIS-S1, XMM-LSS and Chandra Deep Field South (CDFS). The fields are summarised in Table 2.1.

The 5σ depth of the $3.6\,\mu$m imaging in the SWIRE data is 7.3 μJy or 21.8 magnitudes (AB). As the conversion from 3.6μm magnitude to $K-$band magnitude will depend on both the redshift of the sources and also its spectral energy distribution, I use an alternative method to determine the redshift of a typical radio galaxy at this depth, which is not based on the $K-z$ diagram. For this I use the large *Spitzer* survey of known high-redshift powerful radio galaxies from Seymour et al. (2007). These authors targeted a large fraction of known radio galaxies at

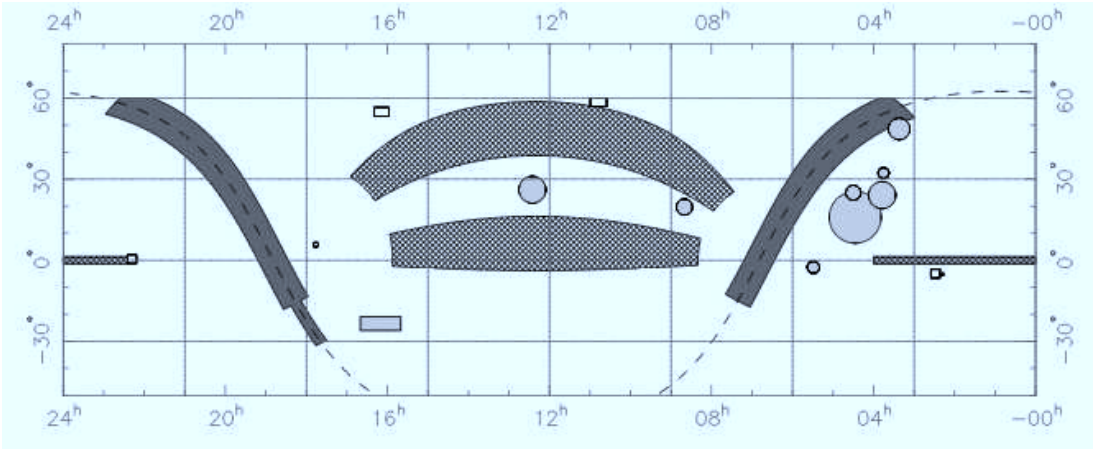

Figure 2.2: The sky coverage of the UKIDSS survey. Cross-hatch : Large Area Survey. Dark Grey : Galactic Plane Survey. Light Grey : Galactic Clusters Survey. Open rectangles : Deep Extragalactic Survey. Note that the Ultra Deep Survey lies just to the west of the DXS field at 02h18m -05°10'. The dashed line marks the Galactic plane. Taken from Lawrence et al. (2007).

Table 2.1: Summary of the fields that were targeted as part of the SWIRE survey. Positions given are the central coordinates of the fields. Information taken from the SWIRE web page (http://swire.ipac.caltech.edu/swire/public/overview.html).

Field	RA	Dec	Size / degree^2
ELAIS-S1	00 35 00	-43 40 00	7.0
XMM-LSS	02 21 20	-04 30 00	9.2
CDFS	03 32 00	-28 16 00	8.0
Lockman Hole	10 47 00	58 02 00	11.0
ELAIS-N1	16 11 00	55 00 00	9.2
ELAIS-N2	16 36 48	41 02 00	4.8

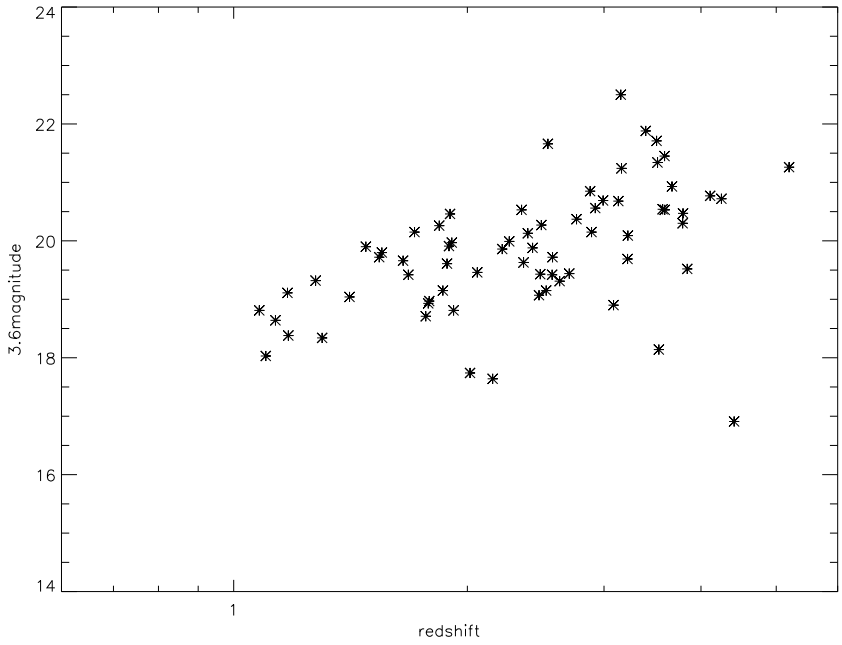

Figure 2.3: The 3.6μm magnitude versus redshift diagram for radio galaxies from Seymour et al. (2007).

$z > 1$ from a combination of radio samples which had large spectroscopic campaigns dedicated to obtaining their redshifts. Although the sample is not complete and almost certainly suffers from biases associated with only obtaining redshifts for sources with relatively bright emission lines, it does serve to give an idea of the redshifts that the SWIRE survey is sensitive to in terms of powerful radio sources. Fig. 2.3 shows the AB magnitude at 3.6 μm against the redshift for the radio galaxies in the Seymour et al. (2007) study. One can immediately see that the scatter in the 3.6μm–z diagram appears to be larger than in the $K-$ case, which may be due to the lower resolution 3.6 μm imaging leading to additional confusion noise in the form nearby sources contributing to the aperture extracted fluxes. However, an investigation of this is beyond the scope of this thesis. In spite of this, there is clearly a correlation between the 3.6μm magnitude and the redshift of the high-redshift radio galaxies in this sample. Due to the fact that the number density of high redshift radio galaxies is very small compared to their low redshift counterparts, the SWIRE depth of 21.8 magnitudes could be a crucial tool to filter out the low redshift radio galaxies, as even using a magnitude of 20 at 3.6 μm, radio galaxies with redshift $z < 1.5$ should be filtered out.

2.3 The Radio Surveys

Although near-infrared surveys reaching sufficient depth to eliminate low-redshift $z < 2$ radio galaxies now exist, appropriate radio data is still also required. However, different populations dominate radio surveys at difference flux-density limits and it is clear that in order to find high-redshift radio sources, in particular those that reside within the epoch of reioinisation,

just using radio data to very faint levels is not ideal. This is because powerful radio sources would still have a relatively bright radio flux density, even if they are at $z > 6$, and obtaining a 21 cm absorption spectrum against a fainter source would require much longer integration times than for a brighter sources. In order to find the best flux density at which to cut any radio data I consider several aspects of radio sources.

The first is that they need to be bright enough to obtain a 21 cm absorption line spectrum in a reasonable amount of integration time with a telescope such as LOFAR. For this I use numbers quoted in Carilli et al. (2003) which suggest a 151 MHz flux density of $S_{151} \sim 20$ mJy is reasonable. This then corresponds to a 1.4 GHz flux-density limit of $S_{1.4} > 3$ mJy. In fact, as I show below, this is probably fainter than I really want to probe.

The second consideration is the efficiency with which spectroscopic redshifts could be obtained. As the sources that would be targeted are very faint by design, spectroscopic redshifts will only be obtained based on their emission lines. Many groups have investigated the relationship between emission-line luminosity and radio luminosity in radio galaxies. Possibly the most comprehensive study of the link between radio luminosity and emission line luminosity was conducted by Willott et al. (1999) who found a reasonably tight correlation between the luminosity of [OII] at 3727Å and the radio luminosity at 151 MHz. However, the [OII] emission line would shift beyond visible wavelengths at $z > 2$, which renders it useless for our purposes (near-infrared spectroscopy is much less efficient than optical spectroscopy from the ground, principally due to the atmospheric OH lines and the increased sky background). Jarvis et al. (2001b) carried out a similar study to Willott (2001), but using only the highest-redshift radio sources in complete samples, where the Hydrogen Lyα line is redshifted into the visible wavelength window. They found a significant correlation between the Lyα luminosity and the 151-MHz luminosity of the form $L_{\mathrm{Ly}\alpha} \propto L_{151}^{0.87\pm0.10}$. It is therefore clear, that in order to increase the chances of obtaining a spectroscopic redshift then I am better off restricting the search to the more powerful radio sources in the Universe. Finally, this correlation also only exists for the powerful, FRII-type radio sources as the less powerful FRIs tend to exhibit different emission line ratios, leading to some authors to suggest that they may be powered by different accretion mechanisms (e.g. Hardcastle et al., 2007), although this is now thought to be more related to the high-excitation and low-excitation emission line classification rather than the radio structures.

The third consideration is therefore that the sample is restricted to those radio sources that lie above the break of the radio luminosity function, where the powerful sources make up the bulk of the population. This occurs at $L_{151} \approx 10^{27}$ W Hz^{-1} sr^{-1} (Willott et al., 2001). At $z \sim 4$ this corresponds to a flux-density limit of ~ 0.1 Jy at 151 MHz. Assuming a spectral index of $\alpha = 1$ this would correspond to a flux-density of ~ 10 mJy at 1.4 GHz. Thus all of these considerations mean that a flux-density limit at ~ 10 mJy appears to be ideal for finding high-redshift radio galaxies. In Fig. 2.4 I show the expected redshift distribution for a flux-density limit of $S_{1.4} > 10$ mJy. This shows that the vast majority of radio sources above this flux-density lie at or below $z \sim 2$ i.e. ~ 70 per cent of sources lie at $z < 2$ and ~ 30 per cent lie at $z > 2$. Therefore, combining this with near-infrared selection, I should be able to filter out the vast majority of contaminating sources from the sample.

Obviously, to select radio sources at the 10s of mJy level at 1.4 GHz, a survey to this depth or deeper is required. Over past 15-20 years a whole range of radio surveys have been conducted covering large fractions of the sky. The two most prominent of these are the NVSS and the Faint Images of the Radio Sky at Twenty-one Centimetres (FIRST; Becker et al., 1995), which

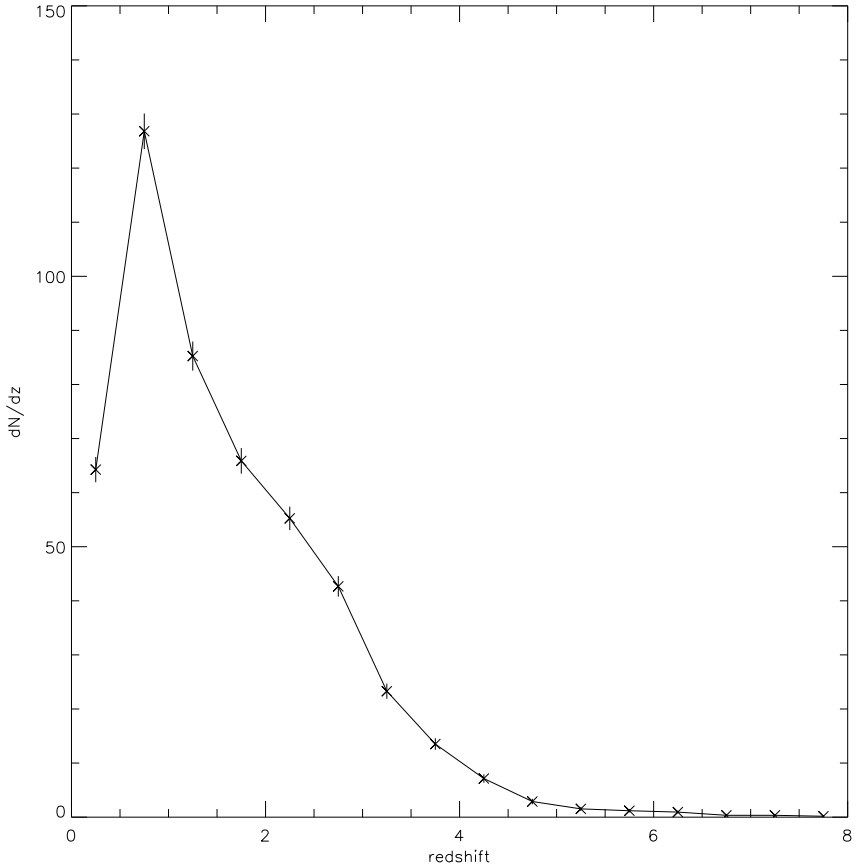

Figure 2.4: The redshift distribution of simulated radio galaxies as a function of redshift from the SKADS simulation, over 34 deg^2 .

were both carried out at 1.4 GHz. The NVSS reaches an rms depth of $\sim$ 1mJy with a spatial resolution of $\sim$ 45 arcsec and is sensitive to extended structure at radio wavelengths, whereas the FIRST Survey reaches $\sim$ 0.15 mJy but at a much higher resolution of 5 arcsec. For the purpose of finding high-redshift radio galaxies I am less concerned about large diffuse radio emission, as it has been shown that radio galaxies at $z > 2$ tend to be compact (e.g. Miley, 1992; Chambers et al., 1996; Miley & De Breuck, 2008) and certainly smaller than 45 arcsec on the sky, which translates to $\sim$ 350 kpc at $z > 2$, and more concerned about the ability to cross-match the radio sources to near-infrared counterparts. Thus, the FIRST survey is more relevant for the focus of this thesis, although as detailed below I also use similar depth data from other radio surveys that cover the SWIRE and/or DXS field.

Faint Images of the Radio Sky at Twenty Centimeters

The Faint Images of the Radio Sky at Twenty Centimeters (FIRST; Becker et al. (1995)) radio survey started in 1993 to produce the centimetre-wavelength equivalent of the Palomar observatory sky survey, which covers 10000 deg^2 of the sky. The observations were made in the B-configuration of the VLA and the data calibrated using the AIPS data reduction package

which provides the angular resolution of 5″ and $\sigma_{RMS} \sim 0.13$ mJy. The FIRST catalogue is a good option for matching with optical surveys while the radio structures down to 5″ are resolved. In the catalogue, both peak and integrated flux density measurements are provided. They were measured by fitting a two-dimensional Gaussian to each intensity peak. The scientific properties of the FIRST survey are the following: good positional accuracy to have a large number of optical identification, the sensitivity to detect the radio sources below the break in the radio source counts ($\log N - \log S$) curve and angular resolution high enough to provide morphological classification of the sources.

The Australia Telescope Large Area Survey

The Australia Telescope Large Area Survey (ATLAS; Norris et al., 2006) of the Chandra Deep Field-South (CDFS) and European Large Area ISO Survey-South (ELAIS-S1) has produced a 6 deg^2 deep radio survey with 10-15 μJy rms. The survey overlaps with the SWIRE area in the chosen fields thus the optical and infrared data are available for most of the radio objects. The scientific aim of the ATLAS is to understand the galaxy formation and evolution in the early universe while it is targeted on wide areas, which have been studied at other wavelengths. Some of the specific scientific aims of the ATLAS are the following: to test the radio-FIR correlation and understand whether it changes with the redshift or other galaxy properties, search for overdensities of high redshift ultra luminous infrared galaxies (ULIRGs) and help to find protoclusters in the early universe and to understand the radio luminosity function at high redshift (Middelberg et al. (2007)). I use the data from this survey over the CDFS and ELAIS-S1 field as the FIRST survey does not extend to these Declinations.

Giant Meterwave Radio Telescope data

Tasse et al. (2006) have conducted a deep low-frequency survey of the XMM-LSS field at 74 and 325 MHz, using the VLA telescope with the flux density limit of $\sim$ 162 and 4 mJy/beam which is able to detect $\sim$ 1500 radio sources over $\sim$ 130 and 15 degree^2 with resolution of $30''$ and $6.7''$. Tasse et al. (2007) increased the size of the low frequency sample using the Giant Meterwave Radio Telescope (GMRT) at 240 and 610 MHz. Compared to the VLA, the GMRT detected a further $\sim$ 200 radio sources. Some scientific aims of the survey are: how does the IGM influence the physical properties of the radio sources such as linear size and where are the radio-loud AGN located (Tasse et al., 2007). We use these data over SWIRE XMM-LSS field, as again FIRST does not cover this field.

2.4 The Sample

As highlighted above, the Spitzer SWIRE (Lonsdale et al., 2003) and UKIDSS Deep Extragalactic Survey (DXS; Lawrence et al., 2007) provide good opportunities for finding high-redshift radio galaxies, as they are deep enough to eliminate sources with redshift $z < 2$ (Fig 2.1). The radio sources, which are very faint or not detected in SWIRE (IRAC CH1) or DXS $K-$band are the targets with high probability of residing at high redshift.

To eliminate low-redshift radio galaxies I cross-matched the UKIDSS-DXS survey with the FIRST survey (Becker et al 1995) of radio sources with $S_{1.4} > 10$ mJy in VIMOS4/SSA22 field, using a nearest neighbour search in Topcat, with a 5 arcsec search radius. 5 arcsec is larger than the positional accuracy of the FIRST survey, however, I use this as a conservative first step as all near-infrared identifications are subsequently inspected by eye with the radio maps overlaid.

I also cross-matched the SWIRE sources with the FIRST catalogue of radio sources at > 10 mJy in the Lockman Hole, ELAIS-N1 and ELAIS-N2 fields. For the XMM, ELAIS-S1 and CDFS fields there was no data in the FIRST radio survey. Thus for the XMM field, I use the deep Giant Metrewave Radio Telescope (GMRT) data at 610 MHz presented in Tasse et al. (2007). Similarly to my initial selection, where I used a radio flux-density limit selection of $S_{1.4\mathrm{GHz}} > 10$ mJy to ensure the selection of powerful radio sources at $z > 2$, I adopt a similar flux-density limit at 610 MHz, adjusted assuming a spectral index of $\alpha = 0.8$[1], resulting in a flux-density limit at 610 MHz of $S_{610\mathrm{MHz}} > 19$ mJy, and cross-matched all radio sources above this radio flux-density with the SWIRE 3.6 μm catalogue.

In the case of CDFS and ELAIS-S1 I used the deep Australia Telescope Large Area Survey data at 20 cm and follow the same basic procedure as detailed above. In order to restrict myself to only the most distant radio sources I then impose an upper limit to the flux density at 3.6 μm of 50 μJy. Based on the $K - z$ and $3.6 - z$ diagrams of radio galaxies this should ensure that I only include radio sources with redshift $z > 2$ where the bright Lyα emission line, which is redshifted to the optical part of the spectrum (Jarvis et al., 2001b; Willott et al., 2003), should be observable. Following the sample selection, I found a total of 498 radio sources in CDFS, ELAIS-N1, ELAIS-N2, ELAIS-S1, Lockman Hole, VIMOS/SSA22 and XMM-LSS fields.

One issue associated with finding optical/near-infrared identifications for distant powerful radio sources is that many may be double sources, where the core is not detected but the hot spots associated with the lobes are. In these cases the near-infrared identification may not be easy to identify. Thus, at this point I make an additional cut to the sample and only consider compact (unresolved) radio sources where the position of the optical identification can be associated with the centroid of the radio emission. This led to a decrease in the number of sources in the sample to 220 radio sources. Tables 2.3-2.7 lists the whole sample of radio sources from the FIRST/GMRT/ATLAS radio surveys cross-matched to the SWIRE and DXS field in VIMOS4/SSA22.

[1]We use the definition for the radio spectral index α, $S_\nu \propto \nu^{-\alpha}$

Table 2.2: This table shows the number of sources after the various cuts. The second column presents the number of sources with $S_{1.4} > 10$mJy, the third column presents the number of compact sources with $S_{1.4} > 10$mJy and the last column presents the number of compact sources with $S_{1.4} > 10$mJy and $S_{3.6} < 50\mu$Jy.

Field	$S_{1.4} > 10$mJy	compact structure	$S_{3.6} < 50\mu$Jy
ELAIS-N1	142	61	27
ELAIS-N1	69	39	25
Lockman Hole	176	81	51
XMM-LSS	111	67	58
ELAIS-S1	50	30	17
CDFS	76	44	23
VIMOS	68	25	19

Table 2.3: FIRST radio sources in the ELAIS-N1 field with radio flux $S_{1.4} > 10$mJy cross-matched with the SWIRE survey. $S_{3.6}$ is the flux-density measurement at 3.6 μm. The separation between the radio position and the near-infrared counterpart is also given (Sep) in arcsec, if the separation value is not shown the sources are not detected in the SWIRE catalogues. The structure of the radio sources are given for the compact (c) and not compact (nc). For the undetected sources in the SWIRE catalogues at 3.6μm, the lower limit of 7.3 μJy is shown. The rms of the FIRST survey is 0.147mJy. The $\star$ sign marks those which are not covered in the IRAC imaging and the $\wr$ sign denotes two possible identifications and we provide the fluxes for all possible IDs.

ID	**RA**	**DEC**	$S_{1.4}$ / **mJy**	$S_{3.6}$ / μ**Jy**	**Sep**	**Struc**
EN1_01	15:58:08.19	+54:49:58.21	16.80	231.41 ± 23.18	0.18	c
EN1_02	15:58:27.13	+54:50:44.45	18.42	58.34 ± 5.89	2.4	c
EN1_03	16:00:15.34	+55:02:40.62	17.97	141.41 ± 14.18	0.35	c
EN1_04	16:00:40.17	+55:12:53.94	28.43	57.11 ± 5.79	0.07	c
EN1_05	16:00:57.18	+55:13:31.96	11.29	52.49 ± 1.05	0.25	c
EN1_06	16:01:40.06	+54:55:02.58	19.10	< 7.3		nc
EN1_07	16:02:03.89	+54:54:42.96	20.21	96.64 ± 9.75	1.43	c
EN1_08	16:02:32.43	+54:54:08.19	10.28	37.16 ±4.28$\wr$9.92 ±1.56		nc
EN1_09	16:03:33.66	+54:05:38.87	14.59	27.42 ± 3.30		c
EN1_10	16:03:35.25	+54:05:14.37	25.14	146.254 ± 15.20		c
EN1_11	16:04:21.91	+55:05:45.39	20.12	< 7.3		c
EN1_12	16:04:35.18	+55:35:48.13	13.66	190.87 ± 19.18	0.34	nc
EN1_13	16:04:35.50	+53:59:36.73	16.47	< 7.3		c
EN1_14	16:04:39.71	+54:31:40.03	20.21	98.96 ± 10.79		c
EN1_15	16:04:40.71	+54:38:26.56	16.14	56.18±6.25		nc
EN1_16	16:04:54.73	+55:59:49.40	79.15	< 7.3		c
EN1_17	16:05:00.69	+55:23:55.35	20.77	69.01 ± 7.00	0.19	c
EN1_18	16:05:03.84	+55:00:36.63	14.09	19.10±2.48		nc

Continued on next page

Table 2.3 – continued from previous page

ID	RA	DEC	$S_{1.4}$ / mJy	$S_{3.6}$ / μJy	sep	struc
EN1_19	16:05:06.59	+55:00:54.58	17.38	15.60±2.10		nc
EN1_20	16:05:11.14	+55:38:56.87	18.12	125.9 ± 12.68	1.19	c
EN1_21	16:05:15.42	+55:55:51.43	14.91	41.01 ± 4.18	0.29	c
EN1_22	16:05:38.04	+54:39:18.23	127.37	856.88 ± 85.78	0.39	nc
EN1_23	16:05:38.77	+54:39:28.65	99.48	< 7.3		nc
EN1_24	16:05:59.70	+54:53:59.71	120.28	< 7.3		nc
EN1_25	16:06:00.22	+54:54:12.06	130.76	16.7 ± 1.83	1.3	nc
EN1_26	16:06:00.45	+53:48:02.47	25.99	< 7.3		nc
EN1_27	16:06:04.97	+56:10:45.72	10.19	< 7.3		nc
EN1_28⋆	16:06:05.74	+54:28:08.97	12.0	74.92 ± 7.57	0.66	c
EN1_29	16:06:06.02	+55:53:59.85	12.68	72.97 ± 7.36	0.2	c
EN1_30	16:06:06.39	+53:48:27.11	18.63	< 7.3		nc
EN1_31	16:06:07.59	+55:21:35.54	326.0	247.35 ± 24.83	0.44	c
EN1_32	16:06:09.67	+54:03:25.35	29.29	51.96 ± 5.25	0.25	c
EN1_33	16:06:22.18	+54:13:36.47	25.16	47.47 ± 4.80	0.63	c
EN1_34	16:06:23.56	+54:05:55.66	166.23	874.93 ± 87.56	0.15	c
EN1_35	16:06:34.71	+53:53:37.92	16.83	348.28 ± 34.91	2.09	nc
EN1_36	16:06:34.78	+53:53:51.10	22.0	< 7.3		nc
EN1_37	16:06:35.24	+53:53:44.62	14.07	< 7.3		nc
EN1_38	16:07:21.63	+53:46:39.30	13.15	56.06 ± 5.67	2.04	c
EN1_39	16:07:32.39	+56:24:46.06	37.9	< 7.3		c
EN1_40	16:07:36.69	+56:24:42.99	18.65	< 7.3		c
EN1_41	16:07:44.52	+54:50:21.76	12.28	44.7 ± 4.59	0.2	c
EN1_42	16:07:44.80	+55:48:41.14	13.23	27.19 ± 3.34		c
EN1_43	16:07:59.52	+56:06:08.00	14.26	181.52±18.81		nc
EN1_44	16:08:20.74	+56:13:56.47	249.61	358.98 ± 35.98	0.07	c
EN1_45	16:08:28.34	+54:10:30.82	23.17	339.19 ± 33.98	0.41	c
EN1_46	16:08:34.22	+55:32:41.24	11.07	116.78 ± 11.76	0.34	c
EN1_47	16:08:35.64	+53:38:21.72	40.34	1064.91 ± 106.54	0.37	c
EN1_48	16:08:46.65	+56:11:21.23	23.8	< 7.3		nc
EN1_49	16:09:03.22	+56:13:15.41	13.55	88.17 ± 8.91	1.46	nc
EN1_50	16:09:03.78	+56:10:42.02	12.23	< 7.3		c
EN1_51	16:09:07.09	+53:54:27.71	21.26	< 7.3		nc
EN1_52	16:09:07.89	+53:54:24.65	23.19	< 7.3		nc
EN1_53	16:09:13.20	+53:54:29.74	43.82	537.75 ± 53.82	0.22	c
EN1_54	16:09:22.63	+56:15:10.54	40.63	186.09 ± 18.69	1.19	c
EN1_55⋆	16:09:29.72	+53:15:13.27	30.77	< 7.3		c
EN1_56	16:09:30.92	+55:24:59.51	12.36	< 7.3		nc
EN1_57	16:09:43.43	+53:57:39.96	12.53	37.44 ± 3.82	0.27	c
EN1_58	16:09:53.28	+53:44:49.38	24.65	21.65 ± 2.24	0.14	c
EN1_59	16:10:02.62	+54:16:38.43	11.47	182.51 ± 18.35	1.71	c
EN1_60	16:10:02.77	+55:52:42.65	109.52	37.43 ± 3.80	0.1	c

Continued on next page

Table 2.3 – continued from previous page

ID	RA	DEC	$S_{1.4}$ / mJy	$S_{3.6}$ / μJy	sep	struc
EN1_61	16:10:16.46	+56:48:08.29	95.48	96.74 ± 9.75	0.52	c
EN1_62	16:10:18.38	+53:15:52.01	92.0	32.15 ± 3.26	1.64	nc
EN1_63	16:10:18.94	+53:15:47.78	69.58	< 7.3		nc
EN1_64	16:10:35.82	+56:48:47.16	19.16	< 7.3		c
EN1_65	16:10:37.39	+53:24:35.47	16.96	1303.51±131.69		nc
EN1_66	16:10:51.58	+56:44:19.94	10.97	39.63 ± 4.06	1.12	nc
EN1_67	16:10:57.65	+55:35:27.80	19.22	716.49 ± 71.71	0.96	c
EN1_68	16:11:00.28	+54:42:07.82	14.03	129.09 ± 12.97	2.94	nc
EN1_69	16:11:00.31	+54:42:00.62	16.82	< 7.3		nc
EN1_70	16:11:15.65	+53:10:08.30	16.98	68.72 ± 6.90	2.79	nc
EN1_71	16:11:18.15	+55:33:44.99	14.45	442.44 ± 44.31	2.41	nc
EN1_72	16:11:20.03	+55:28:46.17	15.44	17.96< 7.32.38		c
EN1_73	16:11:29.60	+53:27:06.08	233.38	< 7.3		c
EN1_74	16:11:29.90	+53:27:12.21	287.76	85.79 ± 8.63	2.84	c
EN1_75	16:11:37.85	+53:59:32.42	12.79	76.59 < 7.38.26		nc
EN1_76	16:12:11.95	+55:22:49.89	131.57	< 7.3		nc
EN1_77	16:12:12.39	+55:23:08.95	225.2	< 7.3		nc
EN1_78	16:12:22.33	+54:52:21.91	11.14	520.67 ± 52.12	0.16	c
EN1_79	16:12:23.58	+55:25:55.35	12.68	21.74 ± 2.25	1.55	c
EN1_80	16:12:24.81	+55:54:36.84	23.87	437.31 ± 43.79	0.97	c
EN1_81	16:12:28.96	+55:06:37.42	12.2	62.29 ± 6.32	1.93	c
EN1_82	16:12:35.15	+56:28:27.18	174.8	48.55 ± 5.63		c
EN1_83	16:12:40.22	+53:35:57.81	17.88	941.68 ± 94.20	0.86	c
EN1_84	16:13:07.59	+55:59:43.27	18.43	157.42 ± 15.82	1.21	c
EN1_85	16:13:16.54	+56:01:22.48	11.36	< 7.3		nc
EN1_86	16:13:27.80	+55:51:57.69	14.76	43.93 ± 4.47	0.49	c
EN1_87	16:13:28.35	+55:15:50.39	10.29	< 7.3		nc
EN1_88	16:13:31.31	+54:27:18.20	93.16	36.99 ± 3.82	0.39	c
EN1_89	16:13:47.95	+54:14:05.59	10.03	61.73 ± 6.28	0.41	nc
EN1_90	16:14:00.02	+53:57:16.99	10.18	260.277 ±26.86		nc
EN1_91	16:14:01.13	+54:44:17.69	12.18	< 7.3		nc
EN1_92	16:14:03.16	+54:44:21.75	14.43	< 7.3		nc
EN1_93	16:14:06.23	+56:09:25.87	11.51	51.28 ± 5.19	0.19	c
EN1_94	16:14:06.26	+53:19:12.48	15.1	< 7.3		c
EN1_95	16:14:15.73	+54:43:28.54	10.82	47.05±5.33		c
EN1_96	16:14:21.20	+55:36:44.57	23.63	< 7.3		nc
EN1_97	16:14:22.02	+55:37:00.33	14.25	< 7.3		nc
EN1_98	16:14:38.52	+54:22:48.35	12.2	39.7 ± 4.09	0.68	c
EN1_99	16:15:07.55	+55:45:40.43	130.11	73.49 ± 7.45	0.62	c
EN1_100	16:15:36.61	+53:46:39.56	22.98	< 7.3		nc
EN1_101	16:15:38.81	+53:46:53.82	23.98	< 7.3		nc
EN1_102	16:15:49.27	+55:16:53.20	11.42	< 7.3		nc

Continued on next page

Table 2.3 – continued from previous page

ID	RA	DEC	$S_{1.4}$ / mJy	$S_{3.6}$ / μJy	sep	struc
EN1_103	16:15:49.75	+55:16:43.42	16.14	< 7.3		nc
EN1_104	16:16:23.36	+54:57:38.65	12.42	11.34 ± 1.27	0.24	c
EN1_105	16:16:23.88	+55:27:02.80	10.06	387.67 ± 38.84	1.72	nc
EN1_106	16:16:28.54	+53:59:29.61	12.6	< 7.3		nc
EN1_107	16:16:39.34	+55:45:25.51	73.82	114.1 ± 11.51	0.53	c
EN1_108	16:16:40.15	+55:40:13.95	13.96	21.25 ± 2.27	2.91	nc
EN1_109	16:16:40.16	+53:58:07.57	155.19	123.33 ± 12.38	1.67	nc
EN1_110	16:16:40.54	+53:58:17.53	216.97	161.5 ± 16.21	2.86	nc
EN1_111	16:16:42.32	+55:40:20.35	12.84	< 7.3		nc
EN1_112	16:17:10.11	+55:17:46.88	31.48	14.10 ± 2.18		c
EN1_113	16:17:16.28	+55:15:47.20	50.82	240.0 ± 24.59		c
EN1_114	16:17:24.07	+55:56:10.84	13.04	34.47 ± 3.52	0.46	c
EN1_115	16:17:56.35	+54:50:51.19	10.95	< 7.3		nc
EN1_116	16:18:01.02	+54:26:45.61	10.48	30.61 ± 3.17	1.2	c
EN1_117	16:18:25.85	+54:25:42.63	11.72	232.12 ± 23.28	0.13	nc
EN1_118	16:18:32.90	+54:31:36.35	22.02	< 7.3		nc
EN1_119	16:18:32.94	+54:31:42.98	23.5	81.18 ± 8.70		nc
EN1_120	16:18:33.13	+54:32:03.34	13.72	< 7.3		nc
EN1_121	16:18:34.07	+55:17:51.42	17.42	523.89 ± 52.45	1.0	nc
EN1_122	16:18:58.71	+54:52:27.21	24.47	639.49 ± 64.05	0.65	c
EN1_123$\star$	16:19:00.28	+54:53:06.65	15.31	< 7.3		c
EN1_124	16:19:00.45	+54:29:27.81	132.99	< 7.3		c
EN1_125	16:19:00.84	+54:29:49.27	124.27	< 7.3		c
EN1_126	16:19:19.67	+55:35:55.79	15.93	< 7.3		nc
EN1_127	16:19:20.01	+55:36:03.63	32.35	508.16 ± 50.90	0.16	nc
EN1_128	16:19:20.16	+54:48:17.29	60.33	137.27 ± 15.15		c
EN1_129	16:19:22.61	+55:17:55.60	10.62	140.39 ± 14.11	0.06	c
EN1_130	16:20:37.96	+54:51:28.66	12.75	49.96 ± 5.08	0.87	nc
EN1_131	16:20:55.03	+54:48:54.66	48.15	854.1 ± 85.47	0.22	c
EN1_132	16:21:13.87	+55:23:49.92	50.41	< 7.3		c
EN1_133	16:21:16.28	+55:17:59.27	13.6	< 7.3		nc
EN1_134	16:21:32.53	+55:12:59.45	33.07	152.98 ± 15.37	0.31	c
EN1_135	16:21:53.20	+55:31:31.58	31.5	13.05 ± 1.41	0.51	c
EN1_136	16:22:09.27	+55:23:11.79	19.98	< 7.3		nc
EN1_137	16:22:16.21	+55:22:05.87	19.54	115.82 ± 11.63	2.32	c
EN1_138	16:22:26.85	+55:23:14.57	16.95	148.94 ± 14.97	0.91	nc
EN1_139	16:22:33.15	+55:12:57.96	25.12	< 7.3		c
EN1_140	16:22:35.00	+55:13:02.18	22.79	196.13 ± 19.65	0.05	c
EN1_141	16:22:36.97	+54:51:58.77	10.51	79.28 ± 7.98	0.64	c
EN1_142	16:23:47.42	+54:43:02.91	21.85	33.96 ± 3.46	0.09	c

Table 2.4: FIRST radio sources in the ELAIS-N2 field with radio flux $S_{1.4} > 10$mJy cross-matched with the SWIRE survey. $S_{3.6}$ is the flux-density measurement at 3.6 μm. The separation between the radio position and the near-infrared counterpart is also given (Sep) in arcsec, if the separation value is not shown the sources are not detected in the SWIRE catalogues. The structure of the radio sources are given for the compact (c) and not compact. For the undetected sources in the SWIRE catalogues at at 3.6, the lower limit of 7.3 μJy is shown.The rms in FIRST survey is 0.147mJy. The $\star$ sign mark those which are not covered in the IRAC imaging and the $\wr$ sign shows either of both fluxes could be the ID.

ID	**RA**	**DEC**	$S_{1.4}$ / **mJy**	$S_{3.6}$ / μ**Jy**	**Sep**	**Struc**
EN2_01	16:30:08.16	+41:06:05.95	11.79	54.03 ± 5.50	1.0	c
EN2_02	16:30:30.58	+40:46:22.68	30.99	27.61 ±3.40		c
EN2_03$\star$	16:31:52.87	+40:19:42.67	52.0	< 7.3		c
EN2_04	16:32:12.60	+41:05:21.12	16.21	32.07±3.79		c
EN2_05	16:32:12.68	+40:46:25.22	20.51	46.30±5.26		nc
EN2_06	16:32:16.27	+40:56:32.71	203.15	29.63 ± 3.09	0.25	c
EN2_07	16:32:43.94	+40:53:37.81	21.47	154.98±16.21		nc
EN2_08	16:33:13.28	+40:13:38.61	10.47	907.68 ± 90.85	0.39	c
EN2_09	16:33:15.55	+40:10:59.46	10.54	466.42±47.68		nc
EN2_10	16:33:29.35	+40:54:32.95	11.65	59.15 ± 5.98	0.11	c
EN2_11	16:34:42.87	+41:44:12.66	16.49	< 7.3		nc
EN2_12	16:34:43.22	+41:44:26.65	16.29	< 7.3		nc
EN2_13	16:35:02.73	+40:08:00.58	13.9	22.8 ± 2.41	0.31	c
EN2_14	16:35:18.24	+40:22:19.96	53.99	< 7.3		c
EN2_15	16:35:20.65	+41:30:40.03	28.22	28.55 ± 2.95	0.23	c
EN2_16	16:35:22.42	+40:11:31.71	42.15	85.47 ± 8.63	0.68	c
EN2_17	16:35:23.65	+41:39:47.13	11.54	226.25 ± 22.71	0.25	c
EN2_18	16:35:53.49	+40:05:17.51	77.0	38.59± 4.51		c
EN2_19	16:36:12.62	+40:08:26.22	47.6	562.54 ± 56.32	0.81	nc
EN2_20	16:36:17.50	+41:13:10.82	16.55	20.7 ± 2.20	0.03	c
EN2_21	16:36:37.42	+41:07:29.59	10.59	213.19 ± 21.41	0.83	nc
EN2_22	16:36:38.49	+40:11:56.89	172.24	19.10± 2.54		c
EN2_23	16:36:45.00	+40:54:44.15	11.27	< 7.3		c
EN2_24	16:36:52.05	+40:56:34.73	47.65	< 7.3		nc
EN2_25	16:36:58.03	+40:58:20.54	124.53	49.35 ± 5.00	0.32	c
EN2_26	16:36:59.62	+41:30:27.32	55.95	< 7.3		nc
EN2_27	16:37:00.31	+41:30:26.73	37.56	< 7.3		nc
EN2_28	16:37:03.98	+41:30:14.23	37.23	< 7.3		nc
EN2_29	16:37:04.83	+41:30:15.35	64.95	< 7.3		nc
EN2_30	16:37:05.31	+41:50:17.81	10.86	128.01 ± 12.86	0.25	c
EN2_31	16:37:16.77	+41:34:53.86	10.24	179.52±18.57		c
EN2_32	16:37:20.13	+40:09:34.60	13.4	240.37 ± 24.10	0.19	c
EN2_33	16:37:28.49	+41:14:30.80	66.98	100.9 ± 10.16	0.13	c

Continued on next page

Table 2.4 – continued from previous page

ID	RA	DEC	$S_{1.4}$ / mJy	$S_{3.6}$ / μJy	Sep	Struc
EN2_34	16:37:51.30	+41:46:47.95	15.1	< 7.3		nc
EN2_35	16:37:54.46	+41:45:14.06	14.76	< 7.3		nc
EN2_36	16:37:54.89	+41:45:06.12	15.68	< 7.3		nc
EN2_37	16:37:55.99	+41:48:47.45	18.43	27.38 ± 2.82	0.19	c
EN2_38	16:37:58.19	+40:16:55.37	11.89	< 7.3		nc
EN2_39	16:38:02.12	+42:08:19.58	40.11	18.23 ± 1.97	0.57	c
EN2_40	16:38:12.79	+40:16:34.41	11.25	< 7.3		nc
EN2_41	16:38:17.40	+41:27:29.72	38.44	56.03 ± 5.67	0.34	c
EN2_42	16:38:44.33	+41:07:03.92	10.28	22.65 ± 2.39	0.1	c
EN2_43	16:38:50.57	+41:28:54.36	17.14	32.58±3.81		c
EN2_44	16:39:06.20	+41:45:04.12	23.1	57.17 ± 5.79	0.41	c
EN2_45	16:39:12.10	+40:52:36.72	22.51	< 7.3		c
EN2_46	16:39:15.81	+41:28:33.61	91.76	328.0 ± 32.87	0.09	c
EN2_47	16:39:18.58	+42:17:48.23	13.92	23.42±3.00		nc
EN2_48	16:39:19.22	+42:17:49.40	19.06	< 7.3		nc
EN2_49	16:39:29.64	+42:04:37.18	85.79	83.37 ± 8.40	0.06	c
EN2_50	16:39:45.38	+40:32:57.88	21.58	294.34 ± 29.53	0.93	c
EN2_51	16:39:47.08	+40:39:34.94	16.31	40.59±4.61		nc
EN2_52⋆	16:39:47.31	+40:21:13.98	184.83	< 7.3		c
EN2_53	16:40:18.22	+40:52:00.90	13.49	< 7.3		nc
EN2_54	16:40:34.36	+41:24:23.12	23.13	< 7.3		nc
EN2_55	16:40:34.71	+40:48:48.63	14.72	27.32 ± 2.84	0.15	c
EN2_56	16:40:34.86	+41:24:33.89	43.26	< 7.3		nc
EN2_57	16:40:42.91	+40:43:35.62	15.2	24.59±3.00		nc
EN2_58	16:40:43.45	+40:43:39.28	14.3	< 7.3		nc
EN2_59	16:41:16.78	+41:27:21.41	56.47	42.65 ± 4.35	0.13	c
EN2_60	16:41:53.48	+41:42:20.83	12.41	< 7.3		c
EN2_61	16:42:23.68	+41:04:38.18	32.24	45.51±5.15		nc
EN2_62	16:42:39.72	+41:02:38.34	103.09	< 7.3		nc
EN2_63	16:42:44.19	+41:02:23.20	47.47	< 7.3		nc
EN2_64	16:42:44.53	+41:02:20.60	45.93	< 7.3		nc
EN2_65⋆	16:42:50.12	+41:23:18.27	26.69	< 7.3		c
EN2_66	16:43:02.48	+41:16:58.01	19.23	23.82±3.03		c
EN2_67	16:43:03.67	+40:47:19.87	10.1	550.77 ± 55.16	0.24	c
EN2_68	16:43:11.16	+40:43:42.82	10.65	103.59±10.96		c
EN2_69	16:43:26.24	+41:03:43.31	65.01	46.97 ± 4.79	0.08	c

Table 2.5: FIRST radio sources in the Lockman Hole field with radio flux $S_{1.4} > 10$mJy cross-matched with the SWIRE survey. $S_{3.6}$ is the flux-density measurement at 3.6 μm. The separation between the radio position and the near-infrared counterpart is also given (Sep) in arcsec, if the separation value is not shown the sources are not detected in the SWIRE catalogues. The structure of the radio sources are given for the compact (c) and not compact (nc). For the undetected sources in the SWIRE catalogues at at 3.6, the lower limit of 7.3 μJy is shown.The rms in FIRST survey is 0.147mJy. The $\star$ sign mark those which are not covered in the IRAC imaging and the $\wr$ sign shows either of both fluxes could be the ID.

ID	**RA**	**DEC**	$S_{1.4}$ / **mJy**	$S_{3.6}$ / μ**Jy**	**sep**	**struc**
LH01	10:30:39.62	+58:06:11.41	121.7	5435.81 ± 543.62	0.01	c
LH02	10:31:05.10	+57:53:54.66	63.49	26.59 ±3.29		c
LH03	10:33:33.22	+58:15:02.08	1473.6	< 7.3		nc
LH04	10:33:33.56	+58:14:53.82	464.93	< 7.3		nc
LH05	10:33:34.35	+58:14:25.35	658.45	< 7.3		nc
LH06	10:33:34.58	+58:14:12.78	1253.51	< 7.3		nc
LH07	10:34:17.23	+58:51:27.13	17.25	35.78±4.19		c
LH08	10:35:32.93	+59:04:05.81	62.99	74.76±8.09		c
LH09	10:35:59.61	+58:34:07.08	395.82	93.63 ± 9.42	0.4	c
LH10	10:36:48.51	+57:23:37.88	36.95	51.58 ±5.74		c
LH11	10:36:50.24	+58:46:59.11	42.87	72.62±7.88		c
LH12	10:36:51.70	+58:47:03.27	16.63	< 7.3		c
LH13	10:37:30.60	+57:17:53.07	13.04	97.44 ± 9.84	0.23	c
LH14	10:37:44.32	+57:11:55.57	130.02	5827.99 ± 582.87	0.14	c
LH15	10:38:15.17	+58:30:15.97	56.96	106.56± 11.29		c
LH16	10:38:30.59	+57:23:17.91	128.03	< 7.3		nc
LH17	10:38:32.14	+57:22:59.74	90.86	< 7.3		nc
LH18	10:38:33.94	+58:02:57.13	29.16	< 7.3		nc
LH19	10:38:35.64	+58:03:06.65	35.25	< 7.3		nc
LH20	10:38:50.85	+56:59:17.11	21.58	158.28± 16.53		c
LH21	10:38:52.60	+57:53:15.37	30.15	< 7.3		nc
LH22	10:38:54.31	+57:53:06.54	89.5	< 7.3		nc
LH23	10:38:58.54	+57:52:15.10	46.49	< 7.3		nc
LH24	10:38:59.88	+57:52:27.47	23.53	< 7.3		nc
LH25	10:38:59.94	+59:05:42.37	30.83	< 7.3		nc
LH26	10:39:00.56	+59:05:53.71	32.4	186.78±19.36		nc
LH27	10:39:06.38	+57:01:16.12	15.89	153.361±16.19		c
LH28	10:39:13.94	+59:14:35.16	35.14	< 7.3		c
LH29	10:39:13.96	+58:14:50.67	12.65	< 7.3		nc
LH30	10:39:14.40	+59:14:15.44	26.62	< 7.3		nc
LH31	10:39:17.25	+57:25:46.08	10.65	106.13 ± 10.66	0.27	c
LH32	10:39:22.39	+58:29:12.51	95.58	370.33 ± 37.12	0.58	nc
LH33	10:39:23.58	+59:38:04.46	13.05	16.32 ± 1.77	0.56	c

Continued on next page

Table 2.5 – continued from previous page

ID	RA	DEC	$S_{1.4}$ / mJy	$S_{3.6}$ / μJy	sep	struc
LH34	10:39:42.04	+58:06:15.44	163.66	< 7.3		nc
LH35	10:39:44.12	+58:06:18.32	46.44	< 7.3		nc
LH36	10:39:58.57	+58:48:13.59	50.69	24.26 ± 2.51	0.43	c
LH37	10:40:02.46	+59:25:12.82	12.41	15.96±2.25\12.15±1.82		c
LH38	10:40:04.73	+59:25:13.56	17.38	20.23±2.63		c
LH39	10:40:19.38	+56:48:34.88	10.39	< 7.3		c
LH40	10:40:31.29	+59:21:04.84	11.44	42.88 ± 4.37	0.33	c
LH41	10:40:32.14	+59:42:41.38	11.45	19.81±2.52		nc
LH42	10:40:33.56	+59:42:30.19	16.02	< 7.3		c
LH43	10:41:14.06	+59:29:33.68	11.82	19.44 ± 2.08	0.36	c
LH44	10:41:27.62	+59:26:34.77	30.92	206.88 ± 20.74	0.24	c
LH45	10:41:30.23	+57:59:42.34	15.29	460.9 ± 46.18	0.58	nc
LH46	10:41:30.41	+58:59:19.85	22.26	47.12 ± 4.84	0.85	c
LH47	10:42:00.71	+59:27:41.34	27.69	88.69 ± 8.96	0.71	c
LH48	10:42:05.95	+58:58:22.09	18.25	< 7.3		nc
LH49	10:42:07.12	+58:58:17.00	24.1	< 7.3		nc
LH50	10:42:18.08	+57:47:53.01	15.41	53.6 ± 5.43	0.36	c
LH51	10:42:19.82	+56:44:34.68	135.59	55.57 ± 5.61	0.59	c
LH52	10:42:21.38	+58:33:17.51	39.35	34.61 ± 3.58	0.1	c
LH53	10:42:23.59	+58:11:54.52	26.12	13.54±1.88		c
LH54	10:42:33.84	+56:45:37.91	25.43	37.94 ± 3.87	0.49	c
LH55	10:42:37.00	+59:39:56.88	18.17	24.09 ± 2.53	0.2	c
LH56	10:42:43.09	+59:30:48.36	22.69	144.36 ± 14.49	0.36	c
LH57	10:42:55.48	+56:38:03.63	20.73	22.01 ± 2.34	0.29	c
LH58	10:43:16.04	+57:24:53.83	41.53	< 7.3		c
LH59	10:43:28.06	+57:58:07.31	14.68	481.94 ± 48.26	0.17	c
LH60	10:44:40.91	+57:06:18.68	103.0	69.21 ± 7.01	0.76	c
LH61	10:45:14.78	+56:20:48.17	16.06	< 7.3		nc
LH62	10:45:15.55	+56:20:16.21	16.07	< 7.3		nc
LH63	10:45:22.36	+57:48:26.47	12.72	2865.82±287.21		c
LH64	10:45:27.63	+57:29:28.04	12.81	< 7.3		c
LH65	10:45:28.31	+59:13:26.66	12.07	32.18 ± 3.27	0.16	c
LH66	10:45:29.93	+57:38:17.07	69.73	16.88 ± 1.83	0.86	c
LH67	10:45:33.91	+57:10:02.96	11.91	496.45 ± 49.69	0.18	nc
LH68	10:45:39.27	+58:07:10.72	35.05	184.99 ± 18.60	0.9	c
LH69	10:45:46.33	+56:24:45.71	23.77	76.7 ± 7.76	0.58	c
LH70	10:45:46.48	+58:06:21.88	12.3	421.43±42.73		c
LH71	10:45:51.43	+57:00:23.02	37.39	< 7.3		nc
LH72	10:45:52.45	+57:00:04.85	51.6	< 7.3		nc
LH73	10:46:02.99	+57:38:51.12	35.1	< 7.3		c
LH74	10:46:04.23	+57:38:17.88	10.49	183.6 ± 18.41	0.48	nc
LH75	10:46:05.15	+57:37:58.38	10.97	< 7.3		nc

Continued on next page

Table 2.5 – continued from previous page

ID	RA	DEC	$S_{1.4}$ / mJy	$S_{3.6}$ / μJy	sep	struc
LH76	10:46:08.19	+59:40:13.48	17.39	44.57±5.07		nc
LH77	10:46:24.60	+57:42:00.04	14.56	< 7.3		nc
LH78	10:46:24.79	+59:04:45.94	13.89	< 7.3		c
LH79	10:46:30.70	+58:28:20.65	13.31	< 7.3		nc
LH80	10:46:44.90	+56:48:21.29	27.94	53.27±5.92		nc
LH81	10:46:46.09	+56:47:20.67	55.19	36.91±4.38		c
LH82	10:46:46.56	+59:46:13.46	13.44	< 7.3		nc
LH83	10:46:59.67	+56:27:25.05	70.52	26.12 ± 2.68	0.43	c
LH84	10:47:00.85	+59:19:02.07	21.81	< 7.3		c
LH85	10:47:12.30	+59:39:31.46	14.08	118.37 ± 12.02	0.55	c
LH86	10:47:19.01	+59:32:43.90	24.03	14.65±2.05		c
LH87	10:47:19.22	+58:21:17.18	52.1	325.16 ± 32.57	0.28	c
LH88	10:47:23.48	+57:37:02.91	26.25	37.43±4.31		nc
LH89	10:48:04.71	+56:01:12.71	20.89	86.75 ± 8.70	0.49	c
LH90	10:48:19.29	+59:41:42.07	15.2	97.88 ± 9.87	0.12	c
LH91	10:48:22.47	+58:24:34.73	17.29	71.83 ± 7.29	0.2	c
LH92	10:48:32.42	+56:32:55.87	33.95	100.64 ± 10.18	0.16	c
LH93	10:48:39.76	+58:13:33.74	10.13	18.84±2.42		c
LH94	10:48:41.81	+59:46:39.62	30.02	34.75±4.11		nc
LH95	10:48:42.23	+59:46:34.09	37.01	< 7.3		nc
LH96	10:48:44.12	+58:23:06.82	11.25	224.12 ± 22.49	0.73	nc
LH97	10:48:53.47	+59:06:09.74	12.82	< 7.3		c
LH98	10:49:07.14	+57:11:51.82	10.25	< 7.3		nc
LH99	10:49:14.18	+55:56:59.27	15.56	< 7.3		nc
LH100	10:49:16.22	+58:36:40.27	31.72	< 7.3		nc
LH101	10:49:16.25	+56:01:17.55	28.12	20.57±2.70		c
LH102	10:49:16.89	+56:01:18.28	29.49	< 7.3		c
LH103	10:49:18.57	+58:36:10.12	11.82	< 7.3		nc
LH104	10:49:19.00	+58:28:00.58	27.45	119.26 ± 12.03	0.14	c
LH105	10:49:30.40	+59:01:44.75	23.25	61.09±6.70		c
LH106	10:49:40.28	+58:35:30.16	200.44	66.77 ± 6.77	0.42	c
LH107	10:50:01.01	+59:11:11.64	22.19	199.25 ± 20.01	0.42	c
LH108	10:50:09.08	+55:56:40.28	10.75	45.94 ± 4.67	0.06	c
LH109	10:50:14.55	+56:32:09.98	12.16	20.49 ± 2.15	0.16	c
LH110	10:50:21.72	+58:42:57.80	19.3	39.68 ± 4.07	0.31	c
LH111	10:50:43.21	+57:52:31.18	37.42	48.95 ± 4.98	0.93	nc
LH112	10:50:53.84	+58:32:32.86	156.23	17.42 ± 1.80	0.21	c
LH113	10:50:55.92	+56:29:45.59	54.41	< 7.3		nc
LH114	10:51:04.57	+57:54:12.93	15.52	94.16 ± 9.49	0.25	nc
LH115	10:51:06.85	+57:57:49.28	13.53	185.45 ± 18.62	0.37	nc
LH116	10:51:13.81	+55:59:40.36	19.8	67.44± 7.40		c
LH117	10:51:19.56	+56:40:16.84	12.32	61.19 ± 6.21	0.13	c

Continued on next page

Table 2.5 – continued from previous page

ID	RA	DEC	$S_{1.4}$ / mJy	$S_{3.6}$ / μJy	sep	struc
LH118	10:51:21.06	+58:26:51.12	21.72	46.68±5.24		nc
LH119	10:51:21.72	+58:26:44.95	23.52	< 7.3		nc
LH120	10:51:31.22	+58:49:47.13	15.02	< 7.3		c
LH121	10:51:32.80	+57:11:10.18	10.2	< 7.3		nc
LH122	10:51:38.92	+58:07:47.63	11.51	< 7.3		nc
LH123	10:51:39.05	+58:08:02.70	11.55	< 7.3		nc
LH124	10:51:40.14	+59:13:04.65	108.25	< 7.3		nc
LH125	10:51:42.16	+59:13:06.42	110.05	< 7.3		nc
LH126	10:52:25.43	+57:55:05.60	28.08	30.94 ± 3.16	0.13	c
LH127	10:52:30.34	+57:56:22.29	18.87	133.41 ± 13.42	0.05	c
LH128	10:52:36.54	+57:30:49.21	32.68	< 7.3		nc
LH129	10:52:37.96	+57:31:16.77	27.11	< 7.3		nc
LH130	10:52:52.96	+56:31:59.50	10.4	< 7.3		nc
LH131	10:53:08.70	+58:55:33.09	48.55	< 7.3		nc
LH132	10:53:10.13	+58:55:32.97	15.93	219.29 ± 22.01	0.47	nc
LH133	10:53:11.25	+58:55:35.21	17.11	< 7.3		nc
LH134	10:53:18.18	+58:56:23.23	78.4	< 7.3		c
LH135	10:53:27.15	+56:23:20.38	20.44	< 7.3		c
LH136	10:53:29.24	+56:23:51.38	22.0	< 7.3		c
LH137	10:53:51.16	+58:25:09.47	25.78	< 7.3		nc
LH138	10:53:52.27	+58:25:29.07	26.34	< 7.3		nc
LH139⋆	10:53:54.50	+59:13:02.36	17.57	< 7.3		c
LH140	10:53:56.69	+59:09:15.41	17.44	689.76± 71.09		c
LH141	10:54:10.97	+58:54:06.27	27.2	247.2 ± 24.81	0.21	c
LH142	10:54:12.27	+58:29:41.20	13.13	11.69 ± 1.39	0.21	c
LH143	10:54:21.45	+58:00:59.55	10.41	25.53 ± 2.70	0.37	c
LH144	10:54:24.76	+57:37:02.07	79.56	< 7.3		nc
LH145	10:54:28.94	+57:36:35.39	83.18	< 7.3		nc
LH146	10:54:29.47	+57:36:26.03	12.42	< 7.3		nc
LH147	10:55:23.09	+56:50:17.34	17.89	< 7.3		c
LH148	10:55:30.03	+58:32:32.22	17.99	< 7.3		c
LH149	10:55:48.53	+57:18:27.69	14.19	< 7.3		c
LH150	10:55:49.33	+56:48:04.44	12.06	88.35 ± 8.93	0.58	c
LH151	10:55:58.29	+56:53:19.35	21.18	< 7.3		nc
LH152	10:56:00.39	+56:53:18.13	16.01	< 7.3		nc
LH153	10:56:04.76	+57:09:33.32	50.72	45.58 ± 4.68	0.39	c
LH154	10:57:05.81	+58:47:03.84	22.31	< 7.3		nc
LH155	10:57:06.72	+58:47:00.44	17.95	< 7.3		nc
LH156	10:57:07.33	+58:46:53.53	55.31	< 7.3		nc
LH157	10:57:15.91	+57:23:13.90	133.32	< 7.3		c
LH158	10:57:29.90	+58:20:03.69	26.38	66.12±7.19		nc
LH159	10:57:30.85	+58:19:57.17	22.59	< 7.3		nc

Continued on next page

Table 2.5 – continued from previous page

ID	RA	DEC	$S_{1.4}$ / mJy	$S_{3.6}$ / μJy	sep	struc
LH160	10:57:46.04	+58:08:46.32	85.01	< 7.3		nc
LH161	10:57:46.33	+58:08:36.29	47.3	44.99±5.22		nc
LH162	10:58:24.12	+58:34:43.77	28.6	23.00± 2.90		c
LH163	10:58:30.15	+58:34:53.90	10.7	< 7.3		nc
LH164	10:59:04.76	+57:30:19.33	161.67	116.86 ± 11.73	0.85	c
LH165	10:59:04.83	+58:21:46.25	13.91	< 7.3		nc
LH166	10:59:05.13	+58:21:36.51	10.95	< 7.3		nc
LH167	10:59:14.88	+57:14:42.58	170.6	143.51±15.00 ≀15.30±2.16		nc
LH168	10:59:15.48	+57:14:52.26	63.07	< 7.3		nc
LH169	10:59:32.99	+57:45:37.50	132.93	168.28 ± 16.92	0.03	c
LH170	10:59:37.99	+57:26:52.27	31.33	63.39 ± 6.45	0.37	c
LH171	10:59:47.56	+57:08:43.40	30.17	34.52± 4.05		c
LH172	10:59:48.48	+57:21:13.15	98.01	33.05 ± 3.44	0.18	c
LH173	11:00:27.44	+57:38:17.41	10.34	30.36±3.65		nc
LH174	11:01:09.46	+57:27:15.63	73.91	15.87 ± 1.74	0.42	c
LH175	11:02:24.03	+57:47:25.08	493.14	68.93 ± 7.01	0.45	c
LH176⋆	11:04:12.96	+57:52:12.89	92.56	< 7.3		c

Table 2.6: GMRT 610 MHz radio sources in the XMM-LSS field with radio flux density $S_{610} >$ 19mJy cross-matched with the SWIRE survey. $S_{3.6}$ is the flux-density measurement at 3.6 μm. The separation between the radio position and the near-infrared counterpart is also given (Sep) in arcsec, if the separation value is not shown the sources are not detected in the SWIRE catalogues. The structure of the radio sources are given for the compact (c) and not compact (nc). For the undetected sources in the SWIRE catalogues at at 3.6, the lower limit of 7.3 μJy is shown.The rms in GMRT data at 610 MHz is 0.3 mJy/Beam. The ⋆ sign mark those which are not covered in the IRAC imaging and the ≀ sign shows either of both fluxes could be the ID.

ID	RA	DEC	S_{610} / mJy	$S_{3.6}$ / μJy	Sep	Struc
xmm_01	02:16:35.47	-04:46:59.85	32.0	27.70±1.95		nc
xmm_02	02:16:40.67	-04:44:07.06	156.6	679.28 ±68.57		c
xmm_03	02:16:43.48	-03:58:17.20	32.2	54.32±6.25		c
xmm_04	02:16:45.70	-03:37:19.47	112.9	34.16±3.98≀26.57±3.46		c
xmm_05	02:16:58.90	-04:48:29.08	20.2	< 7.3		nc
xmm_06	02:17:05.48	-04:22:55.77	125.5	89.24±9.51		c
xmm_07	02:17:19.71	-03:26:02.33	84.2	36.67±4.26		c
xmm_08	02:17:21.52	-03:39:46.69	95.1	58.54±6.50		c
xmm_09	02:17:34.18	-03:13:08.71	67.3	61.37±6.80		c
xmm_10	02:17:41.72	-05:41:52.33	168.2	< 7.3		c
xmm_11	02:17:42.74	-03:54:53.37	25.3	35.84 ± 4.17		c

Continued on next page

Table 2.6 – continued from previous page

ID	RA	DEC	S_{610} / mJy	$S_{3.6}$ / μJy	Sep	Struc
xmm_12	02:17:46.94	-05:41:37.45	19.7	157.76 ± 15.84	0.64	c
xmm_13	02:18:00.55	-04:49:44.09	24.5	< 7.3		nc
xmm_14	02:18:03.26	-05:38:25.96	20.6	< 7.3		c
xmm_15	02:18:12.33	-03:20:24.41	57.4	< 7.3		c
xmm_16⋆	02:18:18.05	-04:46:08.50	136.9	< 7.3		c
xmm_17	02:18:18.78	-04:03:28.00	29.5	405.38 ± 40.61	0.75	nc
xmm_18	02:18:23.43	-05:25:00.73	21.1	115.61±12.13		c
xmm_19	02:18:23.49	-04:19:00.72	38.2	< 7.3		c
xmm_20	02:18:27.17	-04:12:20.61	25.0	1190.65 ± 119.17	0.74	nc
xmm_21	02:18:27.28	-04:54:38.44	205.9	123.45±13.05		nc
xmm_22	02:18:33.08	-03:13:31.98	21.9	< 7.3		nc
xmm_23	02:18:34.77	-03:46:15.75	22.3	15.33±2.11		c
xmm_24	02:18:39.42	-04:41:50.43	159.2	12.11±1.74		c
xmm_25	02:18:40.18	-03:23:11.66	68.0	572.73±58.18		c
xmm_26	02:18:51.32	-05:09:02.66	40.1	24.55±3.04		c
xmm_27	02:18:53.57	-04:47:36.99	20.4	14.89±2.05		c
xmm_28	02:18:58.09	-04:09:23.14	35.5	23.47±2.88		c
xmm_29	02:19:00.58	-03:55:57.41	27.3	47.76 ± 4.87	0.77	c
xmm_30	02:19:08.76	-03:58:01.55	87.2	26.66±3.24		c
xmm_31	02:19:11.03	-03:44:29.84	67.3	8.95±1.45		c
xmm_32	02:19:18.60	-05:52:35.74	71.0	< 7.3		nc
xmm_33	02:19:28.21	-05:39:48.23	772.9	38.45±4.41⁀20.12±2.57		c
xmm_34	02:19:35.61	-04:18:38.83	28.8	52.24±5.79		c
xmm_35	02:19:43.41	-05:16:22.52	22.7	17.77±2.41		c
xmm_36	02:19:45.20	-04:53:34.80	30.1	114.18±12.04		c
xmm_37	02:19:53.40	-05:18:37.36	52.0	< 7.3		nc
xmm_38	02:19:55.44	-05:27:50.91	61.1	< 7.3		nc
xmm_39	02:19:57.28	-04:47:53.32	84.6	26.41±3.29		c
xmm_40	02:20:08.41	-03:48:53.59	60.5	359.65±36.77		nc
xmm_41	02:20:08.88	-05:45:53.94	22.0	81.26±8.71		c
xmm_42	02:20:35.30	-05:13:59.31	29.1	12.3 ± 1.42	0.3	c
xmm_43	02:20:49.41	-03:33:16.89	201.1	67.57±7.40		c
xmm_44	02:20:50.13	-03:40:57.96	34.7	< 7.3		c
xmm_45	02:20:50.98	-04:42:22.31	19.4	< 7.3		nc
xmm_46	02:20:55.40	-03:33:30.56	42.0	146.17±16.99		c
xmm_47	02:20:55.72	-03:48:32.64	287.2	39.38 ± 4.04	0.41	c
xmm_48	02:21:16.12	-02:55:49.89	192.2	54.34±6.04		c
xmm_49	02:21:18.34	-04:57:22.23	24.5	< 7.3		c
xmm_50	02:21:19.60	-03:05:48.45	19.7	< 7.3		nc
xmm_51	02:21:25.56	-03:47:20.04	38.7	55.64 ± 5.64	0.52	c
xmm_52	02:21:32.65	-03:44:01.08	20.7	139.04 ± 13.97	0.23	c
xmm_53	02:21:35.61	-05:18:21.89	23.1	< 7.3		c

Continued on next page

Table 2.6 – continued from previous page

ID	RA	DEC	S_{610} / mJy	$S_{3.6}$ / μJy	Sep	Struc
xmm_54	02:21:41.98	-04:51:13.12	138.9	48.06±5.39		c
xmm_55	02:21:43.03	-04:13:44.10	1127.9	56.9 ± 5.77	0.63	c
xmm_56	02:21:43.25	-02:49:27.80	25.2	< 7.3		c
xmm_57	02:21:44.25	-03:57:49.61	20.4	34.15 ±4.02		nc
xmm_58	02:22:00.41	-03:39:34.99	42.0	23.37 ± 2.44	0.94	c
xmm_59⋆	02:22:01.26	-02:40:12.98	365.2	< 7.3		nc
xmm_60	02:22:04.71	-03:38:15.17	88.2	104.42±11.5		c
xmm_61	02:22:06.06	-03:20:38.87	21.9	188.92±19.55		nc
xmm_62	02:22:06.20	-03:34:19.19	25.3	23.46±2.98		c
xmm_63⋆	02:22:20.65	-02:42:14.45	121.8	< 7.3		nc
xmm_64	02:22:28.68	-03:07:42.93	53.0	44.72 ± 4.54	0.62	c
xmm_65	02:22:30.05	-04:47:04.10	34.3	< 7.3		c
xmm_66	02:22:31.66	-04:27:47.09	34.1	< 7.3		nc
xmm_67	02:22:46.11	-03:03:52.82	39.5	123.57 ± 12.43	0.62	c
xmm_68	02:22:47.61	-03:48:15.48	30.0	84.98 ± 8.57	0.58	c
xmm_69	02:22:54.57	-03:11:28.03	23.7	< 7.3		c
xmm_70	02:22:54.68	-04:13:59.20	48.2	< 7.3		nc
xmm_71	02:22:55.76	-05:18:16.41	436.9	63.38±6.93		c
xmm_72	02:22:56.03	-02:43:02.95	1026.0	< 7.3		c
xmm_73	02:22:56.39	-04:24:48.70	49.7	26.09 ± 2.75	0.73	nc
xmm_74	02:22:59.83	-03:54:03.77	40.9	< 7.3		c
xmm_75	02:23:10.14	-04:23:05.57	52.0	88.01 ± 8.91	0.9	c
xmm_76	02:23:20.65	-03:18:23.51	25.2	168.56 ± 16.91	0.97	c
xmm_77	02:23:24.90	-04:27:36.81	35.2	< 7.3		nc
xmm_78	02:23:33.12	-03:01:23.49	99.9	112.68 ± 11.37	0.52	c
xmm_79	02:23:33.97	-04:58:35.83	26.7	< 7.3		nc
xmm_80	02:23:41.66	-02:39:44.29	126.7	33.83±4.02		c
xmm_81	02:23:45.39	-03:40:40.59	70.7	47.05 ± 4.82	0.78	c
xmm_82	02:23:46.56	-03:32:34.44	89.0	34.42±4.07		c
xmm_83	02:23:48.06	-05:51:11.79	164.9	67.27±7.33		c
xmm_84	02:23:48.99	-04:12:10.49	53.3	< 7.3		nc
xmm_85	02:23:52.67	-05:22:24.51	19.8	23.77±2.94		c
xmm_86	02:23:57.07	-04:41:11.44	140.3	< 7.3		c
xmm_87	02:24:10.32	-04:46:07.37	39.2	< 7.3		nc
xmm_88	02:24:15.06	-05:28:44.62	308.9	< 7.3		nc
xmm_89	02:24:18.39	-02:43:28.20	162.4	1812.55±186.65		nc
xmm_90	02:24:18.82	-03:00:20.91	43.1	54.92±6.08		nc
xmm_91	02:24:21.57	-04:25:48.18	45.8	49.28±5.58⁀11.94±1.82		c
xmm_92	02:24:27.47	-02:43:04.94	89.0	39.35±4.54		c
xmm_93	02:24:32.17	-05:34:29.78	20.0	48.56±5.45		c
xmm_94	02:24:32.98	-03:34:11.36	20.3	61.34±6.76		c
xmm_95	02:24:46.03	-03:01:55.69	267.2	< 7.3		c

Continued on next page

Table 2.6 – continued from previous page

ID	RA	DEC	S_{610} / mJy	$S_{3.6}$ / μJy	Sep	Struc
xmm_96	02:24:48.07	-05:45:20.10	108.7	< 7.3		c
xmm_97	02:24:54.88	-03:32:02.16	20.5	167.83±18.73		c
xmm_98	02:24:55.02	-03:29:03.07	20.2	46.94±5.31		nc
xmm_99	02:24:57.69	-05:16:46.89	78.1	< 7.3		c
xmm_100	02:25:00.63	-03:21:07.02	47.9	< 7.3		nc
xmm_101	02:25:05.14	-05:36:46.41	429.5	60.55±6.64		c
xmm_102	02:26:06.90	-05:32:15.46	51.5	< 7.3		c
xmm_103	02:26:15.21	-04:22:34.19	21.9	100.80±10.67		c
xmm_104	02:26:18.75	-04:00:10.78	87.8	< 7.3		nc
xmm_105	02:26:19.88	-04:25:38.49	72.0	59.82±6.59		c
xmm_106	02:26:32.51	-05:13:27.11	131.8	< 7.3		c
xmm_107	02:27:27.97	-04:37:32.23	44.7	34.98±4.10≀36.97±4.30		c
xmm_108	02:27:43.70	-05:02:48.05	19.6	< 7.3		c
xmm_109	02:27:54.07	-04:44:50.67	20.5	< 7.3		nc
xmm_110	02:27:54.91	-04:57:01.73	60.4	57.55±6.56		c
xmm_111	02:28:14.44	-05:02:35.96	22.0	< 7.3		c

Table 2.7: FIRST radio sources in the VIMOS field with radio flux $S_{1.4} > 10$mJy cross-matched with the DXS survey. K-magnitude present the K-band magnitude. The separation between the radio position and the near-infrared counterpart is also given (Sep) in arcsec, if the separation value is not shown the sources are not detected in the SWIRE catalogues. The structure of the radio sources are given for the compact (c) and not compact (nc). The K-band magnitudes are Vega system and for the targets which are undetected in the DXS catalogues the K-band magnitude limit of 21 have been showed. The rms in FIRST survey is 0.147mJy. The $\star$ sign marks those which are not covered in the DXS imaging and the ≀ sign shows either of both magnitudes could be the ID.

ID	RA	DEC	$S_{1.4}$ / mJy	K-magnitude	sep	struc
vimos01	22:15:13.82	0:40:36.29	41.05	< 21		nc
vimos02	22:15:14.49	0:40:39.86	16.85	< 21		nc
vimos03	22:15:15.32	0:40:44.45	26.23	< 21		nc
vimos04	22:15:15.86	0:41:6.010	13.03	< 21		nc
vimos05	22:15:16.82	0:41:5.710	53.95	< 21		c
vimos06	22:15:23.55	0:12:48.22	18.88	17.18±0.03		c
vimos07	22:15:25.06	0:12:50.75	16.06	< 21		c
vimos08	22:16:48.52	0:15:58.09	26.13	16.94±0.009	0.13	c
vimos09	22:16:48.62	1:24:27.31	30.29	17.04±0	0.88	c
vimos10	22:16:48.89	1:9:34.650	12.25	< 21		c
vimos11	22:16:49.70	1:9:33.659	12.08	< 21		c

Continued on next page

Table 2.7 – continued from previous page

ID	RA	DEC	$S_{1.4}$ / mJy	K-magnitude	sep	struc
vimos12	22:16:54.57	1:7:34.349	14.89	< 21		c
vimos13	22:16:57.43	0:24:23.01	16.78	19.29±0.08		nc
vimos14	22:17:25.80	0:31:47.31	17.26	18.31±0.019	0.26	c
vimos15	22:17:26.67	0:1:22.280	11.64	19.39±0.15		c
vimos16	22:17:27.14	0:55:59.20	11.63	19.32±0.039	0.54	c
vimos17	22:17:34.20	0:47:42.84	23.97	< 21		c
vimos18	22:17:42.44	0:3:17.610	40.95	18.95±0.08		c
vimos19	22:17:49.52	1:24:41.27	19.24	< 21		c
vimos20	22:17:53.36	0:4:35.040	141.76	18.60±0.029	0.44	c
vimos21	22:17:54.79	0:35:31.96	207.26	16.78±0	0.25	c
vimos22	22:17:59.47	0:30:54.90	20.95	18.79±0.029	0.64	c
vimos23⋆	22:18:4.975	0:9:54.189	11.6	< 21		c
vimos24	22:18:6.678	0:52:23.97	54.77	15.74±0	0.31	c
vimos25	22:18:9.272	0:11:29.28	15.63	< 21		nc
vimos26	22:18:9.751	0:49:31.37	23.62	< 21		c
vimos27	22:18:23.35	1:11:19.32	15.77	18.02±0.009	0.09	c
vimos28	22:18:28.36	0:12:31.37	117.3	< 21		nc
vimos29	22:18:29.44	0:12:24.11	245.81	< 21		nc
vimos30	22:18:31.31	0:12:17.12	35.71	< 21		nc
vimos31	22:18:32.27	0:12:7.809	24.22	< 21		nc
vimos32	22:18:32.69	0:5:12.350	11.28	19.53±0.059	0.41	nc
vimos33	22:18:34.04	0:11:25.98	16.74	< 21		c
vimos34	22:18:34.66	0:11:22.55	15.51	20.09±0.15		nc
vimos35	22:18:39.49	0:10:38.79	18.59	18.53±0.019	0.27	c
vimos36	22:18:41.45	0:6:56.639	10.93	< 21		nc
vimos37	22:18:51.55	0:13:6.289	30.79	< 21		nc
vimos38	22:18:54.17	0:10:2.640	13.43	18.64±0.029	0.16	c
vimos39	22:19:4.359	0:47:59.75	78.96	19.19±0.039	0.77	c
vimos40	22:19:9.399	0:31:13.72	16.43	$19.66 \pm 0.11 \wr 19.29 \pm 1.10$		c
vimos41	22:19:19.44	0:56:5.280	10.44	18.17±0.019	0.41	c
vimos42	22:19:25.26	0:10:3.220	12.44	19.31±0.10		c
vimos43	22:19:31.95	1:30:0.070	65.24	18.20±0.06		nc
vimos44	22:19:33.05	1:29:53.18	60.74	18.23±0.06		nc
vimos45	22:19:41.53	0:17:39.13	27.77	18.66±0.029	0.13	c
vimos46	22:19:54.59	1:23:56.45	63.18	18.54±0.09		c
vimos47	22:20:32.60	0:25:35.86	95.39	16.91±0.02		c
vimos48	22:20:32.74	1:0:29.649	114.54	19.53±0.13		c
vimos49	22:20:36.31	0:33:33.88	12.68	16.48±0	0.26	c
vimos50	22:20:45.93	0:53:40.34	12.27	< 21		nc
vimos51	22:20:48.44	0:18:41.72	33.67	17.23±0.009	0.045	c
vimos52	22:20:51.52	0:58:14.67	72.78	15.42±0	0.92	nc
vimos53	22:21:6.469	0:24:14.44	125.97	18.00±0.009	0.38	c

Continued on next page

Table 2.7 – continued from previous page

ID	RA	DEC	$S_{1.4}$ / mJy	K-magnitude	sep	struc
vimos54	22:21:8.883	0:38:36.5	22.47	16.53±0	0.06	c
vimos55	22:21:14.03	0:11:14.57	13.11	< 21		c
vimos56	22:21:14.96	1:6:14.729	75.37	17.68±0.04		c
vimos57	22:21:26.75	0:18:14.39	17.82	17.51±0.009	0.28	c
vimos58	22:21:32.43	0:16:45.31	26.87	13.43±0	0.13	c
vimos59	22:21:36.50	0:38:18.80	59.56	17.48±0.05		c
vimos60	22:21:40.63	0:8:11.159	24.35	18.28±0.019	0.06	c
vimos61	22:21:40.97	0:1:58.580	35.92	< 21		nc
vimos62	22:21:41.84	0:2:1.4900	17.86	< 21		nc
vimos63	22:21:45.80	0:2:21.700	21.75	< 21		nc
vimos64	22:21:52.91	1:29:17.34	39.98	19.25±0.10		c
vimos65	22:21:59.64	0:59:10.47	21.3	16.52±0.03		c
vimos66	22:22:3.793	1:5:1	20.34	< 21		c
vimos67⋆	22:22:< 21.93	0:47:49.99	18.52	< 21		c
vimos68⋆	22:22:22.48	1:18:37.38	58.39	18.10±0.019	0.36	c

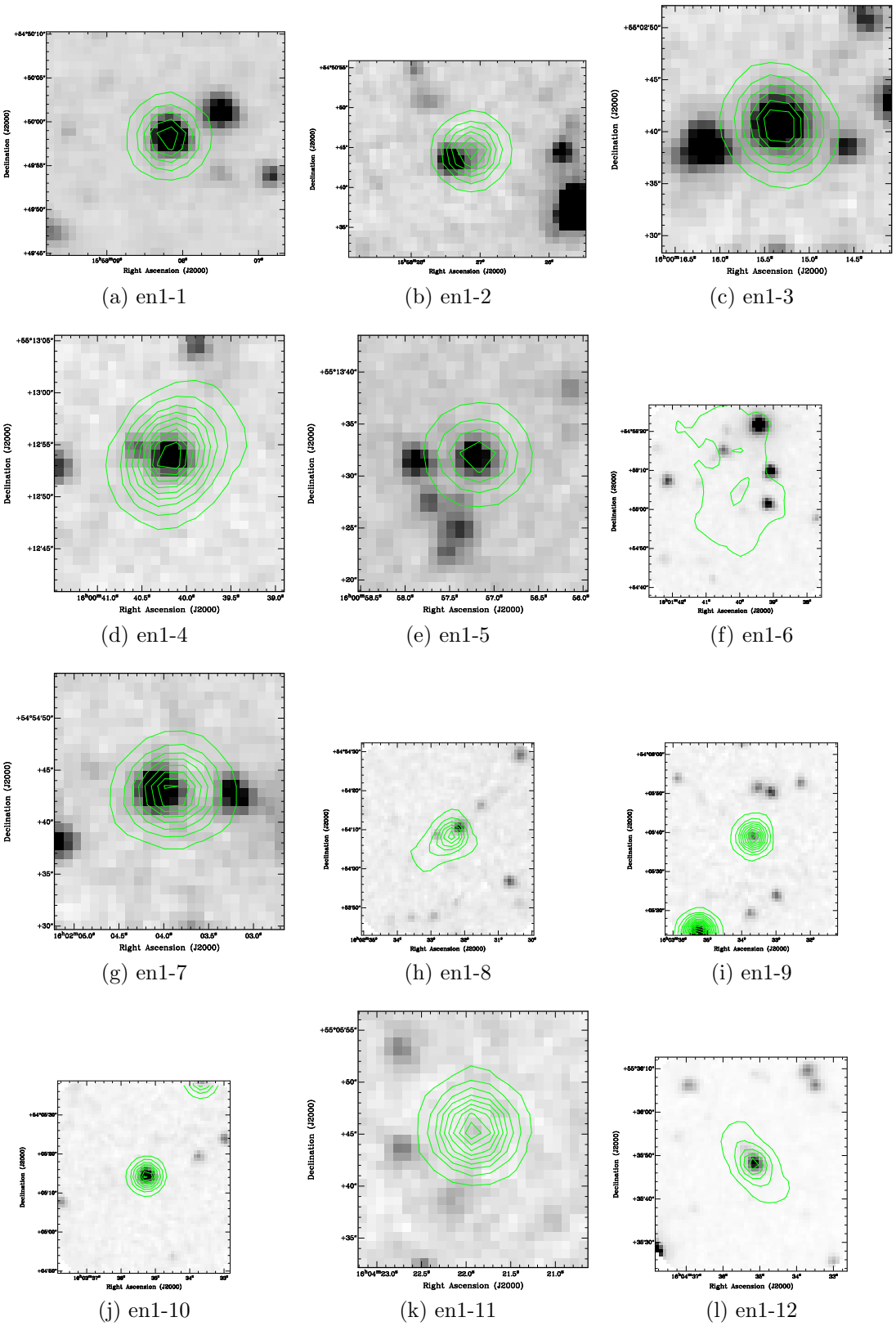

(a) en1-1 (b) en1-2 (c) en1-3

(d) en1-4 (e) en1-5 (f) en1-6

(g) en1-7 (h) en1-8 (i) en1-9

(j) en1-10 (k) en1-11 (l) en1-12

Figure 2.5: The IRAC-3.6μm images from SWIRE in the ELAIS-N1 field, overlaid with the radio image from FIRST survey. Images of all the ELAIS-N1 targets are presented in Appendix A

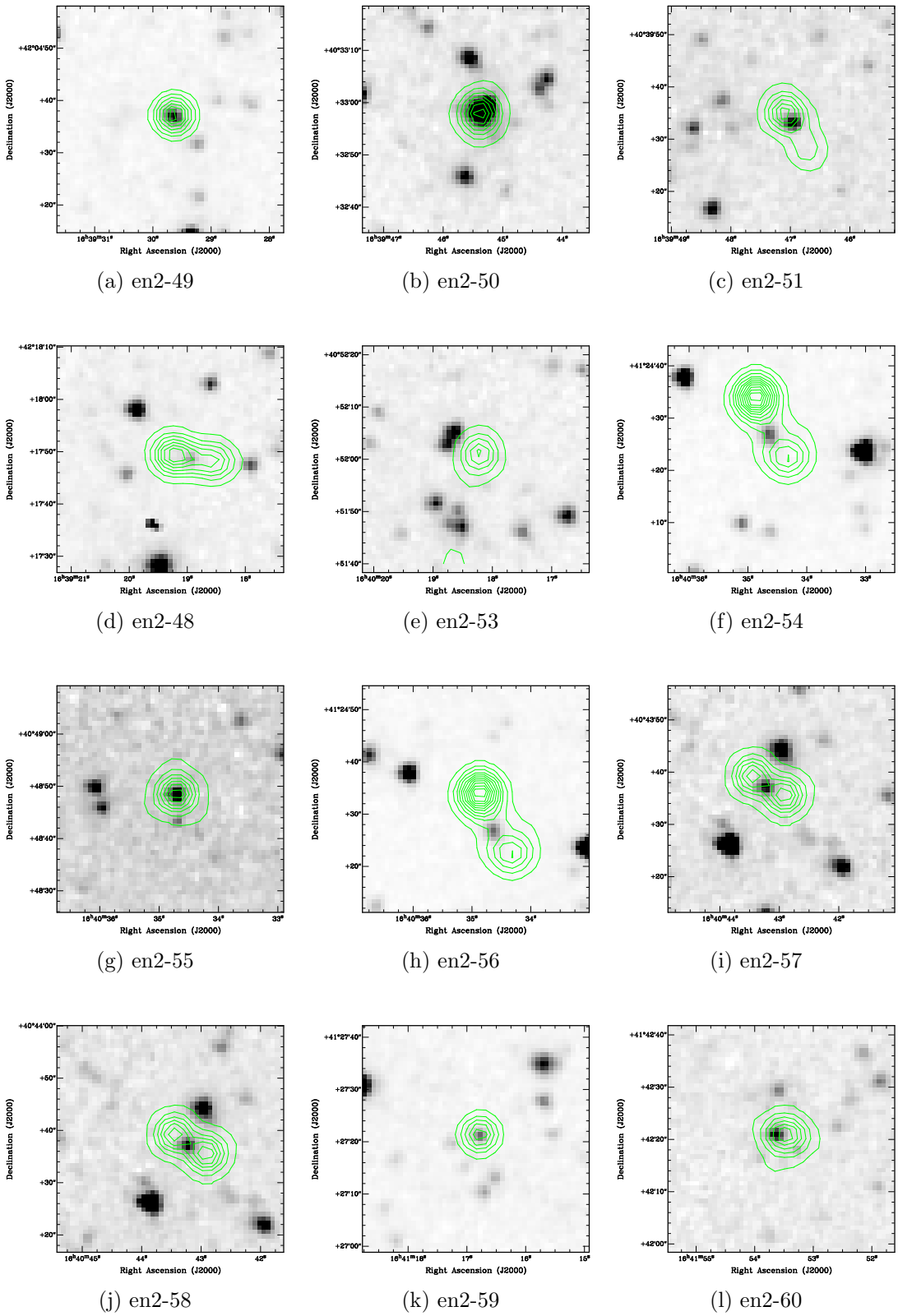

(a) en2-49 (b) en2-50 (c) en2-51

(d) en2-48 (e) en2-53 (f) en2-54

(g) en2-55 (h) en2-56 (i) en2-57

(j) en2-58 (k) en2-59 (l) en2-60

Figure 2.6: The IRAC-3.6μm images from SWIRE in the ELAIS-N2 field, overlaid with the radio image from FIRST survey. Images of all the ELAIS-N2 targets are presented in Appendix A

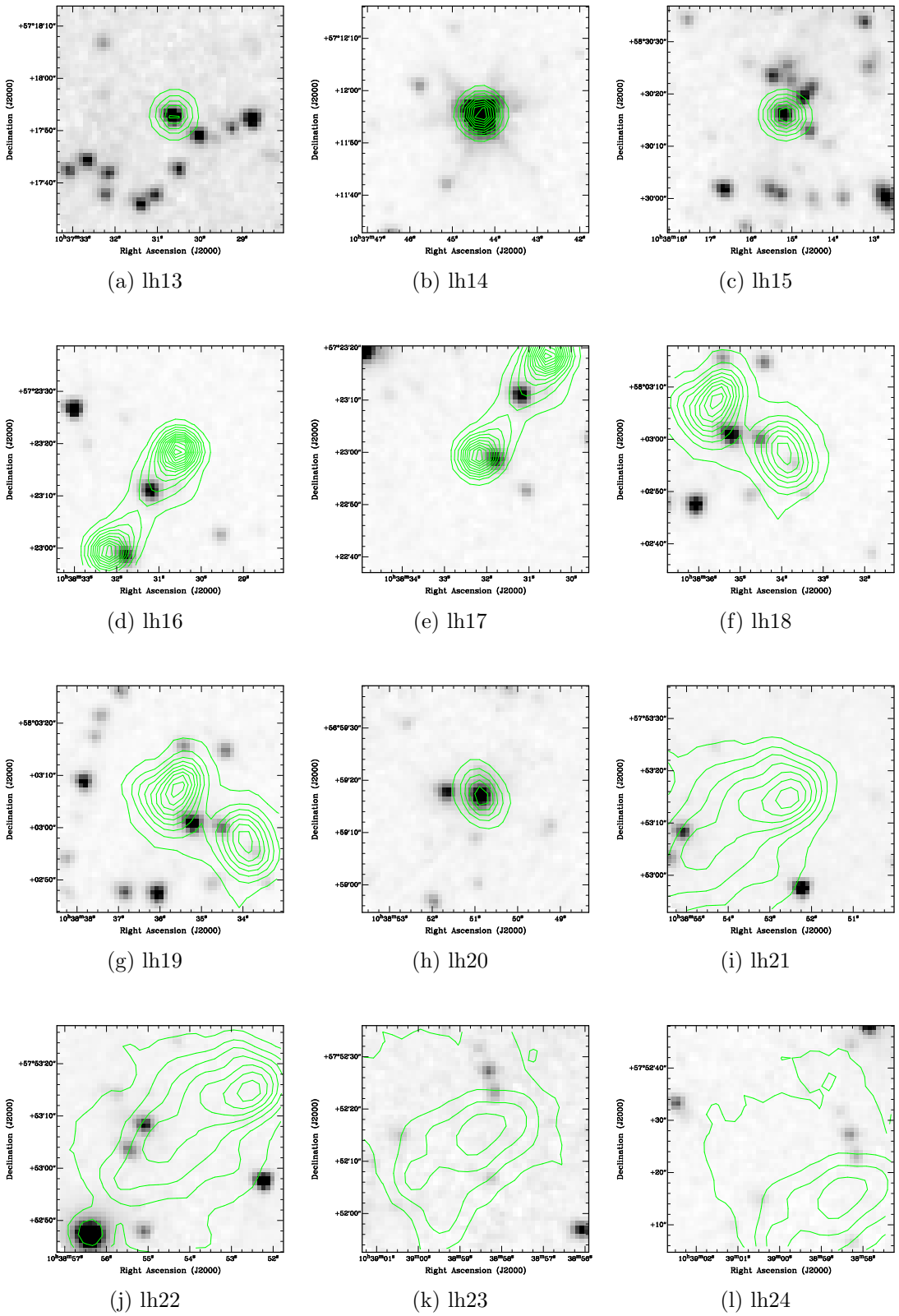

(a) lh13 (b) lh14 (c) lh15

(d) lh16 (e) lh17 (f) lh18

(g) lh19 (h) lh20 (i) lh21

(j) lh22 (k) lh23 (l) lh24

Figure 2.7: The IRAC-3.6μm images from SWIRE in the Lockman Hole field, overlaid with the radio image from FIRST survey. Images of all the Lockman Hole targets are presented in Appendix A

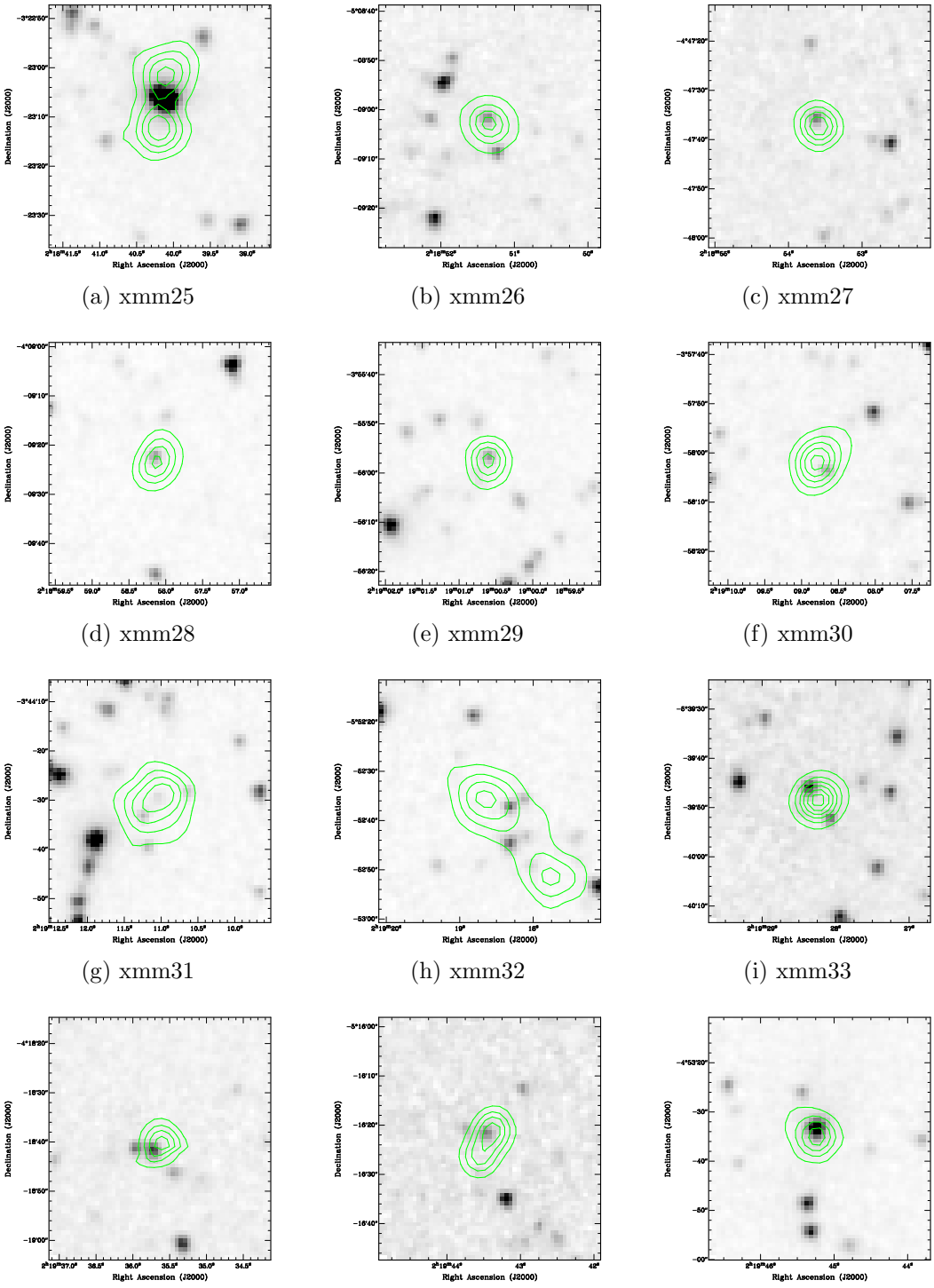

(a) xmm25 (b) xmm26 (c) xmm27

(d) xmm28 (e) xmm29 (f) xmm30

(g) xmm31 (h) xmm32 (i) xmm33

(j) xmm34 (k) xmm35 (l) xmm36

Figure 2.8: The IRAC-3.6μm images from SWIRE in the XMM-LSS field, overlaid with the radio image from GMRT data. For the full image of all the XMM-LSS targets see Appendix A

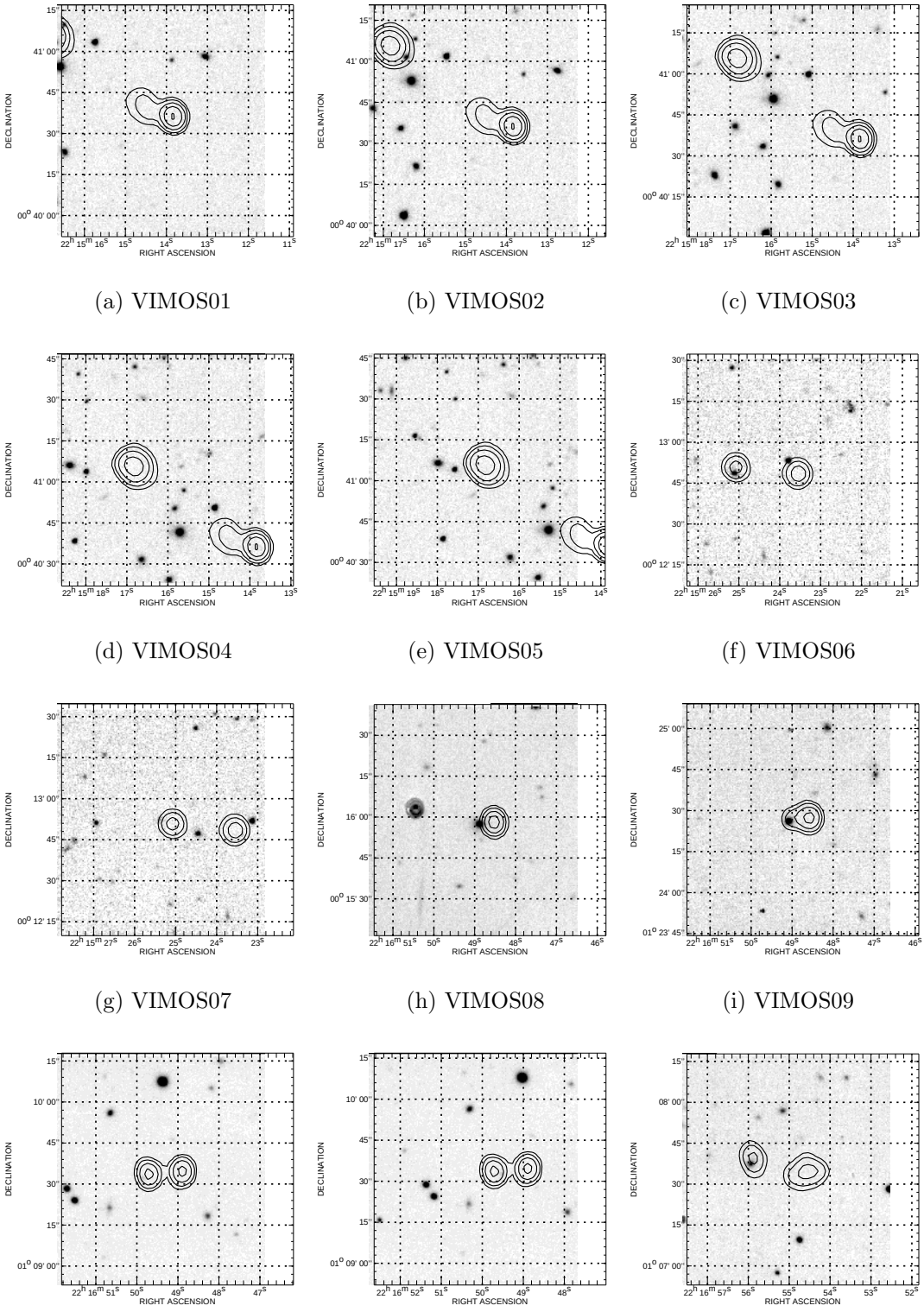

(a) VIMOS01 (b) VIMOS02 (c) VIMOS03

(d) VIMOS04 (e) VIMOS05 (f) VIMOS06

(g) VIMOS07 (h) VIMOS08 (i) VIMOS09

(j) VIMOS10 (k) VIMOS11 (l) VIMOS12

Figure 2.9: The K-band images from DXS in the VIMOS field, overlaid with the radio image from FIRST data. For the full image of all the VIMOS targets see Appendix A

Chapter 3

Spectroscopy and Redshift estimation

3.1 Target selection

To follow up our candidate high-redshift radio sources we were awarded telescope time in April 2009, August 2009, February 2010 and February 2011 with the William Herschel Telescope (WHT). We were also awarded service observations to target high-redshift radio source candidates over the VIMOS4/SSA22 UKIDSS-DXS field with Gemini South. In this chapter I provide a summary of the candidates that were targeted in these observing runs and present the optical spectra and redshifts for those sources where we found a robust redshift measurement. Towards the end of the chapter I use this new sample of high-redshift radio sources, selected in a unique way, to compare with previous samples of high redshift radio galaxies selected by virtue of their steep spectral index and/or their angular size. In particular I investigate their emission line properties through the Hydrogen Lyα emission line, and their host galaxy properties by comparing them to the well know $K-z$ relation.

For all of the observing runs I preferentially targeted the brightest radio sources with the faintest near-infrared emission. I chose this strategy to increase the probability of finding bright emission lines by virtue of the correlation between Lyα luminosity and radio luminosity found by Jarvis et al. (2001b), but also to increase the chance of a finding sources at the highest redshift, which presumably have the faintest host galaxies.

Over the four WHT observing runs I obtained spectroscopic observations for 46 high-redshift radio source candidates. More could have been observed, however, poor weather and technical faults limited the amount of observing possible, particularly on the February 2010 and February 2011 runs. In addition to preferentially selecting faint host galaxies with bright radio emission, the scheduling of the observing runs also restricted which sources we could observe. Therefore, there are more observations of sources in the fields accessible in February and April, namely ELAIS-N1, ELAIS-N2 and the Lockman Hole, with comparatively fewer observations over the XMM-LSS, ELAIS-S1 and CDFS fields.

The candidate high-redshift radio galaxies that we attempted to obtain spectroscopic redshifts for are listed in Table 3.1, along with the dates on which they were observed and the integration times used.

3.2 Spectroscopic Observations

The observational set-up used to obtain spectroscopy of the high-redshift radio galaxy candidates needs to ensure as large a wavelength coverage as possible, to maximize the chances of detecting any emission line. I therefore used the low-resolution grisms in the WHT's Intermediate dispersion Spectrograph and Imaging System (ISIS). This spectrograph is very efficient for this type of work, as it consists of two intermediate dispersion spectrographs which can be operated simultaneously, and are separately optimised for the blue and red spectral regions. At low resolution, this instrument therefore gives almost complete spectral coverage from ~ 3300Å through to just shortward of $1\,\mu$m. The only part of the spectrum that is not useable in this range is the region around which the dichroic splits the light into the blue and red arms. For all the observations presented here, the 5300Å dichroic was used, which gives the best performance over the whole spectral range (see Fig. 3.1).

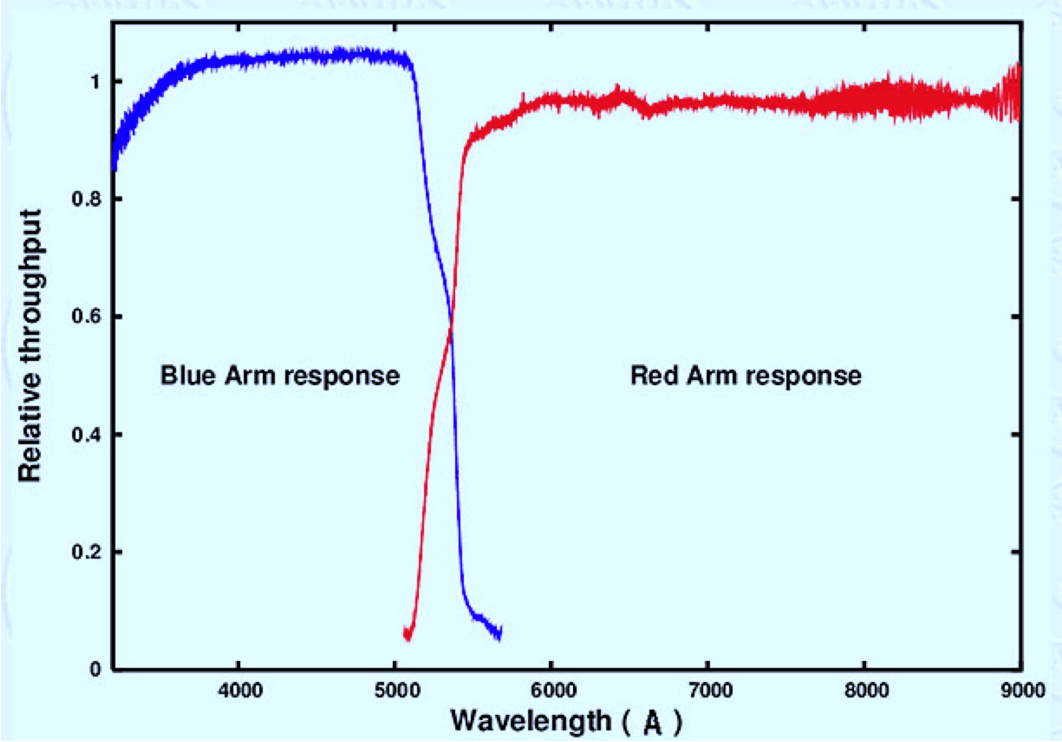

Figure 3.1: Throughput of the 5300Å dichroic. It is better than that of the other dichroic units available (>95 per cent) in the red arm, and also in the blue. Ripples, in particular in the blue arm, are much less pronounced than other available dichroics. The cut-off region is also narrower, with the throughput in both arms below 70 per cent in the 5200-5400Å region. (Figure taken from the ING web page: http://www.ing.iac.es/astronomy/instruments/isis/isis_dich.html)

To maximize the spectral coverage this dichroic was used in conjunction with the R300B and R158R gratings, for the blue and red arms respectively. The detector for the blue arm of ISIS is a EEV12 4096×2048 pixel^2 CCD, which is large enough to sample the whole of

the blue spectral range shortward of the dichroic cut-off, down to the atmospheric cut-off at ~ 3200Å with the R300B grating. The red arm uses a RED+ 4096×2048 pixel^2 CCD, which is large enough to sample the full spectral range up to $\sim 1\mu$m with the lowest resolution grating (R158R). We note that these two gratings have the highest efficiency across the bulk of the spectral range.

As spectral resolution is not a primary driver in obtaining redshift measurements, it is also possible to use a relatively wide slit. Making the slit wide has both advantages and disadvantages for obtaining redshift via emission lines of faint objects. As the objects that we are targeting are selected to be very faint, it is impossible to acquire them directly with the telescope. A different strategy is therefore required. The standard way of doing this is to acquire a brighter target, preferably an unresolved source where the position is not ambiguous, and then make the telescope do a "blind offset" from this bright star to the target of interest. This obviously relies on the telescope being able to perform very accurate movements over a typical offset of < 1 arcmin. For the WHT this is a proven technique and underpinned much of the earlier work of obtaining redshifts for high-redshift radio galaxies (e.g. Rawlings et al., 1996; Jarvis et al., 2001b; Cruz et al., 2006). In such cases, having a wide slit would obviously mitigate, to some extent, uncertainties in the offsets due to the telescope. Another advantage of a wide slit is that many of the objects are not detected at all at visible and near-infrared wavelengths, and the positions of the radio galaxies are derived purely from the radio position. As the radio data is at much poorer resolution than the typical near-infrared/optical imaging this leads to larger uncertainties in the position. Finally, a further advantage is that many high-redshift radio galaxies have extended emission line haloes spanning up to ~ 15 arcsec. Thus a wide slit would enclose much more of the light from an extended emission line halo, which in turn would lead to higher signal-to-noise on this line.

The main disadvantage of a wide slit is the potential for decreasing the signal-to-noise ratio if the target is smaller than the slit width. This would lead to more light entering the slit from the sky, and as the noise in the spectra is dominated by the sky this would in turn lead to lower signal-to-noise on the target. A possible disadvantage is also that with a larger slit width, the spectral resolution will decrease as the light is projected on to many more pixels. If the spectral features that I am interested in, the emission lines, are narrower than this spectral resolution this would also decrease the signal-to-noise on the lines slightly. However, the typical line widths of high-redshift radio galaxies are ~ 1000 km s^{-1} which corresponds to a spectral resolution of around 12Å for the Lyα line at $z \sim 2$.

I used a slit width of 2 arcsec, which gives a resolution of 8.6Å in the blue arm and 16.5Å in the red arm. The choice of 2 arcsec width is a compromise to reduce the offsetting errors and increase the signal to noise to extended emission line halos, but to not make the resolution so bad that significant signal-to-noise is lost on a typical emission line.

Table 3.1: In this table I present the 46 candidates with details of the observations. The exposure time is given for the red and blue arm, labelled with r and b respectively. The rms in FIRST survey is 0.147mJy and this is the typical uncertainty on the radio flux-density measurements for these unresolved sources.

Target	RA	DEC	$S_{1.4}$/ mJy	$S_{3.6}$/ μJy	Telescope	Date of Observation	Exp.Time (s)
EN2_04	16:32:12.60	+41:05:21.12	16.21	32.07±3.79	WHT	20.08.09	B(1800), R(2×900)
EN2_13	16:35:02.73	+40:08:00.58	13.9	22.8 ± 2.41	WHT	20.08.09-22.08.09	B(2×1800), R(2×900)
Continued on next page							

Table 3.2: The candidates in the XMMLSS field for which we obtained optical spectroscopy observations, including the telescope on which the spectra were taken, the date of the observation and the exposure time used for both the blue (B) and red (R) arms.

Target	RA	Dec	S_{610}/ mJy	$S_{3.6}$/ μJy	Telescope	Date of Observation	Exp. Time (s)
XMM_09	02:17:34.18	-03:13:08.71	67.3	61.37±6.80	WHT	19.08.09	B(1800), R(2×900)
XMM_19	02:18:23.49	-04:19:00.72	21.1	< 7.3	WHT	19.08.09-22.08.09	B(2×1800), R(4×900)
XMM_23	02:18:34.77	-03:46:15.75	22.3	15.33±2.11	WHT	19.08.09-21.08.09	B(2×1800), R(4×900)
XMM_56	02:21:43.25	-02:49:27.80	25.2	< 7.3	WHT	20.08.09-21.08.09	B(2×1800), R(4×900)
XMM_58	02:22:00.41	-03:39:34.99	42.0	23.37 ± 2.44	WHT	21.08.09	B(1800), R(2×900)
XMM_86	02:23:57.07	-04:41:11.44	140.3	< 7.3	WHT	21.08.09-22.08.09	B(2×1800), R(4×900)
XMM_106	02:26:32.51	-05:13:27.11	131.8	< 7.3	WHT	22.08.09	B(2×1800), R(4×900)

Table 3.1 – continued from previous page

Target	**RA**	**DEC**	**$S_{1.4}$/ mJy**	**$S_{3.6}$/ μJy**	**Telescope**	**Date of Observation**	**Exp.Time (s)**
EN2_14	16:35:18.24	+40:22:19.96	53.99	< 7.3	WHT	27.04.09	B(1800), R(2×900)
EN2_20	16:36:17.50	+41:13:10.82	16.55	20.7 ± 2.20	WHT	21.08.09	B(1800), R(2×900)
EN2_22	16:36:38.49	+40:11:56.89	172.24	19.10± 2.54	WHT	21.08.09	B(1800), R(2×900)
EN2_23	16:36:45.00	+40:54:44.15	11.27	< 7.3	WHT	20.08.09-21.08.09	B(2×1800), R(2×900)
EN2_37	16:37:55.99	+41:48:47.45	18.43	27.38 ± 2.82	WHT	22.08.09	B(1800), R(2×900)
EN2_39	16:38:02.12	+42:08:19.58	40.11	18.23 ± 1.97	WHT	20.08.09	B(1800), R(2×900)
EN2_42	16:38:44.33	+41:07:03.92	10.28	22.65 ± 2.39	WHT	21.08.09	B(1800), R(2×900)
EN2_45	16:39:12.10	+40:52:36.72	22.51	< 7.3	WHT	27.04.09	B(1800), R(2×900)
EN1_11	16:04:21.91	+55:05:45.39	20.12	< 7.3	WHT	27.04.09	B(1800), R(2×900)
EN1_16	16:04:54.73	+55:59:49.40	79.15	< 7.3	WHT	27.04.09	B(1800), R(2×900)
EN1_50	16:09:03.78	+56:10:42.02	12.23	< 7.3	WHT	27.04.09	B(1800), R(2×900)
EN1_64	16:10:35.82	+56:48:47.16	19.16	< 7.3	WHT	27.04.09	B(1800), R(2×900)
EN1_94	16:14:06.26	+53:19:12.48	15.1	< 7.3	WHT	20.08.09-22.08.09	B(1800), R(2×900)
EN1_112	16:17:10.11	+55:17:46.88	31.48	14.10 ±2.18	WHT	20.08.09-22.08.09	B(1800), R(2×900)
EN1_135	16:21:53.20	+55:31:31.58	31.5	13.05 ± 1.41	WHT	20.08.09-22.08.09-05.02.11	B(2×1800), R(3×900)
LH10	10:36:48.51	+57:23:37.88	36.95	51.58 ±5.74	WHT	11.02.10	B(2×1800), R(4×900)
LH33	10:39:23.58	+59:38:04.46	13.05	16.32 ± 1.77	WHT	02.02.11	B(2×1800), R(4×900)
LH42	10:40:33.56	+59:42:30.19	16.02	< 7.3	WHT	12.02.10	B(2×1800), R(4×900)
LH43	10:41:14.06	+59:29:33.68	11.82	19.44 ± 2.08	WHT	02.02.11	B(2×1800), R(4×900)
LH53	10:42:23.59	+58:11:54.52	26.12	13.54±1.88	WHT	05.02.11	B(2×1800), R(4×900)
LH57	10:42:55.48	+56:38:03.63	20.73	22.01 ± 2.34	WHT	02.02.11-11.02.10	B(4×1800), R(8×900)
LH66	10:45:29.93	+57:38:17.07	69.73	16.88 ± 1.83	WHT	05.02.11-10.02.10	B(3×1800), R(5×900)
LH78	10:46:24.79	+59:04:45.94	13.89	< 7.3	WHT	27.04.09	B(1800) , R(3×900)
LH84	10:47:00.85	+59:19:02.07	21.81	< 7.3	WHT	02.02.11	B(2×1800), R(4×900)
LH97	10:48:53.47	+59:06:09.74	12.82	< 7.3	WHT	02.02.11	B(2×1800), R(4×900)
LH101	10:49:16.25	+56:01:17.55	28.12	20.57±2.70	WHT	10.02.10	B(2×1800), R(4×900)
LH109	10:50:14.55	+56:32:09.98	12.16	20.49 ± 2.15	WHT	10.02.10	B(2×1800), R(4×900)
LH112	10:50:53.84	+58:32:32.86	156.23	17.42 ± 1.80	WHT	10.02.10	B(2×1800), R(4×900)
LH120	10:51:31.22	+58:49:47.13	15.02	< 7.3	WHT	02.02.11	B(2×1800), R(3×900)
LH134	10:53:18.18	+58:56:23.23	78.4	< 7.3	WHT	27.04.09-11.02.10-03.02.11	B(6×1800), R(12×900)
LH142	10:54:12.27	+58:29:41.20	13.13	11.69 ± 1.39	WHT	10.02.10	B(2×1800), R(3×900)
LH143	10:54:21.45	+58:00:59.55	10.41	25.53 ± 2.70	WHT	10.02.10	B(2×1800), R(3×900)
LH148	10:55:30.03	+58:32:32.22	17.99	< 7.3	WHT	02.02.11	B(2×1800), R(3×900)
LH149	10:55:48.53	+57:18:27.69	14.19	< 7.3	WHT	27.04.09-03.02.11	B(4×1800), R(8×900)
LH157	10:57:15.91	+57:23:13.90	133.32	< 7.3	WHT	27.04.09-05.02.11-10.02.10	B(5×1800), R(10×900)
LH174	11:01:09.46	+57:27:15.63	73.91	15.87 ± 1.74	WHT	10.02.10	B(1800), R(2×900)

3.2.1 WHT Data reduction

In this section I give the details of the reduction steps necessary to obtain redshifts from the spectroscopic observations described in Sec. 3.2. In order to reduce and calibrate the data we used the following steps:

Table 3.3: The candidates in the VIMOS field for which we obtained optical spectroscopy observations, including the telescope on which the spectra were taken, the date of the observation and the exposure time.

Target	RA	Dec	$S_{1.4}$/ mJy	K-mag	Telescope	Date of Observation	Exp. Time (s)
VIMOS_17	22:17:34.20	0:47:42.84	23.97	< 21	GEMINI	24.08.09	609
VIMOS_26	22:18:9.751	0:49:31.37	23.62	< 21	GEMINI	24.08.09	609
VIMOS_42	22:19:25.26	0:10:3.220	12.44	19.31 ± 0.10	GEMINI	24.08.09	609
VIMOS_64	22:21:52.91	1:29:17.34	39.98	19.25 ± 0.08	GEMINI	24.08.09	609

Bias subtraction: A bias image is a zero second exposure, which measures the value of an unexposed pixel on the CCD. A bias is added to a CCD because if it was not added it would mean that positive and negative noise spikes are just as likely. But as electronics cannot deal with negative sigma from a CCD a positive offset is added and the noise can then fluctuate around this positive value. When the CCD is exposed it is therefore necessary to remove this "artificial" offset from every exposure. To do this I combined the average of around ten bias frames for each night with the Iraf task Imcombine and subtracted the average bias from all of science and calibration frames, using the Iraf task Imarith.

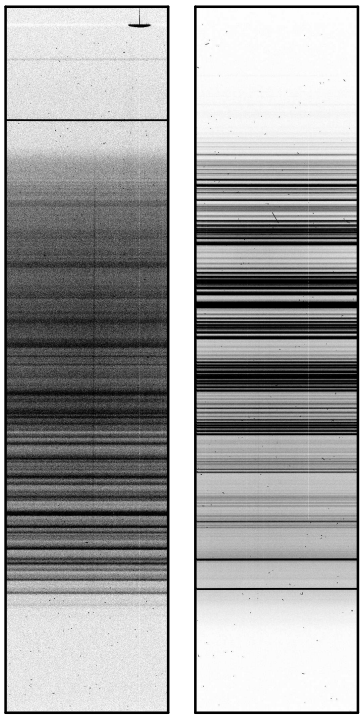

(a) Blue arm (b) Red arm

Figure 3.2: Bias subtracted 2D spectrum of EN2_45 in both the blue (left) and red arm (right).

Lamp flats: Variations of the pixel sensitivity in the CCD can be caused by the optical system. This variations need to be corrected for. Flat field images are taken to overcome this problem. Exposures of a white light source are usually used for this purpose and in the case of my observations this is done using a Tungsten lamp. The CCDs were exposed to this Tungsten lamp several times, so as to remove any anomalous noise properties in single exposures. When

reducing these images, I combined all flat frames and normalised them using the IRAF task RESPONSE, which divides the combined flat by a smoothly varying fit to the data along the dispersion axis.

Sky flats: As many of our sources are expected to be extended, particularly the emission line halos, I also obtain twilight flat-field observations so that the illumination pattern across the detector after being dispersed through the slit can be measured. I calculated the illumination of the CCDs again using multiple sky flats, using the task ILLUMINATION.

After doing this these combined flats are used to flat-field the science frames to account for both the response of the CCD and the illumination through the slit, by dividing through by the combined slit response function.

Wavelength Calibration: To wavelength calibrate the data I use observations of the CuNe +CuAr lamps. The spectrum of the arc lamps was compared to the known wavelength of the spectral lines of these elements. To do this I used the IDENTIFY task in IRAF, which allowed me to identify the lines over the central column of each CCD. I then used the same solution from the data base and applied it over all columns with task REIDENTIFY. At this point I also used observations of the standard star, which was detected at very high signal-to-noise across the whole wavelength range to measure any curvature in the spectrum along the dispersion axis. It traced the standard star spectrum and saved the traced solution, again using the IRAF tasks IDENTIFY and REIDENTIFY. To define the full wavelength solution as a function of x and y coordinates I used the task FITCOORDS which fits a polynomial function to the x and y coordinate solutions based on the arc lamps and the standard star respectively. This fit was finally applied to the science frames using the task TRANSFORM.

Sky subtraction: The emission from molecules and elements in the atmosphere contribute to the brightness of the sky, along with the reflected light from the moon (in non-dark time). The strong, background, skylines need to be removed from the science frames. In order to do this I used the IRAF task BACKGROUND. With this package I sample regions either side of the target and fit a polynomial in the spatial direction (the x axis of the chip) to each row. These polynomials generally have the same form independent of the row due to the flat-field corrections performed earlier, but their normalisation changes due to the intensity of sky lines at specific wavelengths.

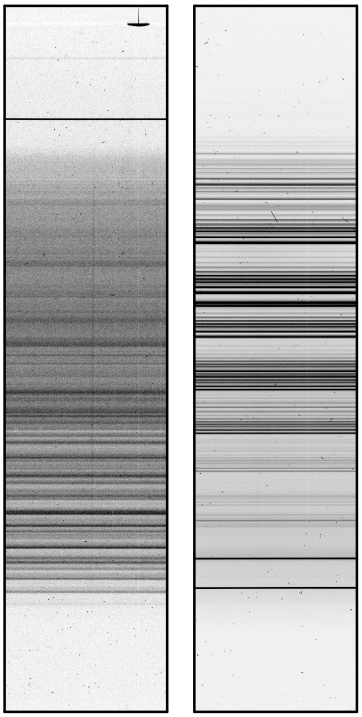

(a) Blue arm (b) Red arm

Figure 3.3: Flat fielded 2D spectrum of EN2_45 in both blue (left) and red (right) arms.

Flux calibration: The final step is the flux calibration which basically converts the flux scale counts in the spectra to the real flux density scales. This can be done by observing standard stars of known spectral energy distribution across the spectral range that I observe. Initially I use the same reduction procedures that were done for the science frames. Once the standard star frames have been flat-fielded I extract a one-dimensional spectra of the stars, ensuring that all of the light is included into the collapsed 1-D spectrum. I then use the Sensfunc package to produce a sensitivity function along the dispersion axis by comparing the known flux-density distribution to the observed one. Once I have determined the sensitivity function I use the the task fluxcalib to produce the final flux-calibrated 2-D spectra. It is also worth noting that different standard stars were used at different times of the year and at different points in the night. The standard stars used were Feige35, BD284211, BD332642 and GD50.

Extracting 1-D spectra of the targets: Once all of the data are reduced I then extract 1-dimensional spectra at the position of the radio galaxy. Generally the radio galaxies are undetected in the continuum, therefore a good knowledge of the position of the radio galaxy on the slit beforehand is required. The WHT is a stable telescope and the offsetting from bright stars in the field ensures that the radio galaxy should appear in the same column for every individual night's observations, including those of the standard stars. I therefore, searched for continuum and line emission in the same column as the standard star observations on the same night. As an additional check I attempted to confirm the column at which the radio galaxy should fall using other objects along the slit and then comparing them to the imaging data of the same field. Where this was possible, i.e. where bright object fell on the slit, the column

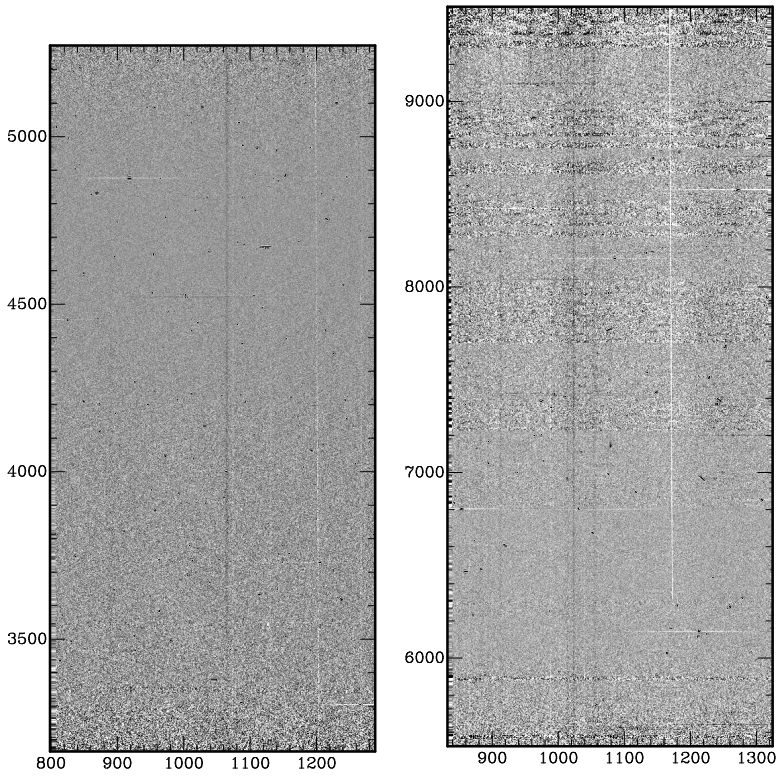

(a) Blue arm (b) Red arm

Figure 3.4: Final reduced 2D spectra of EN2_45 in both blue (left) and red (right) arms. The wavelength (in Angstroms) is given along the y-axis of both the blue and red arms.

was found to be consistent with the expected column to within 5 pixels (~ 2 arcsec).

3.2.2 GEMINI Observations & Data Reduction

My GEMINI observations were carried out with the Gemini Multi-Object Spectrograph (GMOS) on the 8-m Gemini South telescope in queue-scheduled mode in the VIMOS field in September 2009. I used EEV 2037-06-03, EEV 8194-19-04 and EEV 8261-07-04 (6144×4608 pixel^2) CCDs using the R150 grating for blue and red part of the spectrum at a central wavelength of 660 and 655 nm in the Nod-and-shuffle mode with a 2.0 arcsec nod along a 2-arcsec slit. Data reduction was carried out with Gemini IRAF package using similar steps to those outlined for the WHT reduction, thus I do not given full details but only highlight the packages used for the different steps.

Data preparation: The first step in the GMOS data reduction is to prepare raw images using GPREPARE to attach the Mask Definition Files (MDF) to GMOS spectra. After being processed with GPREPARE, GMOS data are then able to be read by the subsequent tasks.

Flat fielding: I trimmed the image and subtracted the combined bias to generate a normalised lamp spectroscopic flat field using GSFLAT, which removes the normalised flat field and the GMOS spectral response and the uneven illumination from the flat field image and leaves only the pixel-to-pixel variations and the fringing. Using the task GSREDUCE I trimmed, dark

subtracted and flat fielded all our science frames and then used GNSCOMBINE to combine all the data frames into a single file. Finally I used the task GSREDUCE again to mosaic and cut the science frames.

Wavelength calibration: I used the task GSTRANSFORM to make the wavelength calibration for each frame but first the database directory with the appropriate wavelength transformations needs to be defined. This is achieved by running GSWAVELENGTH on the appropriately reduced arcs.

Flux calibration: All science frames have to be corrected for extinction and calibrated to a flux scale using the sensitivity function made using GSSTANDARD. This uses the standard star to create the flux scale information for the sensitivity function using a fitted polynomial. Both the GSEXTRACT and GSCALIBRATE tasks were used for the science frames to complete the flux calibration.

Cosmic rays: As cosmic rays are narrower than the spectral resolution of the observations, and they exist over one or two spatial pixels while real lines are spatially extended, distinguishing between the real lines and cosmic rays is relatively straightforward and we remove them from the 1-D spectra using IRAF after inspection of the 2-D spectra.

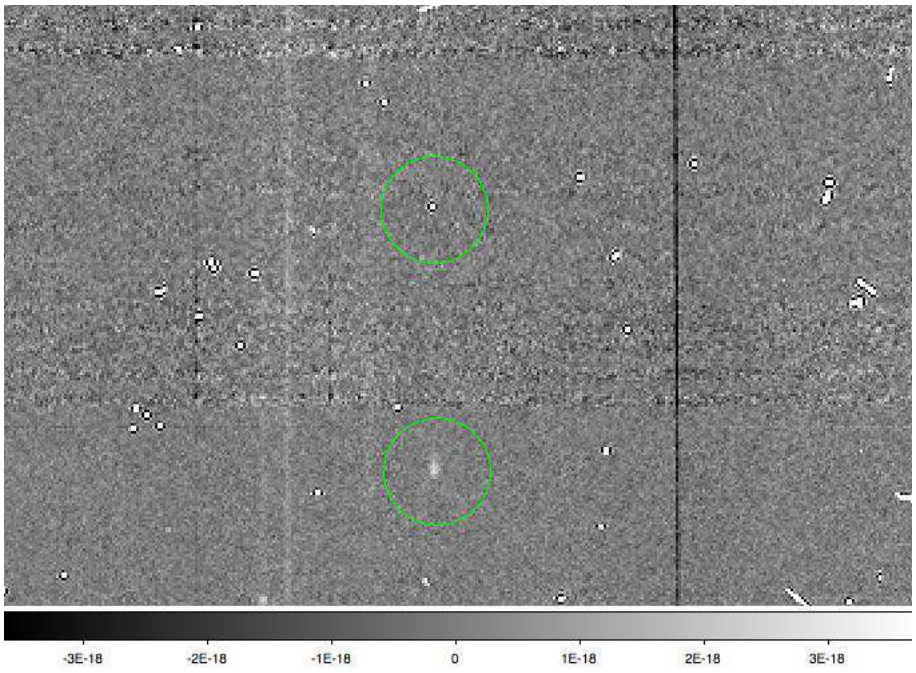

Figure 3.5: 2D spectra of EN2-45. The two green circles in the image at the top and the bottom highlight the position of a cosmic ray and a real line at 7146Å, respectively. As one can see the spatial and spectral extent of the emission line are larger than the cosmic ray.

3.3 Notes on Individual Sources

J160421.90+55.0545.39(EN1_11) The observations of this target were carried out with the WHT in April 2009. The radio flux density at 1.4GHz is $S_{1.4}$=20.12 mJy and there is no identification in the SWIRE survey. The spectrum of this source displays just a single bright

extended emission line at 6696Å which could be Lyα at z=4.50, however further spectroscopy is needed to confirm the result.

J160454.72+55.5949.40(EN1_16) This source has a compact structure with a flux density of $S_{1.4}$=79.15 mJy in the FIRST survey, however it has no identification in the SWIRE survey. The spectrum which was taken in April 2009 does not show any emission line, we therefore cannot obtain a redshift.

J160421.90+550545.39(EN1_50) The observation of this target was carried out with WHT on April 2009 and the spectrum of this source does not show any emission line.

J161035.82+564847.16(EN1_64) The observation of this target was carried out with the WHT on April 2009. The radio flux density at 1.4GHz is $S_{1.4}$=19.16 mJy and it has no identification in the SWIRE survey. The spectrum of this source contains a bright line at 8210Å which we take to be the [OII] line at a redshift of z=1.2, although we cannot rule out Lyα at $z = 5.75$. Previous studies of high-redshift radio galaxies have shown that single bright narrow emission lines are usually either [OII] or Lyα because of the dearth of other bright emission lines around these. If this source were at a redshift of $z = 5.75$ it would have a radio luminosity of $L_{1.4} = 3.8 \times 10^{26}$ W Hz^{-1} sr^{-1}, which is close to the break of the luminosity function, where we would expect the bulk of the sources to reside. Higher resolution spectroscopy could confirm which line this is, as the [OII] doublet could be resolved.

J161406.26+531912.48(EN1_94) This compact radio source has a flux density of $S_{1.4}$=15.1 mJy at 1.4 GHz and no identification in the SWIRE survey. Although we observed this target in two different runs on August 2009, I do not detect any emission line or continuum in any of the individual spectra or when they are combined.

J161710.14+551746.88(EN1_112) The observations for this radio galaxy were taken in two nights with the WHT. The source has a compact structure with a flux density of $S_{1.4}$=31.48 mJy in the FIRST survey and flux density of $S_{3.6}$=14.10 μJy in SWIRE. The spectrum of this source does not show any emission line.

J162153.19+553131.58(EN1_135) This target has a flux density of $S_{1.4}$=31.5 mJy and $S_{3.6}$ = 13.05μJy. The observation for this target were accrued in three different runs in February 2011 and August 2009. The spectra show a faint continuum at the expected position of the radio galaxy longward of 4754Å which I take as the continuum longward of Lyα at a redshift of $z = 2.9$. The other interpretation of a 4000Å break would seem unlikely as this would place it at $z = 0.19$, and the radio emission coupled with the 3.6μm flux density could be very faint for such a redshift.

J163212.59+410521.12(EN2_04) This compact source is detect in SWIRE at $S_{3.6}$ = 32.07μJy and its radio flux density is $S_{1.4}$=16.21 mJy. The spectrum of this radio source was taken with the WHT on August 2009 but displays no emission line.

J163502.72+400800.58(EN2_13) This radio galaxy has a compact structure in the FIRST survey with the flux density of $S_{1.4}$=13.9 mJy and also identification in the SWIRE with a flux of $S_{3.6}$=22.8μJy. Although we observed this radio galaxy twice on August 2009, we have not detected any emission line.

163518.24+402219.96(EN2_14) The spectrum showed an extended emission line at 3767$\mathring{A}$ and a weaker line at 5054Å which we take to be the Lyα and HeII lines at $z = 2.1$. However the faintness of the HeII line means that we cannot be 100 per cent confident, but suggest the redshift given as being very likely.

J163617.49+411310.82(EN2_20) The observation for this radio galaxy were carried out in

August 2009. The source has a faint identification in the SWIRE with a flux of $S_{3.6}$=20.7μJy. It has a compact structure in the FIRST survey with a flux density of $S_{1.4}$=16.55 mJy. The only extended and bright emission line which had shown up in the spectrum of this source is at 4753$\mathring{A}$ which we take to be a robust detection of the Lyα line at z=2.90.

J163638.49+401156.89(EN2_22) We have not detected any emission line in the spectrum for this radio galaxy.

J163644.99+405444.15(EN2_23) The spectrum of this source contains an extended bright line at 4243Å which we take as Lyα at a redshift of $z = 2.48$.

J163755.98+414847.45(EN2_37) This radio galaxy has a compact structure in the FIRST survey with a flux density of $S_{1.4}$=18.43 mJy and also identification in the SWIRE with a flux of $S_{3.6}$=27.38μJy. We do not detect any emission lines in the spectrum.

J163802.12+420819.58(EN2_39) The spectrum of this source displays just a single bright extended emission line at 4461Å which we identified as Lyα at z=2.66.

J163844.33+410703.92(EN2_42) The spectrum of this radio source was taken with WHT on August 2009 and displays no emission line.

J163912.10+405236.72(EN2_45) The optical spectroscopy and other optical and radio properties of this source were reported by Jarvis et al.(2009) with a Lyα line at 7146$\mathring{A}$ and redshift of $z = 4.8$. Full details of this source are given in Appendix C.

J103648.50+572337.88(LH_10) This source has identification in the SWIRE with a flux of $S_{3.6}$=51.58μJy and its radio flux at 1.4 GHz is 36.95 mJy. The only emission line shown in the blue part of the spectrum of this target is at 4082Å which we take to be the Lyα line at $z = 2.35$.

J103923.57+593804.46(LH_33) The source is detected in the FIRST radio survey at 1.4 GHz with a flux density of $S_{1.4}$= 13.05 mJy and also in the SWIRE catalogue at 3.6μm with $S_{3.6}$=16.32 μJy. In the spectrum of this source we have not detected any emission lines.

J104033.55+594230.19(LH_42) The observation of this target was carried out with the WHT on February 2010. The source has a compact double structure, which we pointed at the centre. The radio flux density at 1.4GHz was $S_{1.4}$=16.02 mJy and there is no identification in the SWIRE survey. A bright line at 9413Å corresponds to the identification at centre of double radio source, which could be MgII due to its relatively broad nature, which would give a redshift of $z = 2.36$. There is also evidence for Lyα and SiIV lines at 3492Å and 4023Å for the right hand side structure at $z = 1.87$ and a bright extended single line at 3469Å corresponding to the left hand side structure which could be Lyα at $z = 1.85$. Given the close correspondence between the redshifts of the "two" sources either side of the centre. I therefore suggest that the faint line towards the centre of the structure may be spurious or possibly a foreground object and the the radio source is in fact at $z \approx 1.86$.

J104114.06+592933.68(LH_43) The spectrum of this radio source was taken with the WHT on February 2011 with a position angle of 115°. The target has a compact structure in the FIRST survey with a flux density of S=11.82 mJy and is also detected in the SWIRE survey with at 3.6μm with $S_{3.6}$=19.44μJy. The two CII] and CIV lines at 6512Å and 4337Å respectively, give a robust redshift of $z = 1.80$ for this radio galaxy.

J104223.59+581154.52(LH_53) This radio galaxy has a featureless spectrum, taken at a position angle of 243° with WHT on February 2011. I find no emission lines in the spectrum and therefore no redshift measurement is possible.

J104255.47+563803.63(LH_57) This source has a compact structure with a flux density of

$S_{1.4}$=20.73 mJy in the FIRST survey. It has an identification in the SWIRE survey with flux density of $S_{3.6}$=22.01μJy. Although we observed this radio galaxy twice on February 2010 and 2011, we do not find any emission line in the spectrum of this source.

J104529.93+573817.07(LH_66) Observations of this radio galaxy were carried out twice on February 2010 and 2011. The source has a very faint identification in SWIRE with a flux of $S_{3.6}$=16.88μJy. It has a compact structure in the FIRST survey with a flux density of $S_{1.4}$=69.73 mJy. The only extended and bright emission line which is found in the spectrum of this source is at 3958Å which I take as the Lyα line at $z = 2.25$.

J104624.78+590445.94(LH_78) I do not detect any emission line in the spectrum for this radio galaxy, which was observed in April 2009. There is no identification for this source in SWIRE and its radio flux is $S_{1.4}$=13.89 mJy.

J104700.84+591902.07(LH_84) This source has a compact structure with a flux density of $S_{1.4}$=21.81 mJy in the FIRST survey, however it has no identification in the SWIRE survey and the spectrum which was taken in February 2011 does not show any emission lines.

J104853.46+590609.74(LH_97) This compact source has not been detected in SWIRE and its radio flux density is $S_{1.4}$=12.82 mJy. The redshift of this source based on three emission lines in the spectrum, HeII at 5010Å, CIII] at 5824Å and CII] at 7080Å confirm the redshift of $z = 2.05$ for this radio galaxy.

J104916.25+560117.55(LH_101) The presence of three emission lines, SiIV at 4474Å, weak CIV at 4942Å and the HeII line at 5231Å confirm this source as a radio galaxy at $z = 2.19$.

J105014.55+563209.98(LH_109) No emission lines are found in the spectrum for this radio galaxy.

J105053.84+583232.86(LH_112) This source displays just a single emission line at 4248Å, which could be Lyα at $z = 2.49$, however the absence of the other emission lines make us be cautious about our result. The radio flux at 1.4 GHz and the near infrared flux at 3.6 μm for this target are $S_{1.4}$=156.23 mJy and $S_{3.6}$=17.42 μJy respectively. This would give a radio luminosity of 4.8×10^{26} W Hz^{-1} sr^{-1} for $z = 2.49$, again above the break in the radio luminosity function, making it a powerful FRII type source. The 3.6μm flux density converts to AB=20.8 which would place it towards the faint end of the correlation of $3.6_{\rm mag} - z$ shown in Fig. 2.3 but certainly plausible given our biased selection towards faint 3.6μm sources. I therefore suggest that the redshift is indeed $z = 2.49$.

J105131.21+584947.13(LH_120) This source has a compact structure with a flux density of $S_{1.4}$=15.02 mJy in the FIRST survey while there is no identification in SWIRE. The only emission line which has shown up in the spectrum of this source is at 4023Å which I take to be the Lyα line at $z = 2.30$. Again the 3.6μm flux-density (Fig. 2.3) would suggest that this redshift is likely.

J105318.17+585623.23(LH_134) Although the observations for this target were accrued in three different runs in February 2010, 2011 and April 2009, there was no detection of any emission line in its spectrum.

J105412.27+582941.20(LH_142) The spectrum shows a strong extended emission line at 5656Å which we take as Lyα at $z = 3.65$. This is one of the highest redshift radio galaxies ever found (see Table 3 in Miley & De Breuck, 2008).

J105421.44+580059.55(LH_143) This radio galaxy has a compact structure in the FIRST survey with a flux density of $S_{1.4}$=10.41 mJy and an identification in SWIRE with a flux of $S_{3.6}$=25.53μJy. I found only a single emission line at 4498Å in the spectrum from our

observation in February 2010 which could be CIII] at z=2.699, however the absence of other lines could not let us to confirm this.

J105530.03+583232.22(LH_148) No emission lines were detected in the spectrum of this radio galaxy, which was taken in February 2011 with WHT.

J105548.52+571827.69(LH_149) This source has a compact structure with a flux density of $S_{1.4}$=14.19 mJy in the FIRST survey and no identification in the SWIRE survey. Although we observed this radio galaxy twice in February 2010 and April 2009, no emission lines were detected.

J105715.91+572313.90(LH_157) The spectrum of this radio galaxy shows a bright Lyα line at 4814Å which gives a redshift of $z = 2.9$ for this radio source. There is also faint continuum in the red arm and a bright Lyα line at 4820Å from an object 4.6 arcsec away from our target. This may mean that the radio galaxy lies in an overdensity of galaxies at the same redshift, as has been found for other powerful radio galaxies at high redshift (e.g. Venemans et al., 2007).

J110109.46+572715.63(LH_174) This target has a flux density of $S_{1.4}$=73.91 mJy and $S_{3.6}$=15.87 μJy. The spectroscopic observations do not show evidence for any emission lines.

021734.18-031308.71(XMM_09) The observation for this target were carried out in August 2009 with the WHT. The source has a flux density of S_{610}=67.3 mJy in GMRT data at 610MHz and an identification in the SWIRE with a flux of $S_{3.6}$=61.37μJy. The continuum in the blue arm of the spectrum shows the target is not a high redshift source, and identification of the HeII line at 4092Å and CIII] line at 4757Å confirm the redshift as $z = 1.49$.

021823.49-041900.72 (XMM_19) Although the observations for this radio galaxy were taken in two nights with the WHT in August 2009, the spectrum of this source does not display any emission line.

021834.77-034615.75(XMM_23) We have not detected any emission line in the spectrum for this radio galaxy.

022200.34-033934.60 (XMM_58) A bright emission line is found at 7700Å for this source and we defer discussion of this object to Chapter 4.4.

022357.07-044111.44 (XMM_86) The spectra of this radio source were taken with the WHT in August 2009 in two different nights. The redshift of this radio galaxy is based on three emission lines, a very large (3.3 arcsec) extended Lyα at 4018Å, HeII at 5389Å and CIII] at 6296Å which give a secure redshift of $z = 2.3$.

022632.51-051327.11(XMM_106) We have not detected any emission line in the spectrum of this radio galaxy.

Table 3.4: In this table the measurements obtained from the spectra of our candidates are presented. The second column shows the estimated redshift for each target, and the third and fourth columns show the flux density at 1.4 GHz and 3.6 μm respectively and the fifth column shows the emission line which was used to measure redshift, and the radio luminosity and emission line luminosity are given in columns 6 and 7 respectively..

Target	z	$S_{1.4}$/mJy	$S_{3.6}/\mu$Jy	Lines	$\log_{10}(L_{1.4}/\mathrm{W\,Hz^{-1}\,sr^{-1}})$	$\log_{10}(L_{\mathrm{Ly}\alpha}/\mathrm{W})$
EN2_04	-	16.21	32.07	-	-	-
EN2_13	-	13.9	22.8	-	-	-
EN2_14	2.1?	53.99	< 7.3	Lyα,HeII	26.04	35.18
EN2_20	2.9	16.55	20.7	Lyα	25.85	35.52
EN2_22	-	172.24	19.10	-	-	-
EN2_23	2.48	11.27	< 7.3	Lyα	25.53	35.61
EN2_37	-	18.43	27.38	-	-	-
EN2_39	2.66	40.11	18.23	Lyα	26.15	35.42
EN2_42	-	10.28	22.65	-	-	-

Continued on next page

Table 3.4 – continued from previous page

Target	z	$S_{1.4}$ / mJy	$S_{3.6}$ /μJy	Lines	$\log_{10}(L_{1.4}$ / W Hz^{-1} sr$^{-1})$	$\log_{10}(L_{\mathrm{Ly}\alpha}$ / W)
EN2_45	4.8	22.51	< 7.3	Lyα	26.47	35.68
EN1_11	4.5	20.12	< 7.3	Lyα	26.36	35.77
EN1_16	-	79.15	< 7.3	-	-	-
EN1_50	-	12.23	< 7.3	-	-	-
EN1_64	1.2	19.16	< 7.3	[OII]	25.02	-
EN1_94	-	15.1	< 7.3	-	-	-
EN1_112	-	31.48	14.10	-	-	-
EN1_135	2.9?	31.5	13.05	Lyα	26.13	35.61
XMM_09	1.49	67.3	61.37	CIII],HeII	25.79	-
XMM_19	-	38.2	< 7.3	-	-	-
XMM_23	-	22.3	15.33	-	-	-
XMM_56	-	25.2	< 7.3	-	-	-
XMM_58	5.33?	42	18.08	Lyα	26.84	33.35
XMM_86	2.3	140.3	< 7.3	Lyα,HeII,CIII]	26.55	35.12
XMM_106	-	131.8	< 7.3	-	-	-
LH_10	2.35	36.95	51.58	Lyα	25.99	36.89
LH_33	-	13.05	16.32	-	-	-
LH_42	2.36	16.02	< 7.3	MgII	25.63	-
LH_43	1.80	11.82	19.44	CII],CIV	25.23	-
LH_53	-	26.12	13.54	-	-	-
LH_57	-	20.73	22.01	-	-	-
LH_66	2.25	69.73	16.88	Lyα	26.22	35.39
LH_78	-	13.89	< 7.3	-	-	-
LH_84	-	21.81	< 7.3	-	-	-
LH_97	2.05	12.82	< 7.3	CII],CIII],HeII	25.39	-
LH_101	2.19	28.12	20.57	SiIV,CIV,HeII	25.80	-
LH_109	-	12.16	20.49	-	-	-
LH_112	2.49	156.23	17.42	Lyα	26.67	35.06
LH_120	2.30	15.02	< 7.3	Lyα	25.58	35.56
LH_134	-	78.4	< 7.3	-	-	-
LH_142	3.65	13.19	11.69	Lyα	25.97	35.55
LH_143	2.69	10.41	25.53	CIII]	25.57	-
LH_148	-	17.99	< 7.3	-	-	-
LH_149	-	14.19	< 7.3	-	-	-
LH_157	2.9	133.32	< 7.3	Lyα	26.76	35.22
LH_174	-	73.91	15.87	-	-	-

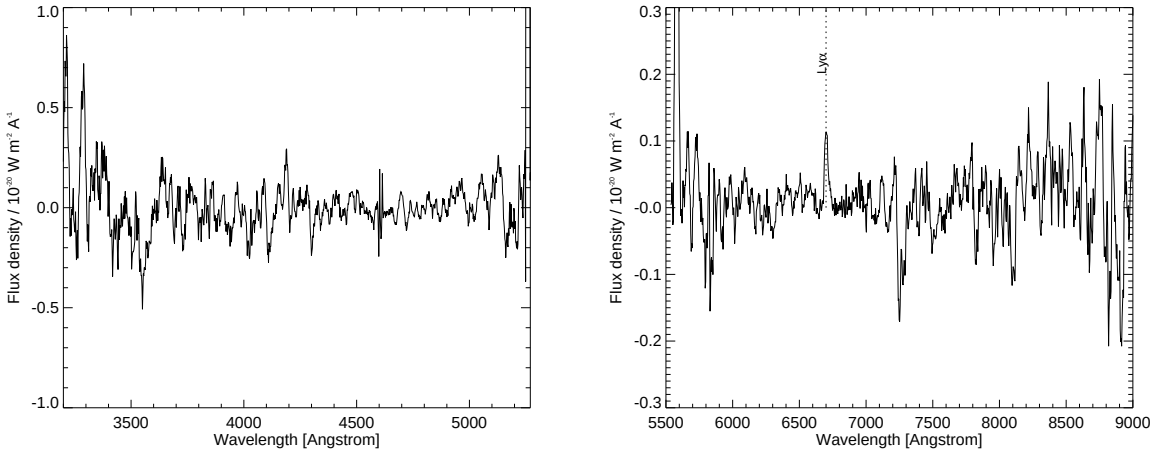

(a) EN1_11B (b) EN1_11R

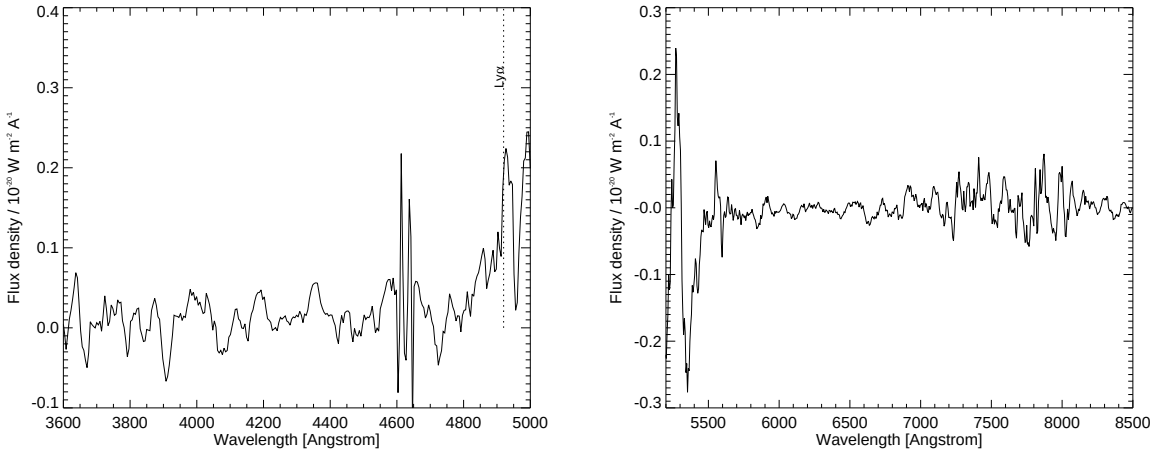

(c) EN1_135B (d) EN1_135R

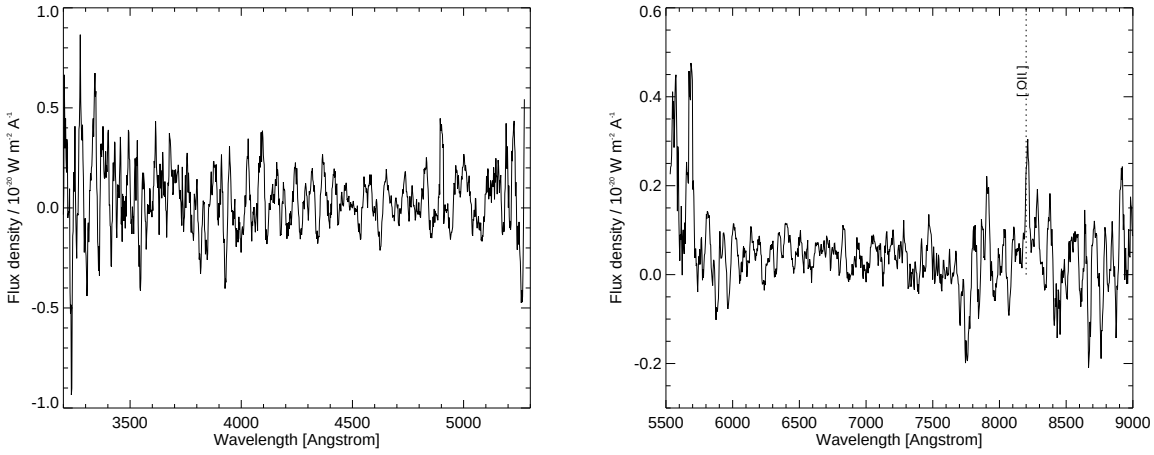

(e) EN1_64B (f) EN1_64R

Figure 3.6: The 1D spectra of the our sources in ELAIS-N1 field with the emission-line identifications.

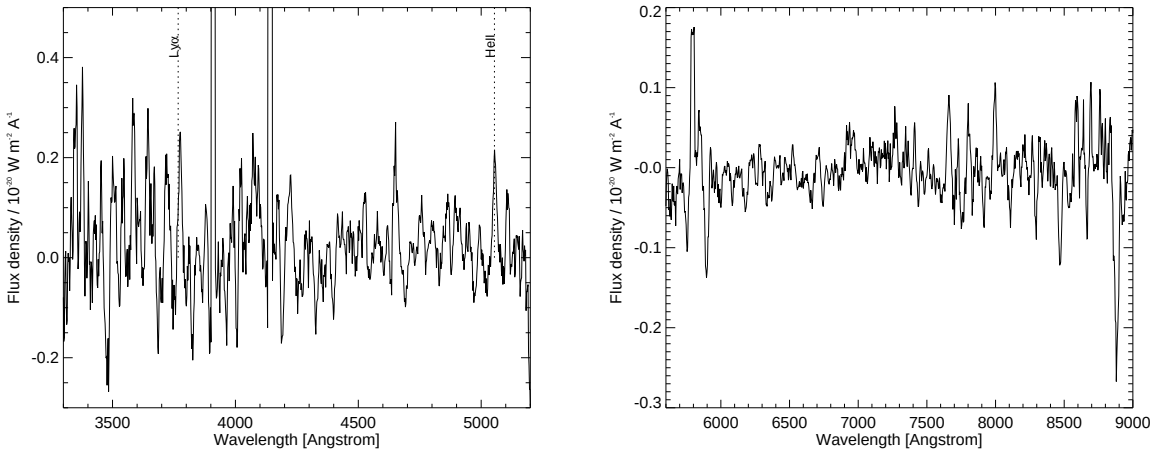

(a) EN2_14B

(b) EN2_14R

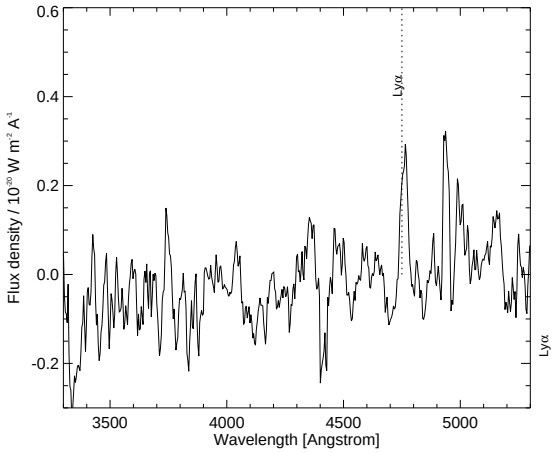

(c) EN2_20B

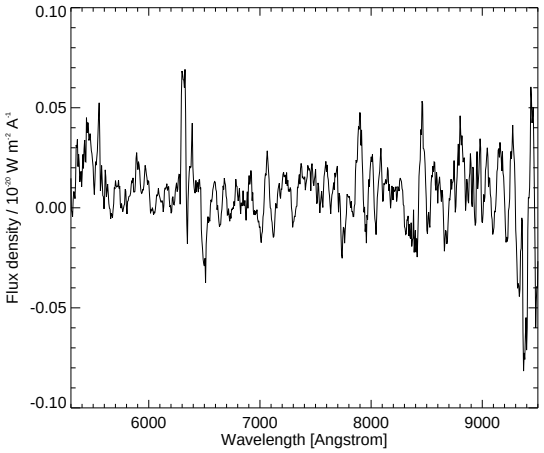

(d) EN2_20R

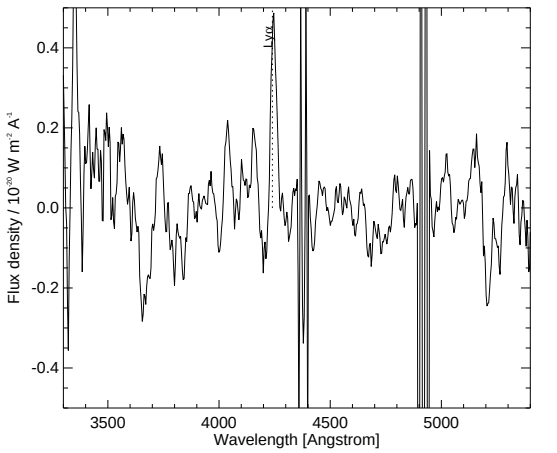

(e) EN2_23B

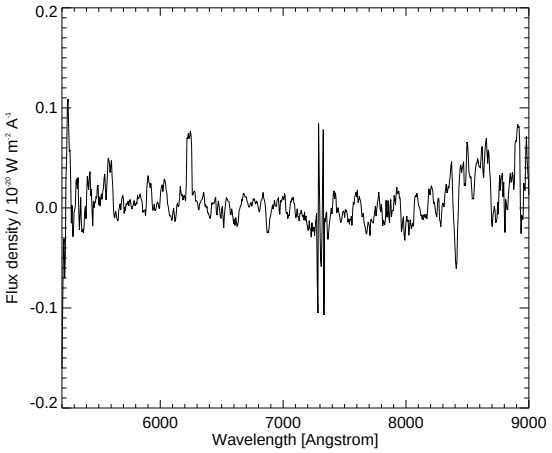

(f) EN2_23R

Figure 3.7: The 1D spectra of the our sources in ELAIS-N2 field with the emission-line identifications.

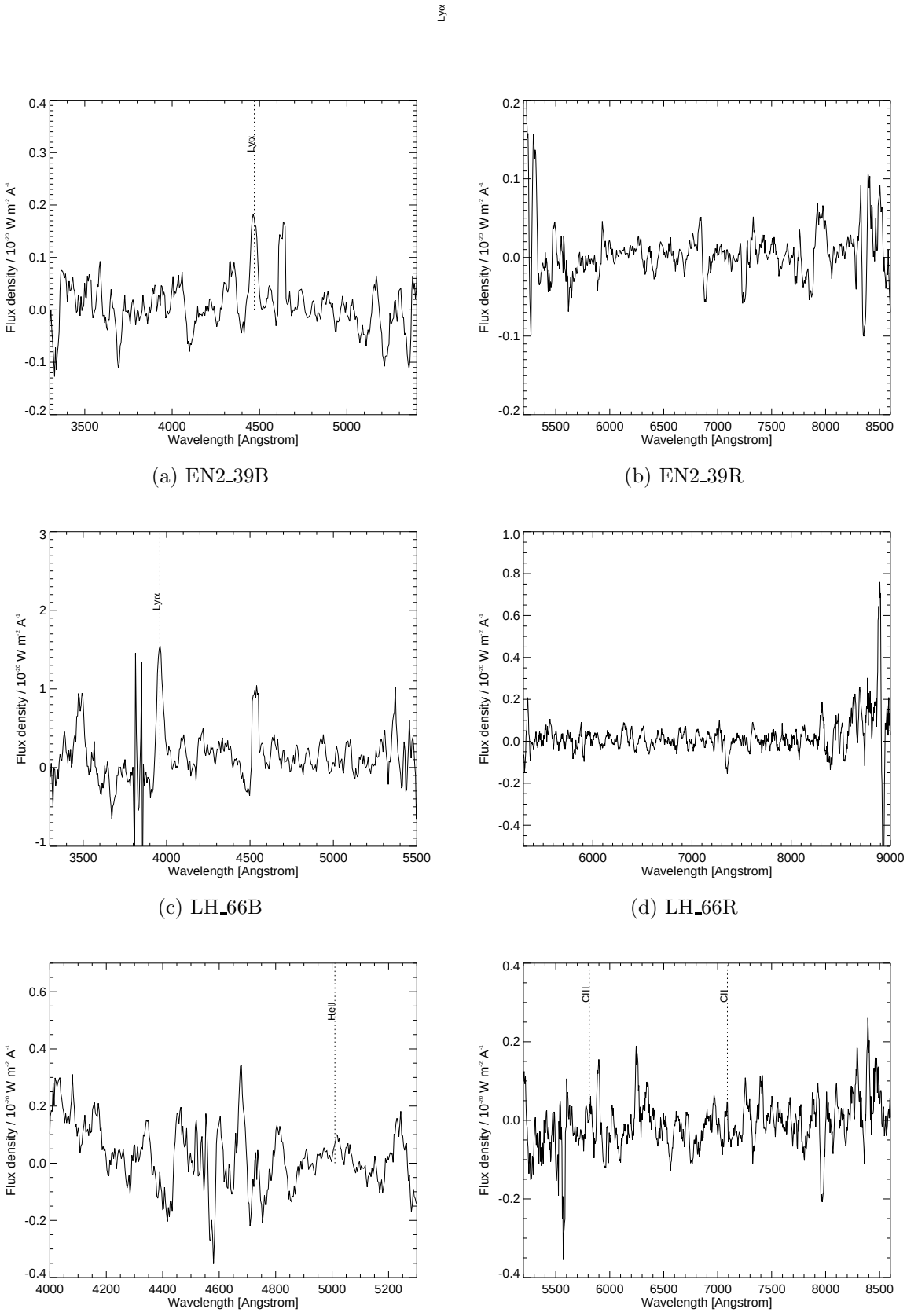

(a) EN2_39B

(b) EN2_39R

(c) LH_66B

(d) LH_66R

(e) LH_97B

(f) LH_97R

Figure 3.8: The 1D spectra of the our sources in ELAIS-N2 and Lockman Hole fields with the emission-line identifications.

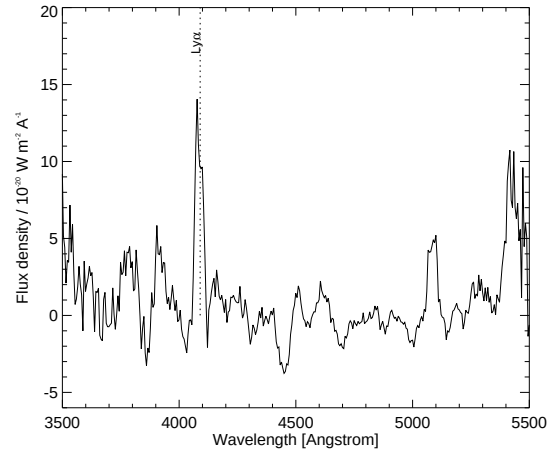

(a) LH_10B

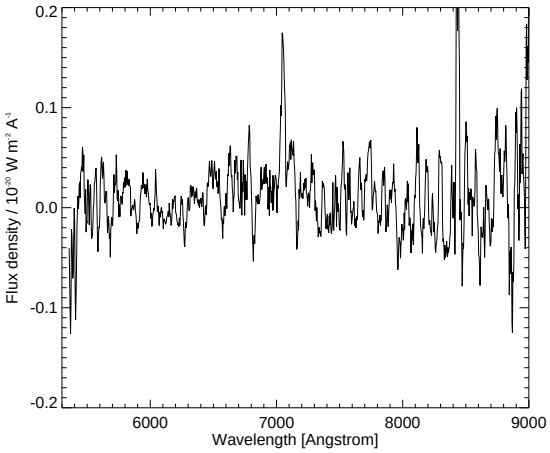

(b) LH_10R

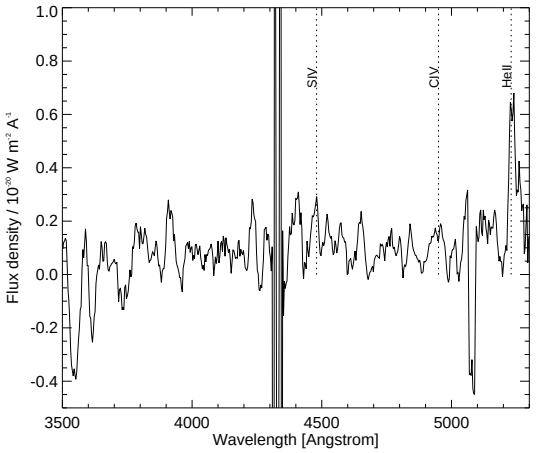

(c) LH_101B

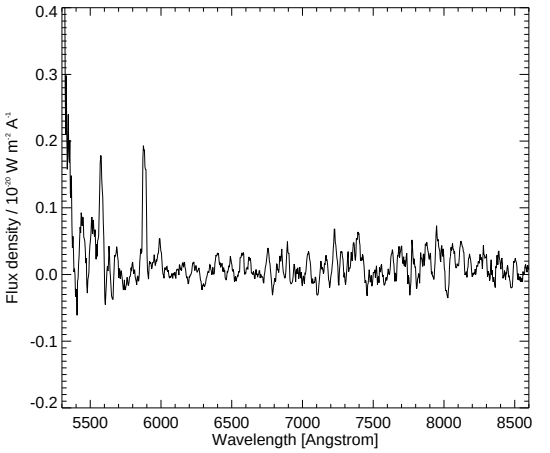

(d) LH_101R

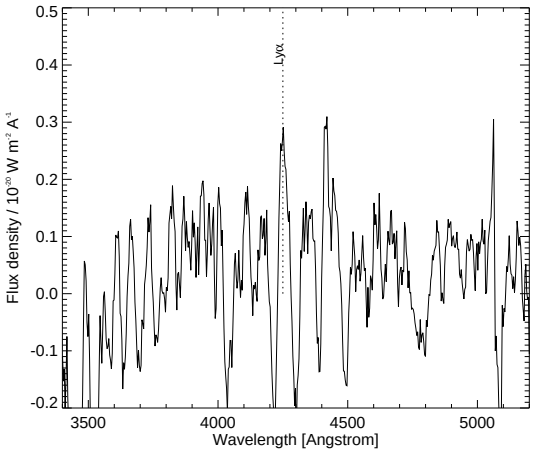

(e) LH_112B

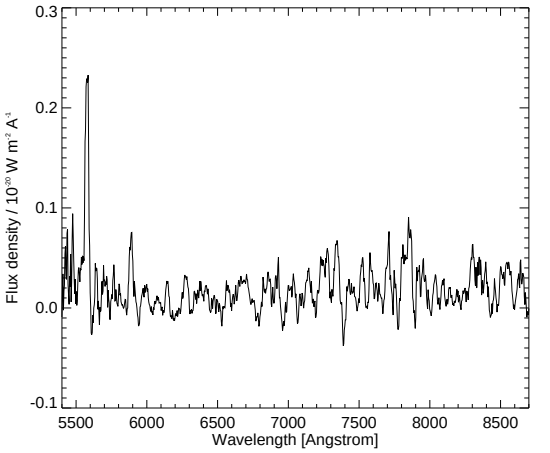

(f) LH_112R

Figure 3.9: The 1D spectra of the our sources in Lockman Hole field with the emission-line identifications.

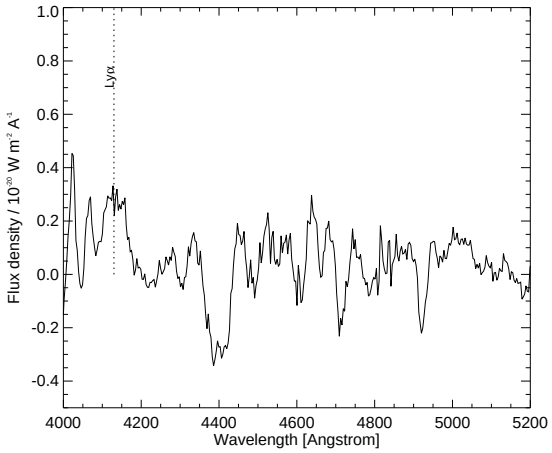

(a) LH_120B

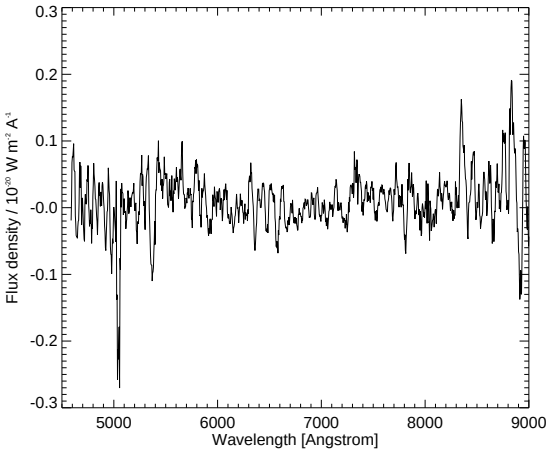

(b) LH_120R

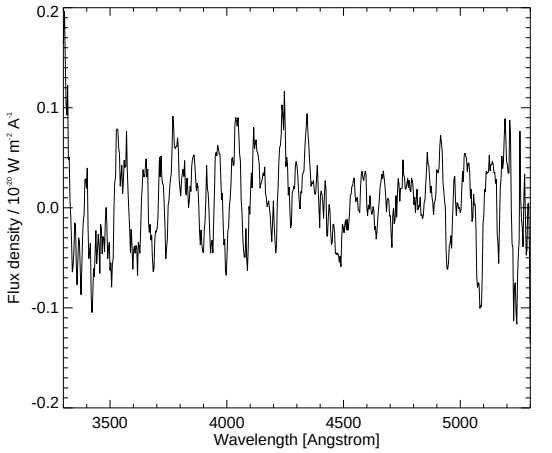

(c) LH_142B

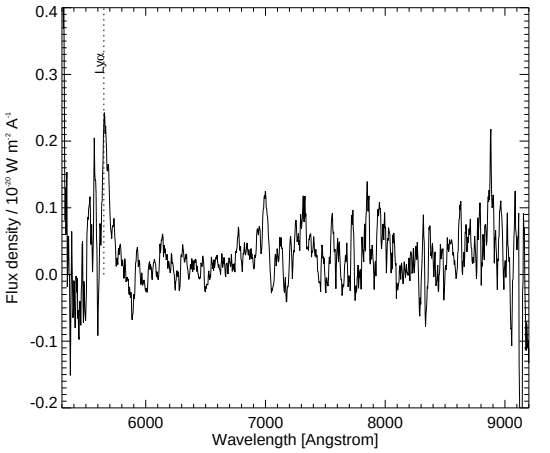

(d) LH_142R

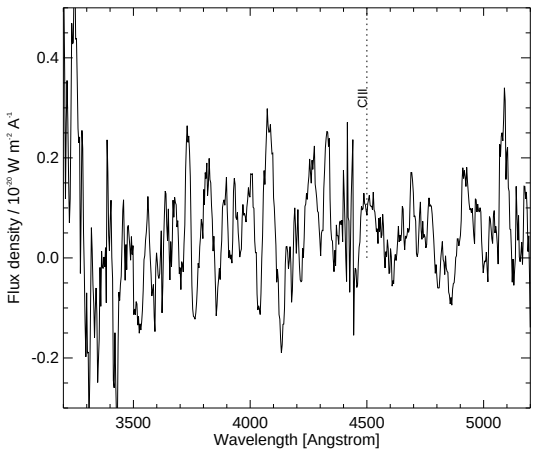

(e) LH_143B

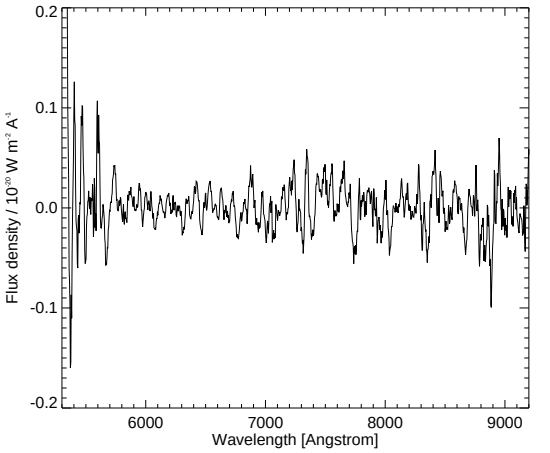

(f) LH_143R

Figure 3.10: The 1D spectra of the our sources in Lockman Hole field with the emission-line identifications.

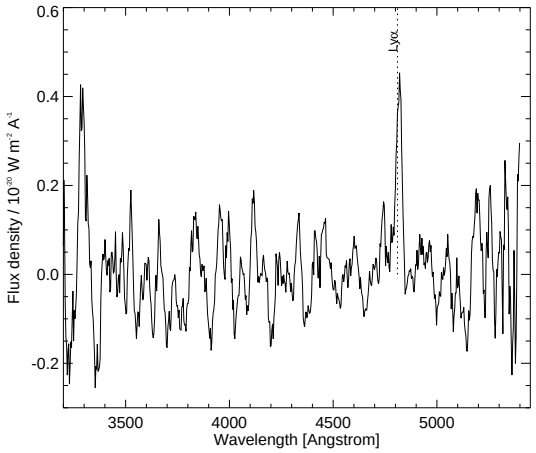

(a) LH_157B

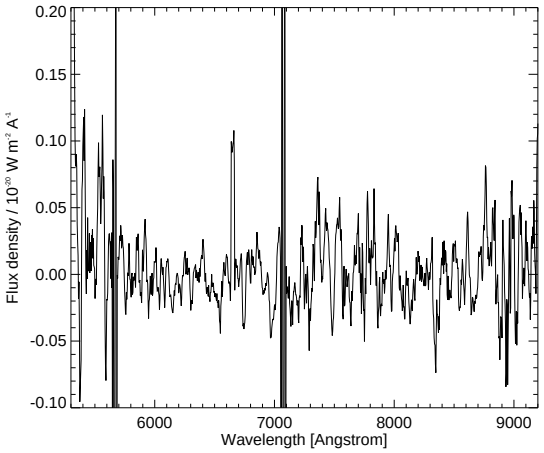

(b) LH_157R

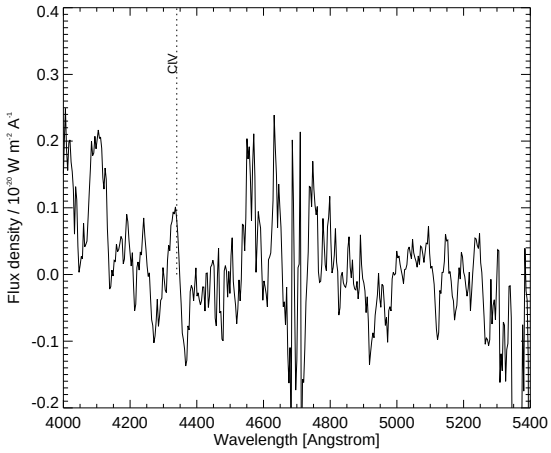

(c) LH_43B

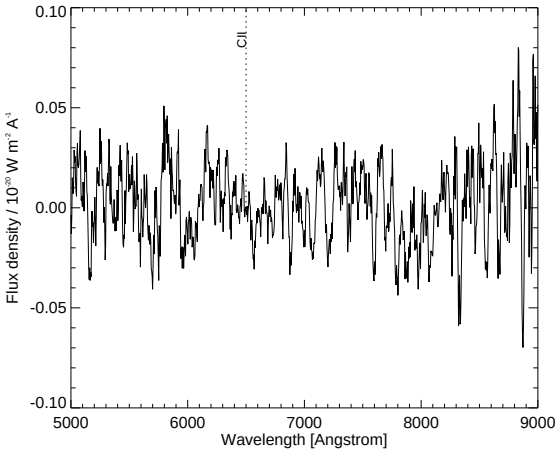

(d) LH_43R

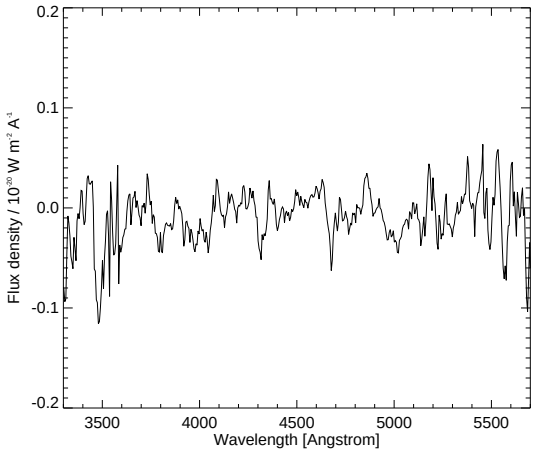

(e) LH_42B

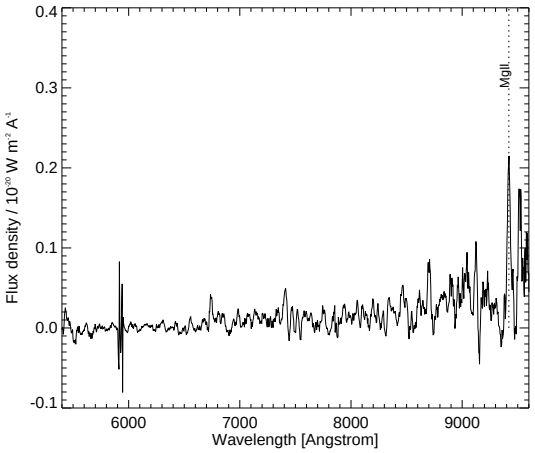

(f) LH_42R

Figure 3.11: The 1D spectra of the our sources in Lockman Hole field with the emission-line identifications.

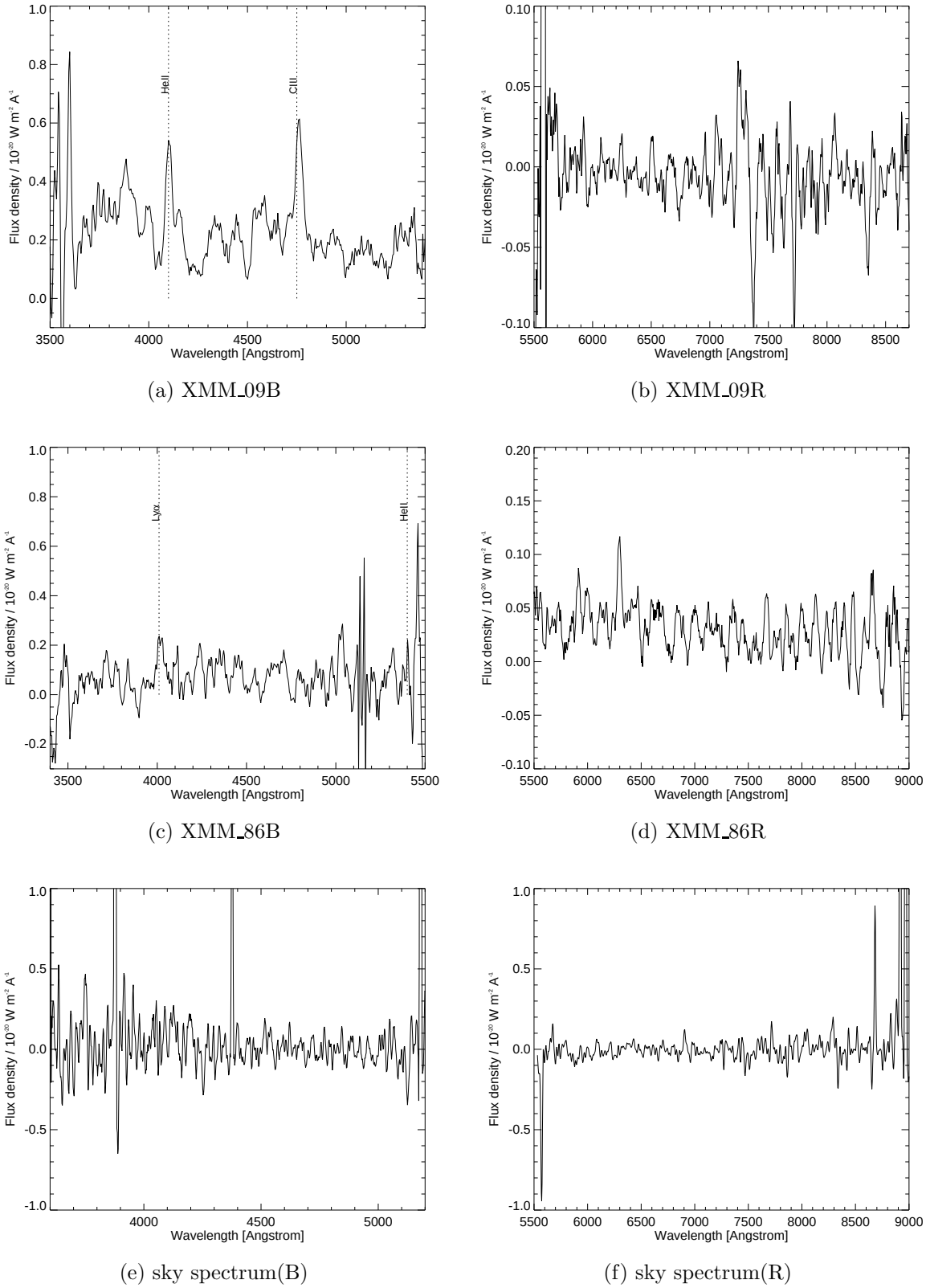

(a) XMM_09B

(b) XMM_09R

(c) XMM_86B

(d) XMM_86R

(e) sky spectrum(B)

(f) sky spectrum(R)

Figure 3.12: The 1D spectra of the our sources in XMM-LSS field with the emission-line identifications. An example sky spectrum in both blue and red arms is also shown.

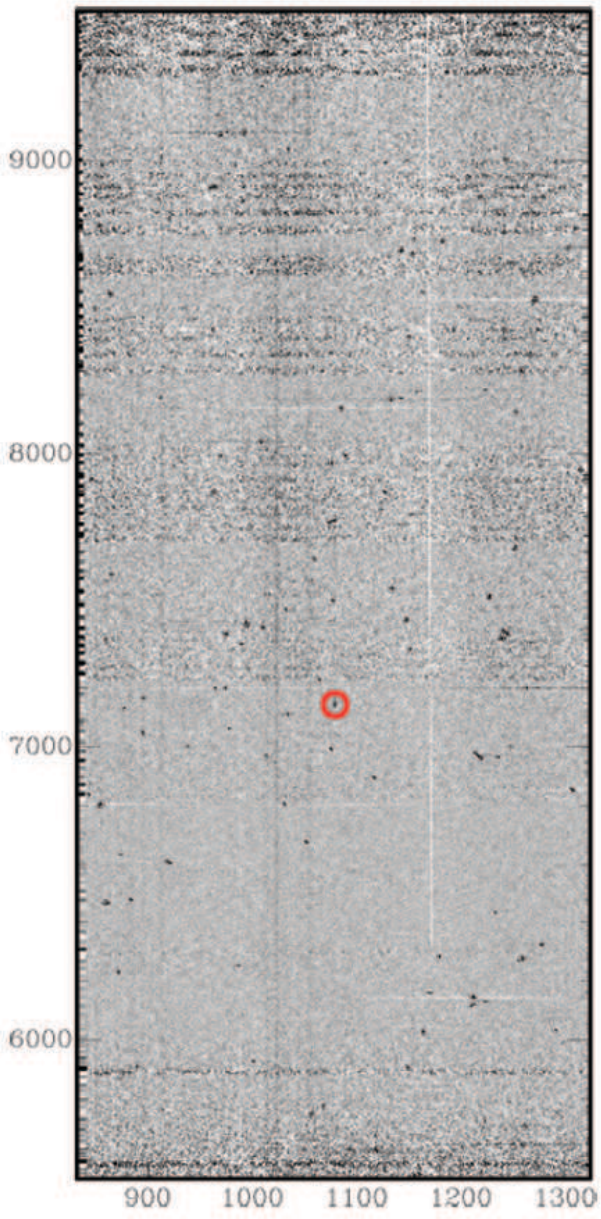

Figure 3.13: 2D spectra of the radio galaxy EN2-45 in the red part, showing the Lyα line at 7146Å and redshift of $z = 4.8$

3.4 Lyα luminosity versus radio luminosity

As mentioned in Chapter 1.7 and Section 2.3 there has been extensive work linking the optical properties of radio sources with their radio properties. Willott et al. (1999) used a combined sample comprising 3CRR and 7CRS radio sources to decouple trends with redshift from trends in luminosity. They found a strong correlation between the narrow emission-line luminosity, traced by [OII] and the rest-frame 151-MHz radio luminosity.

They also investigated links between the luminosity of the narrow emission lines and projected linear size D of the radio galaxies and the radio spectral index, but found a much weaker

Table 3.5: Emission line measurements obtained from the spectra of sources. The '?' denotes an uncertain line identification. The typical uncertainty on the line fluxes is 20-30 per cent due to both sky noise and possible slit losses.

Target	Redshift	Emission Line	$\log_{10}(L_{line}/W)$	$S_{line}/10^{-20}$ W m^{-2}
EN2_14	2.1?	Lyα,HeII	35.18,34.45	4.73,0.882
EN2_20	2.9	Lyα	35.52	4.69
EN2_23	2.48	Lyα	35.61	8.41
EN2_39	2.66	Lyα	35.42	4.58
EN2_45	4.8	Lyα	35.68	2.06
EN1_11	4.5	Lyα	35.77	2.09
EN1_64	1.2	[OII]	34.74	6.85
EN1_135	2.9?	Lyα	35.61	5.84
XMM_09	1.49	CIII],HeII	35.33,35.44	15.6,19.8
XMM_58	5.33?	Lyα	33.35	7.49
XMM_86	2.3	Lyα,HeII,CIII]	35.12,34.72,35.03	3.31,1.30,2.69
LH_10	2.35	Lyα	36.89	184
LH_42	2.36	MgII	35.27	4.35
LH_43	1.80	CII],CIV	34.08,34.71	0.539,2.31
LH_66	2.25	Lyα	35.39	6.42
LH_97	2.05	CII],CIII],HeII	35.00,34.57,35.11	3.32,1.22,4.20
LH_101	2.19	SiIV,CIV,HeII	35.12,34.64,35.86	3.66,1.22,20.01
LH_112	2.49	Lyα	35.06	2.36
LH_120	2.30	Lyα	35.56	9.08
LH_142	3.65	Lyα	35.55	2.93
LH_143	2.69	CIII]	34.98	1.61
LH_157	2.9	Lyα	35.22	2.36

correlation between these properties. Best et al. (2000) used data from a sample of 3CR radio galaxies at $z \sim 1$ and found evidence that the radio sources with small projected linear sizes ($D \sim 100$ kpc) have lower ionisation states, traced by their emission lines, higher [OII] emission-line fluxes and broader [OII] linewidths than the larger sources. Using a sample of 18 objects selected to have good signal-to-noise ratio spectra and UV/optical emission with large spatial extents, van Ojik et al. (1997) found a correlation between the radio source size and the extent of the Lyα emission-line gas in high-redshift ($z > 2.1$) radio galaxies with $10 \leq D \leq 100$ kpc. They also found a high fraction (~ 90 per cent) of HI absorbed Lyα profiles in those with $D < 50$ kpc.

Jarvis et al. (2001b) extended these studies with the 6C* sample of radio galaxies and also found a strong correlation between the low-frequency radio luminosity and the luminosity of the Lyα emission line, which they argue is due to a link between the intrinsic AGN power which is the source of the photoionising photons (most likely a hidden quasar nucleus; See Chapter 1.7) and the power carried by the radio jets. Jarvis et al. (2001b) also investigated the link between radio source size and the emission line properties of the radio galaxies. They also found that those sources with projected linear size $D < 70$ kpc had stronger CII] emission lines relative to the CIII] and CIV lines than the sources with larger ($D > 70$ kpc) radio structures. They interpret this as a boosted low-ionisation component in the smaller sources due to the passage of the radio jet through the interstellar medium in the host galaxy and the intergalactic medium in the immediate vicinity of the host.

In a follow-up study of such links between emission-line luminosity and radio properties, Jarvis et al. (2003) and Wilman et al. (2004) undertook very high spectral resolution studies of the Lyα emission line haloes around several high-redshift radio galaxies. They found that the smaller sources also had a higher probability of exhibiting associated absorption within

their Lyα emission line profiles. Both studies interpreted this as evidence that as the radio jets propagate into the intergalactic medium, they are able to disturb and disrupt the neutral gas in the vicinity of the host galaxy, and essentially shred it up in to small clouds which in turn are not able to absorb the Lyα photons in as efficient a manner as when the neutral gas was surrounding the galaxy in a shell-like structure.

With my sample of high-redshift radio galaxies, I am able to extend this earlier work to a larger parameter space. First, all of the sources in my sample are only tens of mJy at 1.4 GHz, this is much fainter than the sources that have been investigated previously, which were generally selected at low-frequencies at the Jy level. Furthermore, these previous studies also used a steep radio spectral index criteria for filtering out low-redshift radio galaxies which may introduce an unknown bias in these previous studies. Although my selection may also bias our results, the selection is completely different to these previous studies so any consistencies found would suggest that the links are real, rather than due to these unknown biases.

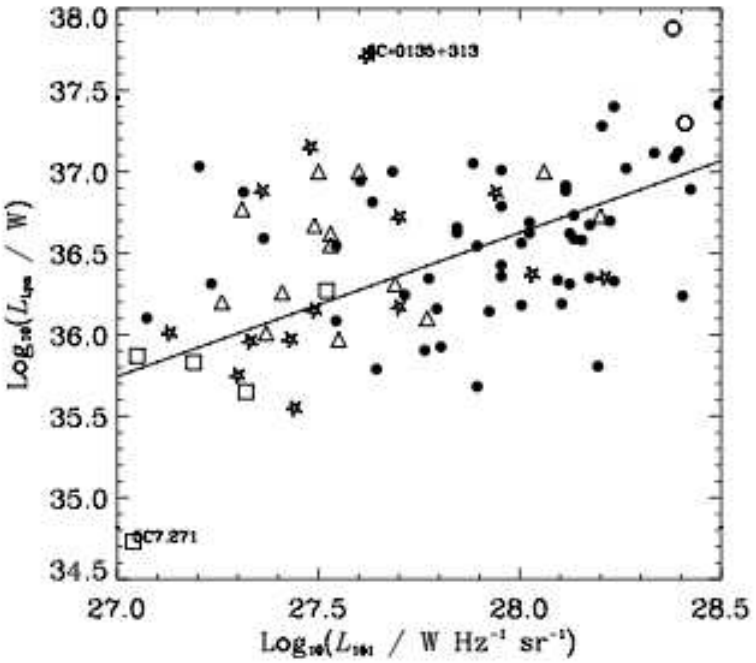

Figure 3.14: Lyα emission line luminosity against rest-frame 151-MHz radio luminosity for radio galaxies at z > 1.75 from the 3CRR (circles), 7CRS (squares), 6CE (triangles) and 6C* (stars) radio samples. The filled circles are the high-redshift sources from De Breuck et al. (2000a) while the solid line shows the best fit. (Jarvis et al. (2001b))

In Fig 3.14 I present the Lyα emission line luminosity against the 151 MHz radio luminosity from a sample of high redshift radio galaxies ($z > 1.75$) used by Jarvis et al. (2001b). It is apparent that there is a strong correlation between the L_{151} and $L_{\mathrm{Ly}\alpha}$, for which they found a slope of 0.87 ± 0.10. Fig 3.15 shows the $L_{Ly\alpha} - L_{151}$ correlation for our sample of radio sources, which have been converted to 151 MHz luminosity using a spectral index of $\alpha = 0.8$. Also shown are the Jarvis et al. (2001b) and De Breuck et al. (2000a) high redshift radio galaxies,

which were selected based on a steep spectral index. The solid line is the slope of Jarvis et al. (2001b) to guide the eye.

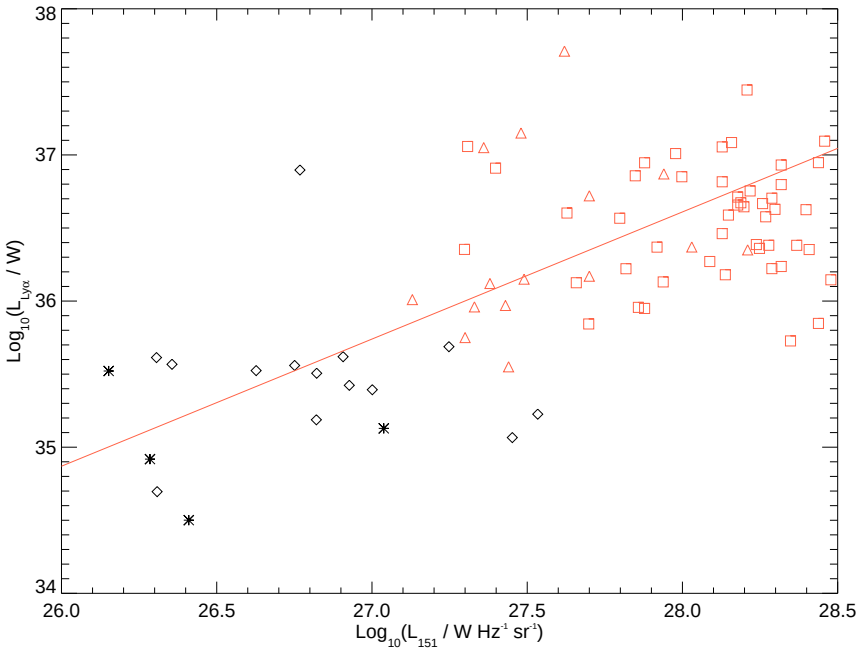

Figure 3.15: Lyα emission line luminosity against rest-frame 151-MHz radio luminosity for radio galaxies at z $>$ 1.75. The red squares and triangles present the Jarvis et al. (2001b) and De Breuck et al. (2000a) sources. The black diamond symbols represent our sources from Lockman Hole, Elais-N1 and Elais-N2 fields and the black symbols are for the XMM field.

Although there are only a small number of sources in my sample, they do lie in a different part of parameter space to those of Jarvis et al. (2001b) and De Breuck et al. (2000a), and thus I am able to explore the consistency of the correlation to an order of magnitude lower radio luminosities. It is clear from Fig. 3.15 that my sample of sources is fully consistent with the correlation found by Jarvis et al. (2001b). This therefore reinforces the suggestion made in Jarvis et al. (2001b) that there is a causal link between the ionising power of the radio galaxy and the power in the radio jets. As the ionising radiation field is emanating from the accretion disk around the central supermassive black hole and the radio jets are powered by a separate process that we currently have very little understanding of, we do not necessarily expect to see such a strong link. However, it is clear that in both cases the mass of the black hole must play an important role, as it governs the gravitational infall of matter to the accretion disk, and in most theories of jet production, more powerful jets emanate from more massive black holes. Indeed, using quasars, where it is possible to measure the black-hole masses through the "virial" black-hole mass estimator, several groups have found evidence that the radio loudness of a quasar is linked to the mass of the central supermassive black hole. Lacy et al. (2001) found a correlation between radio luminosity and black-hole mass using quasars from the FIRST Bright Quasar Survey (FBQS), in the form of continuous variation of radio luminosity with black hole mass. They suggest a new scheme to "unify" radio-loud and radio-quiet objects in which the radio luminosity scales proportionally with $M_{\rm BH}^{1.9\pm0.2}(L/L_{\rm Edd})^{1.0}$ for

$L/L_{\rm Edd} \sim 0.1$, with an apparently weaker accretion rate dependence at low $L/L_{\rm Edd}$, where $L_{\rm Edd}$ is the Eddington luminosity. They also state that the scatter about this relation is ± 1.1 dex and that this may hide significant contributions from other physical effects, such as the black hole spin and radio source environment. McLure & Jarvis (2004) also investigated the dependence of radio luminosity and black-hole mass using optically selected quasars from the SDSS. By cross-matching these quasars with the WENSS, NVSS and FIRST radio surveys they found that radio-loud quasars had black-hole masses restricted to $> 10^8 {\rm M}_{\odot}$, whereas the radio-quiet quasars had black-holes spanning a large range in mass ($10^6 - 10^9 {\rm M}_{\odot}$).

Thus, my results suggest that this link between black-hole mass and radio luminosity holds over at least ~ 2.5 dex in radio luminosity and that other physical mechanisms such as the environmental density and possibly black-hole spin may add to the width of the correlation, but do not hide it. This also suggests that over this luminosity range, the accretion process must be similar and possibly dominated by cold accretion of the intergalactic medium as is inferred for high-excitation radio sources studied in much more detail at low redshifts (e.g. Hardcastle et al., 2007; Herbert et al., 2010; Best & Heckman, 2012b).

However, work by Villar-Martín et al. (2007b) using emission line ratios, particularly Lyα/HeII and Lyα/CIV suggests that, the Lyα emission in high-redshift radio galaxies may have a significant contribution from star-formation in the host galaxy. Unfortunately, we do not have enough sources with detections of Lyα, CIV and HeII to explore this properly. However, in those source with both Lyα and HeII we find ratios of Lyα/HeII =5.4 for EN2_14 and Lyα/HeII =2.54 for XMM_86, which are the only sources with both Lyα and HeII emission lines. The result is not consistent with the ratio of 7.49 which was found by Villar-Martín et al. (2007b). This could be due to the fact that small sources tend to have more HI absorption within their Lyα line (Jarvis et al., 2003, e.g). However, follow-up high-resolution spectroscopy would be needed to prove this. What we can say is that there is no evidence of enhanced star formation in these radio galaxies, as was found by Villar-Martín et al. (2007b).

Although many of our radio galaxies exhibit extended emission line haloes in Lyα it is very difficult to interpret this in the context of the work of Jarvis et al. (2001b) on the link between emission line halo and the radio properties. This is because our selection criteria for the follow-up spectroscopy concentrated on only those sources which had a compact radio morphology and due to this I have no knowledge of the extent of the radio source, other than it is smaller than 5 arcsec. However, more spectroscopy of the whole sample, coupled with higher resolution radio data would obviously help extend these previous studies. Furthermore, as the observations were all carried out at very low spectral resolution I am unable to detect the presence of associated HI absorption within the Lyα emission line. But again this new sample of radio galaxies at much lower radio luminosity but covering the same redshift range as previous studies lends itself to dedicated follow-up studies.

3.5 3.6μm magnitude–redshift relation

Across cosmic time, the host galaxies of powerful radio sources are some of the most massive galaxies in the universe. At low redshift, powerful extragalactic radio sources are associated with massive elliptical galaxies (Matthews et al., 1964) that appear in many cases to be relaxed with little sign of disturbance or star formation activity (e.g. Best et al., 1998; McLure et al.,

1999; Dunlop et al., 2003; McLure et al., 2004). In the high redshift universe there is evidence that these powerful radio sources, not only reside in the most massive galaxies (e.g. Pentericci et al., 2001; Waddington et al., 2002; Zirm et al., 2003), but also act as beacons to some of the most overdense regions in the high-redshift universe (e.g. Stern et al., 2003; Venemans et al., 2007).

However, it is very difficult to study the host galaxies of powerful radio sources at high redshift, due to the fact that even though they are very luminous, the high redshift means that they have faint apparent magnitudes. Due to this many studies of the hosts of powerful radio sources have relied on the use of the $K-z$ diagram (See Section 2.1). The $K-z$ diagram was initially used by Lilly & Longair (1984) to establish that radio galaxy hosts appear consistent with elliptical galaxy spectra out to $z\sim1.6$ using radio sources in the 3CR sample. In subsequent years, many authors have used the $K-z$ diagram to infer properties of the host galaxies of powerful radio galaxies (Eales et al., 1997; Jarvis et al., 2001a; De Breuck et al., 2002; Willott et al., 2003; Rocca-Volmerange et al., 2004; Brookes et al., 2006; Bryant et al., 2009).

The bulk of the earlier work on the $K-z$ relation found that at $z<0.6$ the hosts were consistent with being dominated by a passively evolving stellar population, with little evidence of star formation (e.g. Eales et al., 1997). Jarvis et al. (2001a) extended the $K-z$ diagram up to $z\sim4.5$ using radio galaxies discovered in the 6C* sample, which selected sources on the basis of having a steep radio spectral index and small angular size. Jarvis et al. (2001a), find that these selection criteria do not lead to any differences in the $K-z$ diagram from sources selected from complete radio samples such as those investigated by Willott et al. (2003). Jarvis et al. (2001a) also considered whether the scatter in the $K-z$ relation increased up to these high redshifts to determine whether there was any evidence that the hosts of powerful radio galaxies appeared to reach a point where their properties began to differ, due to differences in age or formation scenario. By considering aperture corrections and in particular emission-line contamination to the $K-$band imaging data, Jarvis et al. (2001b) found no evidence for increased scatter in the $K-z$ relation over all redshifts, leading these authors to suggest that hosts of powerful radio galaxies formed at very high redshift, and have undergone little in the way of evolution since, with a passively evolving stellar population being sufficient to explain the evolution to low redshift.

However, at $z>2$ the radio galaxies are brighter than both the no-evolution and passive evolution curves in (Fig 3.17), which can be explained by the fact that beyond redshift $z>2$ we are beginning to probe the epoch at which these massive galaxies may have been forming. Indeed, van Breugel et al. (1998) found that the near-infrared colours of high redshift radio galaxies are very blue at $z>3$, which may indicate the presence of a young stellar population.

Using the 3CRR, 6C, 6C* and 7CRS samples, Willott et al. (2003) investigated the dependence of the $K-$band magnitude on radio luminosity, something that could only be done with these samples, due to the range of radio flux-densities that the samples were drawn from. Willott et al. (2003) found evidence for a link between the host galaxy magnitude and the radio luminosity in the sources from these samples, which led them to consider that more powerful radio sources are hosted in more massive host galaxies with presumably more massive black holes, due to the correlation between black-hole mass and host galaxy mass (e.g. Magorrian et al., 1998). This is also consistent with the picture that I outlined in Section 3.4, using the Lyα emission line luminosity. This evidence was further reinforced by the study of McLure

et al. (2004) who also found evidence for a dependency on galaxy luminosity/mass for the radio luminosity.

De Breuck et al. (2002) compiled a $K-z$ diagram for an incomplete sample of radio sources, drawn from an Ultra-Steep-Spectrum selection of low-frequency sources in the WENSS. These authors also found a tight relationship for the $K-z$ diagram, although it is worth noting that they could not say whether there are radio luminosity dependencies from their single flux-density limited sample. However, they did highlight how the radio galaxy hosts sit at the bright end of the normal galaxy luminosity function, consistent with the findings of Jarvis et al. (2001a).

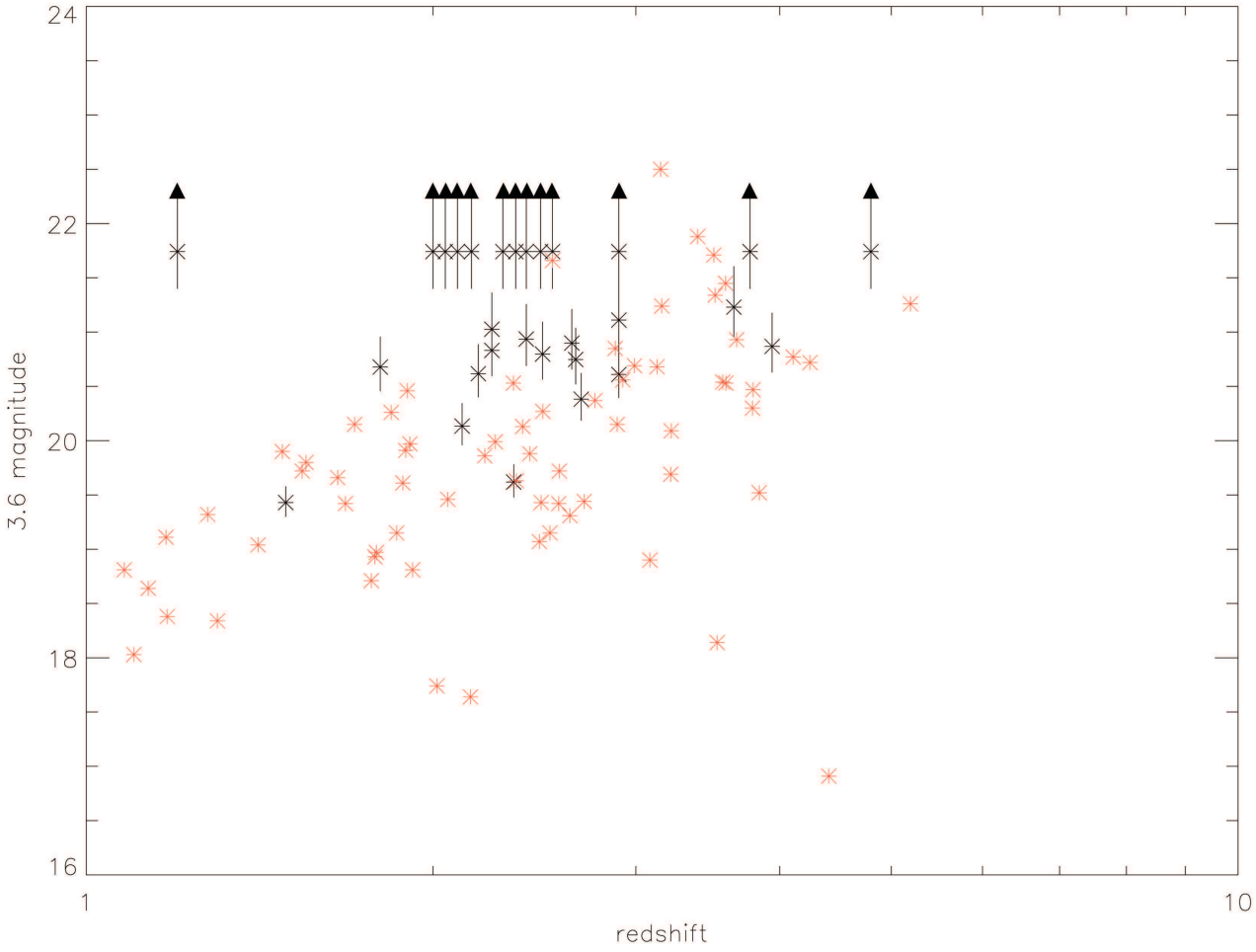

Figure 3.16: The 3.6μm magnitude against redshift diagram for the sample of high redshift radio galaxies from Seymour et al. (2007), overplotted with the radio galaxies from this thesis. The black symbols represent my observed radio galaxies which are biased due to the selection effect and the red symbols represent the Seymour et al. (2007) galaxies.

In my sample, I do not have the $K-$band magnitude detection for our survey, as we used the 3.6μm magnitude. The 3.6μm magnitude should be just as good a proxy for host galaxy mass as the $K-$band magnitude, as they both probe the near-infrared emission which is dominated

by the emission from the old stellar population which makes up the bulk of the stellar mass in galaxies. In actual fact, the 3.6μm emission has the potential to be better measurement of the stellar mass/luminosity of high-redshift radio galaxies due to the fact it is at longer wavelength than the $K-$band, which has a central wavelength of $\sim 2.2\mu$m. This means that it will be able to sample the rest-frame near-infrared light from the galaxy to higher redshifts than the K band. For example the 4000Å break does not reach 3.6μm until $z \sim 8$. To investigate the $3.6-z$ relation we turn to the study of Seymour et al. (2007) who compiled data for 69 radio sources observed with the *Spitzer Space Telescope* at 3.6 μm which have a known redshift. For the sources which do not have an identification at 3.6μm we used the SWIRE survey flux limit of 7.3μJy (5σ).

It is clear from Fig. 3.16 that the majority of the detected radio galaxies in my sample lie on a similar $3.6-z$ relation as those powerful radio galaxies in the study of Seymour et al. (2007), but with some notable differences. The main difference is due to my selection method, particularly the bias to faint near-infrared host galaxies to ensure that I had the best chance of finding the highest redshift sources, which has led to the sources in my sample lying towards the fainter side of the correlation. However, it is possible that the faintness of our sources is also due to the fact that we select our radio galaxies down to $S_{1.4} > 10$ mJy, which is ~ 0.05 Jy at the low-frequency of the studies of Jarvis et al. (2001a); De Breuck et al. (2002); Willott et al. (2003), i.e. much fainter than any of their radio galaxies. Given the link between radio luminosity and host galaxy luminosity found by Willott et al. (2003) my results could easily be consistent with such a scenario, although I would require more complete spectroscopy of my sample, spanning the full range in 3.6μm flux density to say for certain.

Another clear difference is the number of sources that I find at lower redshift but with very faint host galaxies. Although some of these sources do not have robust redshifts, many do, and it is clear that these are possibly a different population of radio sources coming in to my sample. In particular, EN1_64 and XMM_09 have secure redshifts at $z = 1.2$ and $z = 1.49$ respectively, but are not detected at 3.6μm in SWIRE. The radio luminosity of these sources are $L_{1.4} = 1.1 \times 10^{25}$ W Hz^{-1} sr^{-1} and 6.25×10^{25} W Hz^{-1} sr^{-1} for EN1_64 and XMM_09 respectively. This means that they lie just below the break of the radio galaxy luminosity function and have a radio luminosity where a non-negligible fraction of FRI-type sources make up the source counts. However, they still have reasonably bright emission lines which is not a common trait for FRI-type sources, and still suggests that they may have high accretion rates. An alternative explanation is that some of the radio emission could come from star formation in the host galaxy, but the star-formation rate needed to produce this much radio emission is $> 10^5$ M$_\odot$ yr^{-1} using the relation; SFR (M$_\odot$ yr^{-1}) $= 5.9 \times 10^{-22} L_{1.4}$/W Hz^{-1} from Yun et al. (2001). This is highly unlikely, as galaxies do not form at these sorts of rate, particularly when found in what is still quite a small area survey. Thus we are left with the picture that these are under-luminous or under-massive FRII/high-excitation radio galaxies, although further observations are needed to confirm their nature, these would essentially be a new class of powerful radio source which do not adhere to the $K-z$ relation.

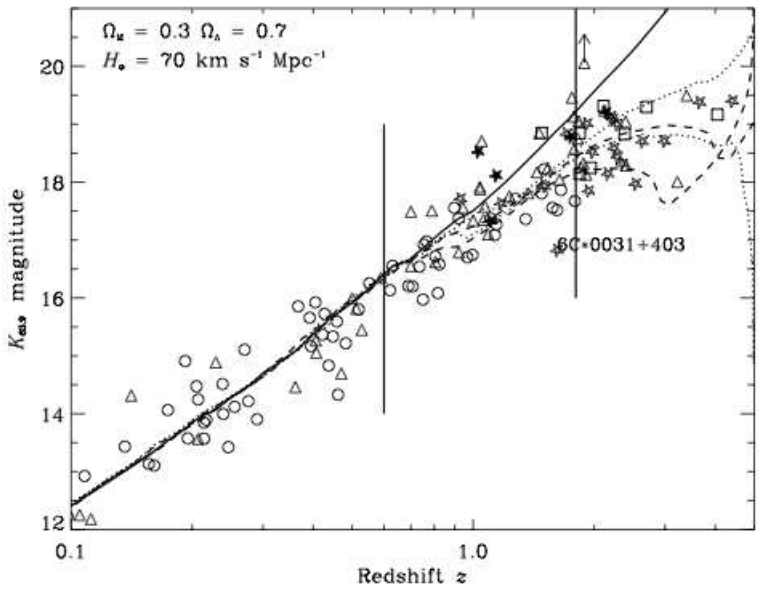

Figure 3.17: The $K-z$ Hubble diagram for radio galaxies from the 3CRR (circles), 6CE (triangles), 6C* (stars) and 7C-III (squares) samples, for a Ω_M=0.3, Ω_Λ=0.7 cosmology with H_0=70 km s^{-1} Mpc^{-1}. The two vertical lines show the redshift above which the alignment effect begins to be seen ($z = 0.6$). The solid lines are the fits to the 3CRR data points at z< 0.6 and $0.6 < z < 1.8$. The dashed line is the fit to the 6CE and 6C* sources at $0.6 < z < 1.8$ and $z > 1.8$. The filled stars represent five of the six objects in 6C* which do not have secure redshifts. From Jarvis et al. (2001a).

Chapter 4

A Radio galaxy at z=5.33?

In this chapter I the present optical and radio properties of a radio galaxy from the XMM-LSS field. The chapter was written as a paper to be submitted to MNRAS on the discovery of the highest redshift radio galaxy ever found at z=5.33. However, at the current time I am unable to confirm the robustness of the redshift as detailed in the following.

4.1 Introduction

4.1.1 The Epoch Of Reionisation

Some of the key aims of current and future facilities are to determine which sources are responsible for reionising the Universe, how quickly this occurred and when it came to an end. Detection of the Gunn-Peterson trough in high-redshift quasi-stellar objects (QSOs; Fan et al., 2006) suggest that the EoR ended around redshift $z \sim 6$, approximately a billion years after the Big Bang. However, the former questions are still open. Great strides have been made in determining which sources are responsible for reionising the Universe, the discovery of star-forming galaxies at $z > 6$ with the Wide-Field Camera 3 on the Hubble Space Telescope and deep near-infrared imaging on 8-m class telescopes suggest that there are too few galaxies to be fully responsible for reionisation (McLure et al., 2010; Bunker et al., 2010). These studies will continue to improve in the coming years with deep surveys with the new VISTA telescope, the launch of the James Webb Space Telescope and further in the future the Extremely Large Telescopes.

To measure the speed at which reionisation occurs, one needs to trace the evolution in the abundance of neutral hydrogen at these early epochs. Using the absorption of Lyman-α photons by clouds of neutral hydrogen is impaired due to its high cross-section to absorption, resulting in a complete loss of flux, i.e. the Gunn-Peterson trough in the spectra of high-redshift QSOs, precluding the accurate measurement of the abundance of neutral hydrogen beyond z$\sim$ 6.3. An alternative method of tracing the neutral hydrogen abundance at these early epochs is to use the hyperfine transition of neutral hydrogen at a rest-frame wavelength of 21 cm, i.e. in the radio waveband. At $z > 6$ this line is redshifted to low frequencies ($\nu < 200$ MHz). It is only now becoming possible to observe these frequencies to sufficient depth where we may detect the signature of reionisation through the 21 cm line with the imminent commissioning of the

Low-Frequency Array (LOFAR) and the Mileura Widefield Array (MWA), both of which lead towards the much larger Square Kilometre Array (SKA).

The evolution of neutral hydrogen within the EoR can be investigated broadly by two methods. The first utilizes the power spectrum variations in the intensity of the 21 cm radiation Iliev et al. (2008); Harker et al. (2010) and is where the majority of current work is concentrated. However, an alternative method would be to measure the 21 cm forest against a background powerful radio sources (e.g. Carilli et al., 2002), in much the same way that the Lyman-α forest is used to probe the intergalactic medium at lower redshifts (e.g. Péroux et al., 2001). The key missing ingredient for this method to be successful is the discovery of powerful radio sources at sufficiently high redshift with which to observe the 21 cm forest.

4.1.2 High redshift radio galaxies

High-redshift radio galaxies are powerful radio sources and hold the promise of being the ideal sources which probe the evolution of HI within the EoR. There have been many surveys which have tried to find high redshift radio galaxies (e.g. De Breuck et al., 2000a; Jarvis et al., 2001b; Best et al., 2003; Jarvis et al., 2004; Cruz et al., 2006, 2007; Brookes et al., 2008), with the highest radio galaxy found thus far having a redshift of $z = 5.19$ (van Breugel et al. (1999)).

The problem that has hindered the discovery of more radio sources at the highest redshifts is not the paucity of deep radio data, but the difficulty of obtaining targeted follow-up spectroscopy of the many candidate sources within a given radio survey. This is due to the fact that powerful radio sources at $z > 5$ make up $<< 1\%$ of the total radio source population (Fig. 4.1; Wilman et al., 2008) in current large area radio surveys such as the Faint Images of the Radio Sky at Twenty-centimetres (FIRST; Becker et al. 1995).

To overcome this problem, previous studies have applied filtering criteria to eliminate lower redshift radio sources on the basis of their spectral index and/or angular size (e.g. Chambers et al., 1996; Blundell et al., 1998; De Breuck et al., 2000a; Cohen et al., 2004; Cruz et al., 2006). Indeed, this selection of Ultra-Steep Spectrum radio sources resulted in the discovery of the highest redshift radio galaxy (van Breugel et al. 1999). However, it is clear that such methods are not 100 per cent efficient and a large number of radio sources at $z > 5$ may also be filtered out. This is crucially important when the space density of the $z > 5$ radio source population is extremely low to start with.

Unlike QSOs, where the stellar emission is outshone by the emission from the accretion disk around the central supermassive black hole, radio galaxies offer the opportunity to study the stellar populations of the most massive galaxies at the highest redshifts. Many studies have shown that powerful radio sources are universally hosted by the most massive galaxies in the Universe at the epoch which they are observed (e.g. Jarvis et al., 2001c; Seymour et al., 2007), with many authors suggesting that they evolve into the brightest cluster galaxies in the low-redshift Universe (e.g. McLure et al., 2004). Thus finding and studying the highest redshift radio sources not only enables the possibility of tracing the evolution of neutral hydrogen within the EoR but also allows us to investigate the speed at which the most massive galaxies form and the role of the central supermassive black hole in regulating the evolution of the host galaxy via AGN-driven feedback (e.g. Bower et al., 2006; Croton et al., 2006).

Here we announce the possible discovery of the highest redshift radio galaxy found to date, from our new and powerful survey, which utilizes the wealth of multi-wavelength data now

available. In Section 4.2 we describe our selection technique used to target the highest redshift radio sources and in Section 4.3 we present the properties of which. In Section 4.4 we show the promise of our technique in the context of future surveys which will run commensally with LOFAR, and as such hold the key to the exploration of the EoR.

I use the AB magnitude system (Oke & Gunn, 1983), and a standard cosmology is assumed in which $H_0 = 72$ km s^{-1}, $\Omega_M = 0.26$ and $\Omega_\Lambda = 0.74$ (Dunkley et al. (2009)).

4.2 Finding the highest redshift radio sources

The basic survey parameters for our search for the highest redshift radio sources have already been presented in Jarvis et al. (2009) and full details will be provided in a forthcoming paper (Teimourian et al. in prep.). Here we only describe the selection of our targets in the XMM-LSS field in which the source that is the subject of this paper was found. We follow the same basic procedure as detailed in Jarvis et al. (2009) with the exception that over the XMM-LSS field of the SWIRE survey there is no radio data from the FIRST survey. We therefore use the deep Giant Metrewave Radio Telescope (GMRT) data at 610 MHz presented in Tasse et al. (2007) to create our parent radio catalogue. In Jarvis et al. (2009) we used a radio flux-density selection limit of $S_{1.4\mathrm{GHz}} > 10$ mJy to ensure the selection of powerful radio sources at high redshift. We adopt a similar flux-density limit, adjusted assuming a spectral index of $\alpha = 0.8$[1], resulting in a flux-density limit at 610 MHz of $S_{610\mathrm{MHz}} > 19$ mJy. We cross-matched all radio sources above this radio flux-density with the SWIRE 3.6 μm catalogue (Lonsdale et al., 2003). We only consider compact radio sources where the position of the optical identification can be associated with the centroid of the radio emission. In order to restrict ourselves to only the most distant radio sources we then impose an upper limit to the flux density at 3.6 μm of 30 μJy. Based on the $K - z$ diagram of radio galaxies this should ensure that we only include radio sources with redshift $z > 2$ (e.g. Jarvis et al., 2001a; Willott et al., 2003). The resulting candidate HzRGs are then the subject of follow-up spectroscopy (Section 4.3.1).

4.3 A RADIO GALAXY at z=5.33?

J022200.34-033934.6 (hereafter J0222-0339) is detected in the GMRT radio data at 610 MHz (Tasse et al., 2007) with a flux density of 42 mJy, The source is also identified in the SWIRE catalogue at 3.6μm with $S_{3.6\mu\mathrm{m}} = 23.37 \pm 0.71$ μJy, thus J022200.34-033934.6 falls within both flux limits, $S_{610\mathrm{MHz}} > 19$ mJy and $S_{3.6\mu\mathrm{m}} < 30\mu$ Jy of our survey. In Fig. 4.2 we show the IRAC-3.6μm image of the source from SWIRE, overlaid with the radio image from GMRT data. The object at the centre of image is J022200.34-033934.6 which we identified as the host galaxy.

In order to obtain the redshift from this object we observed it on 19 August 2009 with the WHT using the ISIS spectrograph. We used the EEV12 (4096×2048 pixel^2) CCD and the R300B grism and REDPLUS (4096×2048 pixel^2) CCD with the R158R grism, for the blue and red arm respectively. We used a slit width of 2 arcsec, which gave us a resolution of 8.6Å in the blue arm and 16.5Å in the red arm. The IRAF standard tasks such as bias subtraction,

[1]We use the definition for the radio spectral index α, $S_\nu \propto \nu^{-\alpha}$

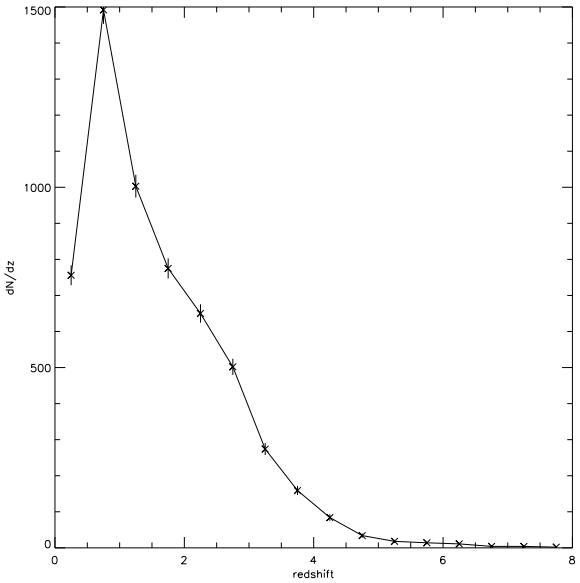

Figure 4.1: The number of sources with the flux density > 10 mJy as a function of redshift, using the semi-empirical method (Wilman et al. 2008). The decline is caused by the lack of radio source population beyond redshift 6.

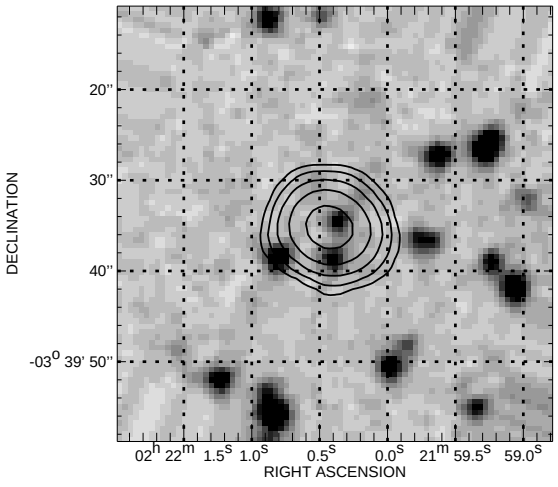

Figure 4.2: The IRAC-3.6μm image from SWIRE, which is overlaid with the radio image from GMRT survey. The faint point in the centre is the host galaxy. Contour levels are 2,4,8,16,32 and 32 mJy/beam.

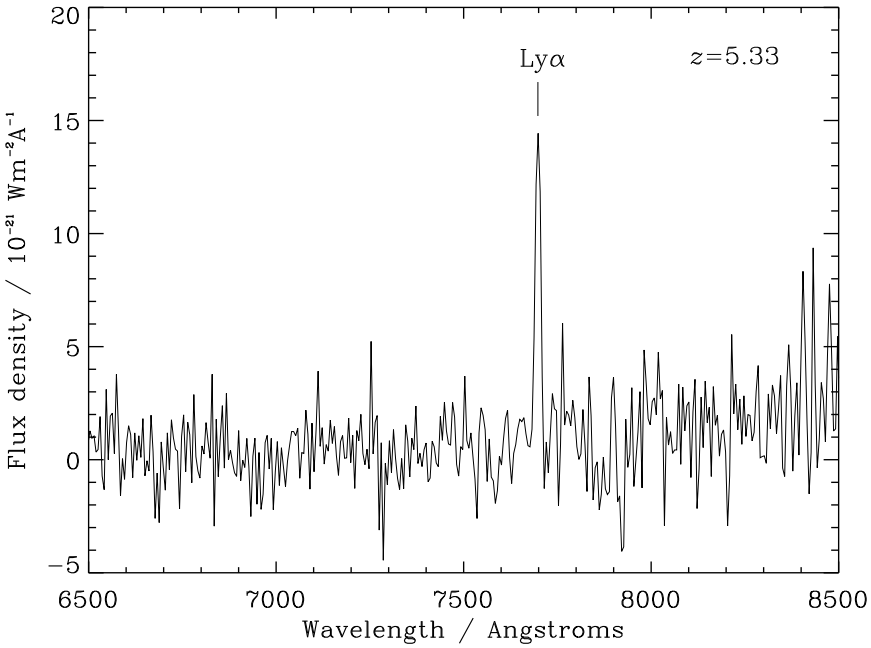

Figure 4.3: 1D spectra of the radio galaxy J022200.34-033934.6 which shows a strong emission line at 7700Å which we tentatively identify as Lyα at $z = 5.33$.

illumination correction and flat fielding were employed for the data reduction while CuNe +CuAr lamps were used for wavelength calibration. Flux calibration was carried out using the spectrophotometric standard Feige 34.

4.3.1 Spectroscopy

The 1D spectra of the J022200.34-033934.6 (Fig. 4.3) shows a strong emission line at 7700Å, which we tentatively associate with Lyα at $z = 5.33$. The line has a flux of 7.49×10^{-20} Wm^{-2} which corresponds to L= 2.27×10^{36} W at a redshift of z=5.33 and the rest-frame full width half maximum of < 650 km s^{-1}. The line is most likely Lyα, but there are still other possibilities for the other common emission lines in radio galaxies. The most probable other line is [OII]λ3727, which would give us a redshift of z = 1.06, thus we should see the [CII] λ2326 and the [CIII]λ1909 emission lines in the blue part of the spectrum at 4791Å and 3932 Å respectively, while there is no evidence for such lines and the noise on the spectra at the position of [CII] line is 3.2×10^{-20} Wm^{-2} and 4.2×10^{-20} Wm^{-2} for the [CIII] line.The imaging data shows that this radio galaxy has a K_{AB} magnitude of ~ 20.7 which is in an area of the $K - z$ diagram which makes it consistent with both $z \sim 1$ and $z \sim 5$.

We note that there is no optical data available for this source as it falls just north of the field covered by the CFHT Legacy survey in XMM-LSS. Fig. 4.4 shows the 2D spectra of the object with two aligned emission lines separated by ~ 3.8 arcsec, both are spatially resolved. These two emission lines are consistent with coming from the radio source and the nearby companion galaxy at α = 02h 22m 0.81s , δ = 03d 39m 38.31s . The brighter emission line component, on the left hand side in Fig. 4.4, is the emission line associated with the targeted radio galaxy,

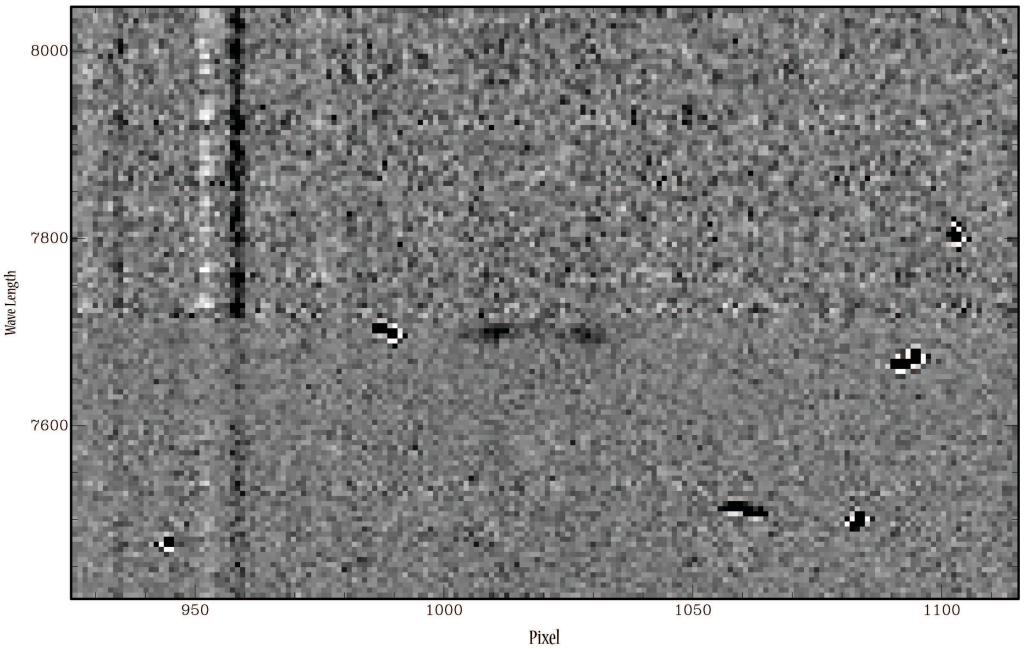

Figure 4.4: 2D spectrum of the radio galaxy J022200.34-033934.6 at PA 170°, showing the emission line from two objects. The line on the left hand side is the line associated with the targeted radio galaxy, J022200.34-033934.6.

and the fainter component, on the right hand side, is associated with the companion galaxy. Such close companions, both having bright Lyα emission are relatively rare, even around high-redshift radio galaxies which have been shown to be surrounded by haloes of Lyα emission line gas (e.g. Reuland et al., 2007). One explanation for this could be that we are seeing a lensed galaxy, where the host galaxy is doubly lensed by some foreground mass concentration. However, if this was the case then we would also expect the radio emission to be lensed by the same amount, assuming it comes from the same region at the gas and stellar emission. We see no evidence that the radio emission is anything but unresolved and point-like in our radio data, thus we suggest that the detection of two regions of Lyα emission is not due to gravitational lensing.

This suggests that the two galaxies are distinct objects at the same redshift. Thus, it is plausible that the two galaxies may be interacting which in turn my stimulate the Lyα emission. A number of theories exist for the production of such Lyα emission at high redshift. The simplest and most common explanations are that the Lyα emission is either powered by a starburst, AGN or from primordial gas powered by the release of gravitational potential energy during the formation of radio galaxy host (Haiman et al., 2000), or by cold accretion (Dekel et al., 2009; Dijkstra & Loeb, 2009; Smith & Jarvis, 2007). The Lyα emission from the radio galaxy is spread over at least 3 arcsec, which at $z = 5.33$ corresponds to $\sim$19 kpc. The extent of this emission falls completely within the beam of our radio data and we also have very little information on the velocity dispersion, other than it begin relatively narrow. Furthermore, we are unable to measure the systemic redshifts from any other lines in our spectra, so it is also impossible to determine how much of the putative Lyα emission is absorbed (e.g. Jarvis et al.,

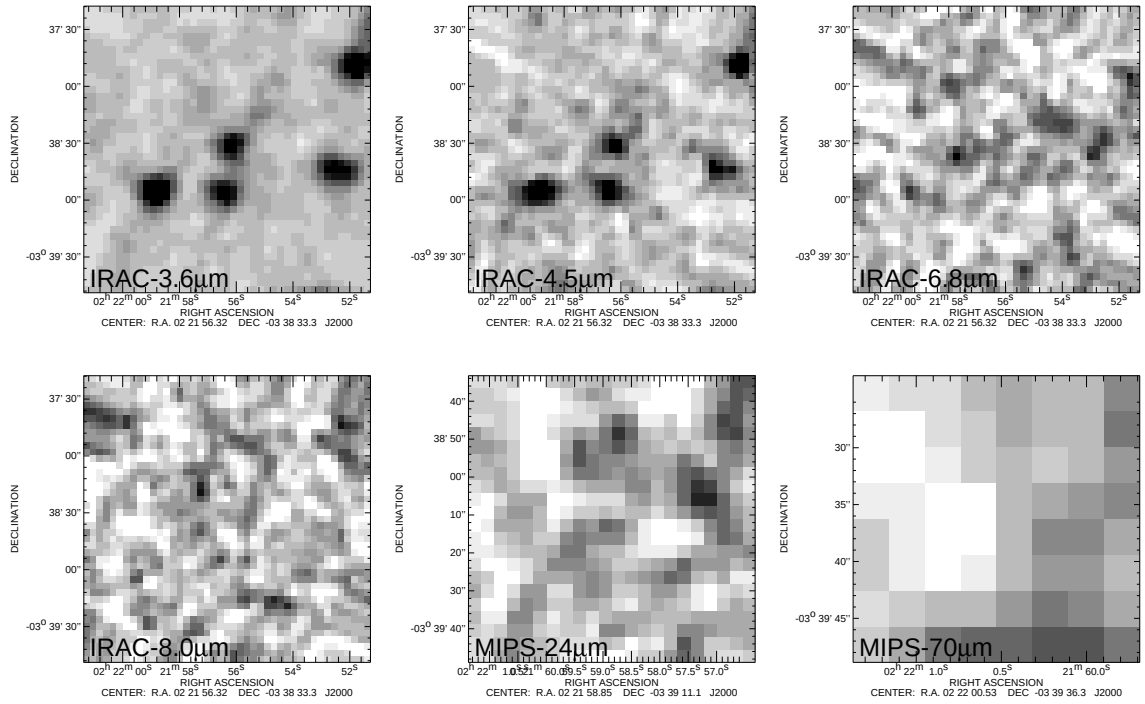

Figure 4.5: IRAC 4-bands and MIPS 2-band images from SWIRE of the J022200.34-033934.6.

2003; Wilman et al., 2004). Thus it is extremely difficult to distinguish the most likely power source of the extended emission line surrounding both the radio galaxy and its companion. We leave this to a future study with higher resolution imaging, spectroscopy and radio data.

4.3.2 Radio properties

J022200.34-033934.6 is detected with a compact structure in the GMRT radio data at 610 MHz (Tasse et al., 2007) with a flux density of 42 mJy and is unresolved in the GMRT data with resolution $\sim$ 6 arcsec. The source is also identified in the GMRT survey at 325 MHz (Tasse et al. 2007) with $S_{325\mathrm{MHz}} = 50$ mJy and also the NVSS (Condon et al., 1998) survey at 1.4 GHz with $S_{1.4\mathrm{GHz}} = 20.5$ mJy, 1.1 arcsec away from the GMRT centre and within the positional uncertainty of the NVSS survey. The power-law spectral index of the source between 325 MHz and 1.4GHz is α=0.62 which is not in the ultra steep category used to find HzRGs in previous studies. Assuming the redshift of z=5.33 the luminosity of the source at 325MHz is $\log_{10}(L_{325MHz}/\mathrm{W\ Hz^{-1}\ sr^{-1}}) = 26.77$ and $\log_{10}(L_{1.4GHz}/\mathrm{W\ Hz^{-1}\ sr^{-1}}) = 26.38$ at 1.4 GHz, which is close to the break in the radio luminosity function of Willott et al. (2001), and is a typical radio galaxy at this redshift, similar to the $z = 4.88$ radio galaxy presented in Jarvis et al. (2009).

4.3.3 Host galaxy properties

The host galaxy of the radio source has flux density $S_{3.6} = 23.37 \pm 0.71$ μJy (AB=20.48 mag) at 3.6μm and a flux density of $S_{4.5} = 18.08 \pm 1.14\mu$Jy (AB=20.76 mag). Using the flux density at 3.6μm and assuming a colour of K_{AB}=2.25 using the evolving elliptical galaxy template from Bruzual & Charlot (2003), the host galaxy would have a K-band magnitude of $K_{AB} = 22.65$. Assuming K_{AB}-K_{Vega} =1.9 and using the K-z relation from Willott et al. (2003) of $K = 17.37 + 4.53\log_{10}(z) - 0.31(\log_{10}(z))^2$, the expected K-band magnitude is K_{AB}=22.39. If the radio galaxy was at $z = 1.06$, i.e. consistent with the line being [OII], then the $K-$band magnitude is expected to be $K_{AB} = 19.4 \pm 0.6$. Using the same Bruzual & Charlot (2003) template for $z = 1.06$ then the expected colour is $K - 3.6 \sim 0.3$ mag, which leads to an expected 3.6μm magnitude of 19.7, which is only ≈ 0.8 magnitudes brighter than observed, and consistent with the observed scatter in the $K - z$ relation of ~ 0.6 dex.

Thus we find that the radio galaxy host is perfectly consistent with an extrapolation of the $K - z$ relation, suggesting that the galaxy is of order 3L* (e.g. Jarvis et al., 2001a). Unfortunately, there is no optical or IRAC CH3,4 detections of our source which prevents us using SED fitting to estimate the mass of the source, however in the study of Seymour et al. (2007), there is a source at a similar redshift to our source, which is the second highest redshift radio galaxy at z =5.19. TNJ0924-2201 has a radio flux density of $S_{1.4}$ =71.1 mJy, thus its radio luminosity is an order of magnitude brighter than our source at 1.4 GHz, with $\log_{10}(L_{1.4GHz}/\mathrm{W\ Hz^{-1}\ sr^{-1}}) = 27.70$. Seymour et al. (2007) estimate a stellar mass of $\log(M^{stel}_{max}/M_\odot)$=11.48 for TNJ0924-2201 as a result of SED fitting, principally over the IRAC bands, where it has a measured flux density of $S_{3.6} = 11.3\mu$Jy. Assuming that the bulk of the stellar mass can be traced by the 3.6 μm emission, and assuming that our source is indeed at $z = 5.33$, then by comparing the fluxes of both radio galaxies in 3.6 μm, we can estimate the J022200.34-033934.6 stellar mass as a factor of two more massive than TNJ0924-2201,with $(\log M^{stel}_{max}/M_\odot)$=11.8, but note that this is very uncertain without other deeper multiband imaging data or deeper spectroscopy.

The companion galaxy, 3.7 arcsec away, has a measured flux density of $S_{3.6} = 24.97 \pm 0.72$ μJy, very similar to the radio galaxy, suggesting that it is also relatively massive with an estimated mass of $\log(M^{stel}_{max}/M_\odot)$ $\sim$11.8. Thus it is plausible that such a system is the progenitor of a site which will become a massive galaxy cluster by the present day.

4.4 Conclusion

We have used the Spitzer-SWIRE, deep infrared survey and the GMRT radio data to begin a new survey with the aim of finding powerful radio sources within the Epoch of Reionisation. With this method we have possibly discovered the highest redshift radio galaxy at z = 5.33. The radio galaxy exhibits a strong Lyα emission line at 7700Å and a radio spectral index of α= 0.62 between 1.4 GHz and 325 MHz, and is therefore not in the ultra-steep spectrum category that has been used for finding such objects in the past. However there is a possibility of the line being [OII]λ3727line, which would give us a redshift of z = 1.06. In this case we should see the [CII] λ2326 and the [CIII]λ1909 emission lines in the blue part of the spectrum while there is no evidence for such lines. This reinforces the view of Jarvis et al. (2009) that previous searches

using the ultra-steep spectrum selection may have missed many high redshift radio sources. J0222.0-0339 has a luminosity very close to the break in the RLF (Willott et al., 2001) and thus is identified as a typical radio galaxy. The two-dimensional spectrum shows two distinct regions of line emission which we associate with the radio galaxy and a companion galaxy $\sim$ 19 kpc to the south. Unfortunately our current data do not allow us to determine the likely power source of the Lyα emission, although we suggest that the two galaxies are likely to be interacting. Using the IRAC photometry data to estimate the K-band magnitude of the host galaxy we find that the radio galaxy host is consistent with a simple extrapolation of the radio galaxy K-z relation, suggesting that the host is of the order of 3L*. Comparing our radio galaxy with the previous highest redshift radio galaxy (TN J0924-2201) in the study of Seymour et al. (2007), we estimate the stellar mass of our source as a factor of two more than TN J0924-2201, with $\log(M^{stel}_{max}/M_{\odot})$=11.8, although note that this is highly uncertain without deeper imaging or spectroscopic data. The discovery of the highest redshift radio galaxy, J022200.34-033934.6, allowed us to confirm our survey strategy is much more efficient than previous methods. The discovery of such a radio galaxy in only $\sim$ 10 square degrees of observed sky thus far, suggests that such a method could be employed with future all-sky radio surveys such as those to be carried out with LOFAR, and further in the future the Evolutionary Map of the Universe (EMU) survey with the Australian SKA Pathfinder telescope, combined with all sky infrared surveys to be produced by the Wide-field Infrared Survey Explorer (WISE) and the VISTA Hemisphere Survey. Furthermore, the narrow and deeper surveys at both radio and infrared wavelengths will allow us to probe much further down the luminosity function and provide the opportunity to determine the black-hole mass function at such early epochs.

Chapter 5

The Comoving Space Density of Radio Sources at $z > 2$

In this chapter I compare the number density of high-redshift radio galaxies with the current best estimates of the comoving space density of the radio source population at high redshift. I do this by comparing the number of objects in my sample with the Square Kilometre Array (SKA) Simulated Skies (S^3). I then consider what the future holds for the method of finding high-redshift radio galaxies discussed in this thesis, using the wealth of near-infrared surveys that are currently being conducted with the European Southern Observatory's (ESO) Visible and Infrared Survey Telescope for Astronomy (VISTA).

5.1 SKADS simulations

The Square Kilometre Array (SKA) Simulated Skies (S^3) are a set of five simulations of the radio and (sub)millimeter universe, S^3-GAL, S^3-PUL, S^3-SEX , S^3-SAX and S^3-EOR with the aim of preparation for the Square Kilometer Array (SKA) and its pathfinders. S^3-GAL is a model of the galactic radio and (sub)millimeter foreground from 10 MHz to 100 GHz (de Oliveira-Costa et al., 2008), S^3-PUL is a simulation of a Galactic population of pulsars (Karastergiou & Johnston, 2007), S^3-SAX is a semi-analytic simulation of neutral atomic (H_1) and molecular (H_2) hydrogen in galaxies and associated radio and (sub)millimeter emission lines (Obreschkow et al., 2009a; Obreschkow & Rawlings, 2009; Obreschkow et al., 2009b), S^3-EOR, is a simulation of the HI-line in of the Intergalactic Medium (IGM) during the Epoch of Reionisation (Santos et al., 2008) and finally the last simulation S^3-SEX, which this thesis focuses on, is a simulation of extragalactic radio continuum sources in a sky area of 20×20 deg^2, up to a redshift of $z = 20$ (Wilman et al., 2008).

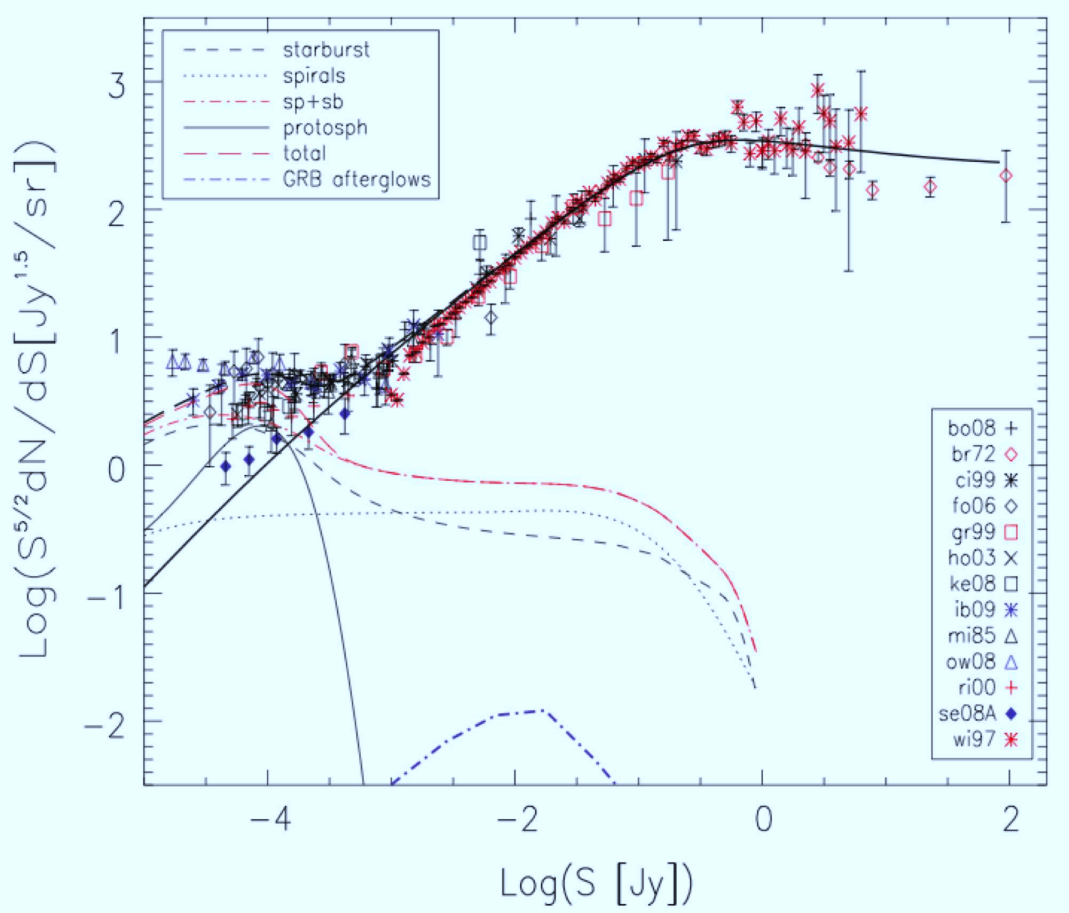

Figure 5.1: The normalised differential source counts at 1.4 GHz. Note that the filled diamonds show the counts of AGNs only, while all the other symbols refer to total counts. A straightforward extrapolation of evolutionary models fitting the far-IR to mm counts of populations of star-forming (normal late-type (spirals or sp), starburst (sb), and proto-spheroidal) galaxies, exploiting the well-established far-IR/radio correlation, naturally accounts for the observed counts below $\sim 30\mu$Jy. At higher flux densities, the counts are dominated by radio-loud AGNs. Taken from de Zotti et al. (2010).

There have been many studies to compute the number density of radio galaxies at high redshift (e.g. Dunlop & Peacock, 1990; Shaver et al., 1996; Jarvis & Rawlings, 2000; Jarvis et al., 2001c; Wall et al., 2005; Rigby et al., 2011), and based on these several groups have attempted to produce simulated source catalogues (e.g. Hopkins et al., 2000; Windhorst, 2003; Jarvis & Rawlings, 2004). Most of these studies were based on extrapolations of the known luminosity function of the various populations that make up the radio source counts, with the earlier works generally considering powerful radio-loud AGN, in the form of FRI and FRII radio galaxies, along with a much fainter population of starburst galaxies. These starburst galaxies were, for many years, invoked to explain the flattening in the radio source counts at around ≤ 100 μJy (Fig. 5.1; see de Zotti et al., 2010, for a review.). However, more recent work implies that this flattening may be caused by a combination of starburst galaxies and radio-quiet AGN

(e.g. Jarvis et al., 2004; Simpson et al., 2006).

Wilman et al. (2008, 2010) produced a semi-empirical model which draws sources at random from the observed, or suitably extrapolated, radio continuum luminosity functions for the extragalactic populations of interest, including different prescriptions for the powerful radio-loud AGN such as the FRIs and FRIIs, the starburst and star-forming galaxies, radio-quiet quasars and Giga-Hertz Peaked (GPS) radio sources. However, in addition to the inclusion of different populations for star-forming and starbursting galaxies and the first prescription for radio-quiet AGN, the main improvement came with the fact that they not only produced a catalogue of fluxes and redshifts, but also positions in the sky based on a model of the spatial clustering for the sources.

The whole simulation covers a sky area of 20×20 deg^2 up to z=20 and down to flux limits of 10 nJy at 151, 610, 1.4, 4860 and 18000 MHz. They start their simulation at $z = 0$, using a dark matter density field consistent with the ΛCDM cosmology (e.g. Dunkley et al., 2009). The density was mapped on to a cuboid grid of $5h^{-1}$ Mpc comoving cells, which makes a $550 \times 550 \times 1550$ array. The sources are then randomly sampled from the radio luminosity function of the parent population, these are then placed within the dark-matter density field according to the dark-matter halo mass which they are thought to reside in, based on angular clustering measurement of existing data.

For the work presented in this thesis, much of the S^3-SEX simulation is not required as I am only concerned with the powerful radio-loud sources which dominate the source counts at $S_{1.4} > 0.5$ Jy. Thus it is worth just highlighting that the radio luminosity function used in the S^3-SEX for the powerful AGN, is model C in the work of Willott et al. (2001). This model shares the same form of the luminosity function as models A and B, where the luminosity function is described by a combination of a low- and high-luminosity population ρ_l and ρ_h. In my work, I only have to consider sources above the break in the radio luminosity function, which is:

$$\rho_h = \rho_{h\circ} \left(\frac{L}{L_{h\star}} \right)^{-\alpha_h} \exp\left(\frac{-L_{h\star}}{L} \right) f_h(z). \tag{5.1}$$

$f_h(z)$ describes the redshift evolution of the luminosity function, and it is this that differs between models A, B and C. For model C, the form of the redshift evolution is given by,

$$f_h(z) = \exp\left[-\frac{1}{2} \left(\frac{z - z_{h\circ}}{z_{h1}} \right)^2 \right] \quad \text{for } z < z_{h\circ}, \tag{5.2}$$

and

$$f_h(z) = \exp\left[-\frac{1}{2} \left(\frac{z - z_{h\circ}}{z_{h2}} \right)^2 \right] \quad \text{for } z \geq z_{h\circ}. \tag{5.3}$$

This ensures that the evolution in the comoving space density above some peak redshift, $z_{h\circ}$, is decoupled from the form of the low-redshift evolution. Although we note that the evolution must always be negative beyond the peak in this model, it can essentially asymptote to a constant comoving scenario if z_{h2} is found to be large. The radio luminosity function is shown in Fig. 5.2. The S^3-SEX uses the best fit parameters given in Willott et al. (2001) for this model, with one adjustment. Namely, the cosmological model. Willott et al. (2001) did not

use the concordance cosmology (Dunkley et al., 2009) and therefore the evolution was adjusted using,

$$\rho_1(L_1, z)\frac{\mathrm{d}V_1}{\mathrm{d}z} = \rho_2(L_2, z)\frac{\mathrm{d}V_2}{\mathrm{d}z}, \tag{5.4}$$

where L_1 and L_2 are the luminosities derived from the flux density and redshift in two different cosmologies, the differential comoving volumes are the enclosed volumes in these two cosmologies.

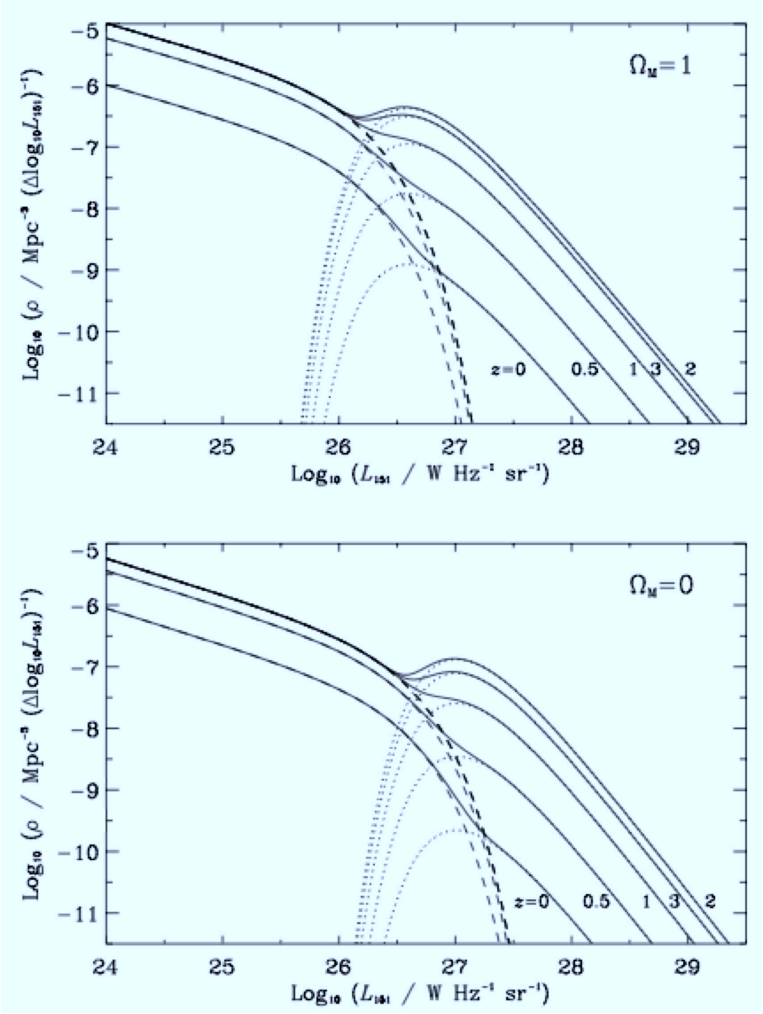

Figure 5.2: The radio luminosity function derived for model C for $\Omega_{\mathrm{M}} = 1$ (top panel) and $\Omega_{\mathrm{M}}0$ (bottom panel). Dashed lines show the low-luminosity population at $z = 0$; $z = 0.5$ and $z = 0.7$ (bottom to top). The dotted lines are the high-luminosity RLF at $z = 0, 0.5, 1, 3$ and 2 (bottom to top). Solid lines show the sum of both components. Taken from Willott et al. (2001).

5.2 Comparison of results

As shown in Chapter 3, of the 42 objects that I obtained spectroscopic observations for, I successfully measured a redshift for 20 of them. 18 of these sources have $z > 2$, 3 of them $z > 3$, 2 (or 1 depending on the reality of the $z = 5.33$ source) of the sources have $z > 4$ and one is a tentative $z = 5.33$ radio galaxy. In this section I compare the redshift distribution of sources in my sample with those expected based on the luminosity function of Willott et al. (2001), through the S^3-SEX simulation.

These 42 objects were drawn from a parent sample from the SWIRE and DXS surveys which together covered a useable area of 34 degree^2 when cross-matched with the various radio surveys described in Section 2.3. I therefore use the full S^3-SEX simulation covering 400 degree^2 and normalize the source density to 34 degree^2 to find how many sources with $S_{1.4} > 10$ mJy should be within this area. I find that in total there should be 490, this is in good agreement with the real data where I found 488 sources.

However, I then undertook a filtering strategy in order to remove all low-redshift $z \lesssim 2$ from my sample. This left 161 sources from which we drew sources for follow-up spectroscopy. To link this to the S^3-SEX simulation I removed all sources from the simulation that had redshifts $z < 2$, this left 147 sources with $z > 2$ in the simulation. Again, it is reassuring that the numbers are consistent with each other, which leads me to suspect that; a) the filtering criteria appear to be effective and do not lose many high-redshift sources, and b) they appear to resemble the source density in the Universe very well. This is not wholly expected, as the radio luminosity function was derived using only sources down to ~ 500 mJy, a factor of 50 brighter than the lower limit of 10 mJy for my sample.

Obviously I was unable to obtain spectroscopic redshift measurements for all sources in my spectroscopic targets. I therefore also impose the "incompleteness fraction" for the observations on the remaining sources in the S^3 simulation. I use the spectroscopic completeness of 22/161, which leads to 20 objects remaining in the S^3 simulation.

I now compare the number density of objects as a function of redshift in my sample with the S^3-SEX simulation (Fig. 5.3). In Table. 5.1 I present the number of sources in above different redshifts for both our sample and the SKADS simulation separately. I used the binomial function (probability $(X \geq V) = \sum_{x=V}^{N} \frac{N!}{x!(N-x)!} \times P^x \times (1-P)^{(N-x)}$) and calculated the probability of finding the number of sources in my sample with the prediction from S^3-SEX for each epoch. In the case of radio galaxies lying at z$>$ 2 the V parameter is 20 which is the number of galaxies at $z > 2$ in our sample, the number of all candidates in our sample N is 161, and P is the probability of the number of sources with $z > 2$ in S^3-SEX which is equal to 20/147. The calculations indicate that my sample is consistent with the S^3-SEX at the 70 percent level for sources with $z > 2$. Furthermore, by increasing the lower-redshift limit, the probability of obtaining the redshift distribution that I find for my sample if it was the same as the S^3 redshift distribution is 95 percent for $z > 3$, 96 per cent for $z > 4$ and 33 per cent for $z > 5$. I note that some of this close correspondence between the model and the observations is driven by the way that I have had to implement the incompleteness correction to the model redshift distribution, which biases the model to the measured values. However, given the relative dearth of redshifts, I am able to conclude that the redshift distribution of my sample is at least consistent with the redshift distribution of the S^3-SEX simulation. Based on this, I use the combination of my selection criteria and the S^3 simulation to determine how well

Table 5.1: The number of radio galaxies with $S_{1.4} > 10$mJy in 34 deg^2 both for SKADS simulation and the real observed data sample, above several redshift limits.

	$z > 2$	$z > 3$	$z > 4$	$z > 5$
S^3-SEX	20	7	4	1
My Sample	20	4	3	1

current and future near-infrared surveys will be able to find high-redshift radio sources in the following section.

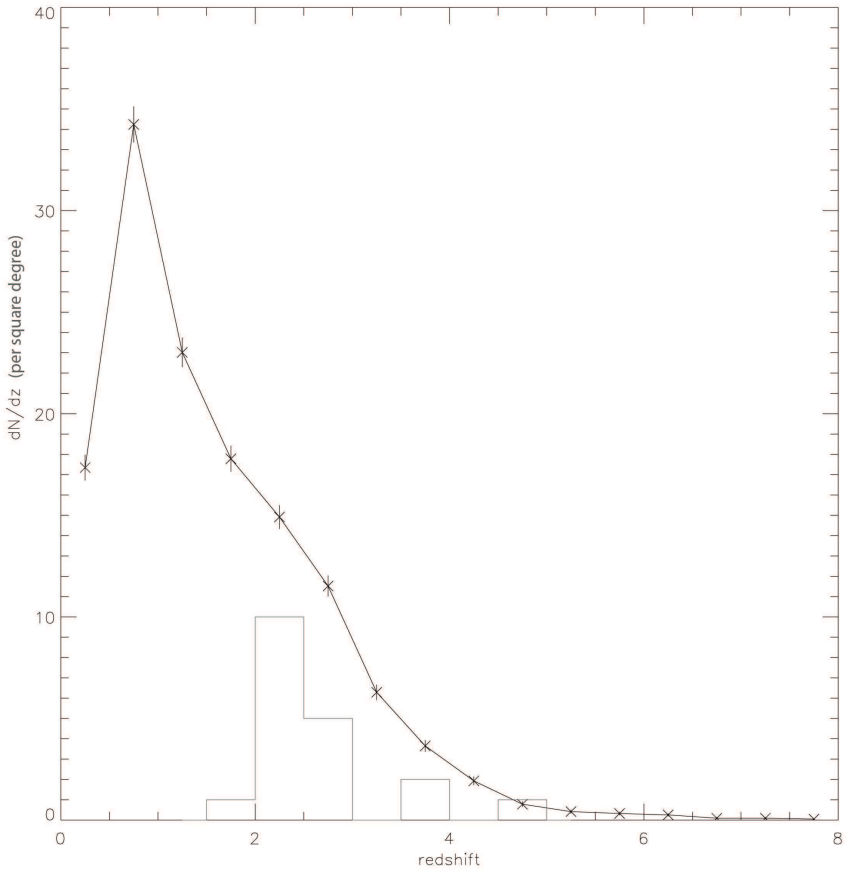

Figure 5.3: The number of sources with the flux density > 10 mJy as a function of redshift for both SKADS targets and our sample. The SKADS source distribution has been corrected for the spectroscopic incompleteness of our observed sample, just by scaling of the successful redshift measurement compared to the fraction observed.

5.3 Predictions for current and future near-infrared surveys

My relatively small survey for high-redshift radio galaxies appears to be fully consistent with the S^3 simulation out to at least $z \sim 5$. I now consider the possibility of extending my technique for finding high-redshift radio galaxies to other areas of sky which have or will soon have near-infrared imaging data to sufficient depth to filter out the many low-redshift contaminating sources.

5.3.1 The Visible and Infrared Survey Telescope for Astronomy (VISTA)

The Visible and Infrared Survey Telescope for Astronomy (VISTA) is a 4-m near-infrared telescope which is part of ESO's Paranal Observatory. VISTA is the worlds largest near-infrared survey telescope due to its large mirror, wide field of view and very sensitive detectors (see Fig. 5.4).

The VISTA filter set includes Z, Y, J, H, and K_s filters and a narrow band filter at 1.18 microns. VISTA observing time, will for the first five years be devoted to six public surveys. In much the same way as UKIDSS, some will study small patches of sky for long periods with the aim of detecting extremely faint objects and others will survey the entire southern sky. The VISTA surveys concerned with investigating galaxy formation and evolution, and therefore not pointing towards the Galactic Plane or Magellanic Clouds, are as follows:

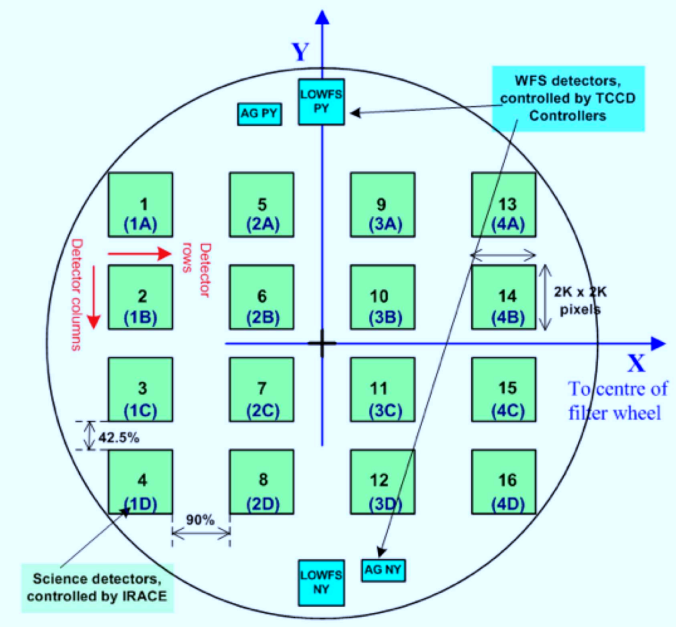

Figure 5.4: The VISTA focal plance with 16 near-infrared detectors which together provide an instantaneous field of view of ~ 0.6 degress^2. Image taken from www.vista.ac.uk.

Ultra-VISTA aims to image the COSMOS (Scoville et al., 2007) field to unprecedented depths. It will use the Y, J, H, and K_s broadband filters and also one narrow band filter which is designed with the aim of studying Lyα emitters up to $z \sim 8$. The three main scientific goals of Ultra-VISTA are to study the first galaxies, the stellar mass within the epoch of star-formation activity and dust obscured star formation. Full details of the initial part of the survey can be found in McCracken et al. (2012).

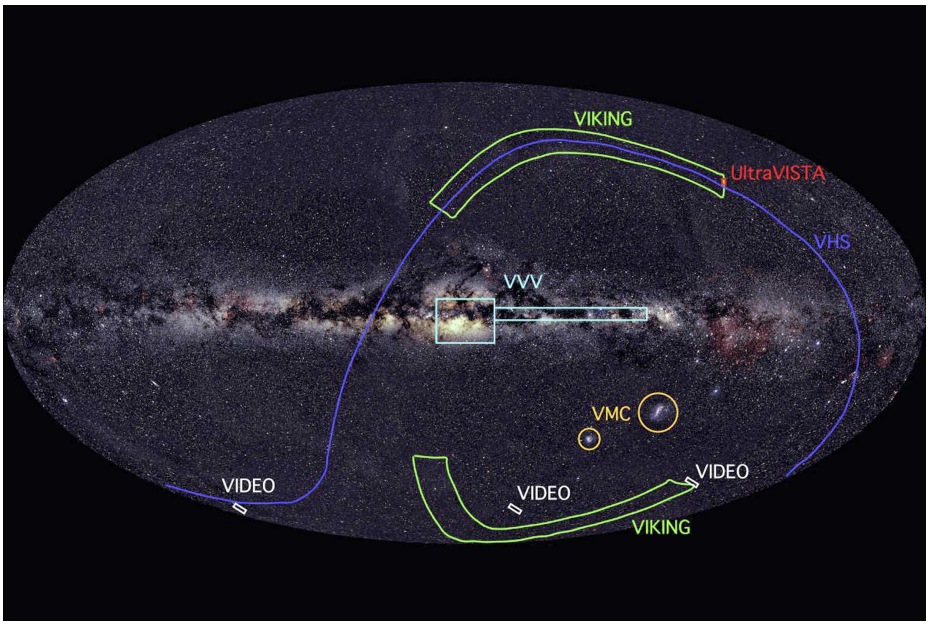

Figure 5.5: A schematic representation of the sky coverage of the various VISTA surveys. Taken from Arnaboldi et al. (2007).

VISTA Deep Extragalactic Observations (VIDEO) Survey: VIDEO covers 12 deg^2 of sky in Z, Y, J, H and K_s filters. VIDEO is a survey to study galaxy evolution using active galactic nuclei, galaxy cluster evolution, and very massive galaxies. The survey fields are three of the most widely covered fields in extragalactic survey astronomy, including the SWIRE survey. The specific fields are 4.5 degree^2 in the Chandra Deep Field South; 4.5 degree^2 of the XMM-Newton Large-Scale Structure Survey and 3 degree^2 in the ELAIS-S1 field. Full details can be found in Jarvis et al. (2012).

VISTA Kilo-Degree Infrared Galaxy Survey (VIKING): The VIKING survey (e.g. Findlay et al., 2012) will cover 1500 deg^2 in Z, Y, J, H and K_s band. The near-infrared data will be used to estimate accurate photometric redshift up to $z \sim 1$. Weak lensing analysis, determination of galaxy stellar masses and searching for high redshift quasars and galaxy clusters are some of the scientific missions for VIKING.

VISTA Hemisphere Survey (VHS) aims to image the entire Southern in J and K_s band. The resulting data will be about four magnitudes deeper than 2MASS and it covers $\sim$ 17,000 deg^2 of sky (the parts of the sky not covered by the other five surveys). The scientific goals of the VHS include, studying the merger history of the Galaxy, probing high redshift quasars and measuring the properties of Dark Energy through the examination of large-scale structure to $z \sim 1$.

Table 5.2: Summary of the key VISTA Surveys that could be used to find high-redshift radio galaxies. Also shown is the expected number of radio galaxies with $S_{1.4} > 10$ mJy in the given survey area from the S^3-SEX simulation. The † denotes that we only consider the 1.5 degree^2 part of the UltraVISTA survey which reaches a shallower depth than the full deep survey which covers only half of this area.

Survey	Area (degree^2)	$K_{\rm Vega}$ limit (5σ)	# $z > 2$	# $z > 3$	# $z > 4$	# $z > 5$
VHS	20,000	18.2	86750	29150	7500	1600
VIKING	1500	19.4	6506	2186	562	120
VIDEO	12	21.7	52	17	4	0.9
Ultra-VISTA	1.5†	22.2	6	2	0.5	0.1

5.3.2 High-redshift radio galaxies in the VISTA surveys

As we mentioned the above infrared surveys with VISTA hold great promise of being suitable surveys to hunt high redshift radio galaxies due to their K_s-band depth. Table 5.2 gives a summary of the depth in the K_s band that each of the survey reaches, along with the number of radio galaxies with radio flux density $S_{1.4} > 10$ mJy expected using the S^3-SEX simulation. We show the expected redshift distribution of radio sources in each of the surveys in Fig. 5.6.

One can immediately see that the number of high-redshift radio galaxies in these surveys is relatively large and scales with the survey area. However, I need to combine the area with the depth of the respective surveys in order to establish how efficient each is for finding the most distant radio galaxies. To do this I use the $K - z$ relation of (Eqn. 1.1; Willott et al., 2003). By using this equation I am able to calculate an approximate redshift limit that each survey is sensitive to. Thus solving the quadratic equation for the $K - z$ relation for each survey I find that the VHS will be able to detect powerful radio galaxies out to $z \sim 1.5$; VIKING to $z \sim 2.9$; VIDEO to $z \sim 11$ and UltraVISTA to $z \sim 14$. Obviously these calculations come with some caveats. First, is that there is scatter in the $K-z$ relation of the order of $\Delta z = 0.6$ mag (Jarvis et al., 2001a). Second is that this assumes that the polynomial form of the $K-z$ relation holds to infinity. This cannot be the case and the $K - z$ relation itself has only been explored to $z \sim 4 - 5$ with any degree of certainty. Thus the redshift limits for VIDEO and UltraVISTA are highly uncertain and maybe overestimated.

To counteract the degree of scatter in the $K - z$ diagram, I adopt a conservative approach which should still hold for the $K-$band magnitudes covered by the VHS and VIKING surveys. For this I assume that the $\Delta K = 0.6$ scatter is indicative of the lower bound in $K-$band magnitude at that redshift. Obviously, in reality it should contain 68 per cent of the sources within the 1σ bound, but as I am just assuming this as a lower limit, I expect that 84 per cent of the radio galaxies lie at $K-$band magnitudes brighter than this limit. Adopting this lower limit to the $K-$band magnitude reduces the redshift limit of each survey to the following; VHS: $z \sim 1.1$, VIKING: $z \sim 2.1$, VIDEO: $z \sim 7.5$ and UltraVISTA: $z \sim 10$. I now use these values for VHS and VIKING to determine how many high-redshift radio galaxies could be found compared to the number that could be filtered out using the S^3-simulation. For both the VIDEO and UltraVISTA surveys, the situation may be somewhat better in terms of being able to select on the basis of redshift. The five near-infrared filters used for VIDEO and the four for UltraVISTA, coupled with the wealth of optical imaging over these fields (e.g. Jarvis et al., 2012;

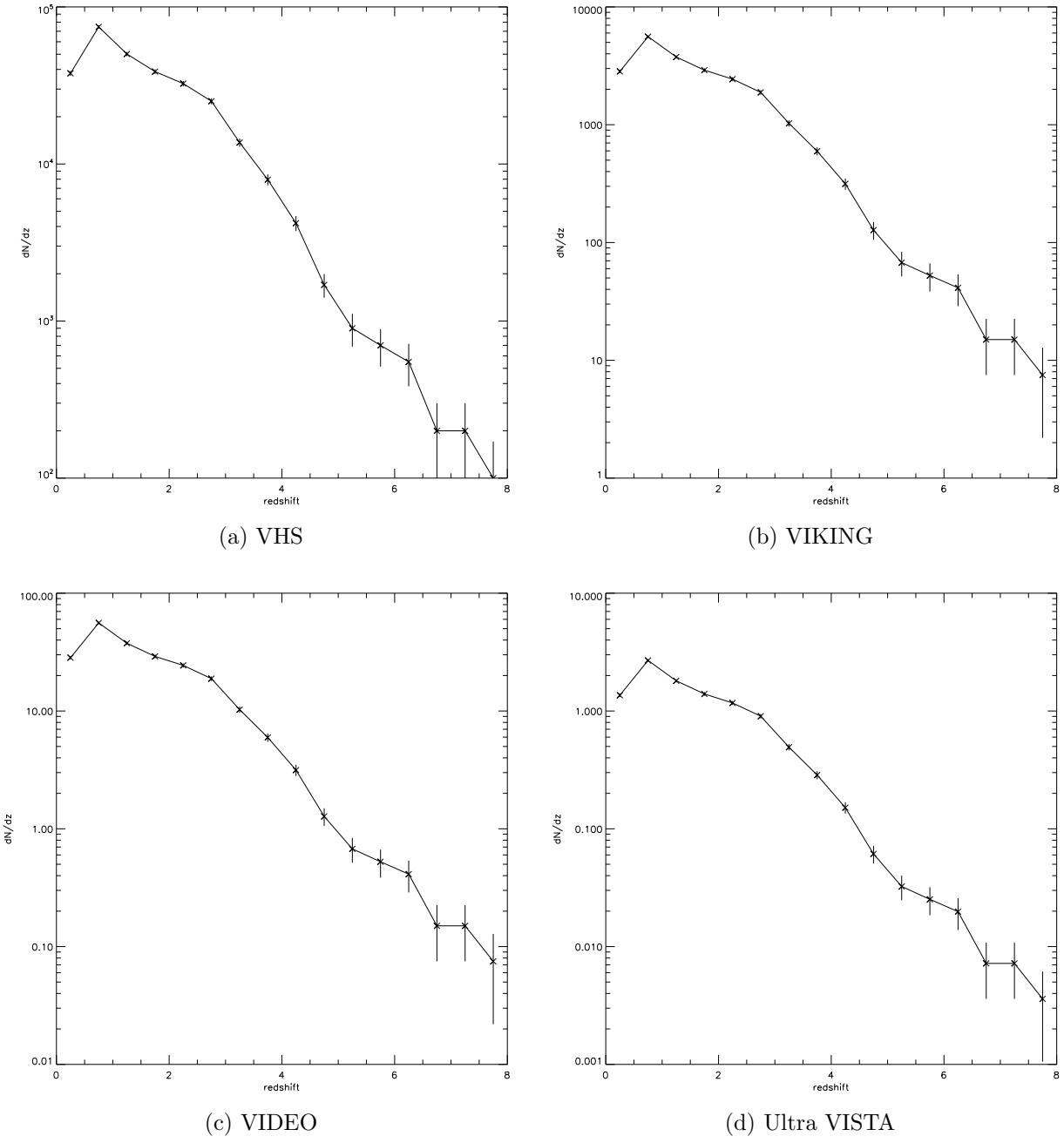

(a) VHS

(b) VIKING

(c) VIDEO

(d) Ultra VISTA

Figure 5.6: Redshift distribution for radio sources with $S_{1.4} > 10$ mJy for the VHS (top left), VIKING (top right), VIDEO (bottom left) and UltraVISTA (bottom right) surveys.

Table 5.3: The total and fraction of $S_{1.4} > 10$ mJy radio galaxies that a given VISTA Survey could isolate above a given redshift based on the S^3-SEX simulation and the limits shown.

Survey	Area (degree^2)	$K_{\rm Vega}$ limit	$z_{\rm lim}$	No. of Sources with $z > z_{\rm lim}$	Fraction of Sources with $z > z_{\rm lim}$
VHS	20,000	17.6	$z > 1.1$	175650	60%
VIKING	1500	18.8	$z > 2.1$	6506	30%
VIDEO	12	21.1	$z > 2$	52	30%
VIDEO	12	21.1	$z > 3$	17	10%
VIDEO	12	21.1	$z > 4$	4	3%
VIDEO	12	21.1	$z > 5$	0.9	0.5%
VIDEO	12	21.1	$z > 6$	0.45	0.2%
UltraVISTA	1.5	21.6	$z > 2$	6	27%
UltraVISTA	1.5	21.6	$z > 3$	2	9%
UltraVISTA	1.5	21.6	$z > 4$	0.5	2.2%
UltraVISTA	1.5	21.6	$z > 5$	0.1	0.4%
UltraVISTA	1.5	21.6	$z > 6$	0.05	0.2%

McCracken et al., 2012) means that is may be possible to use photometric redshifts to curtail the need for spectroscopic observations even further. For example, Willott et al. (2013) and Bowler et al. (2012) used the VIDEO and UltraVISTA surveys respectively to find high-redshift $z > 6$ galaxies via the Lyman-break technique (e.g. Steidel & Hamilton, 1992). Lyman-break galaxies are generally less luminous than the hosts of powerful radio sources which makes the possibility of isolating the highest redshift radio sources from these surveys possible, if the area is large enough. Table 5.3 shows the number of sources that are expected to be isolated in the four VISTA Surveys discussed. For VHS and VIKING I use a single z limit that corresponds to the depth of the $K-$band imaging, whereas for VIDEO and UltraVISTA I assume that all radio galaxies can be detected at $z < 7$.

I find that the VIKING survey occupies a key parameter space for this type of study. It is deep enough to filter out the majority of radio galaxies at $z < 2$ but covers enough area (1500 square degrees) that it will contain around 100 radio galaxies at $z > 5$, with ~ 10 of these expected to lie at $z > 6$. The other survey that may contribute is the VIDEO survey, its greater depth ensures that it could detect radio galaxies all the way up to $z \sim 7$, with the benefit that the vast majority of lower-redshift radio galaxies could be filtered out using multi-wavelength based photometric redshifts, as opposed to the relatively coarse $K - z$ diagram. My calculations shows that their should be ~ 4 radio galaxies at $z > 4$ in VIDEO with one at $z > 5$ if the SKA simulation holds to these redshifts.

On the other hand, the very deep UltraVISTA survey does not have sufficient area to find any bright radio sources at $z > 4$, and although the VHS covers around 20,000 square degrees it does not have sufficient depths to effectively filter out the vast majority of radio sources, as it can only detect sources out to $z \sim 1$.

Chapter 6

Conclusion & Future Work

6.1 Conclusions

The aim of this thesis was to carry out a new survey with the aim of finding powerful radio sources within the Epoch of Reionization. Once such sources have been found they will act as unique probes of the intergalactic medium of this important epoch in the history of the Universe through dedicated 21 cm absorption lines studies with facilities such as LOFAR and eventually the Square Kilometre Array.

High-redshift radio galaxies make up a very small fraction of all radio sources, thus we needed to filter out the low redshift counter parts in order to optimize follow-up spectroscopy so that the key aims can be achieved in a modest amount of observing time. Therefore, I chose only those radio galaxies with a radio flux-density $S_{1.4} > 10$mJy to ensure that sources that we did find could feasibly be used to detect 21 cm absorption against them, but also so that a higher fraction would have bright emission lines in the optical part of their spectrum, allowing spectroscopic redshifts to be measured more easily. To ensure that the vast majority of the targets were actually at high redshift, the main selection criteria was that they must be faint at near-infrared wavelengths. The radio galaxy $K - z$ diagram shows a tight relation between apparent near-infrared magnitude and redshift which means that it should be possible to filter out low-redshift radio galaxies efficiently. A third criterion was to use only compact radio sources, to ensure that the near-infrared identification could be easily associated with the radio emission.

In this thesis I have used these new criteria for selecting high-redshift radio galaxy candidates, using a combination of moderate depth radio data, available across most of the sky, with deep near-infrared data that is only available in a few square degree patches of the sky, concentrated on well-studied extragalactic fields. Specifically, I have used both the *Spitzer*-SWIRE and UKIDSS-DXS deep infrared surveys for the near-infrared data and radio data from the FIRST Survey, the ATCA-ATLAS and GMRT which reach sufficient depth to find powerful radio sources at the highest redshifts.

With follow-up spectroscopy carried out on both the William Herschel Telescope and the Gemini-South Telescope I managed to find redshifts for 22 sources from 46 that were targeted. This led to the first publication from the survey (App. C; Jarvis et al., 2009), the subject of which was the discovery of the second highest redshift radio galaxy ever found. As this was

discovered on the first observing run, this gave great encouragement for the methodology. The other spectroscopic observations also revealed two other radio galaxies at $z > 4$, which is a success fraction of 7 per cent for all galaxies followed up, much higher than any previous work which typically had a $\sim$ 1 per cent success rate (e.g. Jarvis et al., 2001b; De Breuck et al., 2002; Cruz et al., 2006). One of these objects is plausibly at $z = 5.33$, (Chapter 4.4), and if confirmed with higher resolution spectroscopy would be the highest redshift radio galaxy ever found.

I use these spectroscopic data to investigate whether the properties of the high-redshift radio sources selected in this way resembled their generally more powerful counterparts selected in past studies, concentrating on ultra-steep spectrum sources. Where possible I investigated their Lyα emission and how this correlated with the radio luminosity. I found that the sources in my sample extended the correlation between radio luminosity and Lyα emission-line luminosity found previously by Jarvis et al. (2001b). This suggests that the generation of the radio emission and that of the ionizing photons much be closely linked, most easily explained by both being driven by the accretion rate on to the central supermassive black hole.

I also investigated whether the host galaxies of the radio galaxies in my sample were similar to their more powerful counterparts. I found that although the sources selected in this thesis tended to lie towards the faint end of the $K-z$ relation for a given redshift, this can be explained by the selection that I imposed, namely they were selected to be near-infrared faint. However, some radio sources appeared to be much fainter than expected from the $K - z$ diagram, but further studies over much larger areas need to be performed to determine whether these are just odd outliers or a new class of radio source.

In Chapter 5.3.2 I compare the redshift distribution of my spectroscopically confirmed sample to the simulated source density from the SKA simulated continuum survey (Wilman et al., 2008, 2010). I found the redshift distribution of my sample to be consistent with that of the SKA simulation. This is not entirely expected as the SKA simulation only used luminosity functions constrained to much brighter radio flux densities that the 10 mJy that I have used here. This is encouraging as it means that the SKA simulation can be used to predict what may be possible with new near-infrared surveys when combined with moderate-depth radio continuum observations.

Thus in the second part of Chapter 5.3.2 I use the SKA simulation to predict the number of sources that should be present in the areas covered by the new near-infrared surveys that are being carried out with the VISTA telescope. I then impose cuts on the near-infrared magnitude dictated by the depth of each of the VHS, VIKING, VIDEO and UltraVISTA surveys, to determine the redshift of the radio galaxies that could be detected in these surveys, based on the radio galaxy $K-z$ relation. Essentially this is using the sample selection method developed in Chapter 2.4 over different surveys areas. I find that these surveys could play a big role in finding high-redshift radio galaxies in the future. In particular, the VIKING survey occupies a key parameter space for this type of study. It is deep enough to filter out the majority of radio galaxies at $z < 2$ but covers enough area (1500 square degrees) that it will contain around 100 radio galaxies at $z > 5$, with $\sim$ 10 of these expected to lie at $z > 6$. The other survey that may contribute is the VIDEO survey, its greater depth ensures that it could detect radio galaxies all the way up to $z \sim 7$, with the benefit that the vast majority of lower-redshift radio galaxies could be filtered out using multi-wavelength based photometric redshifts, as opposed to the relatively coarse $K - z$ diagram. My calculations show that their should be $\sim$ 4 radio galaxies

at $z > 4$ in VIDEO with 1 at $z > 5$ if the SKA simulation holds to these redshifts.

On the other hand the very deep UltraVISTA survey does not have sufficient area to find any bright radio sources at $z > 4$, and although the VHS covers around 20,000 square degrees it does not have sufficient depths to effectively filter out the vast majority of radio sources, as it can only detect sources out to $z \sim 1$.

6.2 Future Work

In this section I outline some possible avenues for future work in this field, beyond that which I have discussed in Chapter 5.3.2.

The most obvious follow-up at this stage would be to confirm the reliability of the $z = 5.33$ radio galaxy presented in Chapter 4.4. Higher resolution spectroscopy could be used to establish whether the line is in fact Lyα or the other main candidate which is [OII] at $z \sim 1$. At higher resolution it would be possible to see if the line split in to a doublet and therefore confirm that it is indeed [OII], or whether it displayed a sharp cut-off to its blue wing, which would indicate that it was Lyα.

On top of this work, there are still many galaxies that are in my parent sample which I was unable to obtain follow-up spectroscopy of. Some of these could now be eliminated based on new near-infrared and optical imaging from telescopes such as VISTA, CFHT, Subaru and VLT Survey Telescope all of which have taken imaging data over the SWIRE and/or DXS fields since the bulk of the work presented in this thesis was carried out.

However, I believe that a huge breakthrough in this field could come with the massive deep survey that is envisaged for the *Euclid* space mission. *Euclid* is designed to answer some of the fundamental questions in Cosmology, but as a by-product it will survey 20,000 square degrees to an $H-$band limit of $H \sim 24$, roughly the equivalent depth of the VIDEO Survey. This would mean that it should be possibly to robustly rule out all $z < 5$ radio galaxies and leave around 1500 radio galaxies at $z > 5$ and a few hundred at $z > 6$. These could then be observed as part of a 21 cm absorption line experiment with LOFAR or the SKA.

I therefore believe that the strategy defined here will play a big role in exploring the epoch of reionization over the next 5-10 years.

Appendix A

Radio source candidates

Table A.1: ATLAS radio sources in the CDFS field with radio flux > 10mJy cross-matched with the SWIRE survey. $S_{1.4}$ presents the radio flux at 1.4 GHz, $S_{3.6}$ and present the flux density at 3.6 μJy.The separation between the radio position and the near-infrared counterpart is also given (Sep) in arcsec, if the separation value is not shown the sources are not detected in the SWIRE catalogues. The structure of the radio sources are given for the compact (c) and not compact (nc). For the undetected sources in the SWIRE catalogues at at 3.6, the lower limit of 7.3 μJy is shown.The rms in ATLAS survey is 10-15 μJy. the $\star$ sign marks those which are not covered in the IRAC imaging and the $\wr$ sign shows either of both fluxes could be the ID.

ID	**RA**	**DEC**	$S_{1.4}$ / **mJy**	$S_{3.6}$ / μ**Jy**	**sep**	**struc**
C01$\star$	03:26:05.68	- 27:47:34.40	74.7	< 7.3		c
C02$\star$	03:26:11.48	- 27:32:43.80	110.9	< 7.3		c
C03	03:26:17.43	- 28:07:09.90	13.83	28.50±3.40		c
C04	03:26:18.23	- 28:07:03.50	10.29	< 7.3		c
C05	03:26:22.08	- 27:43:24.40	27.81	218.7±21.95	0.27	c
C06	03:26:30.27	- 27:34:45.90	14.54	78.49±8.47		c
C07	03:26:31.78	- 27:34:39.70	14.6	< 7.3		c
C08	03:26:32.22	- 27:46:46.60	24.33	113.6±11.44	0.31	c
C09	03:26:36.62	- 28:07:50.70	11.48	180.75±18.72		c
C10	03:26:42.47	- 28:08:02.50	30.51	381.15±38.93		c
C11	03:26:48.67	- 28:47:35.80	13.81	77.41±7.79	0.26	c
C12	03:27:32.43	- 28:10:07.80	10.28	72.16±7.79		c
C13	03:27:33.00	- 28:10:11.50	11.81	< 7.3		c
C14	03:27:34.01	- 28:46:21.30	133.2	104.3±10.46	0.25	c
C15	03:27:37.74	- 28:01:30.00	96.43	202.1±20.27	0.28	c
C16	03:27:46.87	- 27:17:43.00	11.58	223.6±22.44	0.34	c
C17	03:28:23.67	- 27:17:09.40	12.23	< 7.3		c
C18	03:28:24.57	- 28:40:21.70	11.07	14.73±1.61	0.1	c
C19	03:28:28.57	- 27:16:59.00	21.26	21.76±2.71		c
C20	03:28:32.80	- 28:55:36.30	17.26	42.90±4.31	0.25	c
Continued on next page						

Table A.1 – continued from previous page

ID	RA	DEC	$S_{1.4}$ / mJy	$S_{3.6}$ / μJy	sep	struc
C21	03:28:36.49	- 28:42:00.80	234.8	2215.80±222.45		nc
C22	03:28:36.59	- 28:41:45.50	1123.0	< 7.3		nc
C23	03:28:46.65	- 28:26:16.60	57.96	56.07±6.17		c
C24	03:29:13.84	- 27:23:27.90	46.16	< 7.3		nc
C25	03:29:16.22	- 27:23:40.20	80.34	< 7.3		nc
C26	03:29:23.23	- 28:55:12.00	28.82	133.5±13.47	0.3	c
C27	03:29:33.82	- 28:41:40.20	14.92	157.5±15.85	0.21	c
C28	03:29:41.23	- 28:08:11.50	22.98	141.3±14.23	0.18	c
C29	03:29:45.55	- 27:32:17.90	11.1	65.44±6.60	0.49	c
C30	03:29:48.94	- 27:31:48.90	18.94	23.19±2.87⟅15.59±2.09		c
C31	03:30:01.58	- 27:46:19.80	11.57	< 7.3		nc
C32	03:30:21.90	- 28:02:05.70	15.09	146.6±14.77	0.42	c
C33	03:30:34.66	- 28:27:06.50	18.61	24.56±3.02		c
C34	03:30:42.79	- 28:51:53.70	16.62	403.91±41.33		c
C35	03:30:47.66	- 28:38:54.60	59.12	237.23±24.82		c
C36	03:30:51.41	- 27:30:13.90	43.79	93.58±9.40	0.16	c
C37	03:30:55.62	- 28:48:52.40	10.46	49.68±5.02	0.29	c
C38	03:30:56.95	- 28:56:37.20	22.28	10.04±1.64⟅13.67±1.90		c
C39	03:31:24.89	- 27:52:08.30	35.5	169.29±17.53		c
C40	03:31:25.53	- 28:18:12.10	255.6	< 7.3		nc
C41	03:31:29.82	- 28:18:19.80	116.8	< 7.3		nc
C42	03:31:31.63	- 28:31:49.20	29.19	< 7.3		c
C43	03:31:33.94	- 28:31:21.10	50.34	< 7.3		c
C44	03:32:01.44	- 27:46:47.50	49.13	61.06±6.18	0.66	c
C45	03:32:10.03	- 27:26:39.80	16.58	< 7.3		nc
C46	03:32:10.71	- 27:26:35.50	17.4	777.5±77.81	0.46	nc
C47	03:32:26.98	- 27:41:06.70	16.62	290.34±29.62		c
C48	03:32:32.04	- 28:03:10.20	23.9	91.80±9.28	0.45	c
C49	03:32:33.36	- 28:37:43.60	24.35	167.97±17.48		c
C50	03:32:42.04	- 27:38:18.60	44.93	< 7.3		nc
C51	03:32:43.12	- 27:38:13.40	27.38	< 7.3		nc
C52	03:32:57.21	- 28:02:09.70	19.27	213.7±21.42	0.63	c
C53	03:33:10.19	- 27:48:42.00	19.25	48.06±4.91	0.41	c
C54	03:33:23.78	- 27:24:06.90	27.07	47.68±4.88	0.23	c
C55	03:33:47.58	- 28:55:36.40	82.79	1338.±133.92	0.17	c
C56	03:33:53.28	- 28:05:07.30	11.86	9.30±1.50		c
C57	03:33:56.01	- 27:24:53.70	12.55	< 7.3		nc
C58	03:34:06.69	- 28:41:42.40	10.53	45.99±5.18		c
C59	03:34:09.27	- 28:24:20.10	79.36	68.55±6.94	0.9	c
C60	03:34:13.76	- 28:35:47.40	13.15	18.55±1.99	0.69	c
C61	03:34:23.84	- 27:25:26.70	17.91	42.75±4.39	0.51	c
C62	03:34:26.66	- 27:17:29.40	30.99	< 7.3		c

Continued on next page

Table A.1 – continued from previous page

ID	RA	DEC	$S_{1.4}$ / mJy	$S_{3.6}$ / μJy	sep	struc
C63	03:34:26.91	- 27:44:01.70	51.3	206.3±20.69	0.25	c
C64	03:34:31.12	- 28:25:25.50	39.2	60.91±6.20	0.69	c
C65	03:34:33.88	- 27:18:12.60	10.03	< 7.3		c
C66	03:34:36.19	- 27:26:31.60	13.45	< 7.3		nc
C67	03:34:38.39	- 27:27:20.10	15.24	< 7.3		nc
C68	03:35:22.78	- 27:56:13.70	33.24	< 7.3		nc
C69	03:35:22.83	- 27:55:54.40	31.57	< 7.3		nc
C70	03:35:23.04	- 27:33:30.60	17.92	125.6±12.61	0.89	c
C71	03:35:27.50	- 27:19:50.70	93.53	159.9±16.09	0.15	c
C72$\star$	03:35:31.02	- 27:27:02.20	26.08	< 7.3		c
C73	03:35:37.53	- 27:50:57.80	16.43	25.54±2.68	0.26	c
C74	03:35:48.20	- 28:44:02.30	12.37	74.76±7.56	0.27	c
C75	03:35:49.15	- 27:49:18.50	10.97	600.1±60.06	0.58	c
C76	03:35:53.34	- 27:27:40.40	126.9	404.3±40.48	0.06	nc

Table A.2: ATLAS radio sources in the ELAIS-S1 field with radio flux > 10mJy cross-matched with the SWIRE survey. $S_{1.4}$ presents the radio flux at 1.4 GHz, $S_{3.6}$ and present the flux density at 3.6 μJy. The separation between the radio position and the near-infrared counterpart is also given (Sep) in arcsec, if the separation value is not shown the sources are not detected in the SWIRE catalogues. The structure of the radio sources are given for the compact (c) and not compact (nc). For the undetected sources in the SWIRE catalogues at at 3.6, the lower limit of 7.3 μJy is shown.The rms in ATLAS survey is 10-15 μJy. The $\star$ sign marks those which are not covered in the IRAC imaging and the $\wr$ sign shows either of both fluxes could be the ID.

ID	**RA**	**DEC**	$S_{1.4}$ / **mJy**	$S_{3.6}$ / μ**Jy**	**sep**	**struc**
ES1_01	00:30:39.68	-44:41:59.52	22.32	480.82±48.87		c
ES1_02	00:37:18.12	-44:30:11.53	51.23	116.065±12.18		c
ES1_03	00:37:17.52	-44:30:16.23	46.67	115.30±12.10		c
ES1_04	00:31:11.10	-44:28:57.89	21.42	105.49±11.12		c
ES1_05	00:39:42.45	-44:27:13.77	33.58	17.97 ±1.95	0.06	c
ES1_06	00:35:54.29	-44:26:55.04	33.76	38.3 ± 3.93	0.09	c
ES1_07	00:29:37.77	-44:23:17.62	31.69	< 7.3		c
ES1_08	00:37:23.32	-44:22:44.85	27.05	53.57 ± 5.41	0.32	c
ES1_09	00:32:49.31	-44:21:50.49	44.37	394.13 ± 39.47	0.11	c
ES1_10	00:33:12.20	-44:19:51.40	17.19	95.21 ± 9.59	0.59	c
ES1_11	00:36:38.54	-44:18:14.44	33.98	154.02 ± 15.50	0.55	c
ES1_12	00:30:47.73	-44:14:29.72	10.35	< 7.3		nc
ES1_13	00:32:04.41	-44:11:30.79	36.05	51.42± 5.20	0.12	c
ES1_14	00:37:20.81	-44:07:53.25	21.88	< 7.3		nc
ES1_15	00:37:19.72	-44:07:11.29	24.0	< 7.3		nc
ES1_16	00:38:36.90	-44:06:06.02	12.42	< 7.3		nc
ES1_17	00:34:58.58	-44:04:58.31	20.15	117.05 ± 11.80	0.23	c
ES1_18	00:39:40.36	-44:02:03.41	14.03	218.47±22.63		nc
ES1_19	00:39:39.63	-44:02:16.69	11.02	< 7.3		nc
ES1_20	00:33:09.26	-43:59:26.82	70.71	136.2±13.79	0.23	c
ES1_21	00:34:11.59	-43:58:17.04	21.36	< 7.3		c
ES1_22	00:34:59.05	-43:55:19.66	27.88	< 7.3		nc
ES1_23	00:34:57.74	-43:55:11.90	13.1	< 7.3		nc
ES1_24	00:31:38.63	-43:52:20.80	22.2	< 7.3		c
ES1_25	00:31:16.86	-43:50:54.24	10.79	24.87±2.58	0.20	c
ES1_26	00:39:03.48	-43:49:50.08	23.33	140.68±14.65		nc
ES1_27	00:36:40.21	-43:42:41.56	10.41	253.3±25.43	0.24	nc
ES1_28	00:31:28.83	-43:41:20.64	182.88	48.90±4.98	0.37	c
ES1_29	00:31:28.42	-43:41:32.18	34.88	< 7.3		nc
ES1_30	00:30:20.95	-43:39:42.89	49.58	274.4±27.51	0.26	c
ES1_31	00:38:41.58	-43:39:25.81	10.48	163.4±16.41	0.923	nc
ES1_32	00:36:16.52	-43:39:17.55	13.83	64.73±6.54	0.87	c
ES1_33	00:34:32.51	-43:33:55.79	13.64	31.64±3.28	0.63	c

Continued on next page

Table A.2 – continued from previous page

ID	RA	DEC	$S_{1.4}$ / mJy	$S_{3.6}$ / μJy	sep	struc
ES1_34	00:34:42.88	-43:30:34.36	55.13	91.01±9.20	0.39	c
ES1_35	00:29:46.53	-43:15:54.52	27.34	27.84±2.91	0.12	c
ES1_36	00:32:55.53	-43:16:27.15	16.1	22.24±2.78		c
ES1_37	00:32:47.06	-43:14:33.91	11.42	185.33±19.42		nc
ES1_38	00:31:11.86	-43:08:54.48	13.84	< 7.3		nc
ES1_39	00:36:16.71	-43:09:34.55	167.54	103.6±10.46	0.15	c
ES1_40	00:36:45.86	-43:05:47.39	31.77	< 7.3		c
ES1_41	00:39:15.12	-43:04:28.56	14.4	< 7.3		nc
ES1_42	00:34:22.58	-43:01:31.44	12.08	< 7.3		nc
ES1_43	00:35:08.38	-43:00:04.20	33.18	51.50±5.82		c
ES1_44	00:39:28.27	-42:58:56.51	60.82	< 7.3		c
ES1_45	00:39:24.24	-42:59:02.72	58.38	< 7.3		c
ES1_46	00:32:30.75	-42:58:45.66	29.42	89.33±9.00	0.90	c
ES1_47	00:37:30.00	-42:57:13.23	11.48	< 7.3		nc
ES1_48	00:37:27.08	-42:57:25.49	19.32	< 7.3		nc
ES1_49	00:35:47.97	-42:56:55.40	23.19	18.92±1.98	0.08	c
ES1_50	00:36:58.42	-42:49:55.00	17.37	67.86±6.84	0.59	c

Appendix B

Overlays

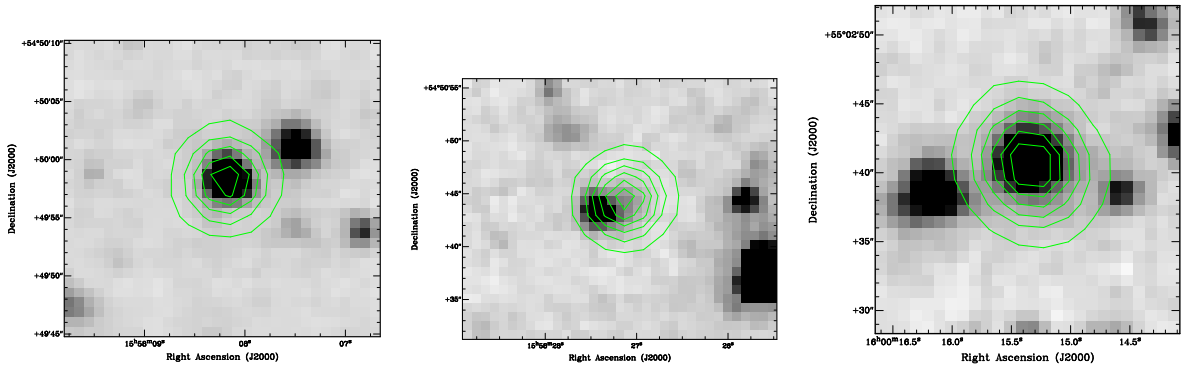

(a) en1-1 (b) en1-2 (c) en1-3

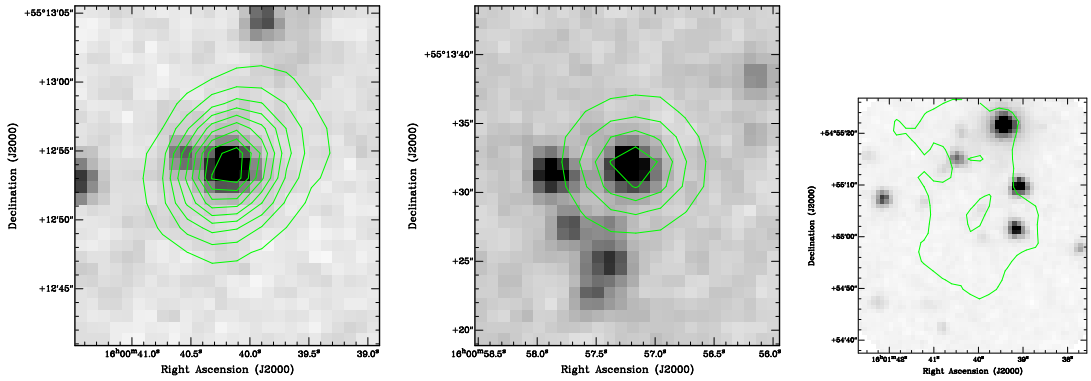

(d) en1-4 (e) en1-5 (f) en1-6

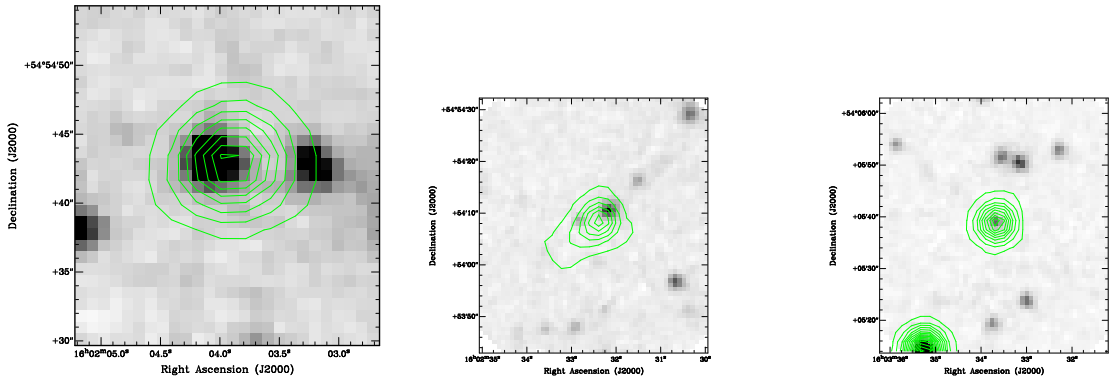

(g) en1-7 (h) en1-8 (i) en1-9

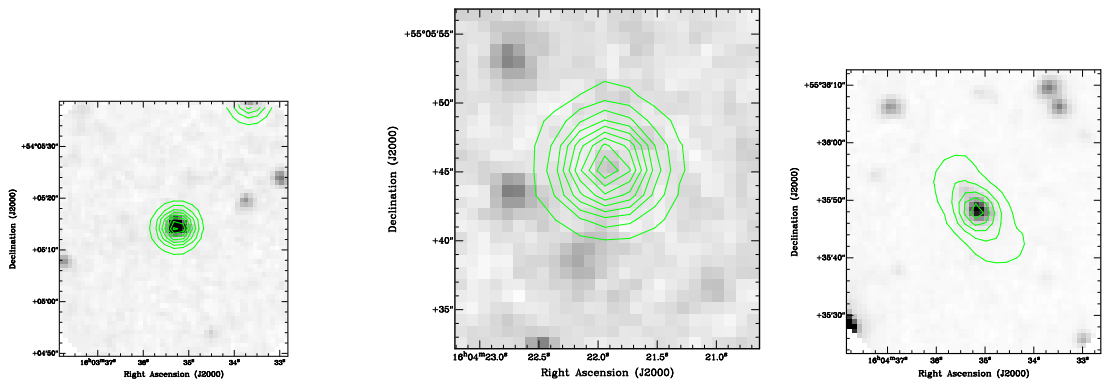

(j) en1-10 (k) en1-11 (l) en1-12

Figure B.1: The IRAC-3.6μm images from SWIRE in the Elais-N1 field, overlaid with the radio image from FIRST.

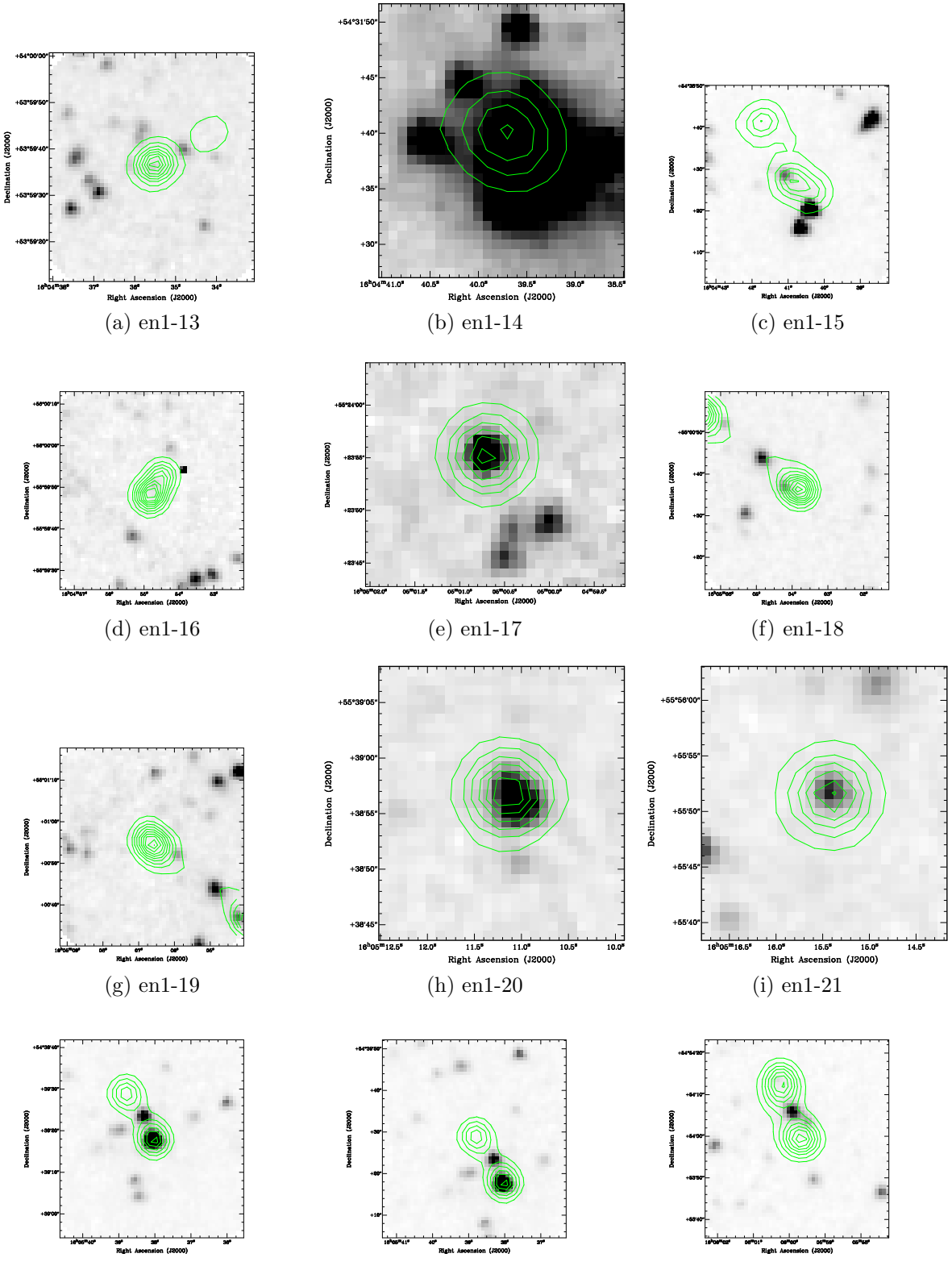

(a) en1-13 (b) en1-14 (c) en1-15

(d) en1-16 (e) en1-17 (f) en1-18

(g) en1-19 (h) en1-20 (i) en1-21

(j) en1-22 (k) en1-23 (l) en1-24

Figure B.2: The IRAC-3.6μm images from SWIRE in the Elais-N1 field, overlaid with the radio image from FIRST.

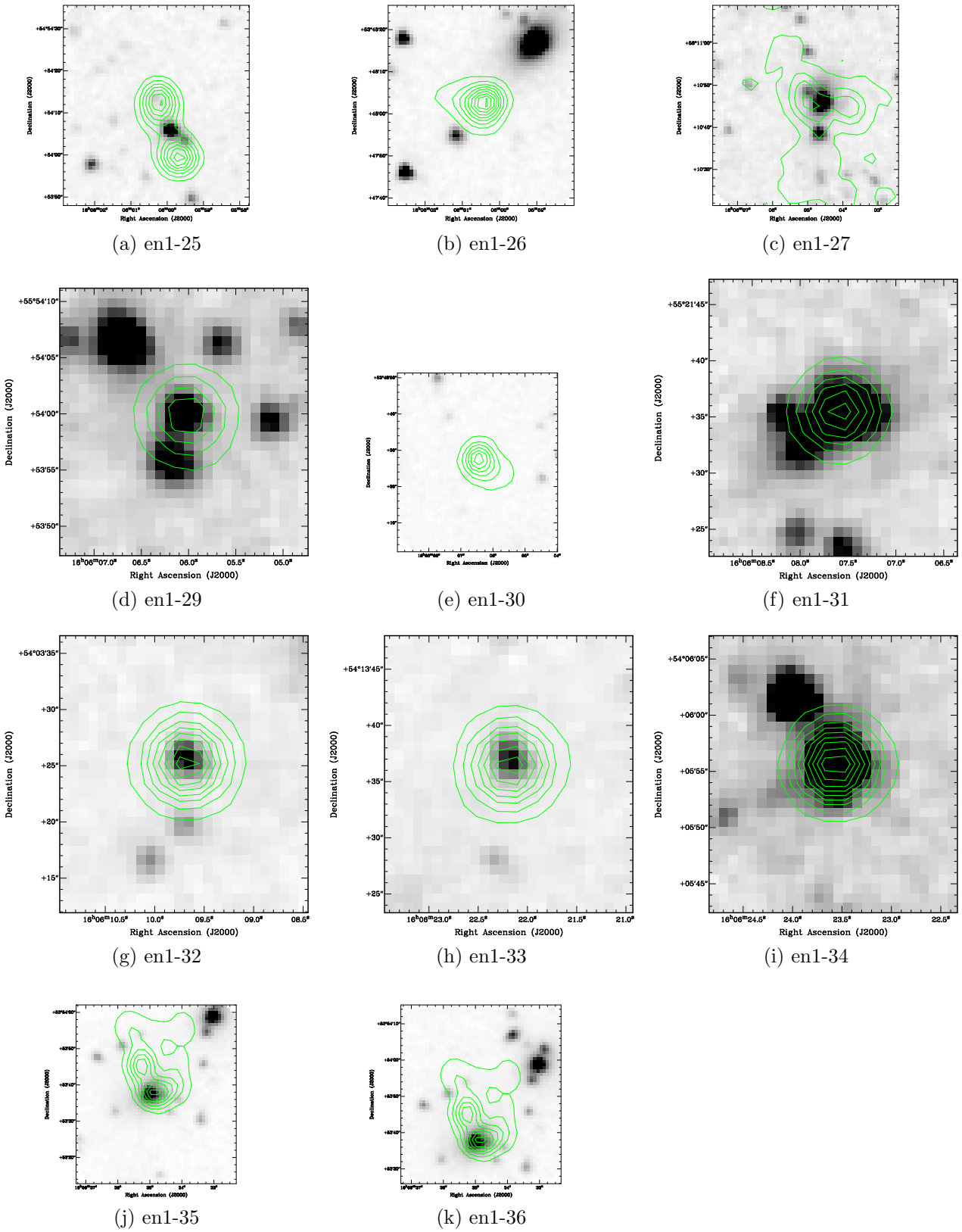

(a) en1-25 (b) en1-26 (c) en1-27

(d) en1-29 (e) en1-30 (f) en1-31

(g) en1-32 (h) en1-33 (i) en1-34

(j) en1-35 (k) en1-36

Figure B.3: The IRAC-3.6μm images from SWIRE in the Elais-N1 field, overlaid with the radio image from FIRST.

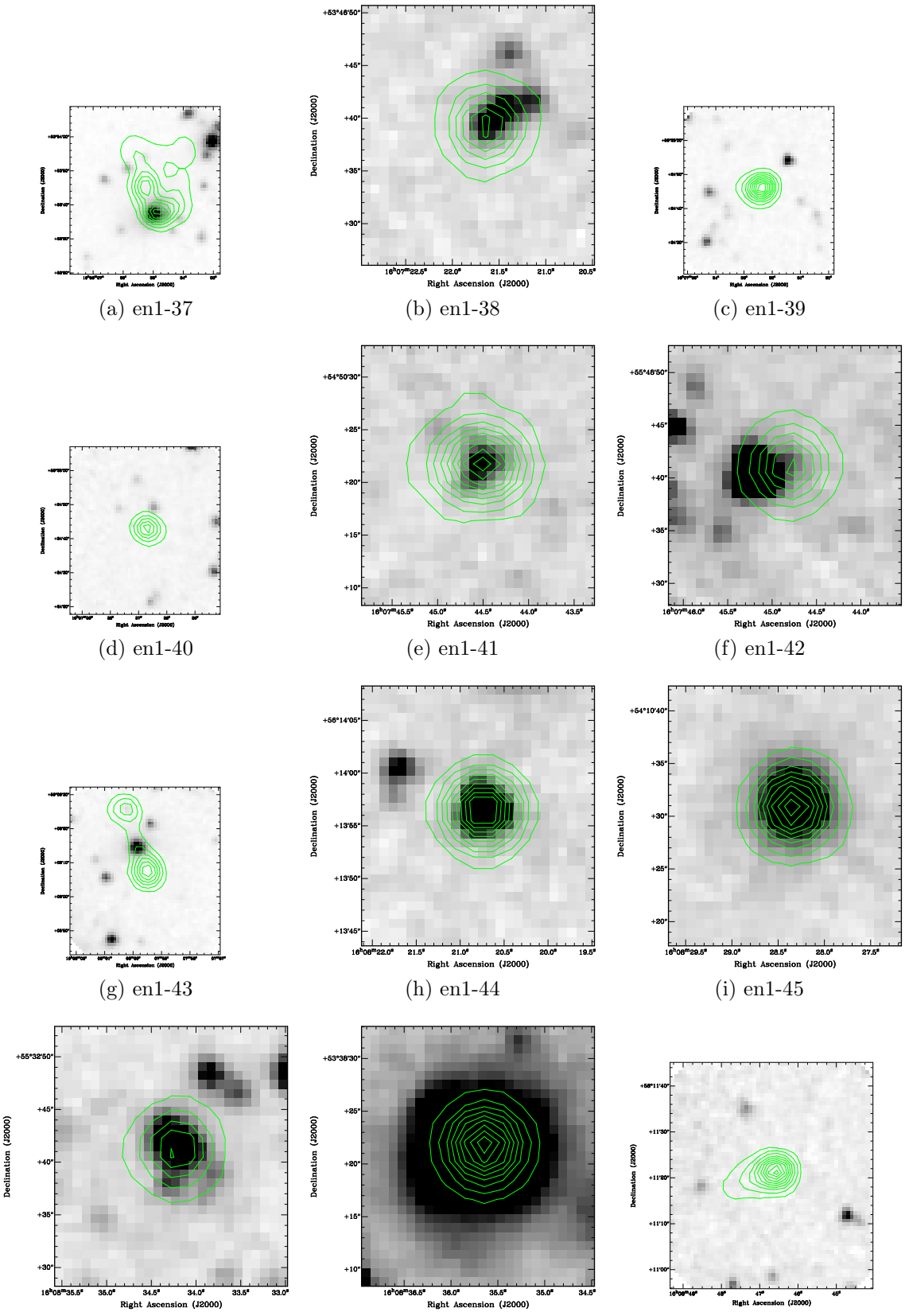

(a) en1-37 (b) en1-38 (c) en1-39

(d) en1-40 (e) en1-41 (f) en1-42

(g) en1-43 (h) en1-44 (i) en1-45

(j) en1-46 (k) en1-47 (l) en1-48

Figure B.4: The IRAC-3.6μm images from SWIRE in the Elais-N1 field, overlaid with the radio image from FIRST.

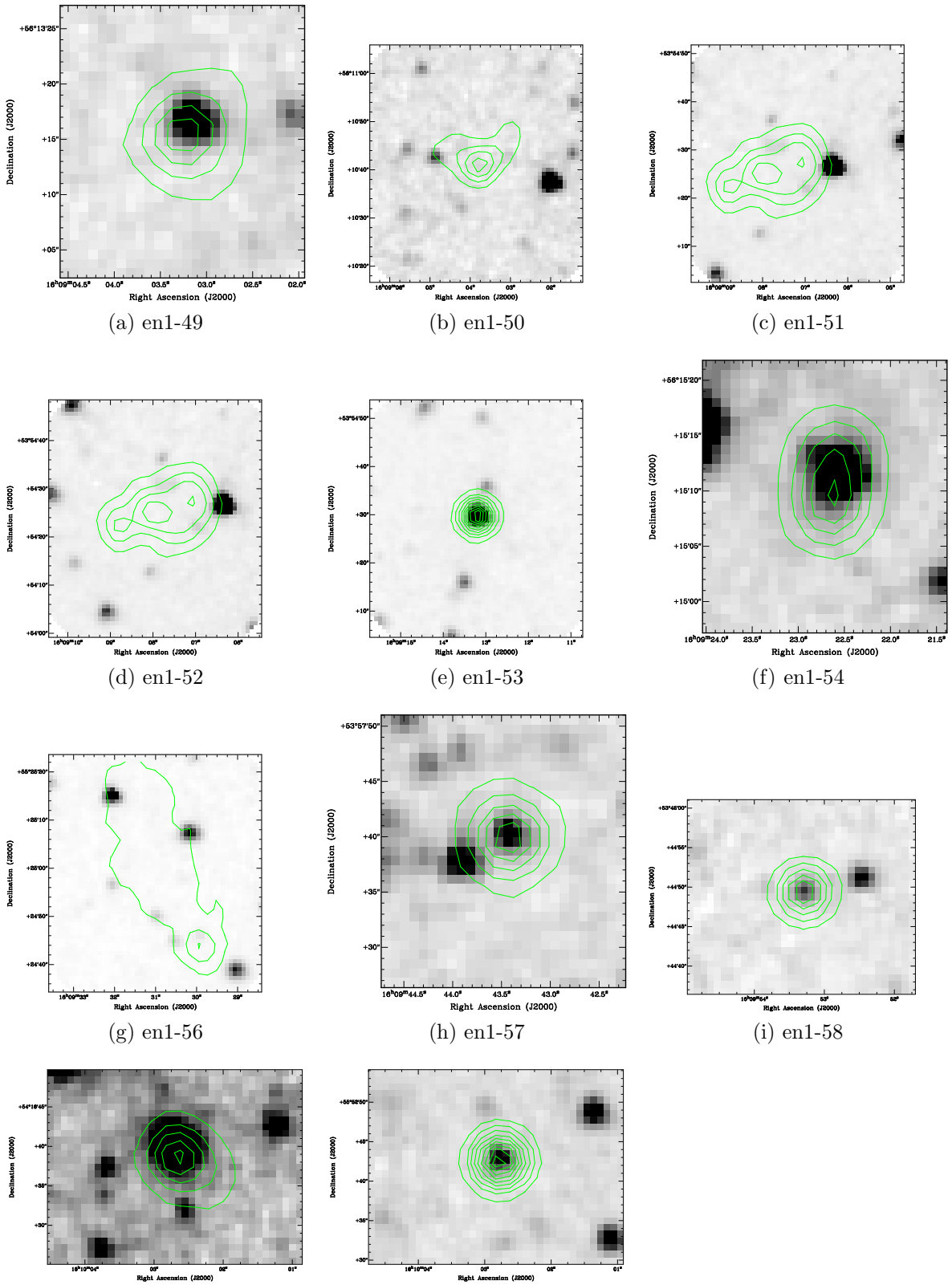

(a) en1-49 (b) en1-50 (c) en1-51

(d) en1-52 (e) en1-53 (f) en1-54

(g) en1-56 (h) en1-57 (i) en1-58

(j) en1-59 (k) en1-60

Figure B.5: The IRAC-3.6μm images from SWIRE in the Elais-N1 field, overlaid with the radio image from FIRST.

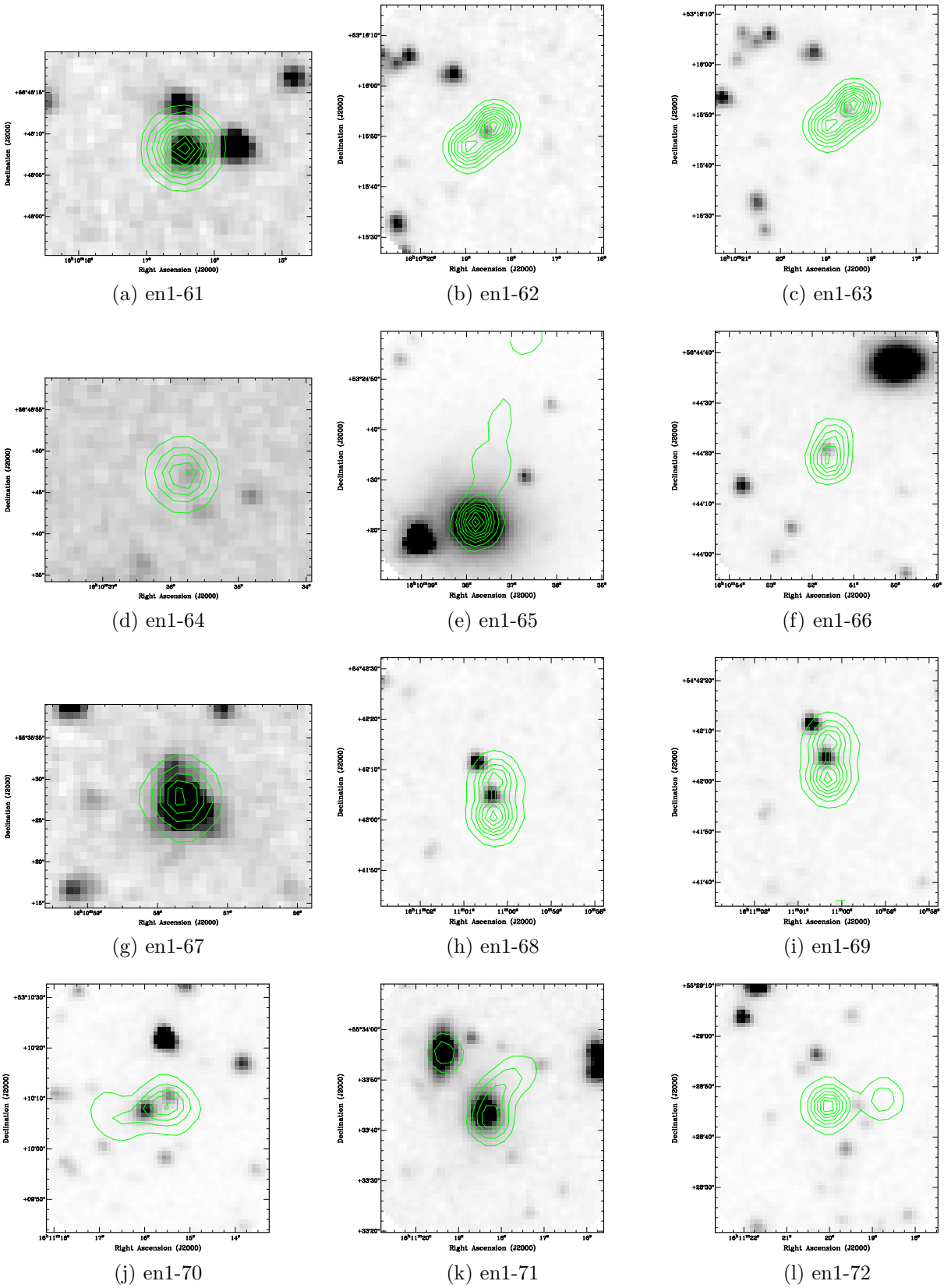

(a) en1-61 (b) en1-62 (c) en1-63

(d) en1-64 (e) en1-65 (f) en1-66

(g) en1-67 (h) en1-68 (i) en1-69

(j) en1-70 (k) en1-71 (l) en1-72

Figure B.6: The IRAC-3.6μm images from SWIRE in the Elais-N1 field, overlaid with the radio image from FIRST.

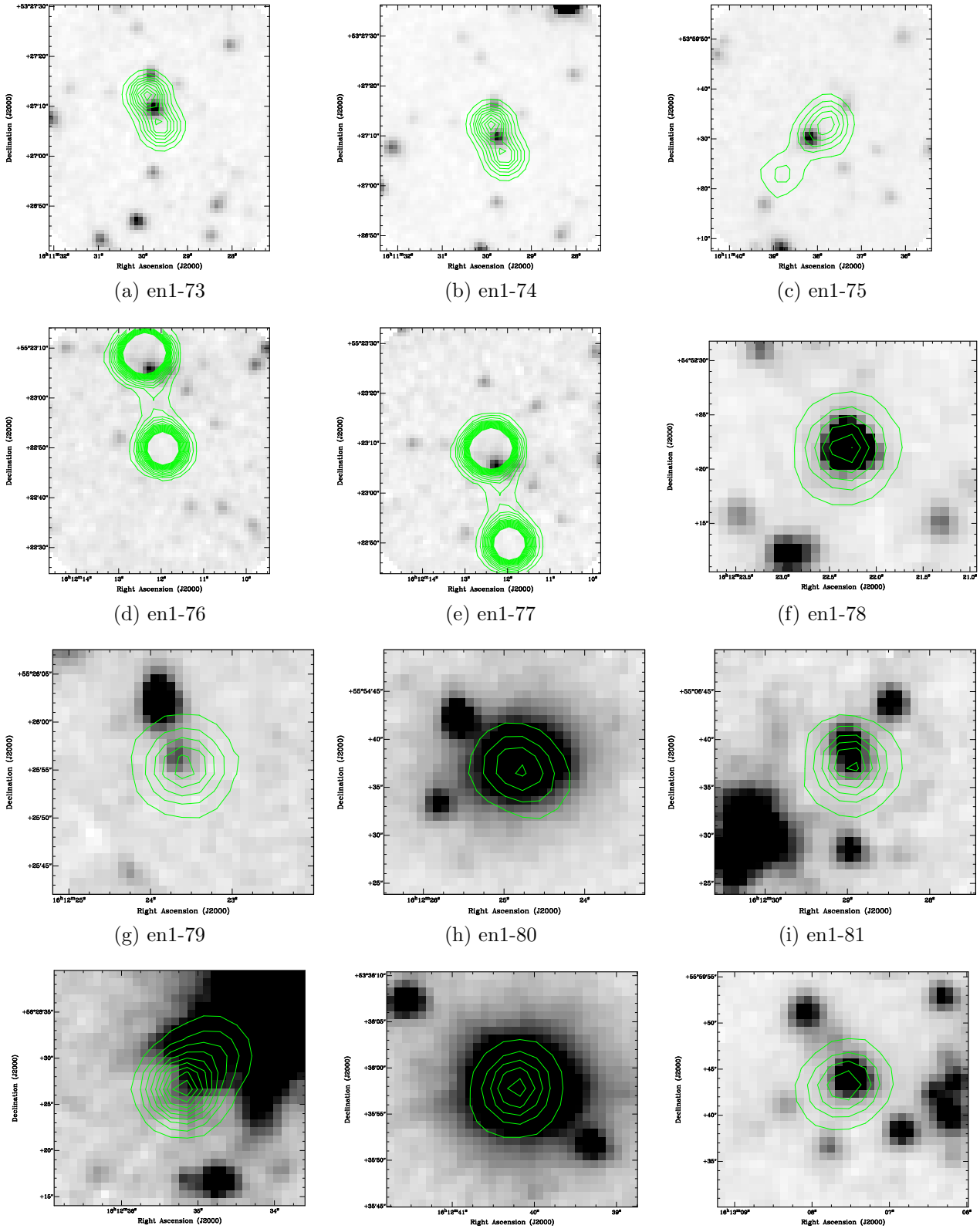

(a) en1-73 (b) en1-74 (c) en1-75

(d) en1-76 (e) en1-77 (f) en1-78

(g) en1-79 (h) en1-80 (i) en1-81

(j) en1-82 (k) en1-83 (l) en1-84

Figure B.7: The IRAC-3.6μm images from SWIRE in the Elais-N1 field, overlaid with the radio image from FIRST.

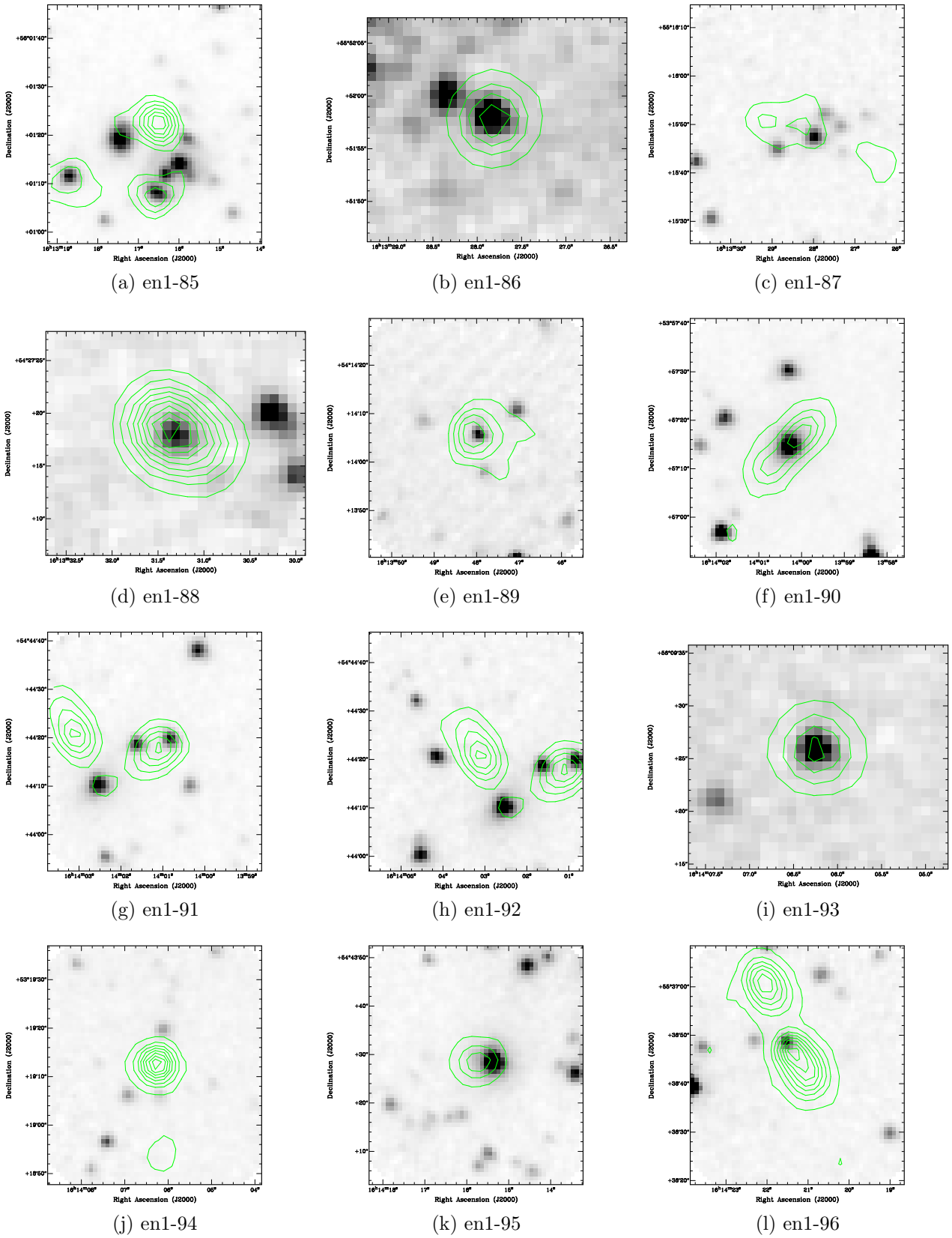

(a) en1-85 (b) en1-86 (c) en1-87

(d) en1-88 (e) en1-89 (f) en1-90

(g) en1-91 (h) en1-92 (i) en1-93

(j) en1-94 (k) en1-95 (l) en1-96

Figure B.8: The IRAC-3.6μm images from SWIRE in the Elais-N1 field, overlaid with the radio image from FIRST.

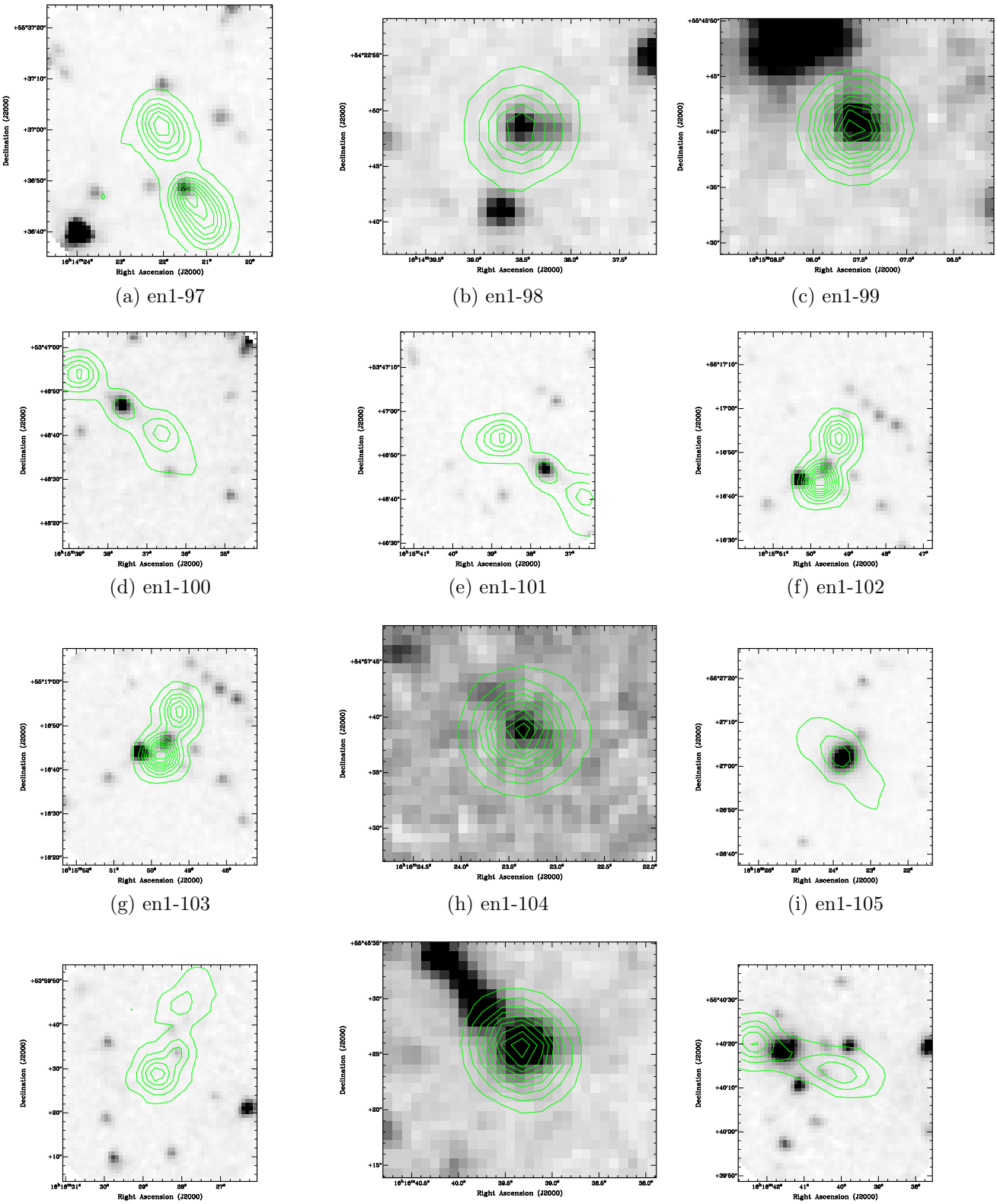

(a) en1-97 (b) en1-98 (c) en1-99

(d) en1-100 (e) en1-101 (f) en1-102

(g) en1-103 (h) en1-104 (i) en1-105

(j) en1-106 (k) en1-107 (l) en1-108

Figure B.9: The IRAC-3.6μm images from SWIRE in the Elais-N1 field, overlaid with the radio image from FIRST.

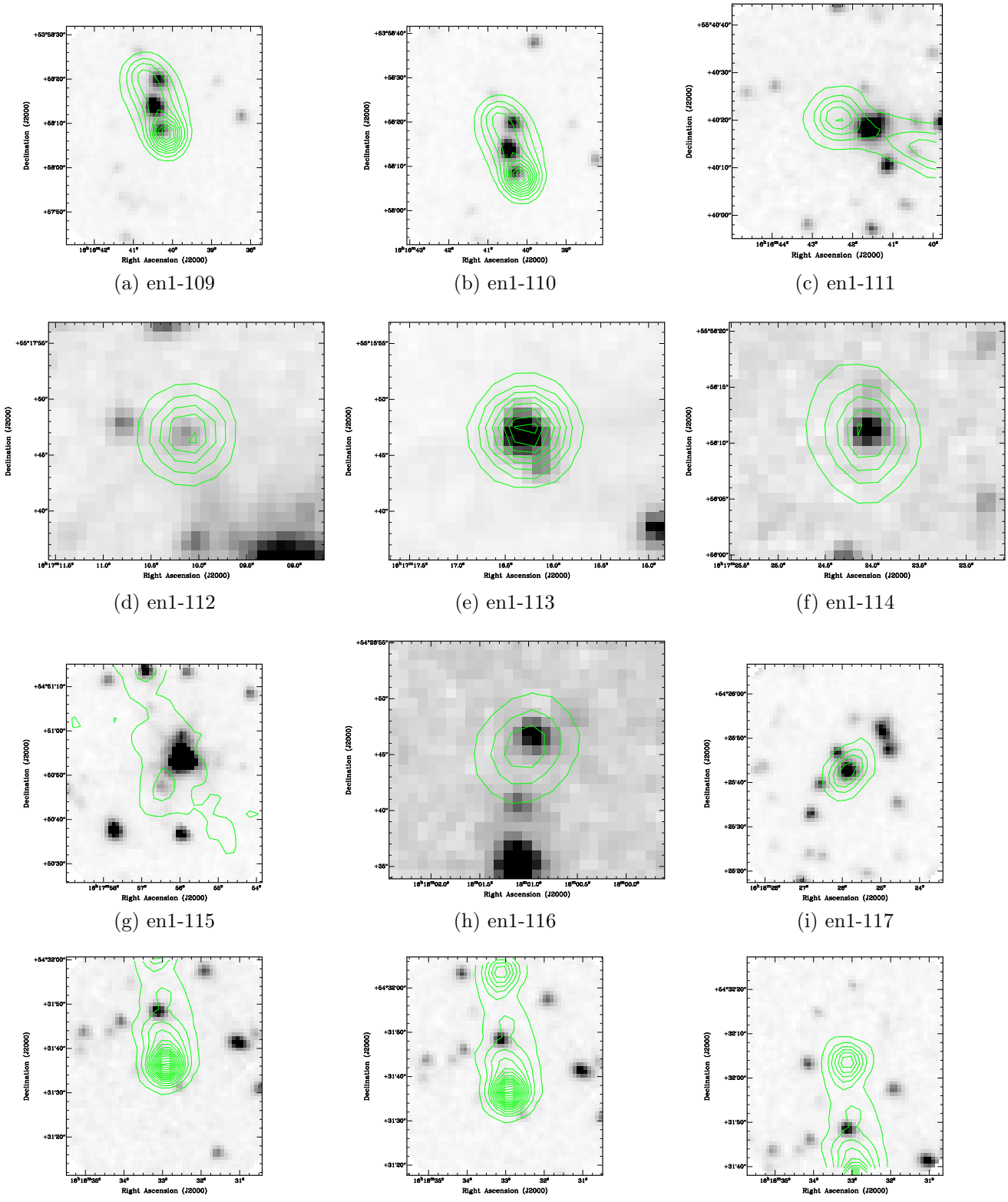

(a) en1-109 (b) en1-110 (c) en1-111

(d) en1-112 (e) en1-113 (f) en1-114

(g) en1-115 (h) en1-116 (i) en1-117

(j) en1-118 (k) en1-119 (l) en1-120

Figure B.10: The IRAC-3.6μm images from SWIRE in the Elais-N1 field, overlaid with the radio image from FIRST.

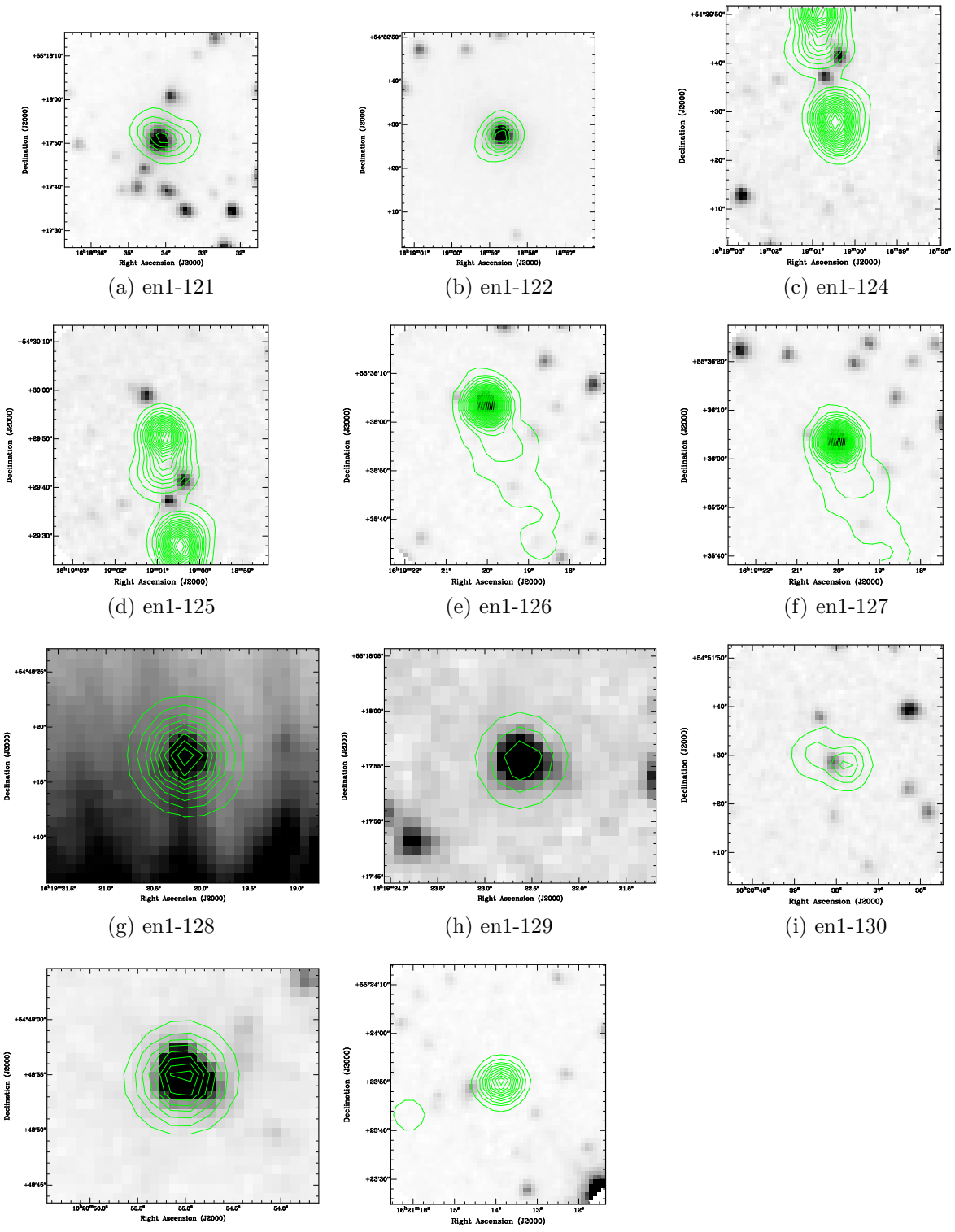

(a) en1-121 (b) en1-122 (c) en1-124

(d) en1-125 (e) en1-126 (f) en1-127

(g) en1-128 (h) en1-129 (i) en1-130

(j) en1-131 (k) en1-132

Figure B.11: The IRAC-3.6μm images from SWIRE in the Elais-N1 field, overlaid with the radio image from FIRST.

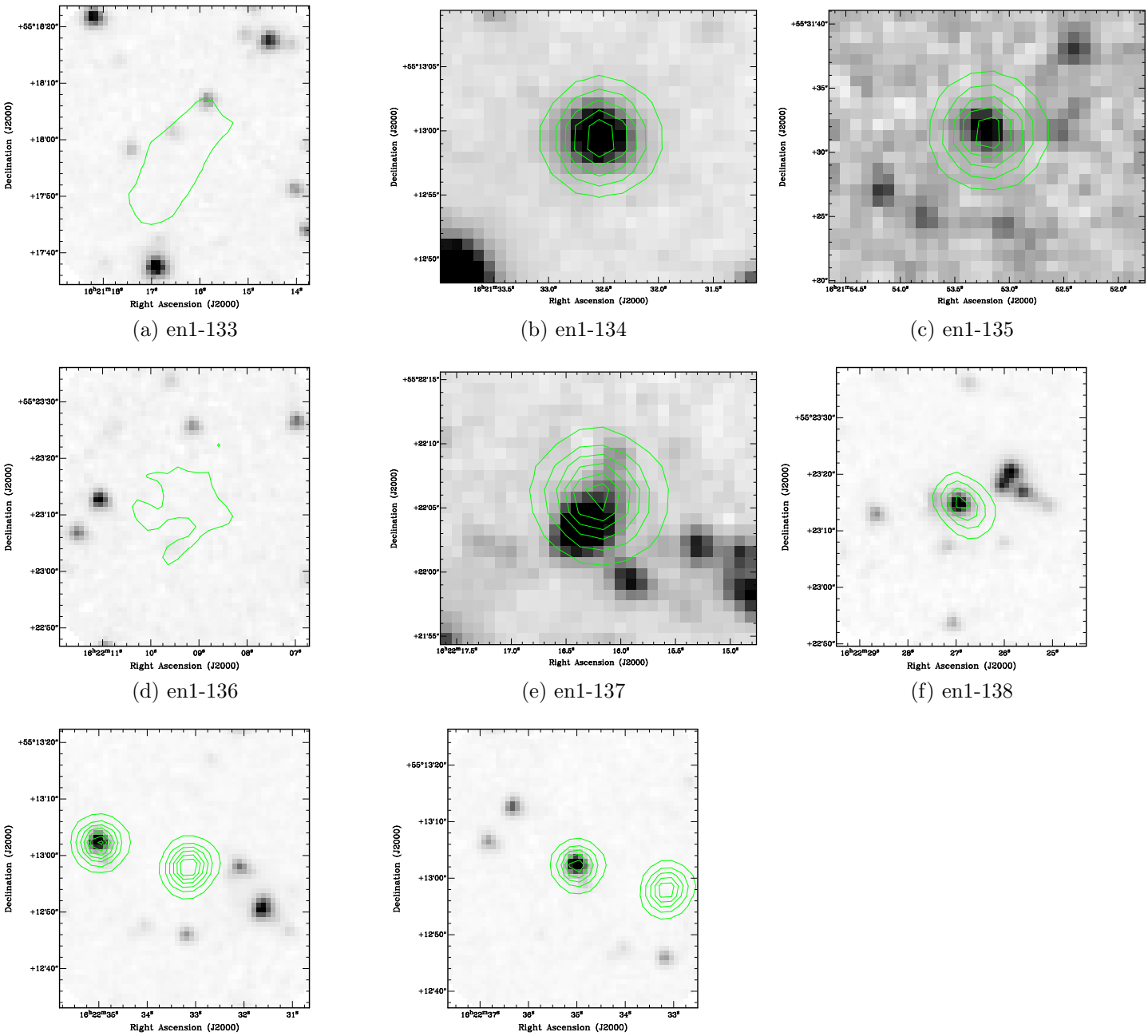

(a) en1-133 (b) en1-134 (c) en1-135

(d) en1-136 (e) en1-137 (f) en1-138

(g) en1-139 (h) en1-140

Figure B.12: The IRAC-3.6μm images from SWIRE in the Elais-N1 field, overlaid with the radio image from FIRST.

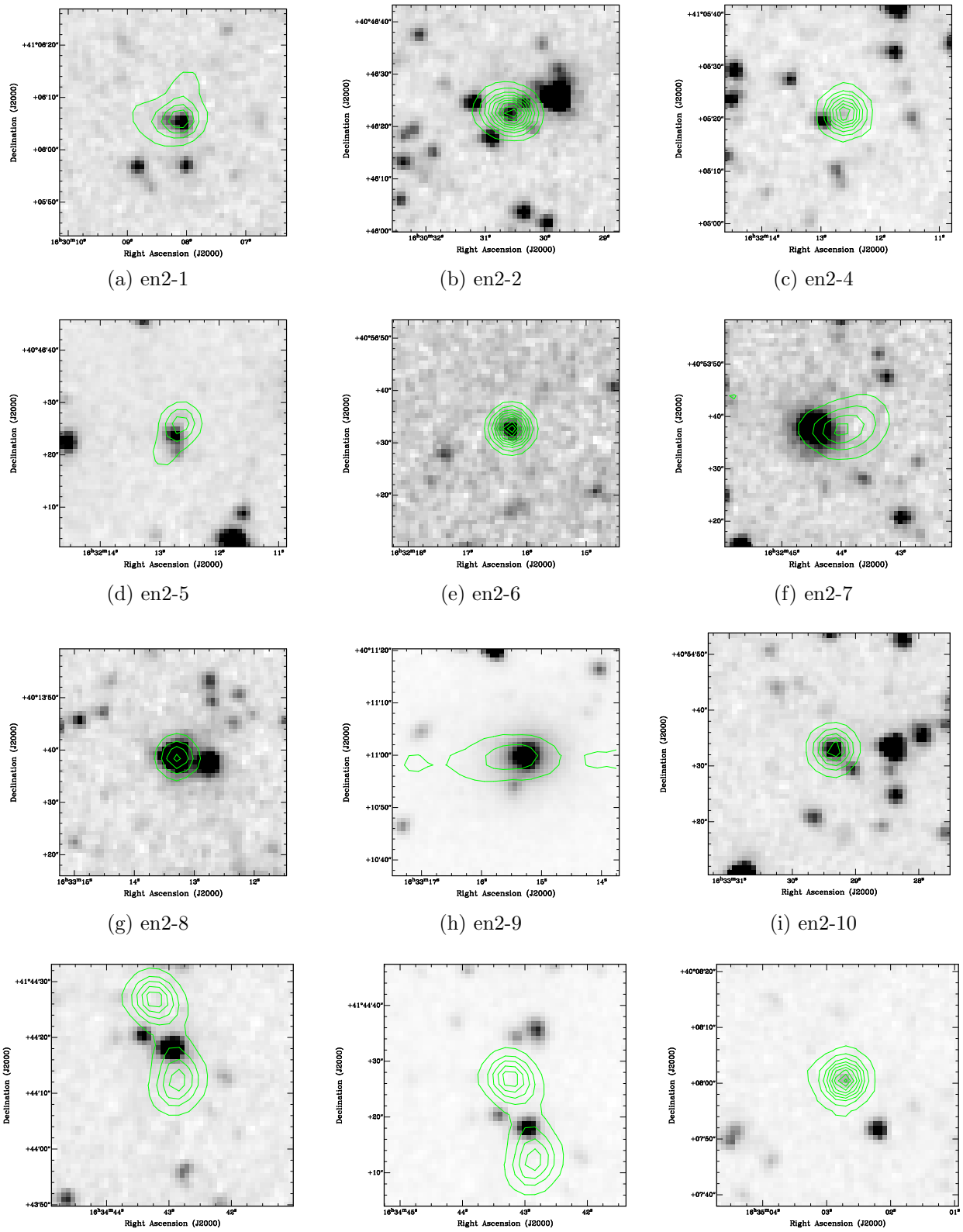

(a) en2-1 (b) en2-2 (c) en2-4

(d) en2-5 (e) en2-6 (f) en2-7

(g) en2-8 (h) en2-9 (i) en2-10

(j) en2-11 (k) en2-12 (l) en2-13

Figure B.13: The IRAC-3.6μm images from SWIRE in the Elais-N2 field, overlaid with the radio image from FIRST.

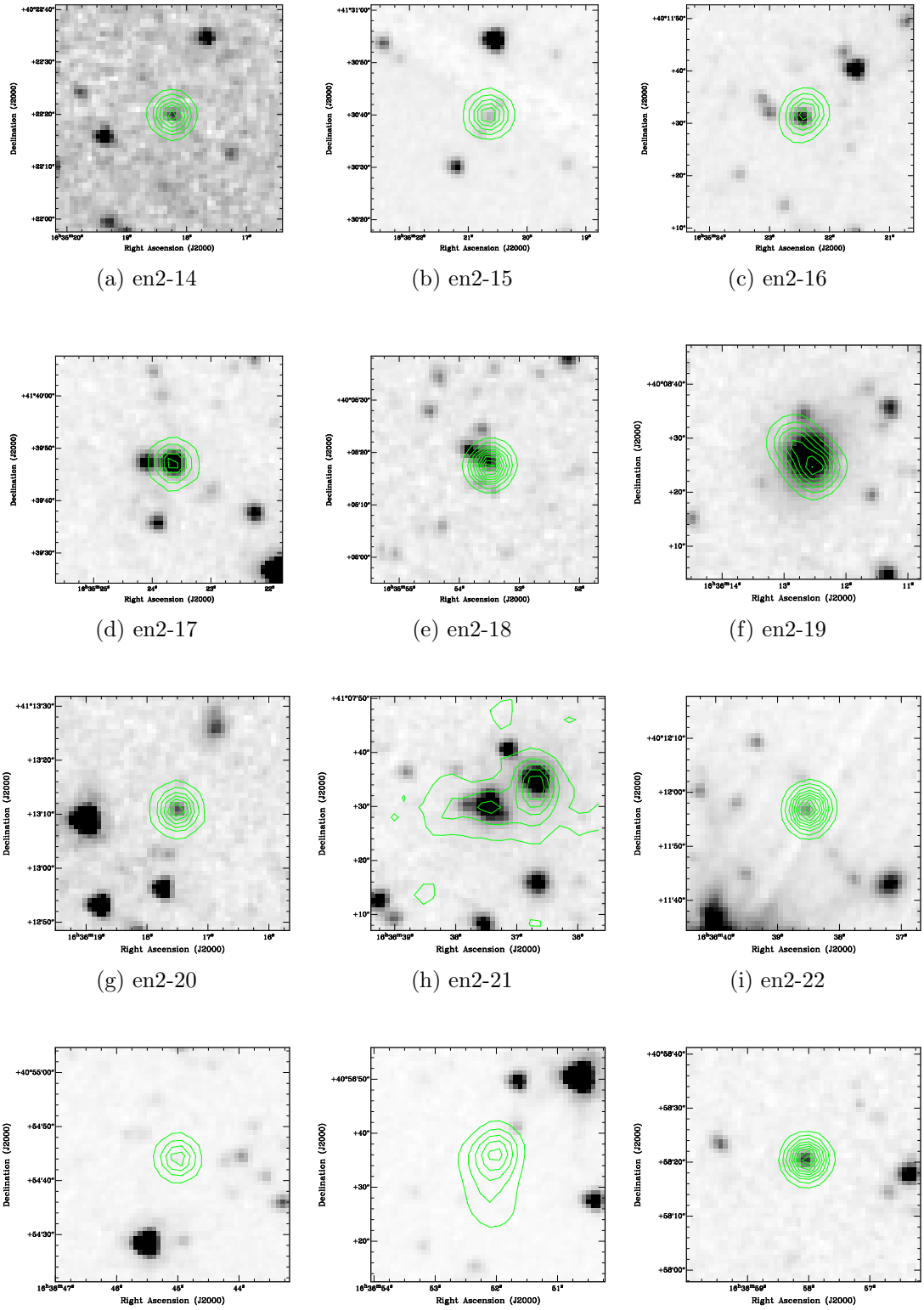

(a) en2-14 (b) en2-15 (c) en2-16

(d) en2-17 (e) en2-18 (f) en2-19

(g) en2-20 (h) en2-21 (i) en2-22

(j) en2-23 (k) en2-24 (l) en2-25

Figure B.14: The IRAC-3.6μm images from SWIRE in the Elais-N2 field, overlaid with the radio image from FIRST.

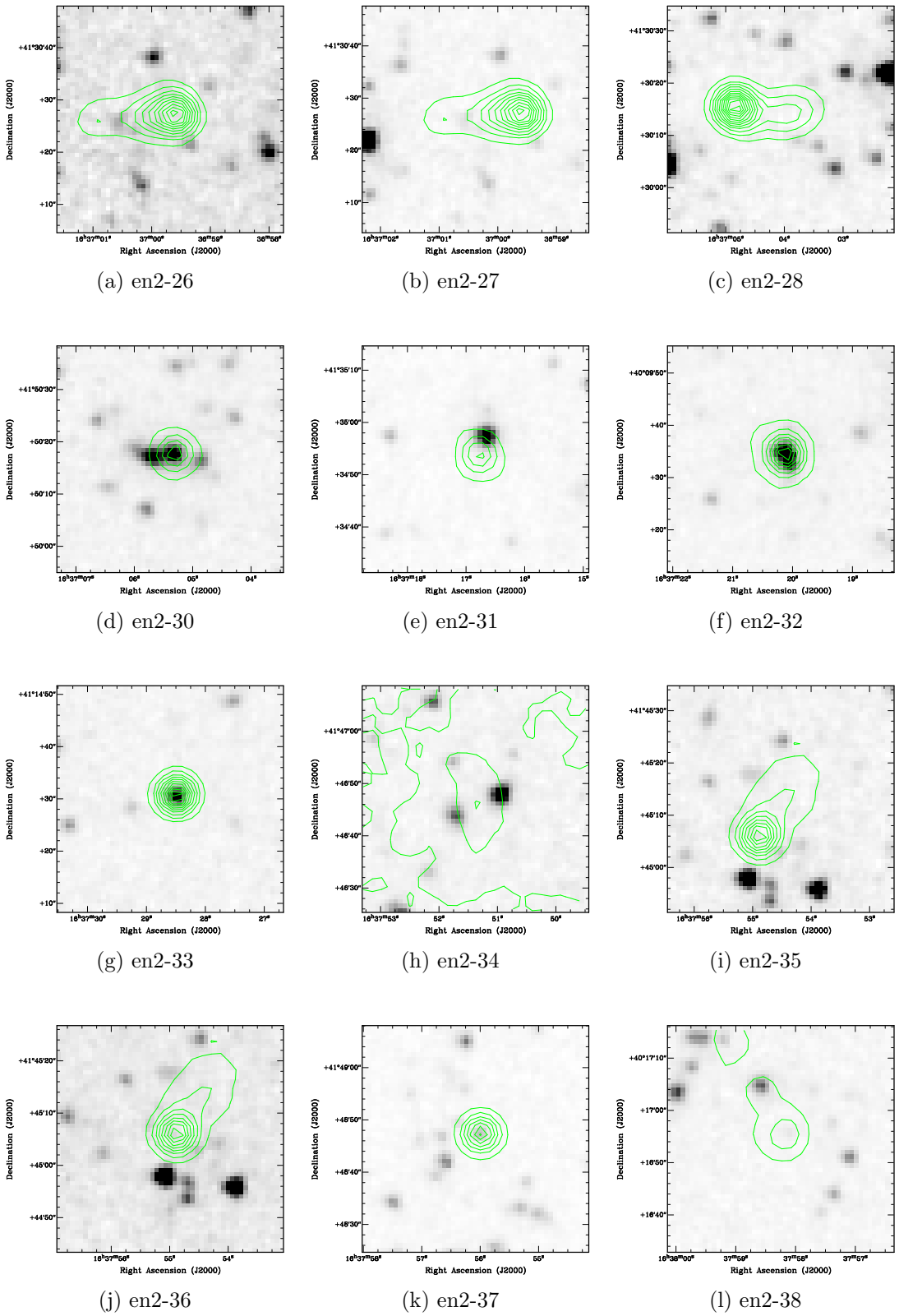

(a) en2-26 (b) en2-27 (c) en2-28

(d) en2-30 (e) en2-31 (f) en2-32

(g) en2-33 (h) en2-34 (i) en2-35

(j) en2-36 (k) en2-37 (l) en2-38

Figure B.15: The IRAC-3.6μm images from SWIRE in the Elais-N2 field, overlaid with the radio image from FIRST.

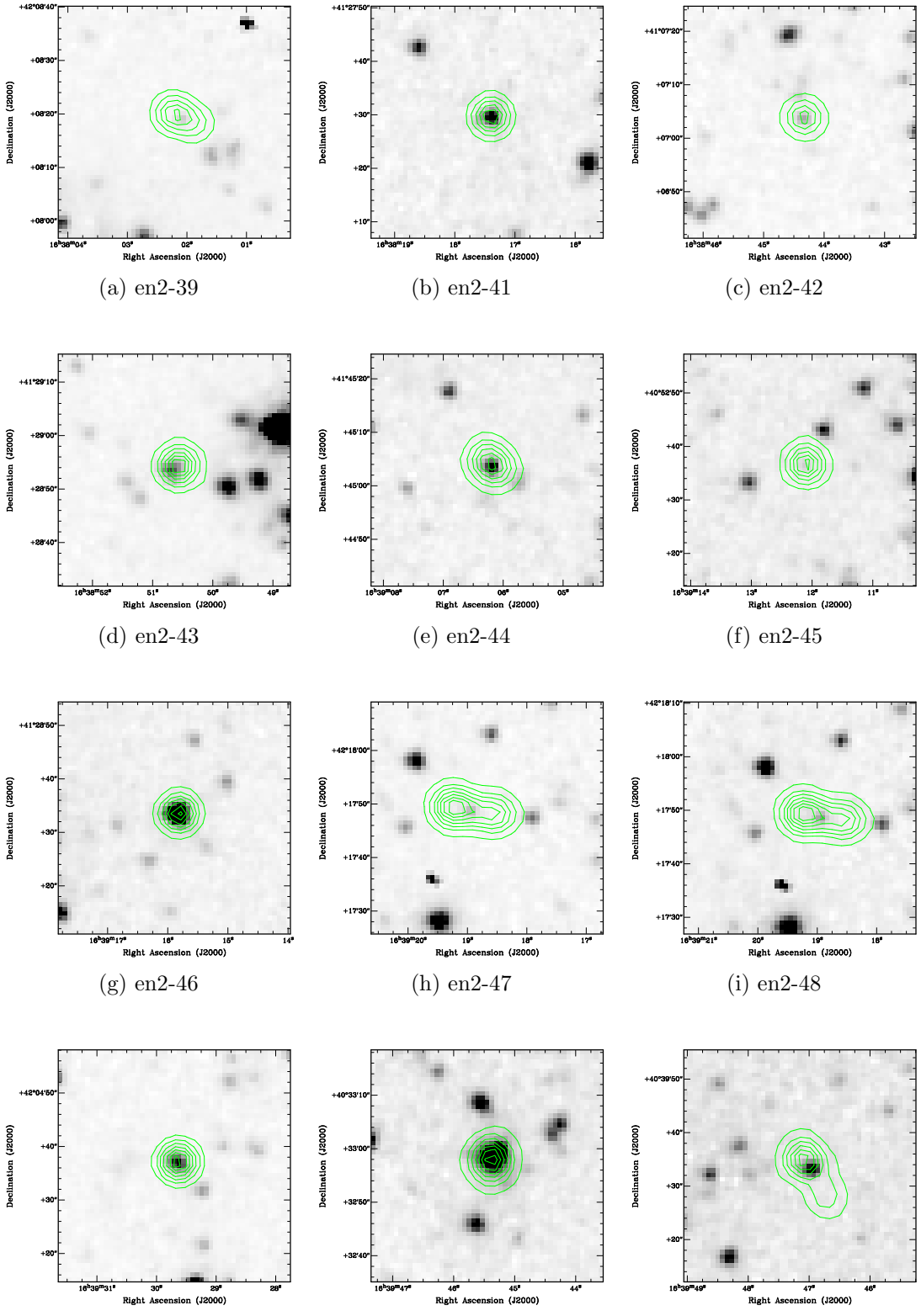

(a) en2-39 (b) en2-41 (c) en2-42

(d) en2-43 (e) en2-44 (f) en2-45

(g) en2-46 (h) en2-47 (i) en2-48

(j) en2-49 (k) en2-50 (l) en2-51

Figure B.16: The IRAC-3.6μm images from SWIRE in the Elais-N2 field, overlaid with the radio image from FIRST.

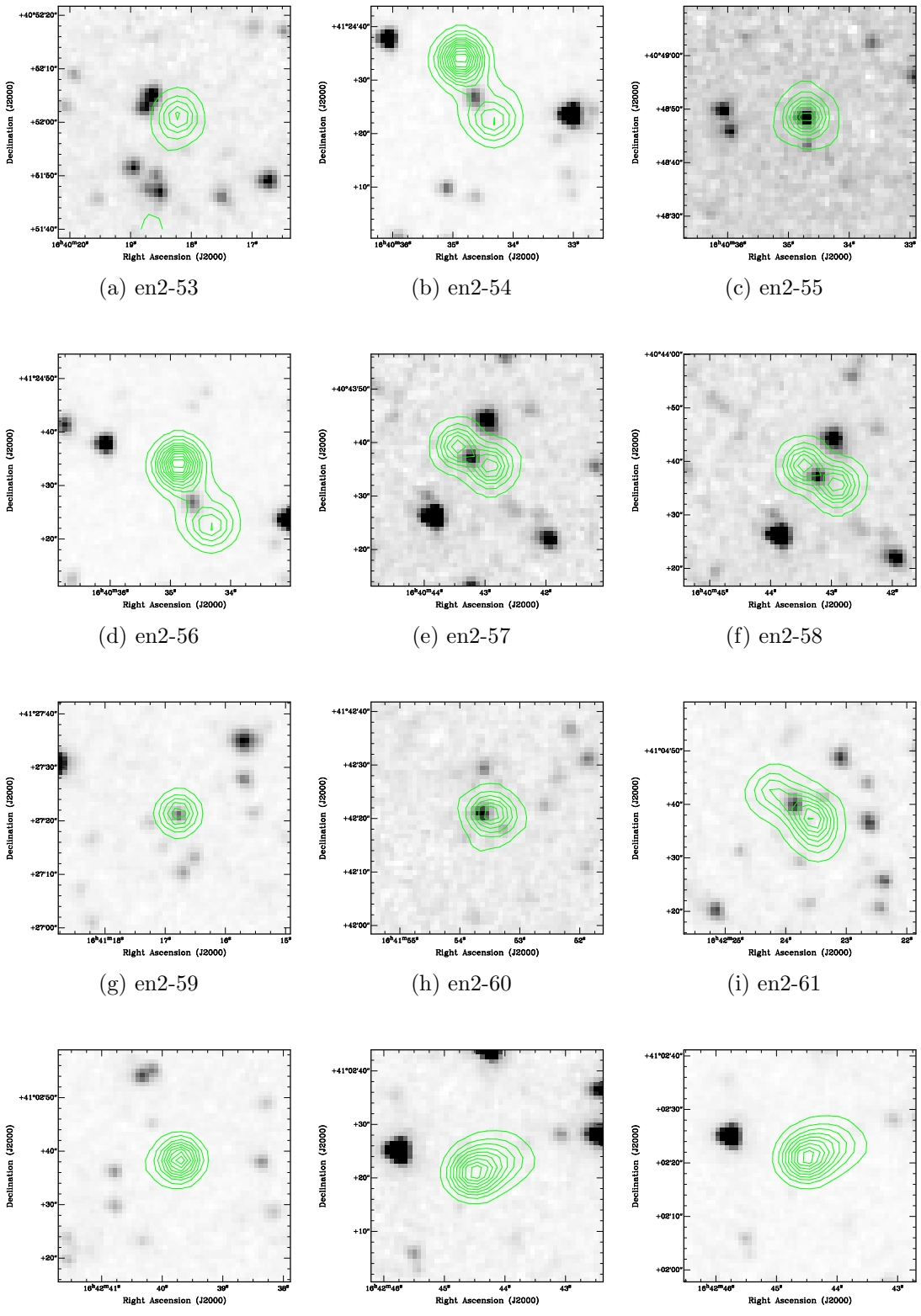

(a) en2-53 (b) en2-54 (c) en2-55

(d) en2-56 (e) en2-57 (f) en2-58

(g) en2-59 (h) en2-60 (i) en2-61

(j) en2-62 (k) en2-63 (l) en2-64

Figure B.17: The IRAC-3.6μm images from SWIRE in the Elais-N2 field, overlaid with the radio image from FIRST.

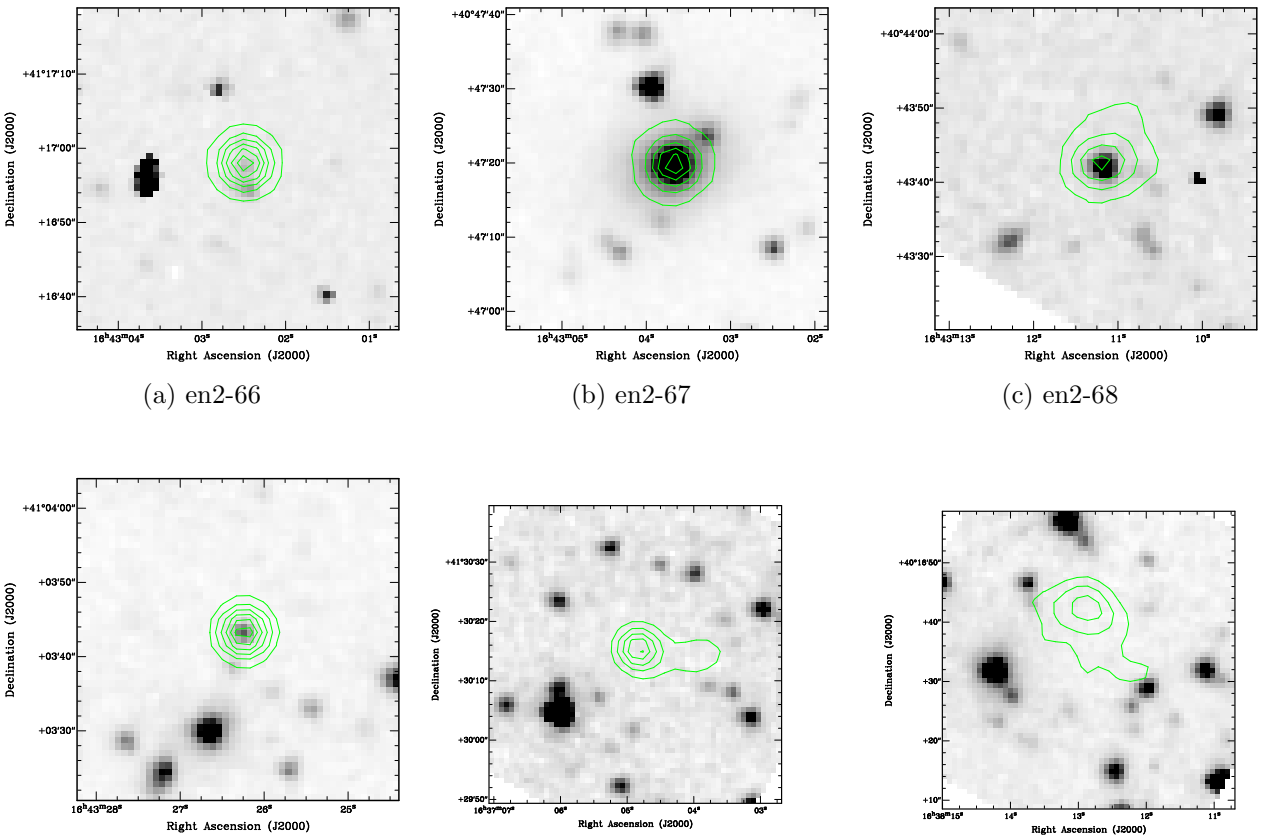

(a) en2-66 (b) en2-67 (c) en2-68

(d) en2-69 (e) en2-29 (f) en2-40

Figure B.18: The IRAC-3.6μm images from SWIRE in the Elais-N2 field, overlaid with the radio image from FIRST.

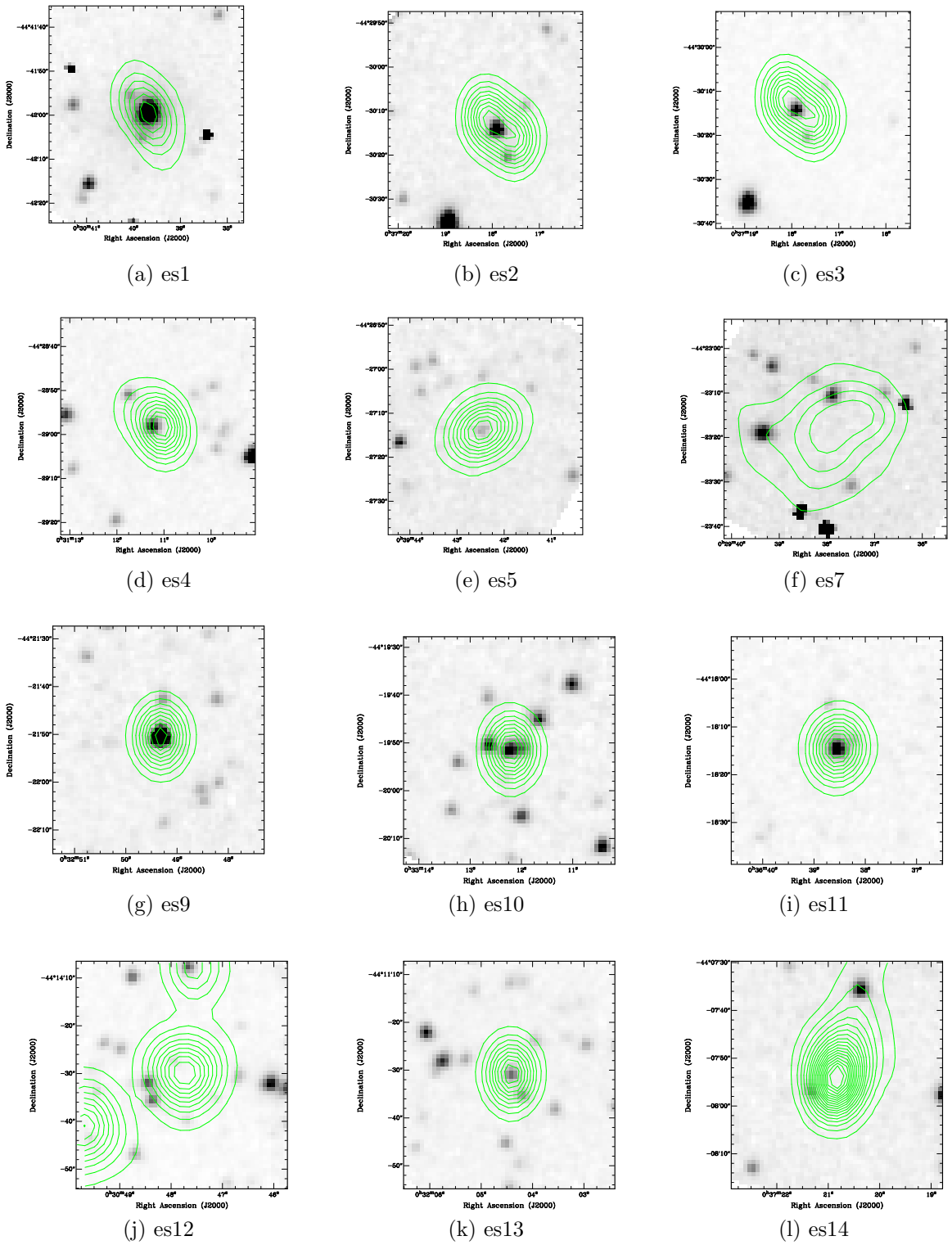

(a) es1 (b) es2 (c) es3

(d) es4 (e) es5 (f) es7

(g) es9 (h) es10 (i) es11

(j) es12 (k) es13 (l) es14

Figure B.19: The IRAC-3.6μm images from SWIRE in the Elais-S1 field, overlaid with the radio image from ATLAS.

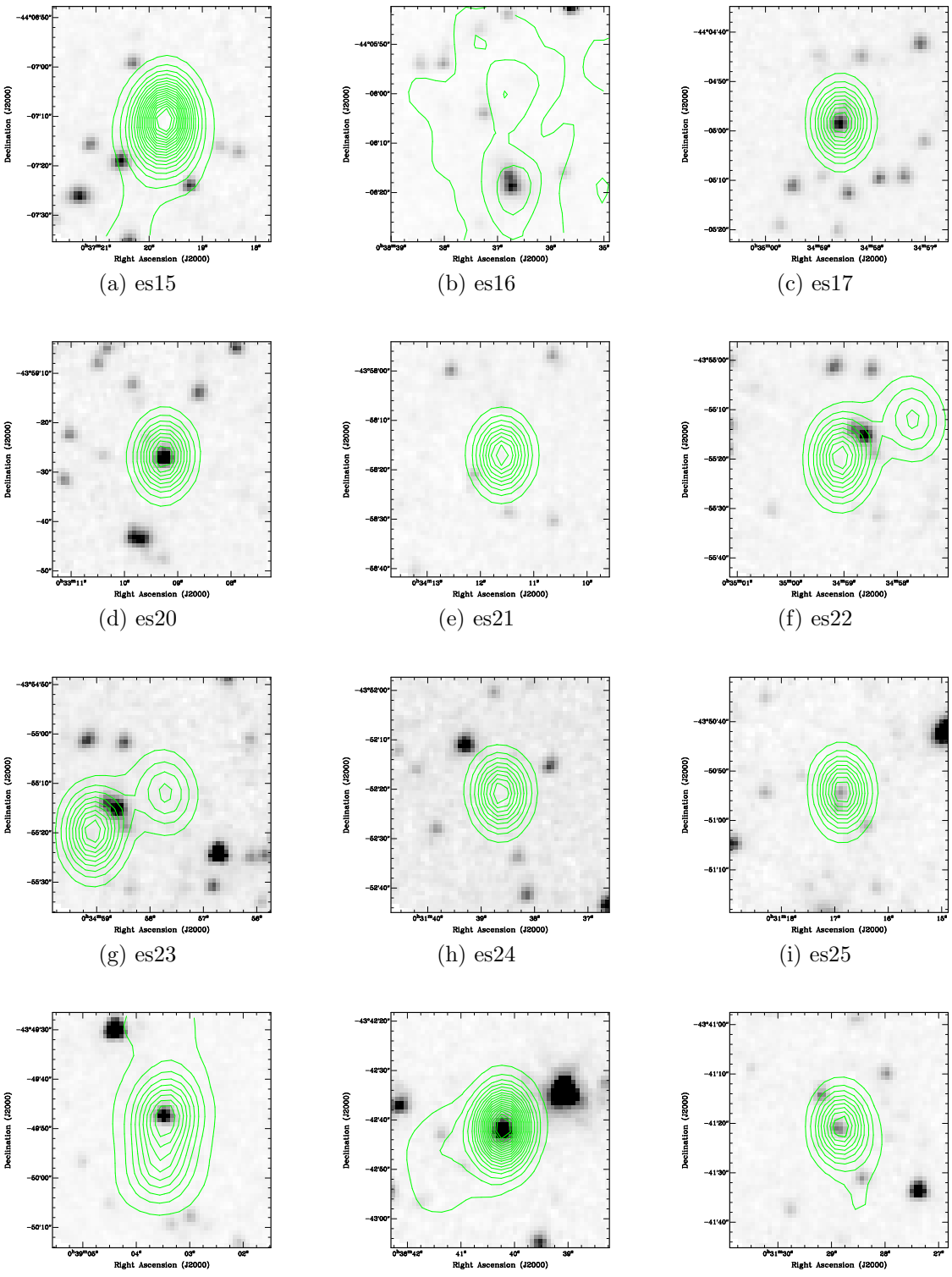

(a) es15 (b) es16 (c) es17

(d) es20 (e) es21 (f) es22

(g) es23 (h) es24 (i) es25

(j) es26 (k) es27 (l) es28

Figure B.20: The IRAC-3.6μm images from SWIRE in the Elais-S1 field, overlaid with the radio image from ATLAS.

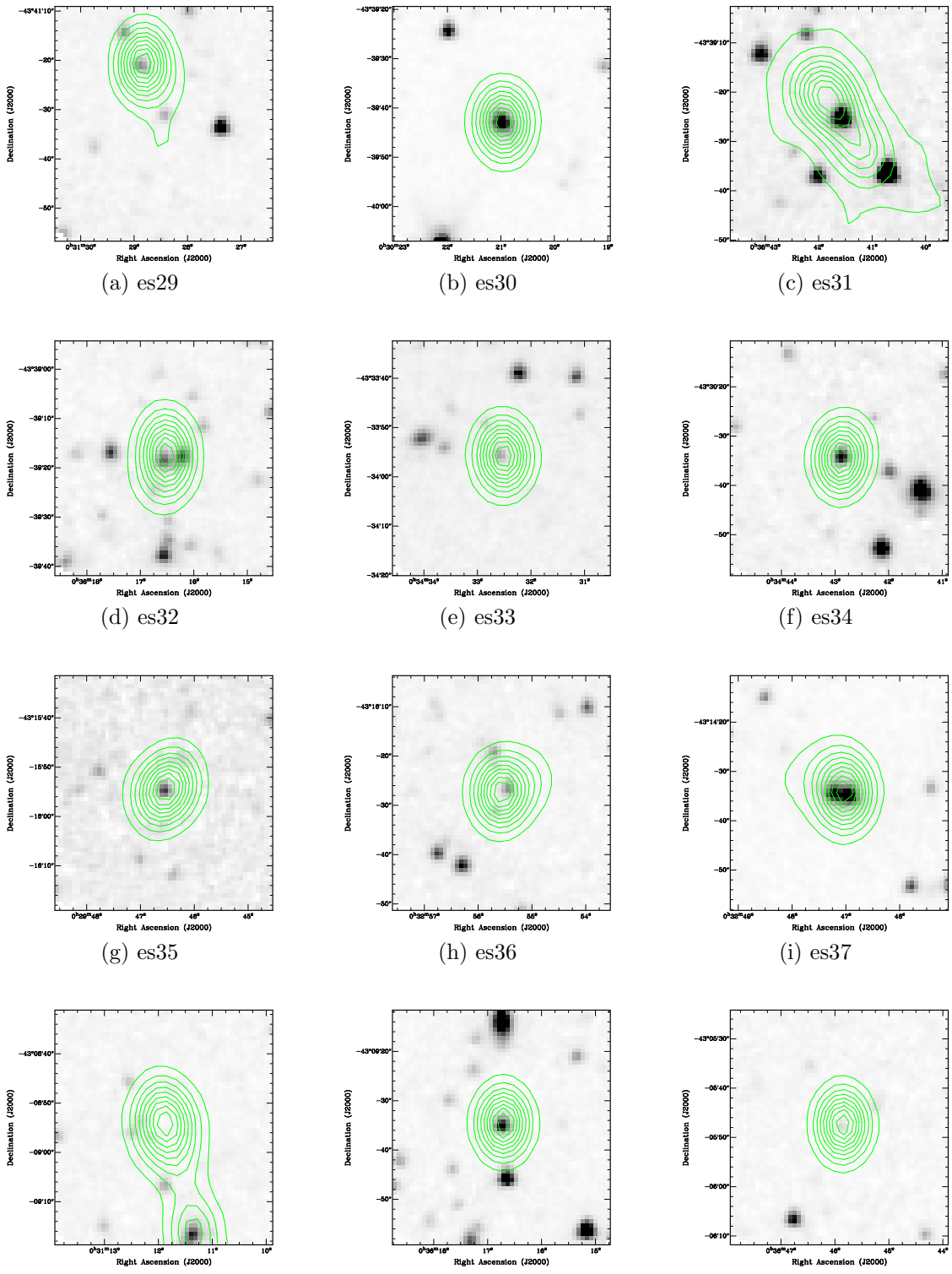

(a) es29 (b) es30 (c) es31

(d) es32 (e) es33 (f) es34

(g) es35 (h) es36 (i) es37

(j) es38 (k) es39 (l) es40

Figure B.21: The IRAC-3.6μm images from SWIRE in the Elais-S1 field, overlaid with the radio image from ATLAS.

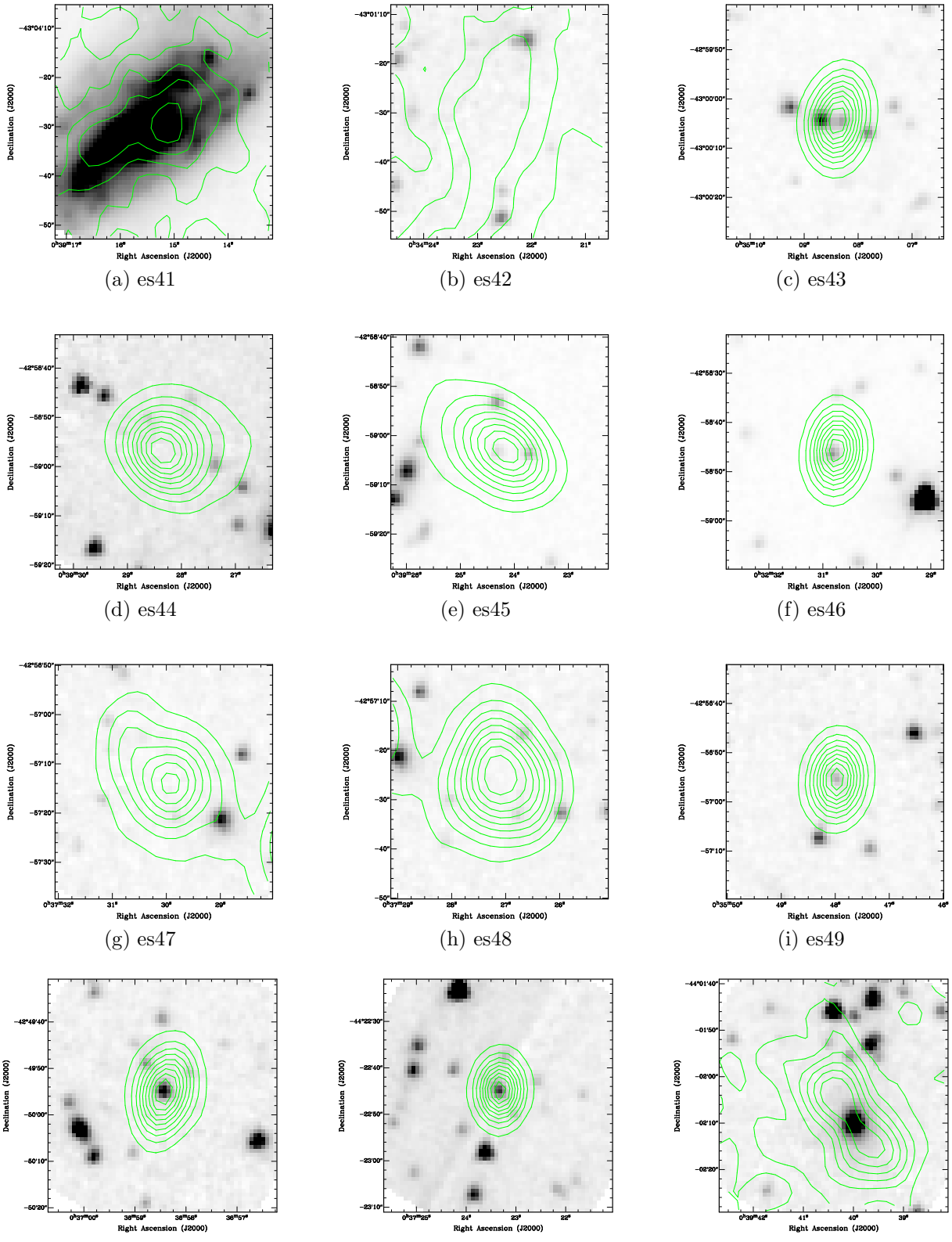

(a) es41 (b) es42 (c) es43

(d) es44 (e) es45 (f) es46

(g) es47 (h) es48 (i) es49

(j) es50 (k) es08 (l) es18

Figure B.22: The IRAC-3.6μm images from SWIRE in the Elais-S1 field, overlaid with the radio image from ATLAS.

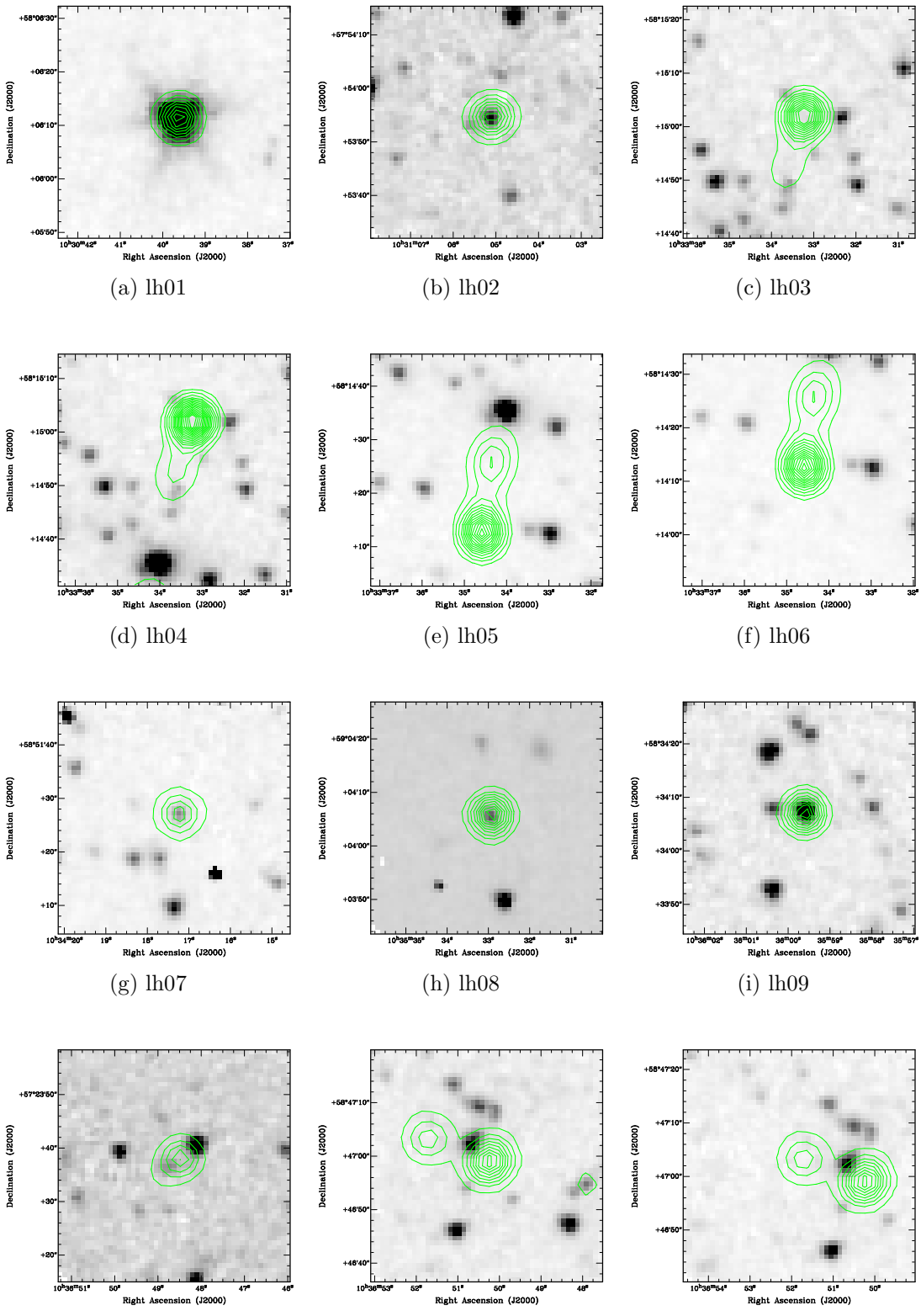

(a) lh01 (b) lh02 (c) lh03

(d) lh04 (e) lh05 (f) lh06

(g) lh07 (h) lh08 (i) lh09

(j) lh10 (k) lh11 (l) lh12

Figure B.23: The IRAC-3.6μm images from SWIRE in the Lockman Hole field, overlaid with the radio image from FIRST.

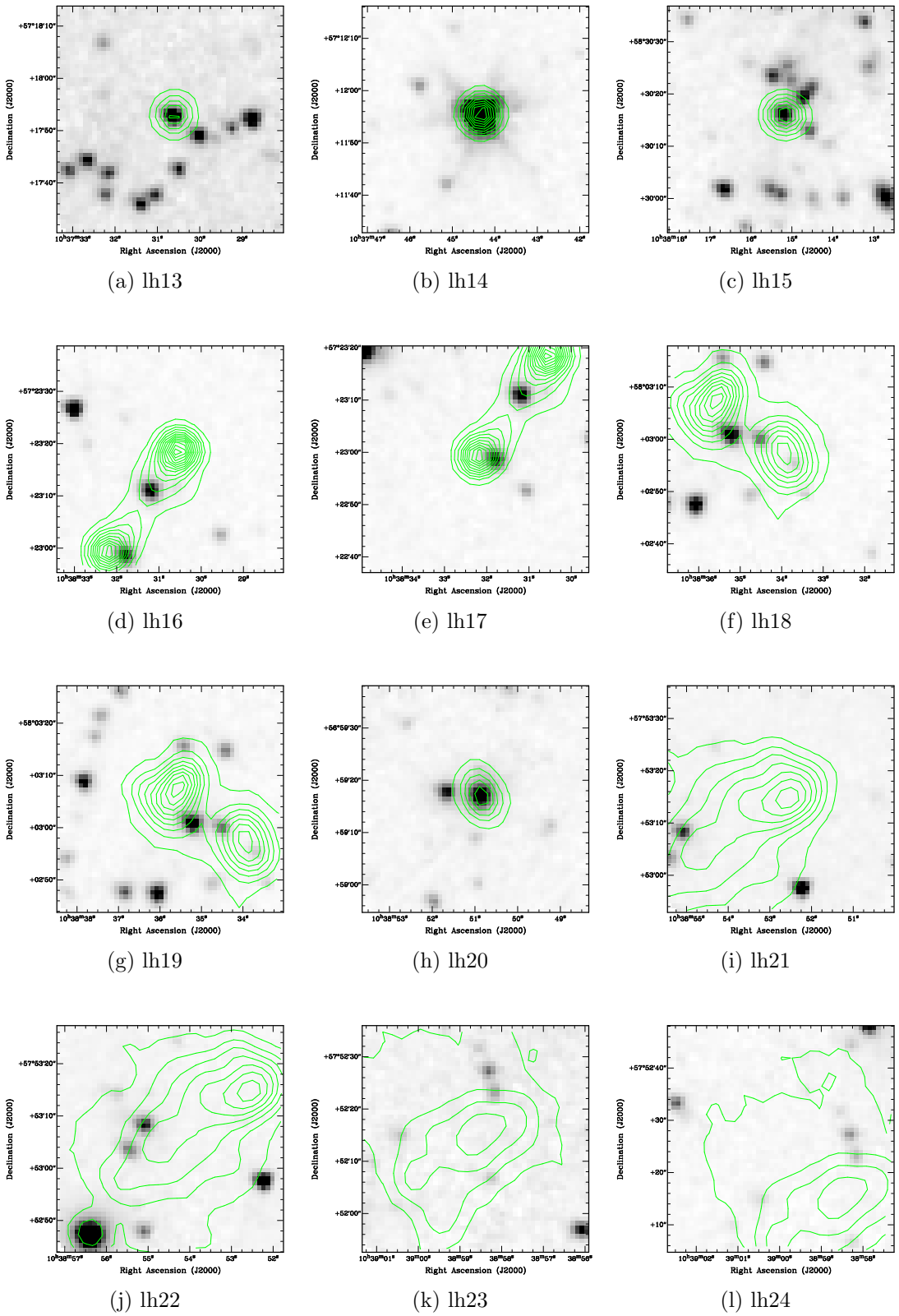

(a) lh13 (b) lh14 (c) lh15

(d) lh16 (e) lh17 (f) lh18

(g) lh19 (h) lh20 (i) lh21

(j) lh22 (k) lh23 (l) lh24

Figure B.24: The IRAC-3.6μm images from SWIRE in the Lockman Hole field, overlaid with the radio image from FIRST.

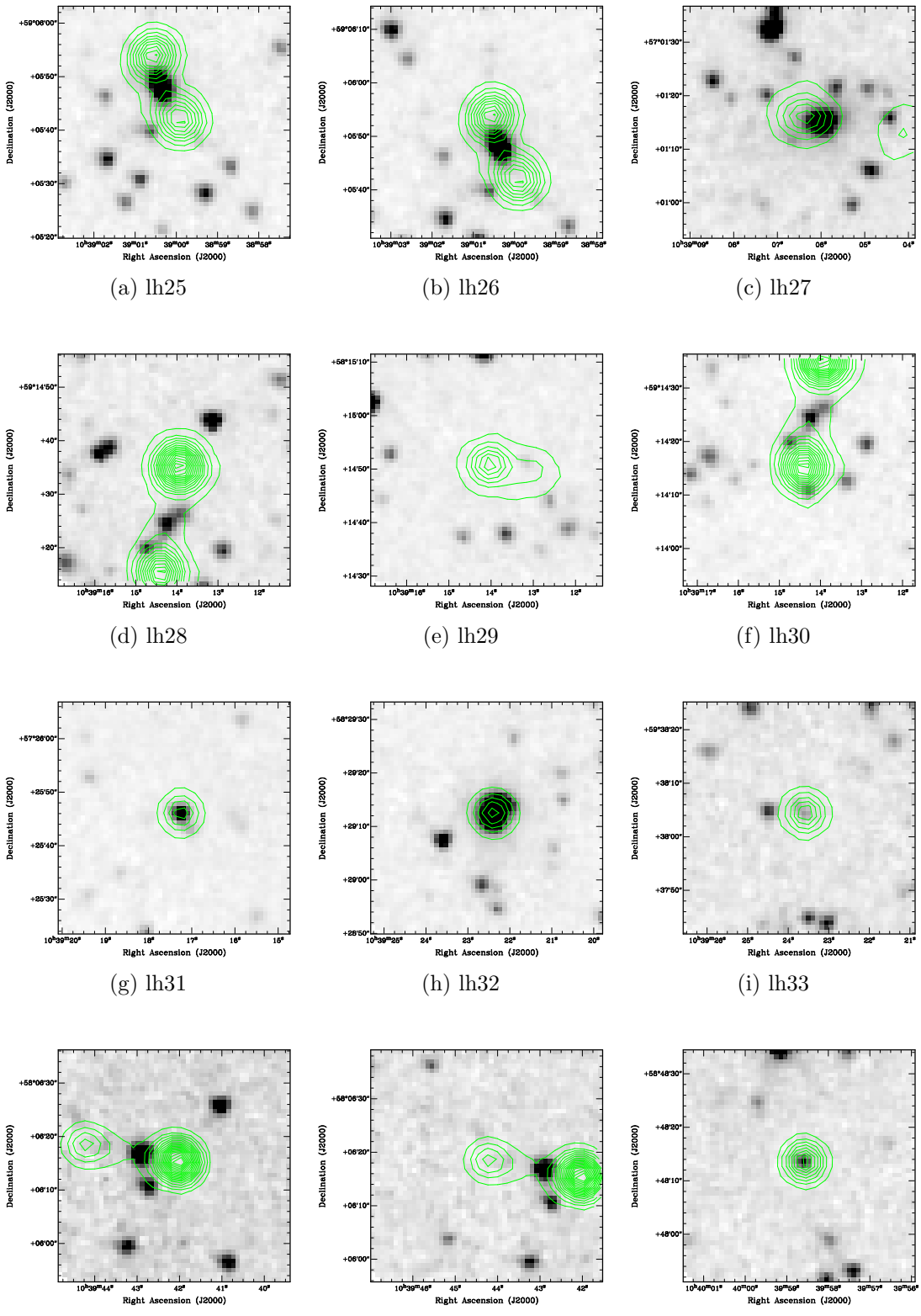

(a) lh25 (b) lh26 (c) lh27

(d) lh28 (e) lh29 (f) lh30

(g) lh31 (h) lh32 (i) lh33

(j) lh34 (k) lh35 (l) lh36

Figure B.25: The IRAC-3.6μm images from SWIRE in the Lockman Hole field, overlaid with the radio image from FIRST.

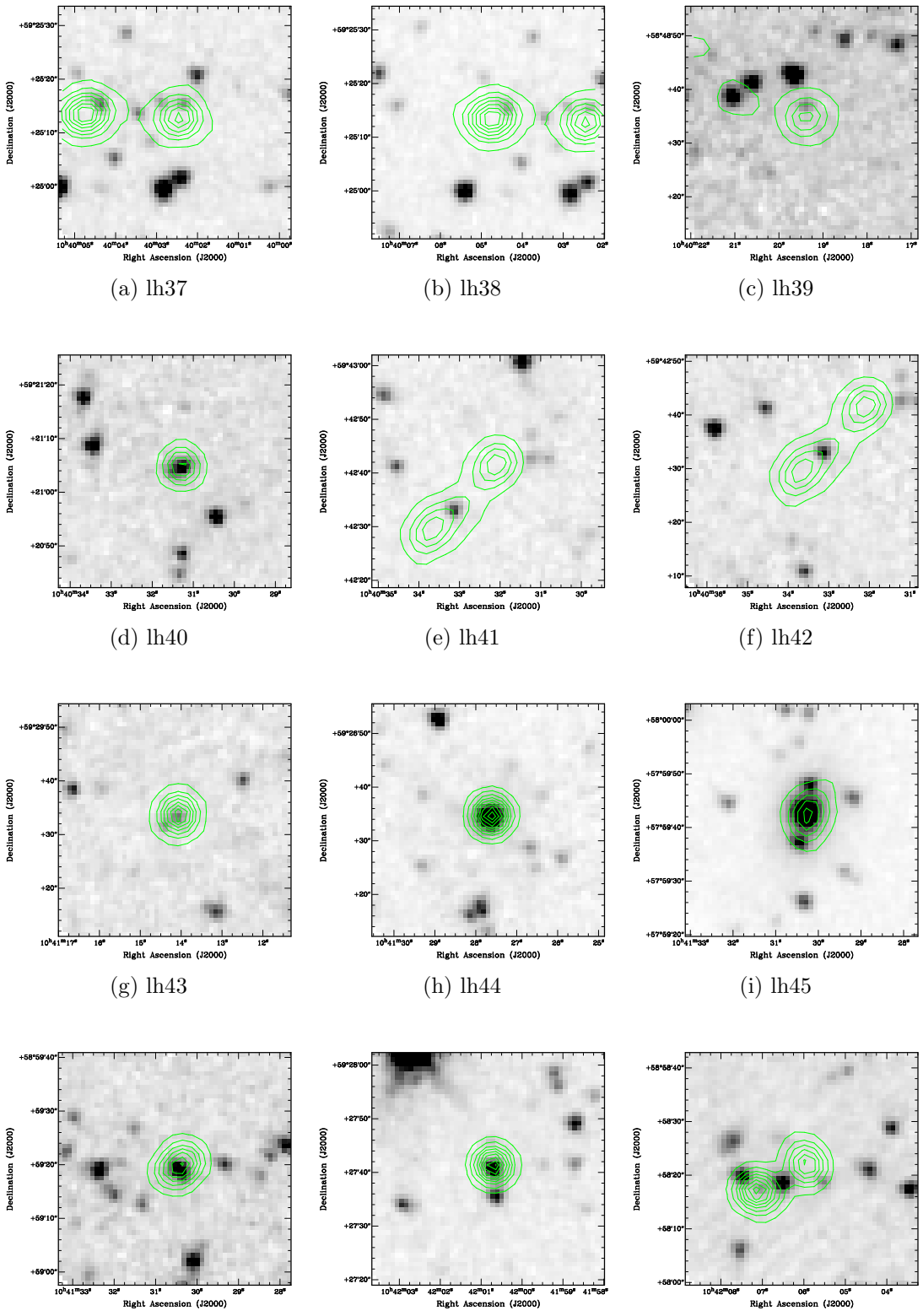

(a) lh37 (b) lh38 (c) lh39

(d) lh40 (e) lh41 (f) lh42

(g) lh43 (h) lh44 (i) lh45

(j) lh46 (k) lh47 (l) lh48

Figure B.26: The IRAC-3.6μm images from SWIRE in the Lockman Hole field, overlaid with the radio image from FIRST.

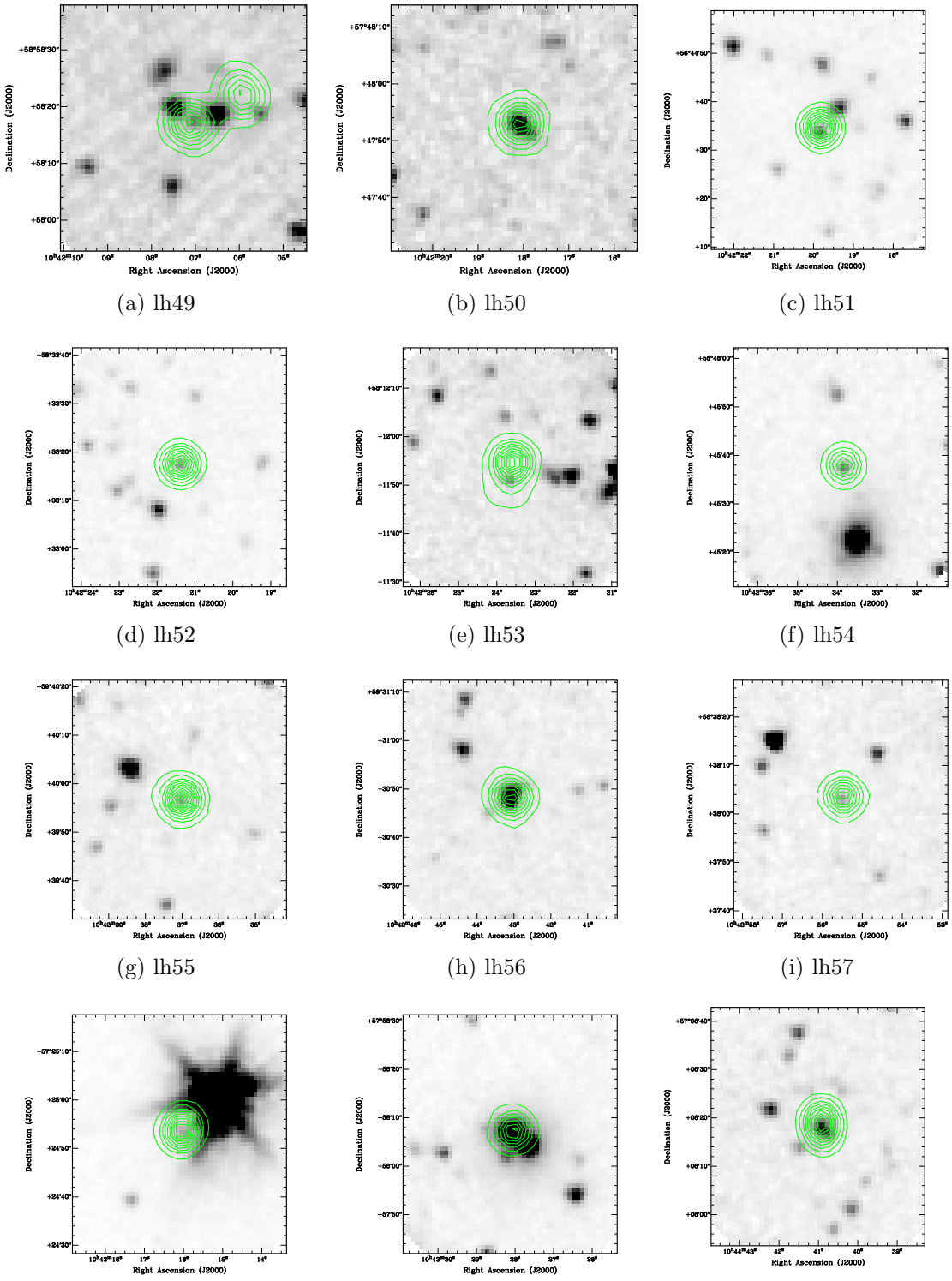

(a) lh49 (b) lh50 (c) lh51

(d) lh52 (e) lh53 (f) lh54

(g) lh55 (h) lh56 (i) lh57

(j) lh58 (k) lh59 (l) lh60

Figure B.27: The IRAC-3.6μm images from SWIRE in the Lockman Hole field, overlaid with the radio image from FIRST.

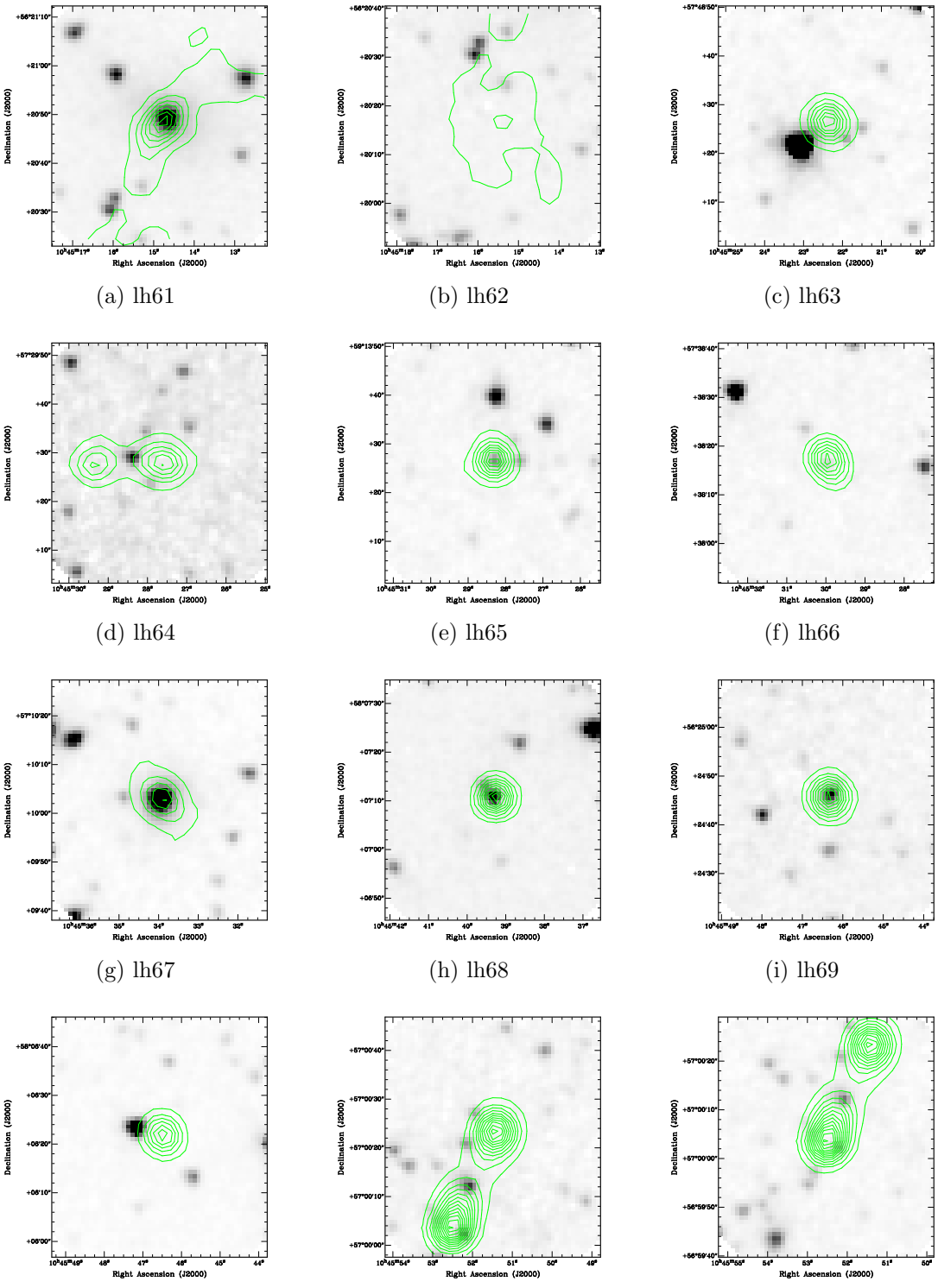

(a) lh61 (b) lh62 (c) lh63

(d) lh64 (e) lh65 (f) lh66

(g) lh67 (h) lh68 (i) lh69

(j) lh70 (k) lh71 (l) lh72

Figure B.28: The IRAC-3.6μm images from SWIRE in the Lockman Hole field, overlaid with the radio image from FIRST.

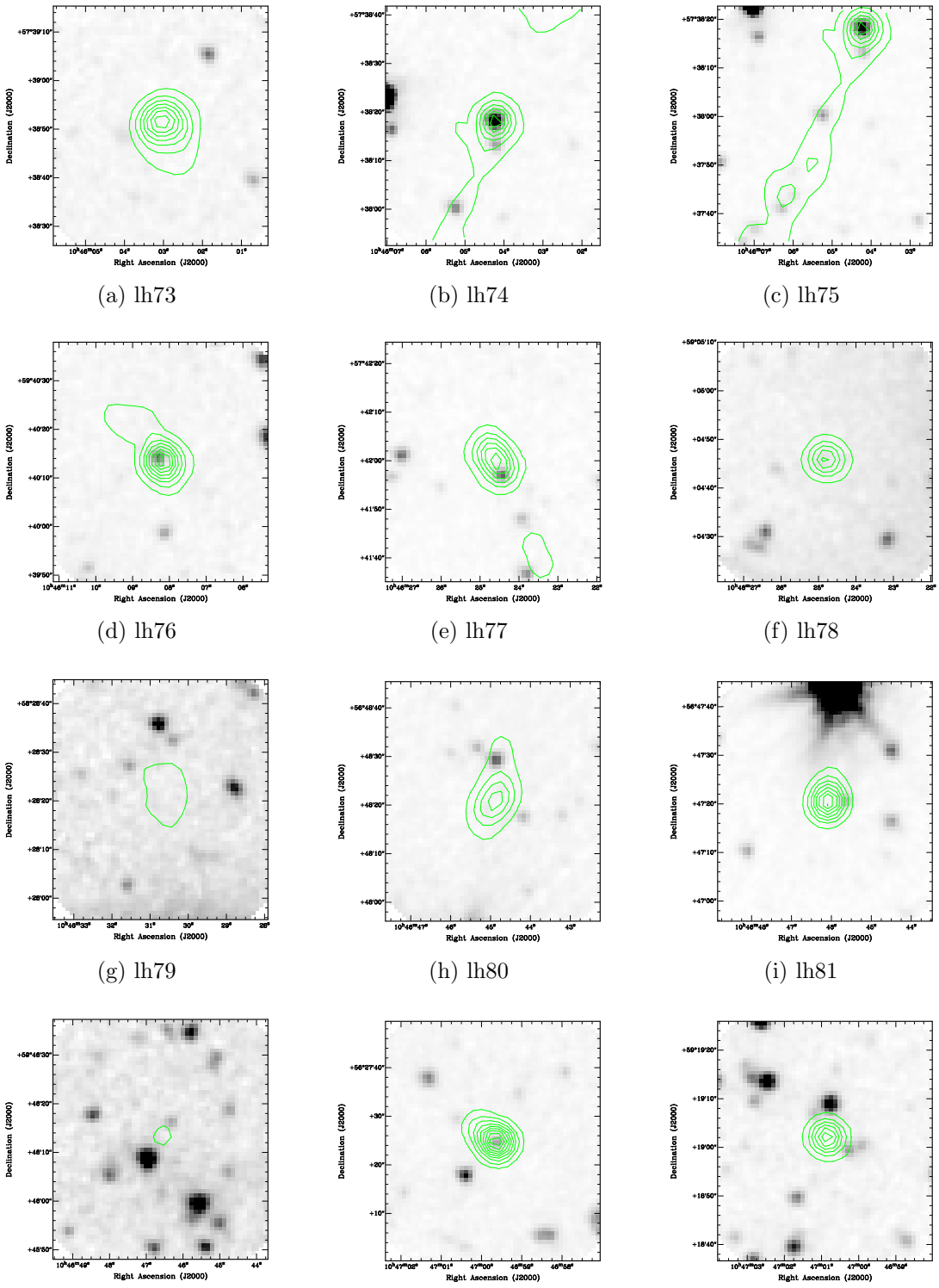

(a) lh73 (b) lh74 (c) lh75

(d) lh76 (e) lh77 (f) lh78

(g) lh79 (h) lh80 (i) lh81

(j) lh82 (k) lh83 (l) lh84

Figure B.29: The IRAC-3.6μm images from SWIRE in the Lockman Hole field, overlaid with the radio image from FIRST.

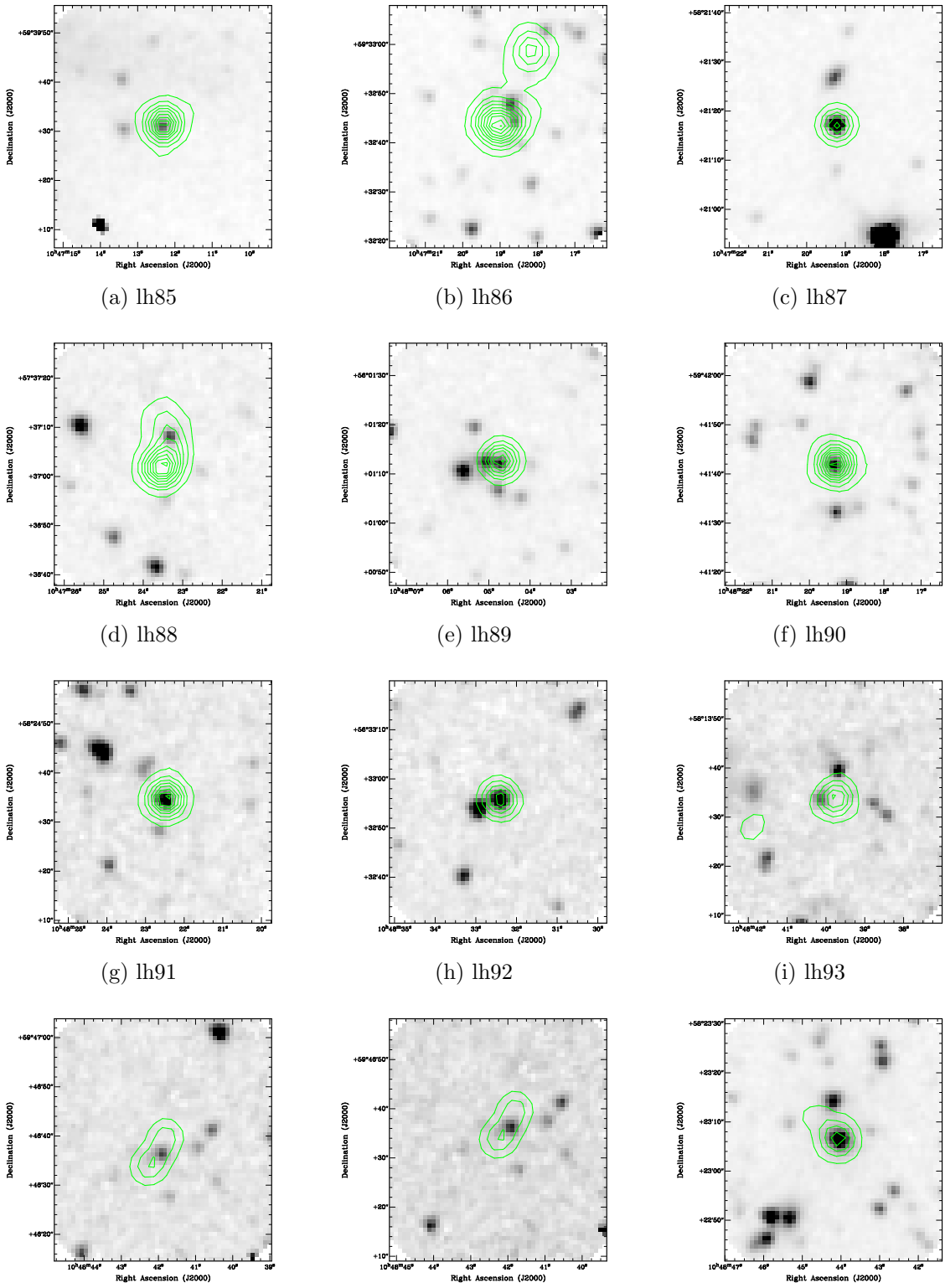

(a) lh85 (b) lh86 (c) lh87

(d) lh88 (e) lh89 (f) lh90

(g) lh91 (h) lh92 (i) lh93

(j) lh94 (k) lh95 (l) lh96

Figure B.30: The IRAC-3.6μm images from SWIRE in the Lockman Hole field, overlaid with the radio image from FIRST.

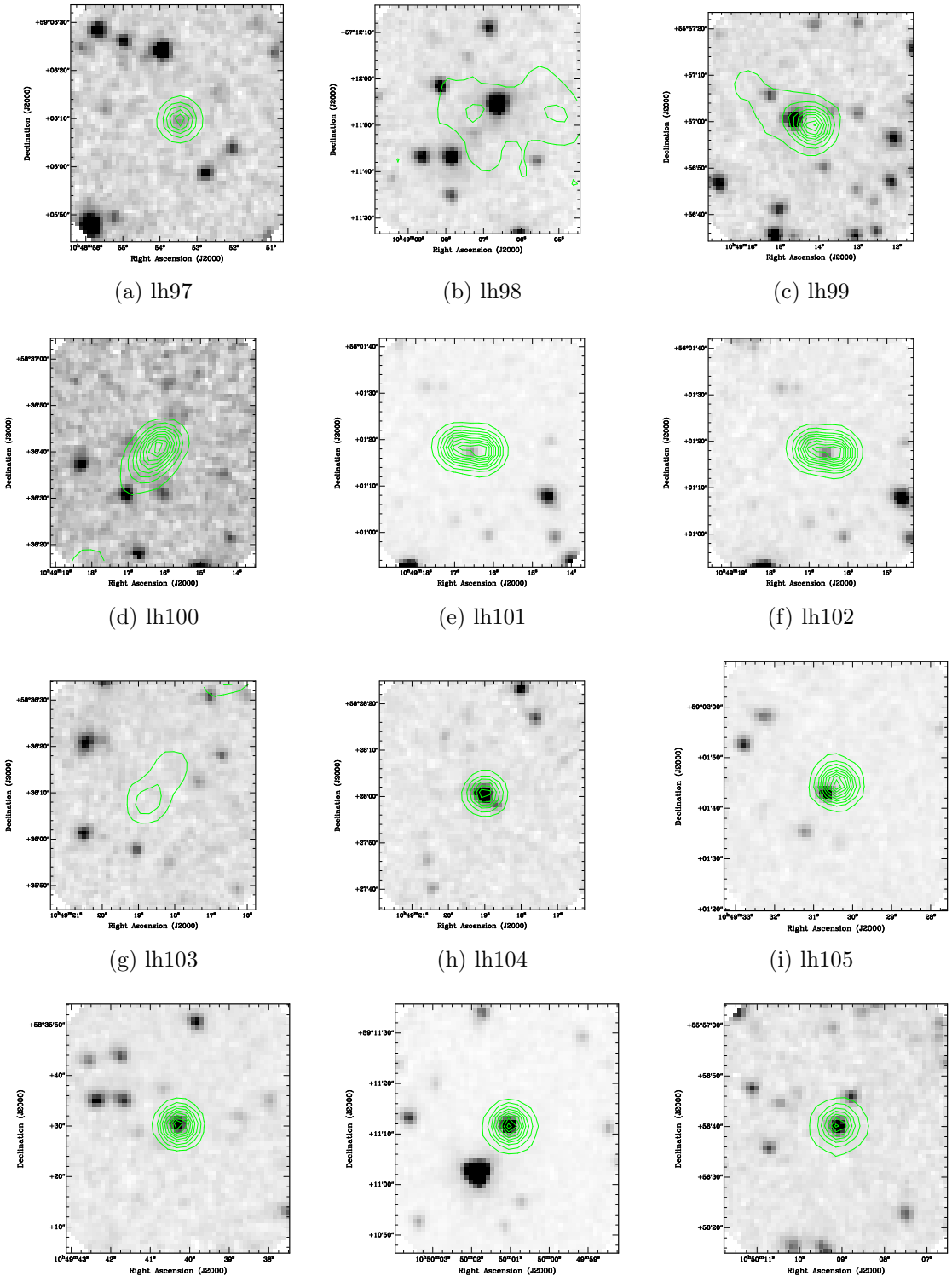

(a) lh97 (b) lh98 (c) lh99

(d) lh100 (e) lh101 (f) lh102

(g) lh103 (h) lh104 (i) lh105

(j) lh106 (k) lh107 (l) lh108

Figure B.31: The IRAC-3.6μm images from SWIRE in the Lockman Hole field, overlaid with the radio image from FIRST.

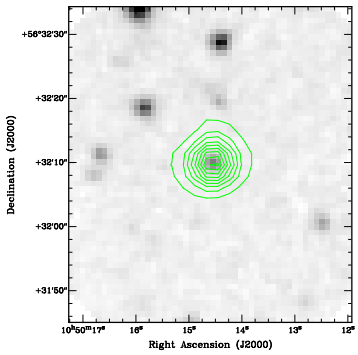

(a) lh109

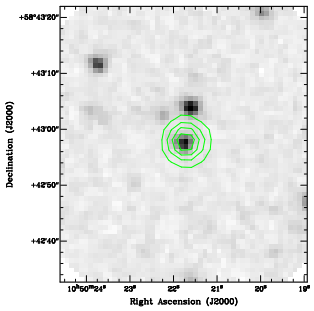

(b) lh110

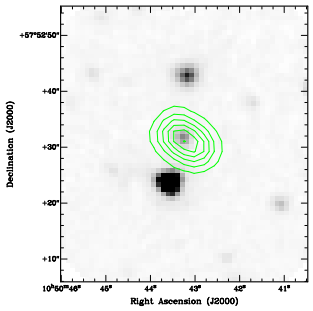

(c) lh111

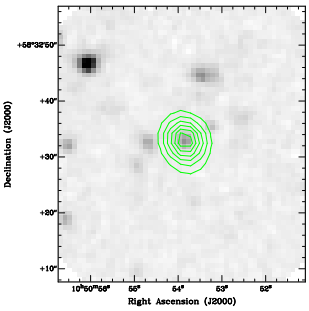

(d) lh112

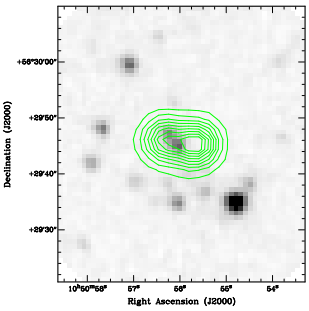

(e) lh113

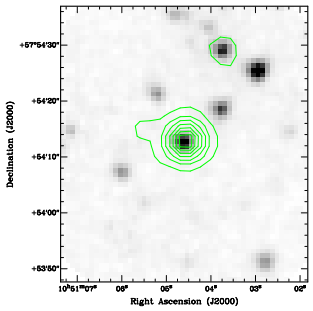

(f) lh114

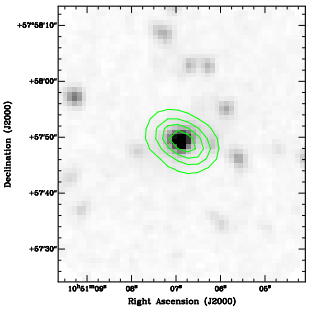

(g) lh115

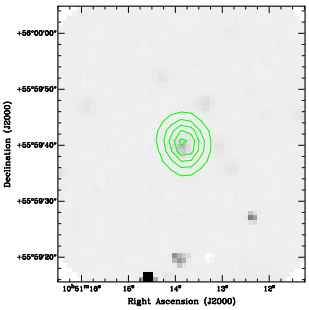

(h) lh116

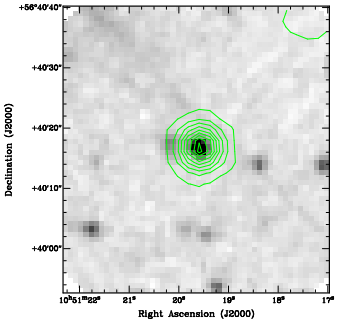

(i) lh117

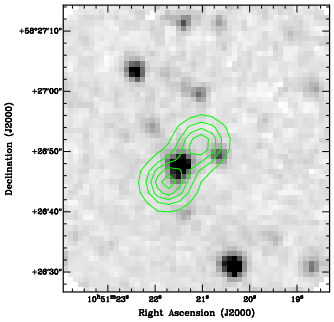

(j) lh118

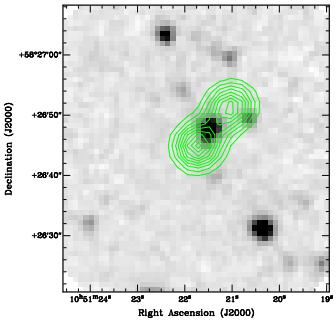

(k) lh119

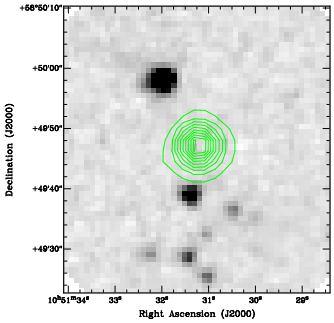

(l) lh120

Figure B.32: The IRAC-3.6μm images from SWIRE in the Lockman Hole field, overlaid with the radio image from FIRST.

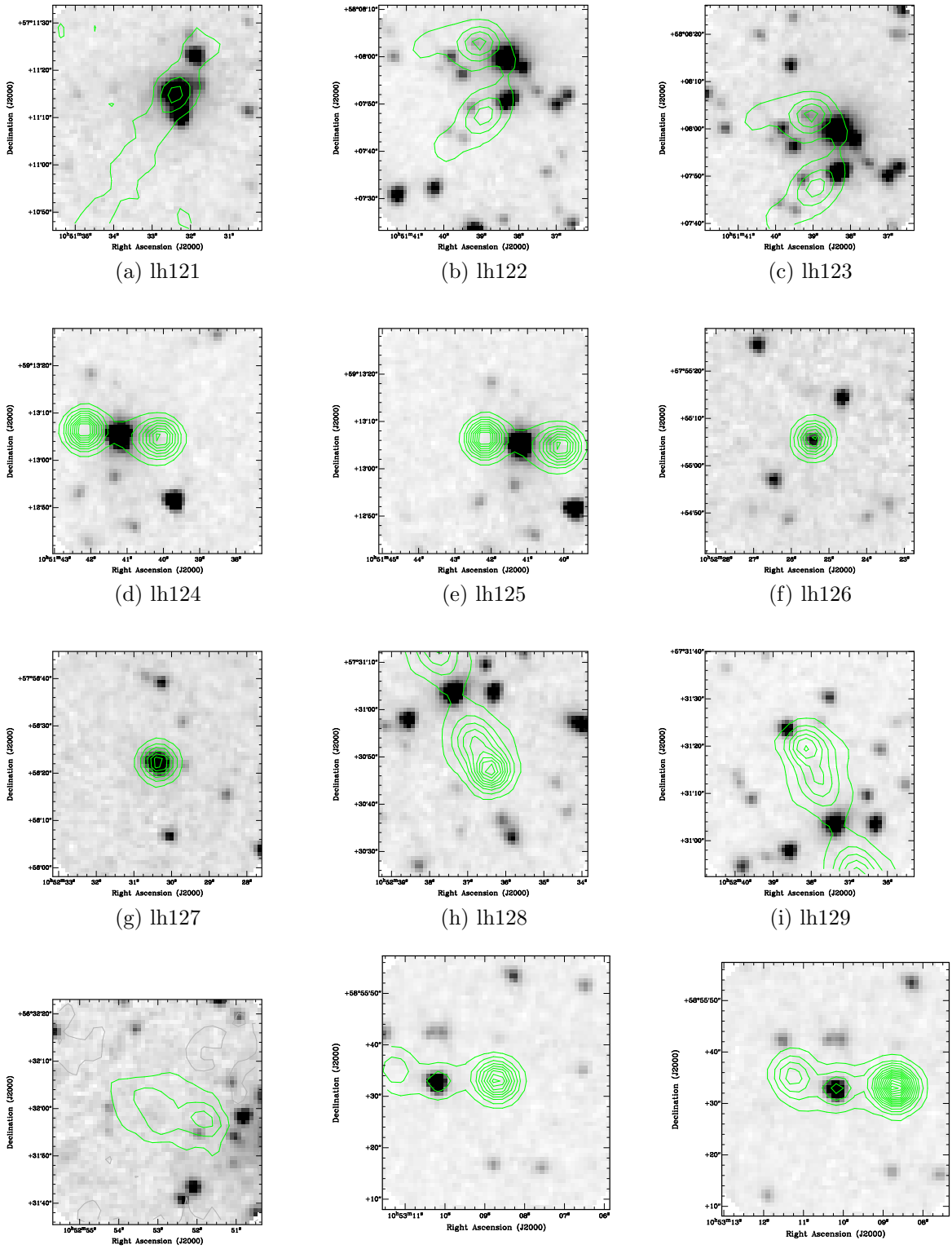

(a) lh121 (b) lh122 (c) lh123

(d) lh124 (e) lh125 (f) lh126

(g) lh127 (h) lh128 (i) lh129

(j) lh130 (k) lh131 (l) lh132

Figure B.33: The IRAC-3.6μm images from SWIRE in the Lockman Hole field, overlaid with the radio image from FIRST.

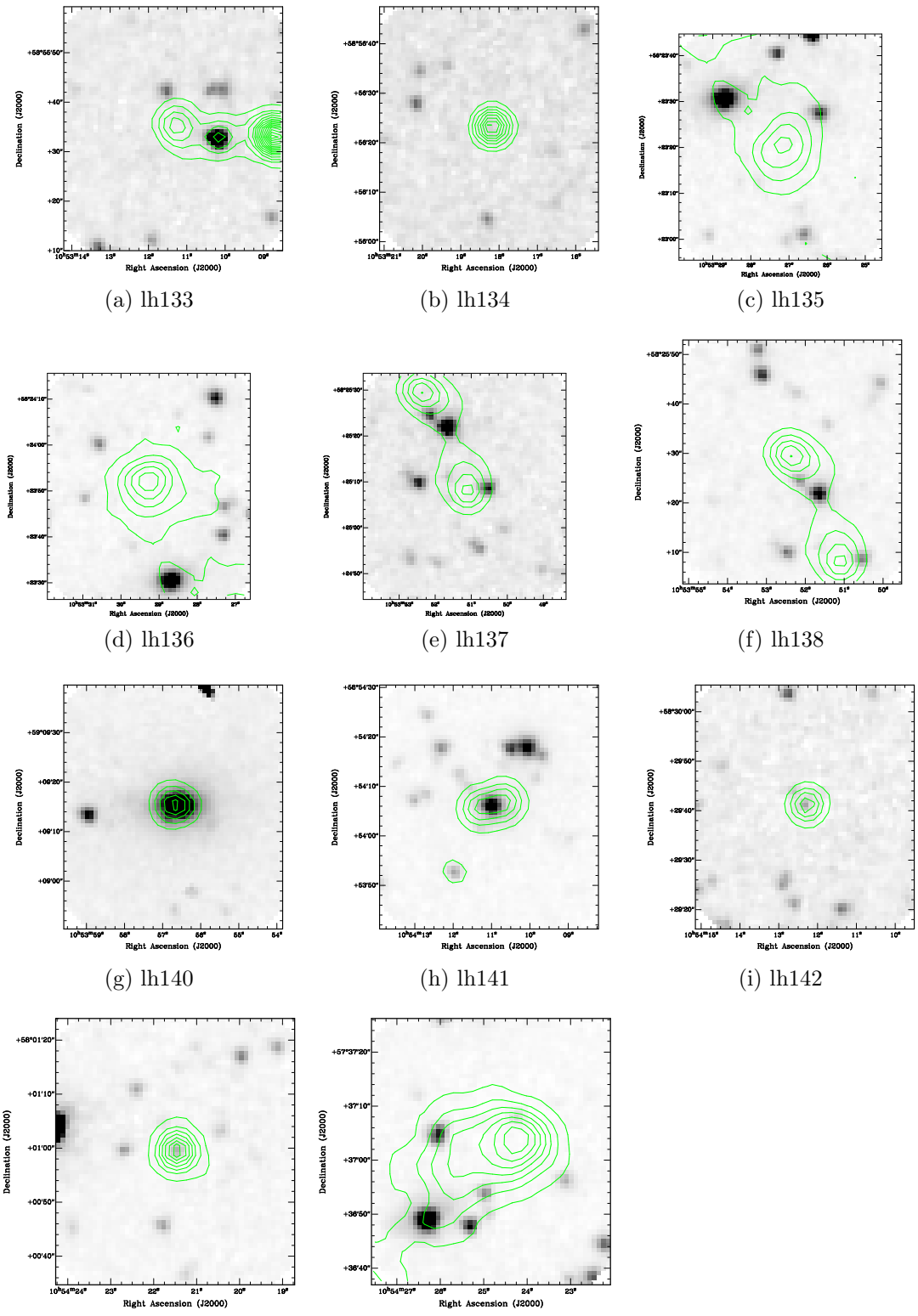

(a) lh133 (b) lh134 (c) lh135

(d) lh136 (e) lh137 (f) lh138

(g) lh140 (h) lh141 (i) lh142

(j) lh143 (k) lh144

Figure B.34: The IRAC-3.6μm images from SWIRE in the Lockman Hole field, overlaid with the radio image from FIRST.

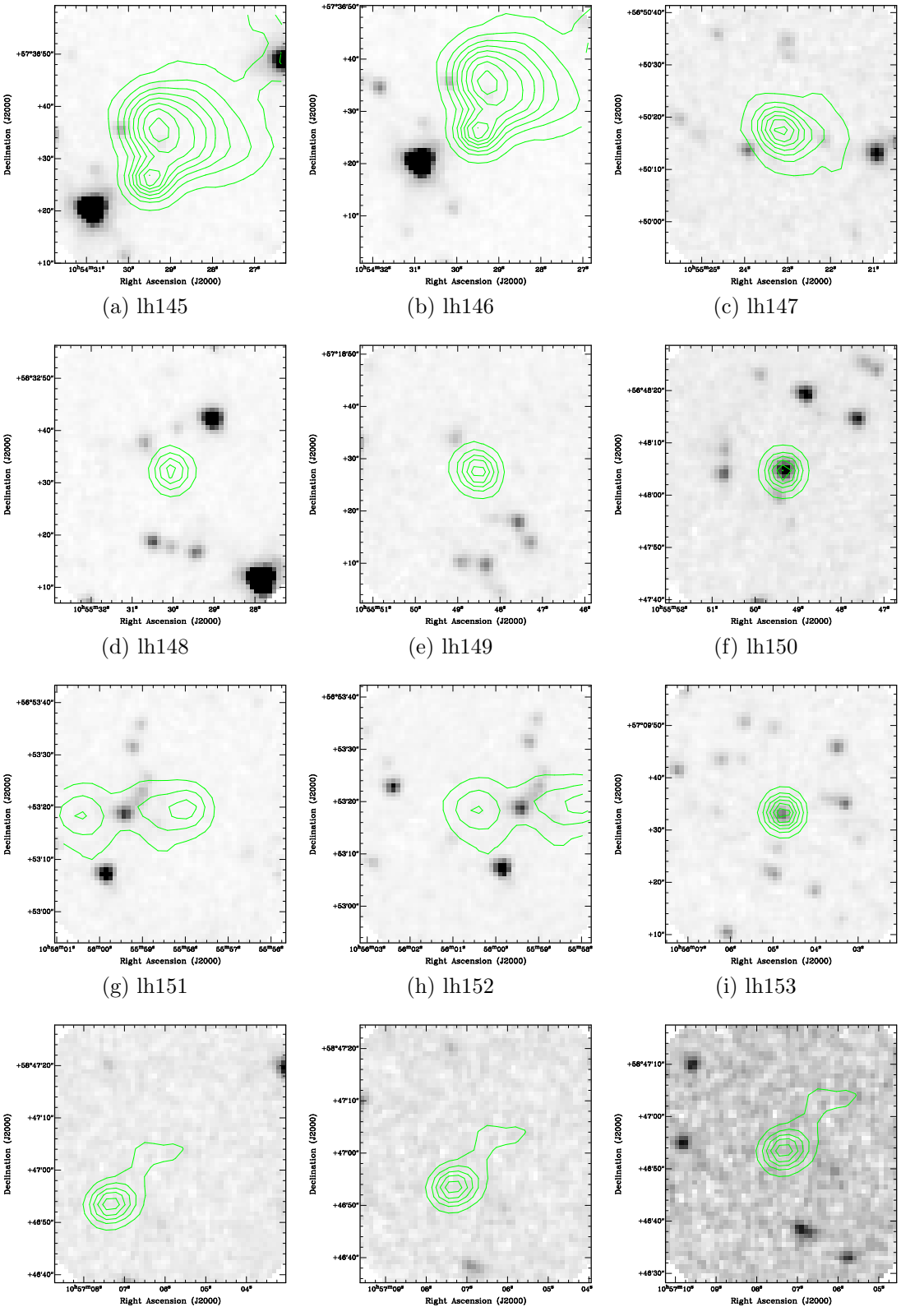

(a) lh145 (b) lh146 (c) lh147

(d) lh148 (e) lh149 (f) lh150

(g) lh151 (h) lh152 (i) lh153

(j) lh154 (k) lh155 (l) lh156

Figure B.35: The IRAC-3.6μm images from SWIRE in the Lockman Hole field, overlaid with the radio image from FIRST.

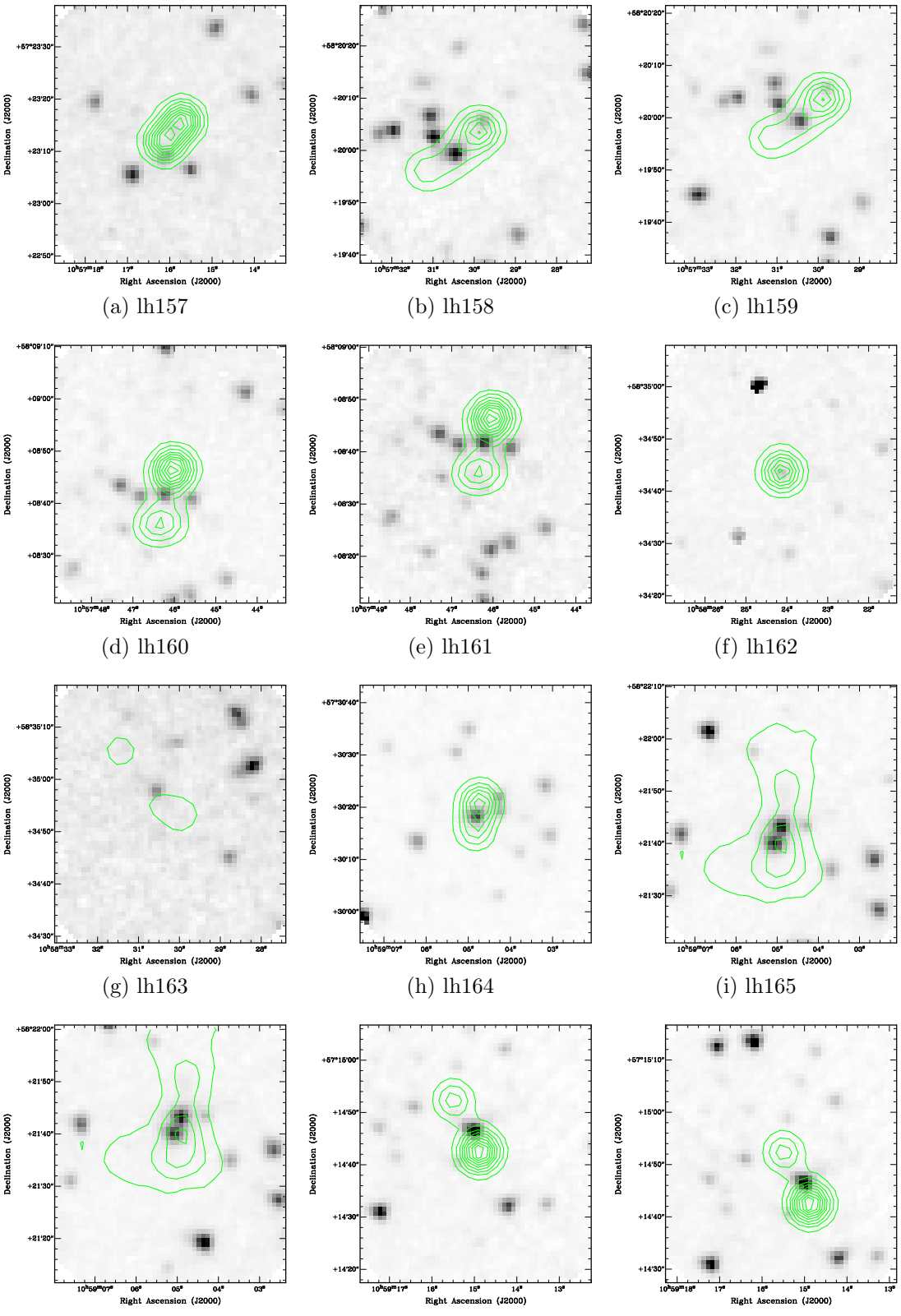

(a) lh157 (b) lh158 (c) lh159

(d) lh160 (e) lh161 (f) lh162

(g) lh163 (h) lh164 (i) lh165

(j) lh166 (k) lh167 (l) lh168

Figure B.36: The IRAC-3.6μm images from SWIRE in the Lockman Hole field, overlaid with the radio image from FIRST.

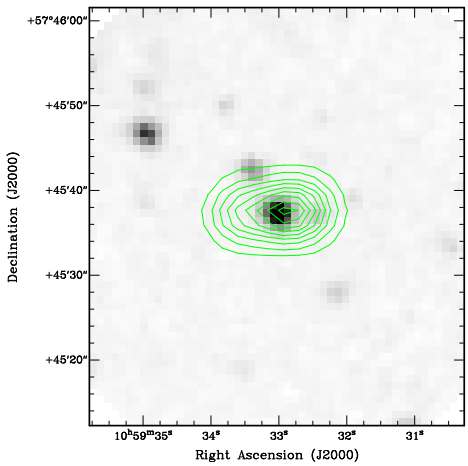

(a) lh169

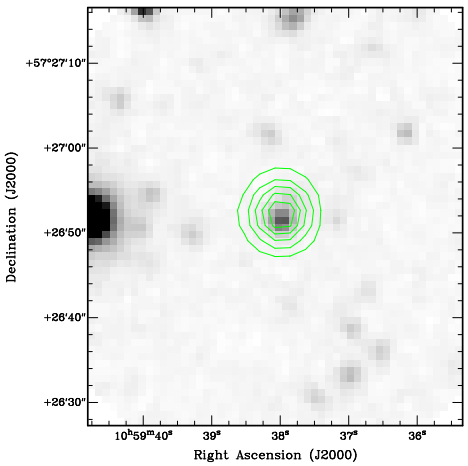

(b) lh170

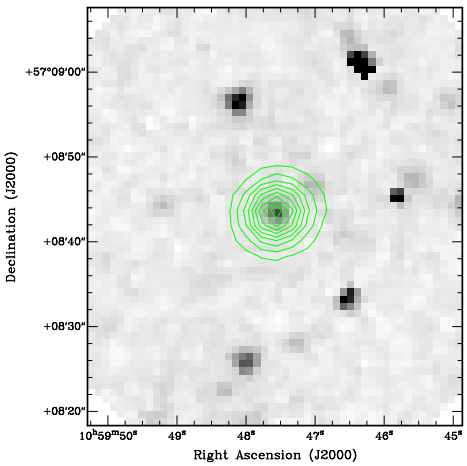

(c) lh171

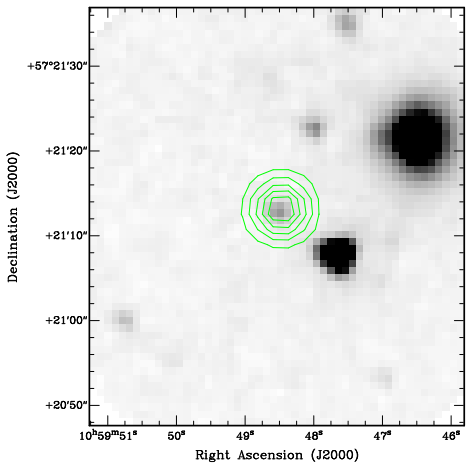

(d) lh172

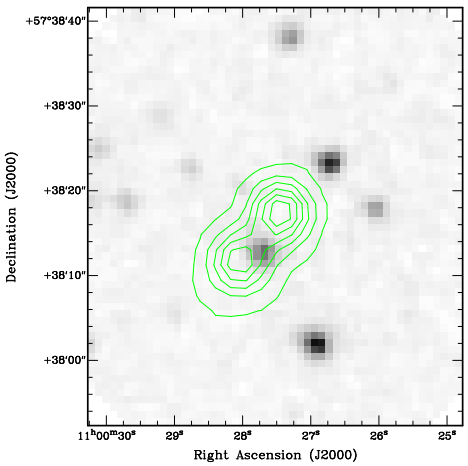

(e) lh173

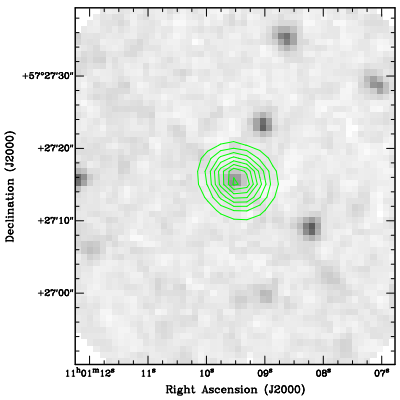

(f) lh174

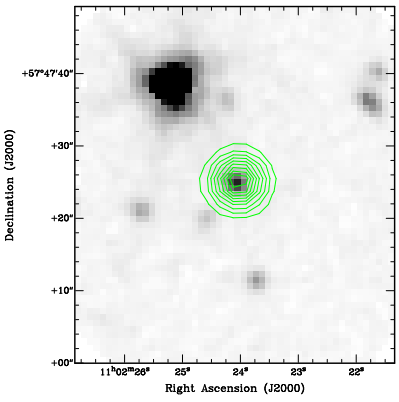

(g) lh175

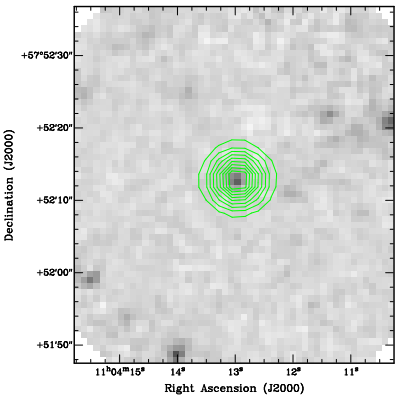

(h) lh176

Figure B.37: The IRAC-3.6μm images from SWIRE in the Lockman Hole field, overlaid with the radio image from FIRST.

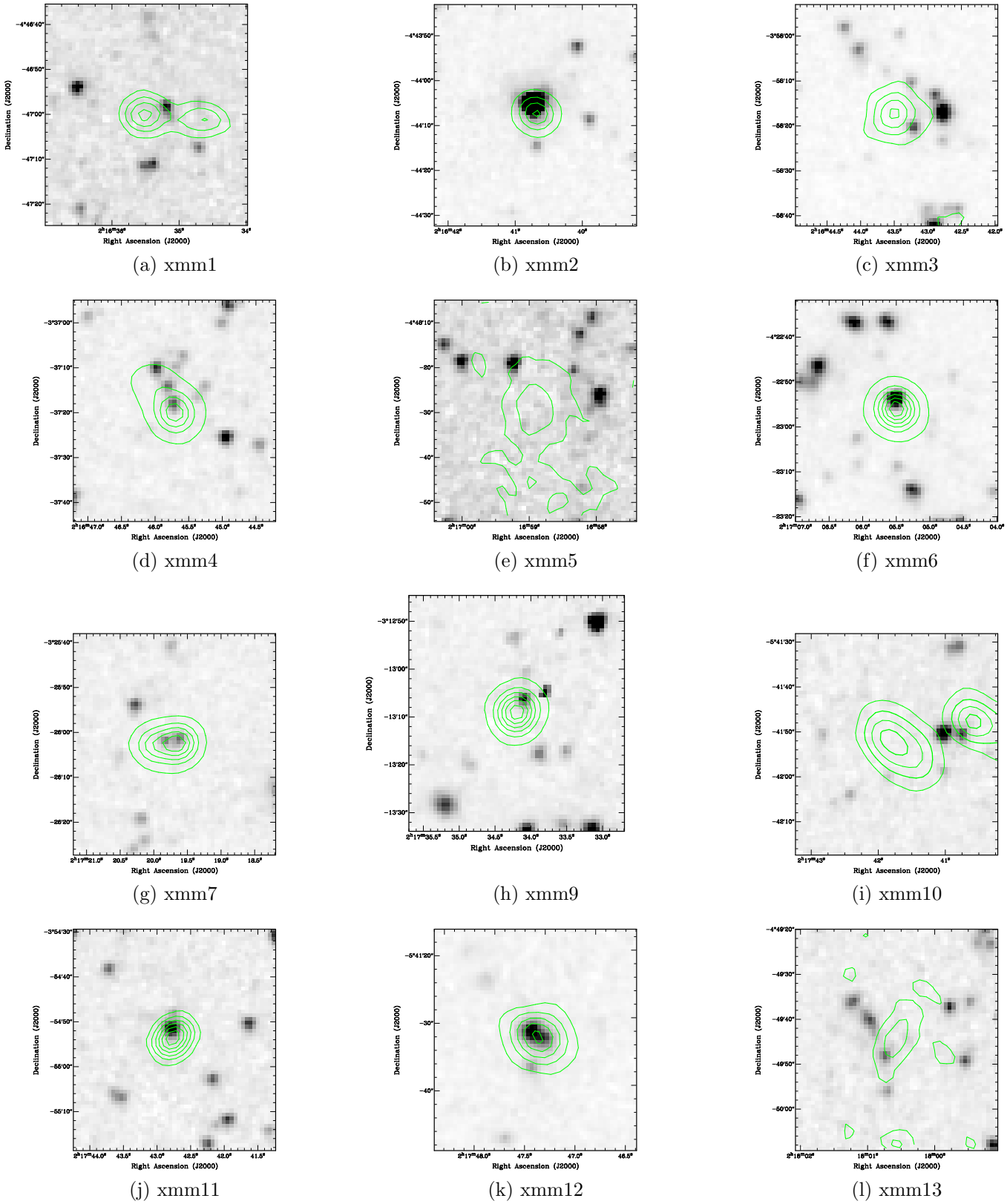

(a) xmm1 (b) xmm2 (c) xmm3

(d) xmm4 (e) xmm5 (f) xmm6

(g) xmm7 (h) xmm9 (i) xmm10

(j) xmm11 (k) xmm12 (l) xmm13

Figure B.38: The IRAC-3.6μm images from SWIRE in the XMM-LSS field, overlaid with the radio image from GMRT data.

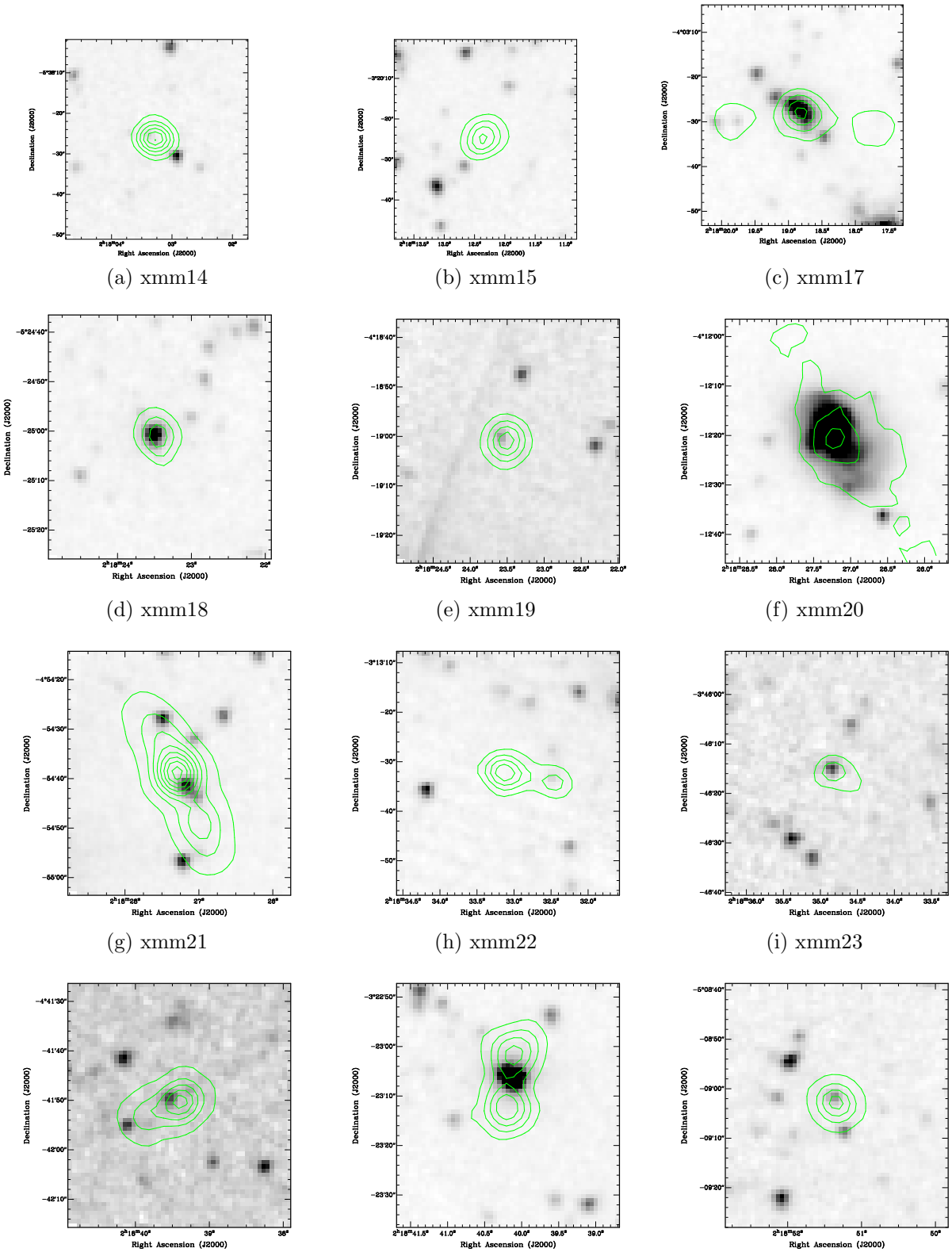

(a) xmm14 (b) xmm15 (c) xmm17

(d) xmm18 (e) xmm19 (f) xmm20

(g) xmm21 (h) xmm22 (i) xmm23

(j) xmm24 (k) xmm25 (l) xmm26

Figure B.39: The IRAC-3.6μm images from SWIRE in the XMM-LSS field, overlaid with the radio image from GMRT data.

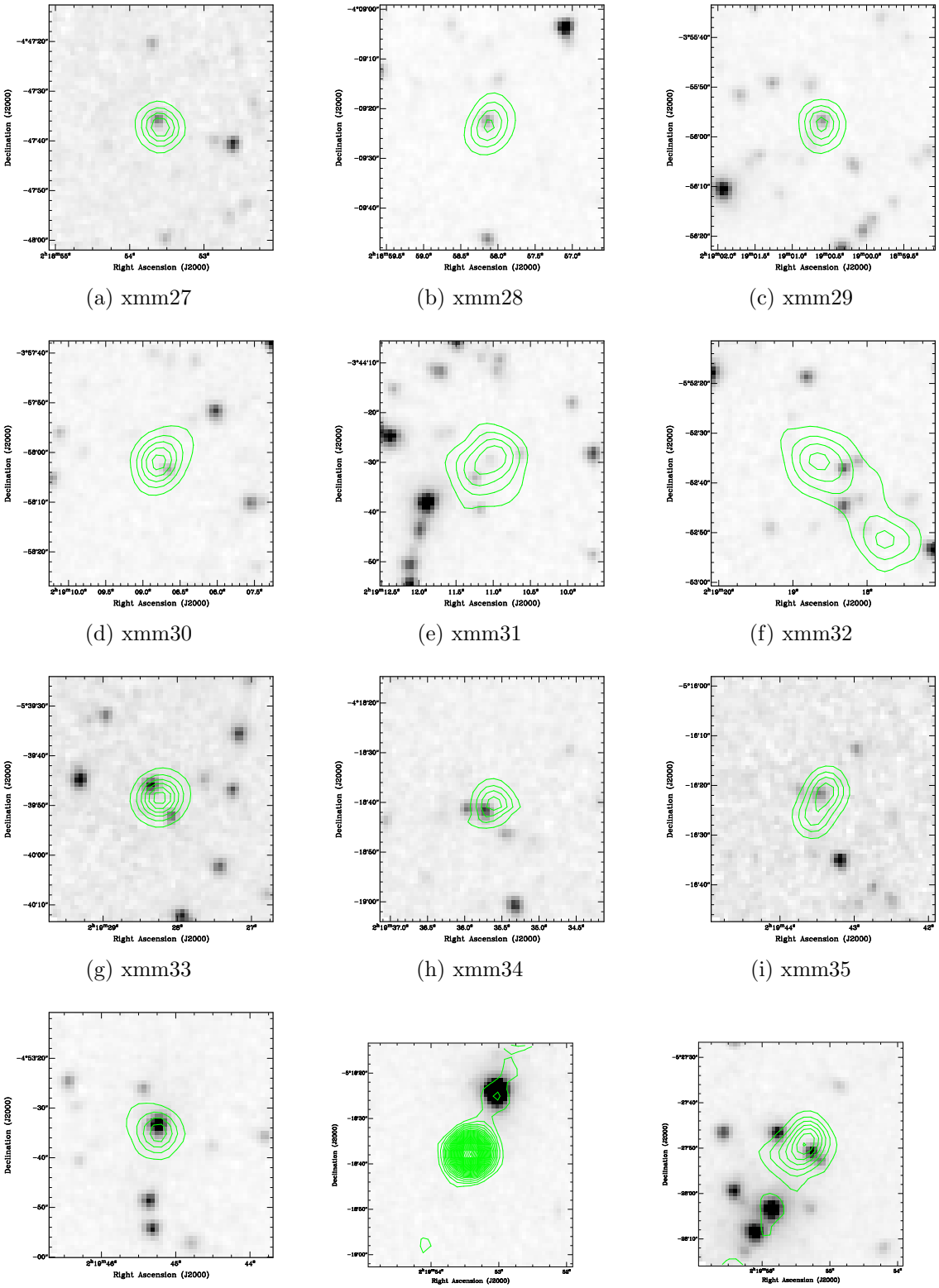

(a) xmm27 (b) xmm28 (c) xmm29

(d) xmm30 (e) xmm31 (f) xmm32

(g) xmm33 (h) xmm34 (i) xmm35

(j) xmm36 (k) xmm37 (l) xmm38

Figure B.40: The IRAC-3.6μm images from SWIRE in the XMM-LSS field, overlaid with the radio image from GMRT data.

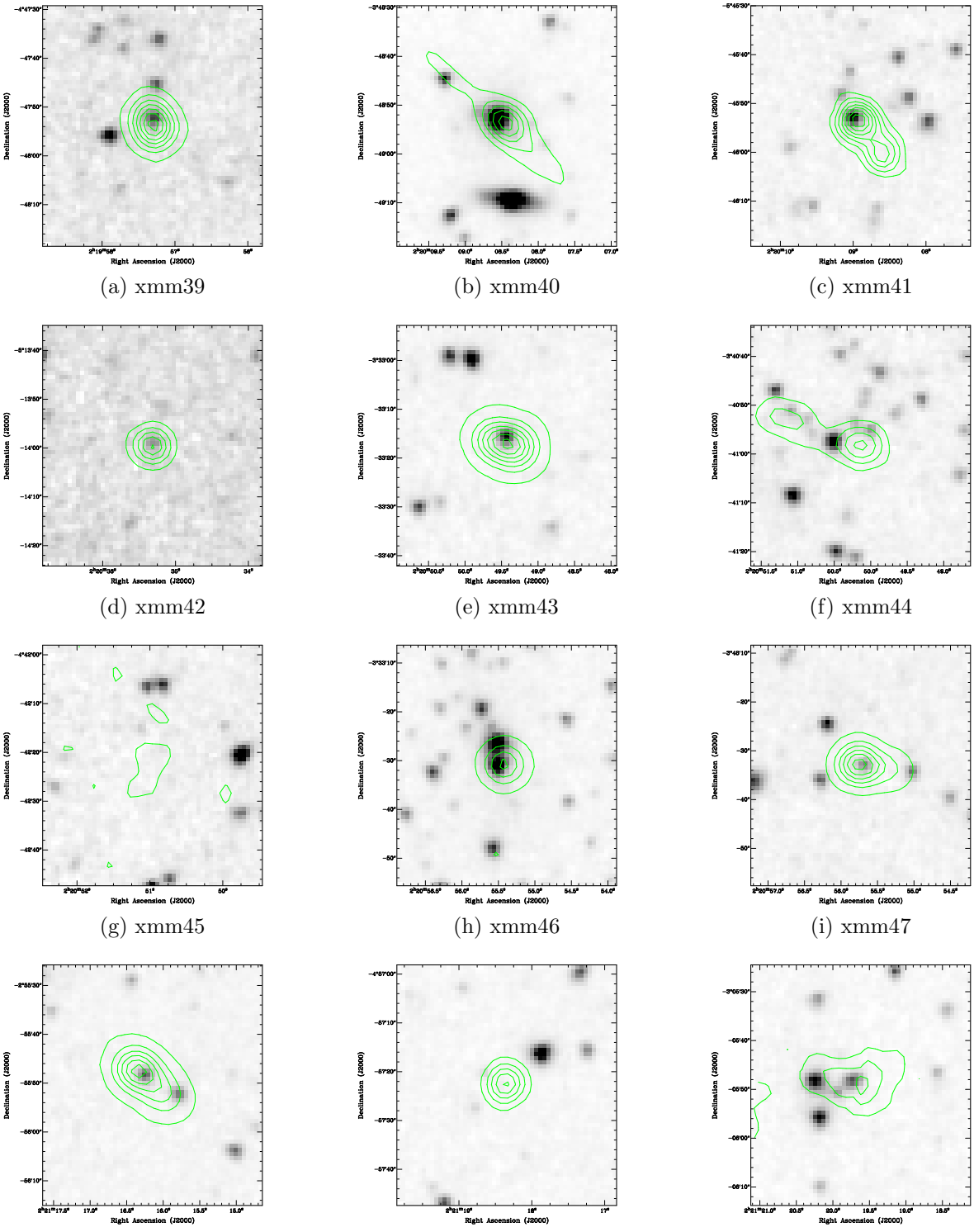

(a) xmm39 (b) xmm40 (c) xmm41

(d) xmm42 (e) xmm43 (f) xmm44

(g) xmm45 (h) xmm46 (i) xmm47

(j) xmm48 (k) xmm49 (l) xmm50

Figure B.41: The IRAC-3.6μm images from SWIRE in the XMM-LSS field, overlaid with the radio image from GMRT data.

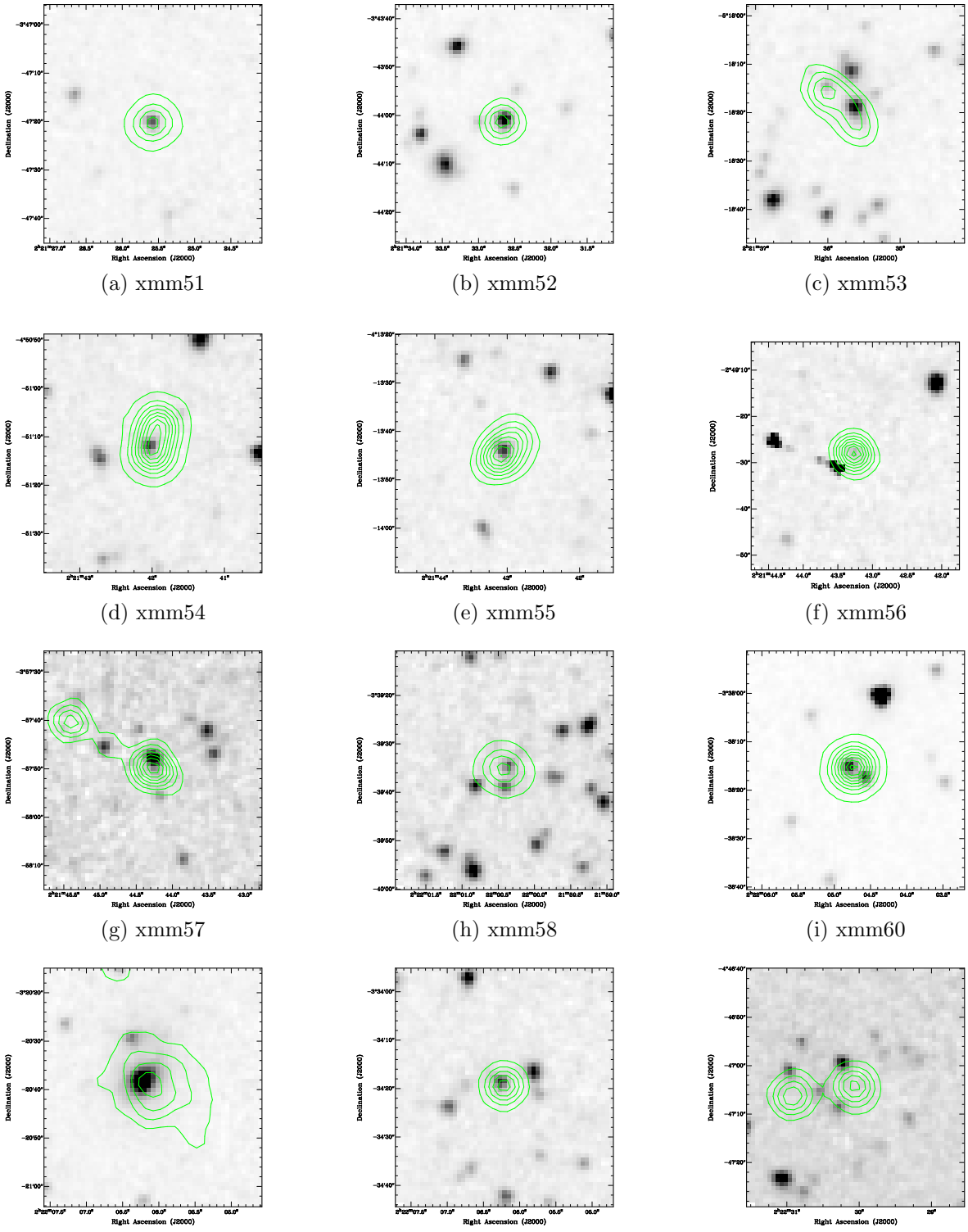

(a) xmm51 (b) xmm52 (c) xmm53

(d) xmm54 (e) xmm55 (f) xmm56

(g) xmm57 (h) xmm58 (i) xmm60

(j) xmm61 (k) xmm62 (l) xmm65

Figure B.42: The IRAC-3.6μm images from SWIRE in the XMM-LSS field, overlaid with the radio image from GMRT data.

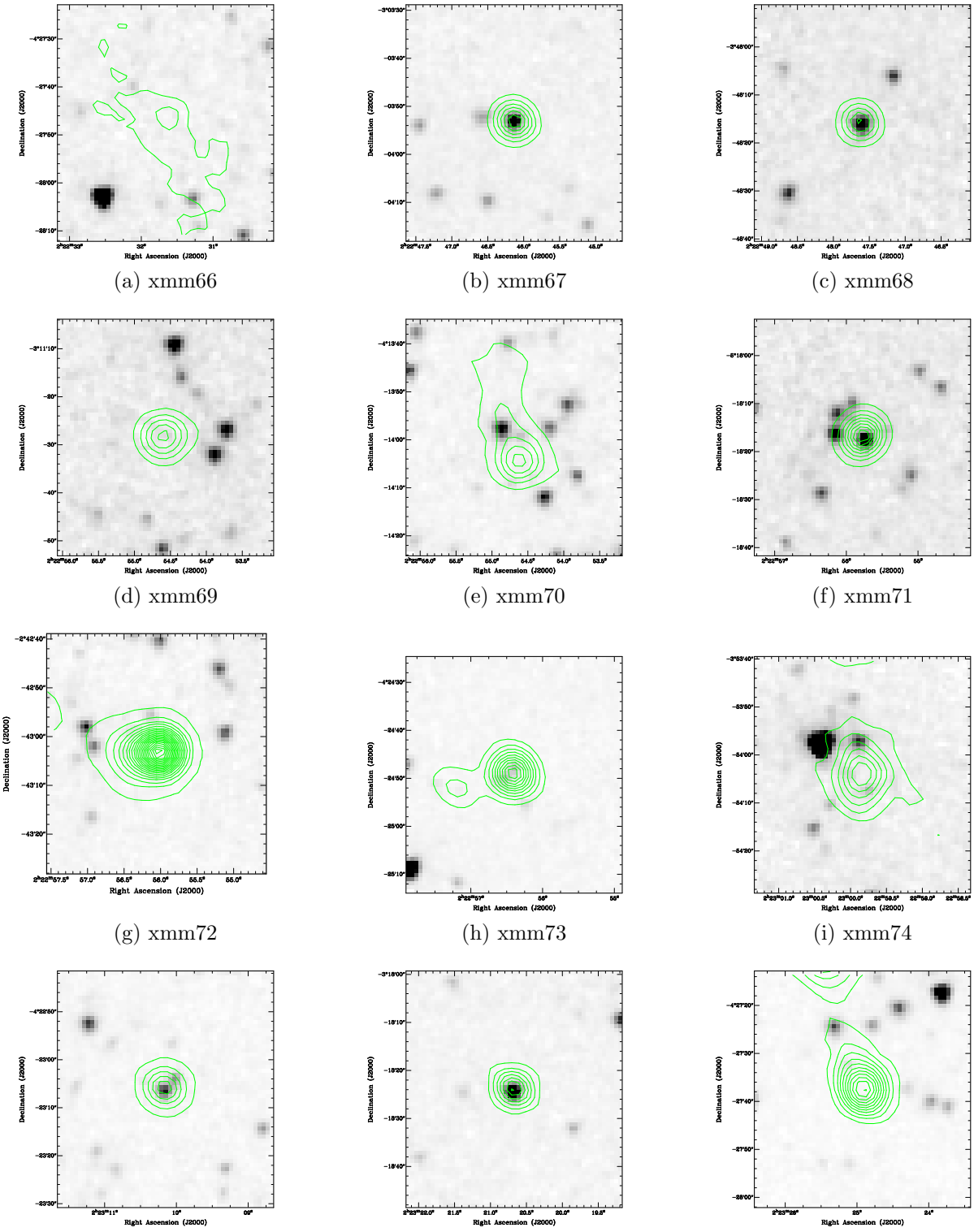

(a) xmm66 (b) xmm67 (c) xmm68

(d) xmm69 (e) xmm70 (f) xmm71

(g) xmm72 (h) xmm73 (i) xmm74

(j) xmm75 (k) xmm76 (l) xmm77

Figure B.43: The IRAC-3.6μm images from SWIRE in the XMM-LSS field, overlaid with the radio image from GMRT data.

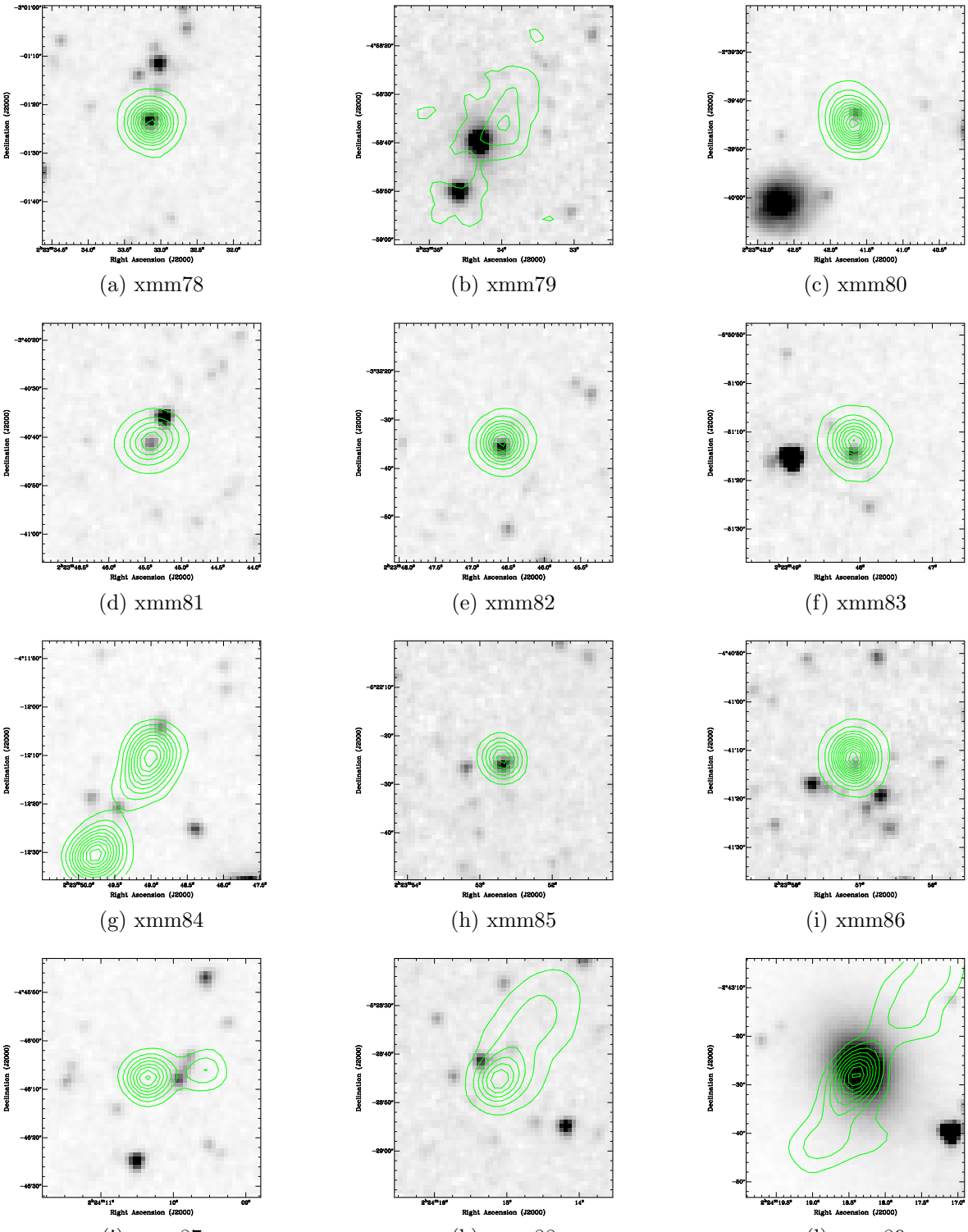

(a) xmm78 (b) xmm79 (c) xmm80

(d) xmm81 (e) xmm82 (f) xmm83

(g) xmm84 (h) xmm85 (i) xmm86

(j) xmm87 (k) xmm88 (l) xmm89

Figure B.44: The IRAC-3.6μm images from SWIRE in the XMM-LSS field, overlaid with the radio image from GMRT data.

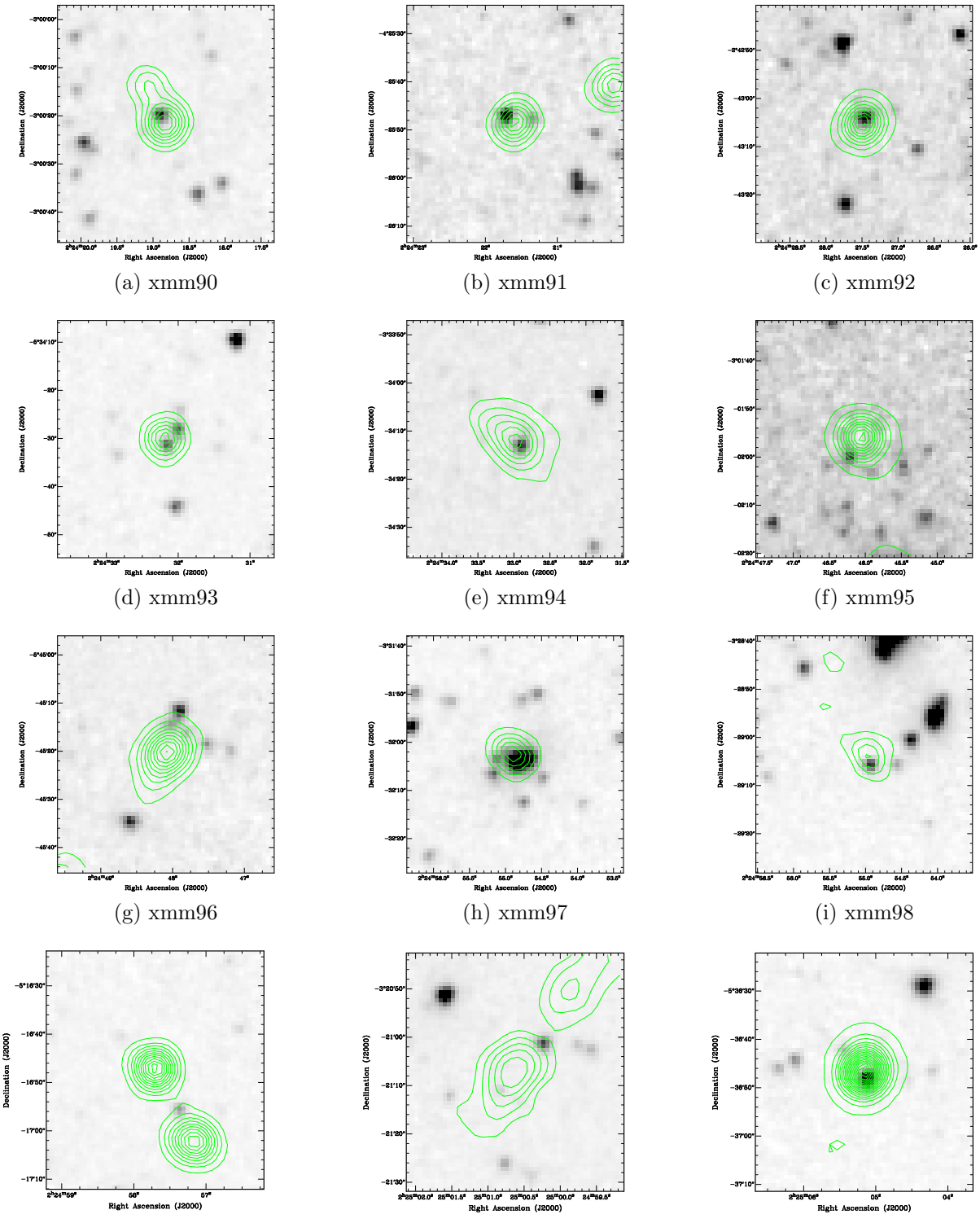

(a) xmm90 (b) xmm91 (c) xmm92

(d) xmm93 (e) xmm94 (f) xmm95

(g) xmm96 (h) xmm97 (i) xmm98

(j) xmm99 (k) xmm100 (l) xmm101

Figure B.45: The IRAC-3.6μm images from SWIRE in the XMM-LSS field, overlaid with the radio image from GMRT data.

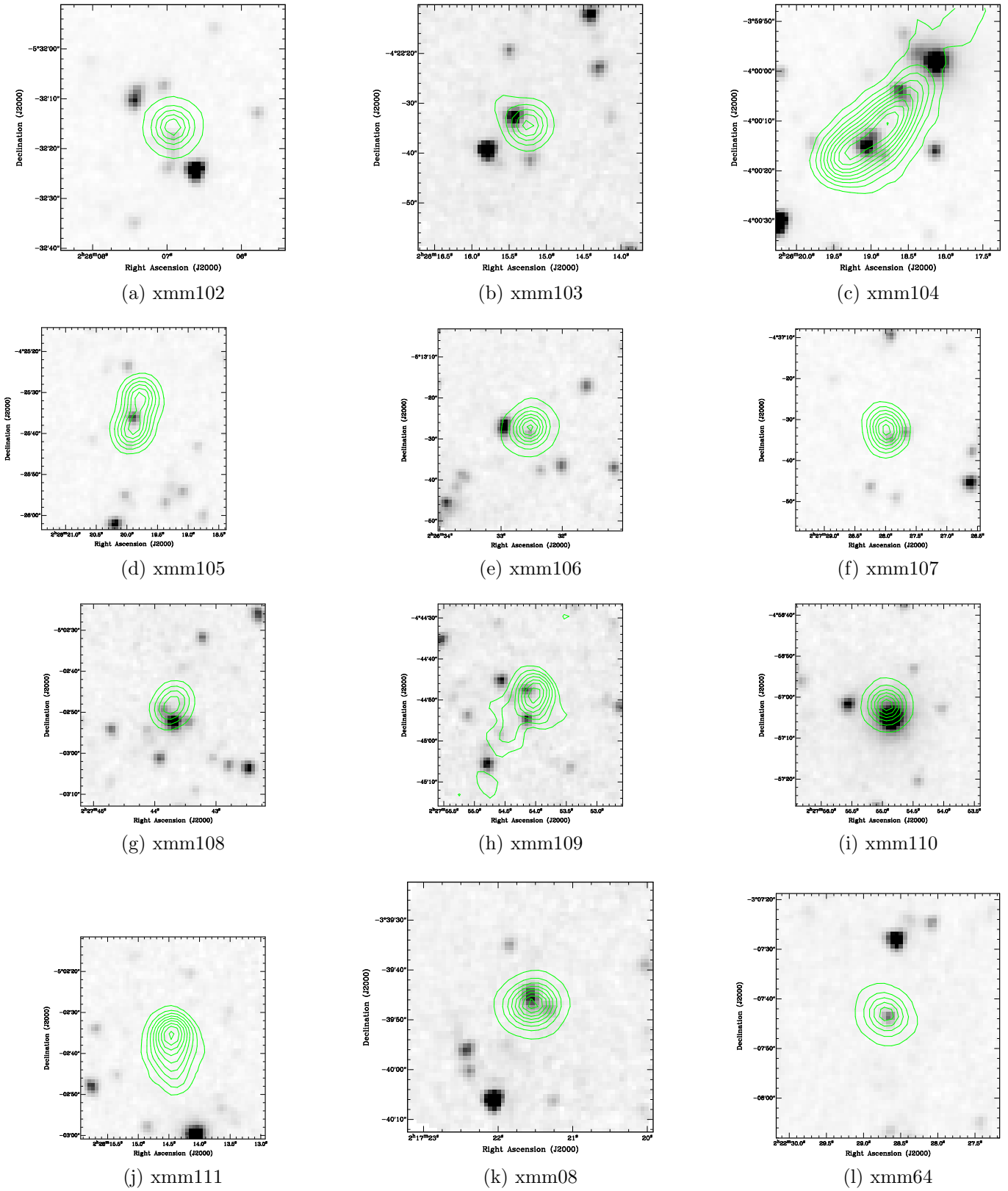

(a) xmm102 (b) xmm103 (c) xmm104

(d) xmm105 (e) xmm106 (f) xmm107

(g) xmm108 (h) xmm109 (i) xmm110

(j) xmm111 (k) xmm08 (l) xmm64

Figure B.46: The IRAC-3.6μm images from SWIRE in the XMM-LSS field, overlaid with the radio image from GMRT data.

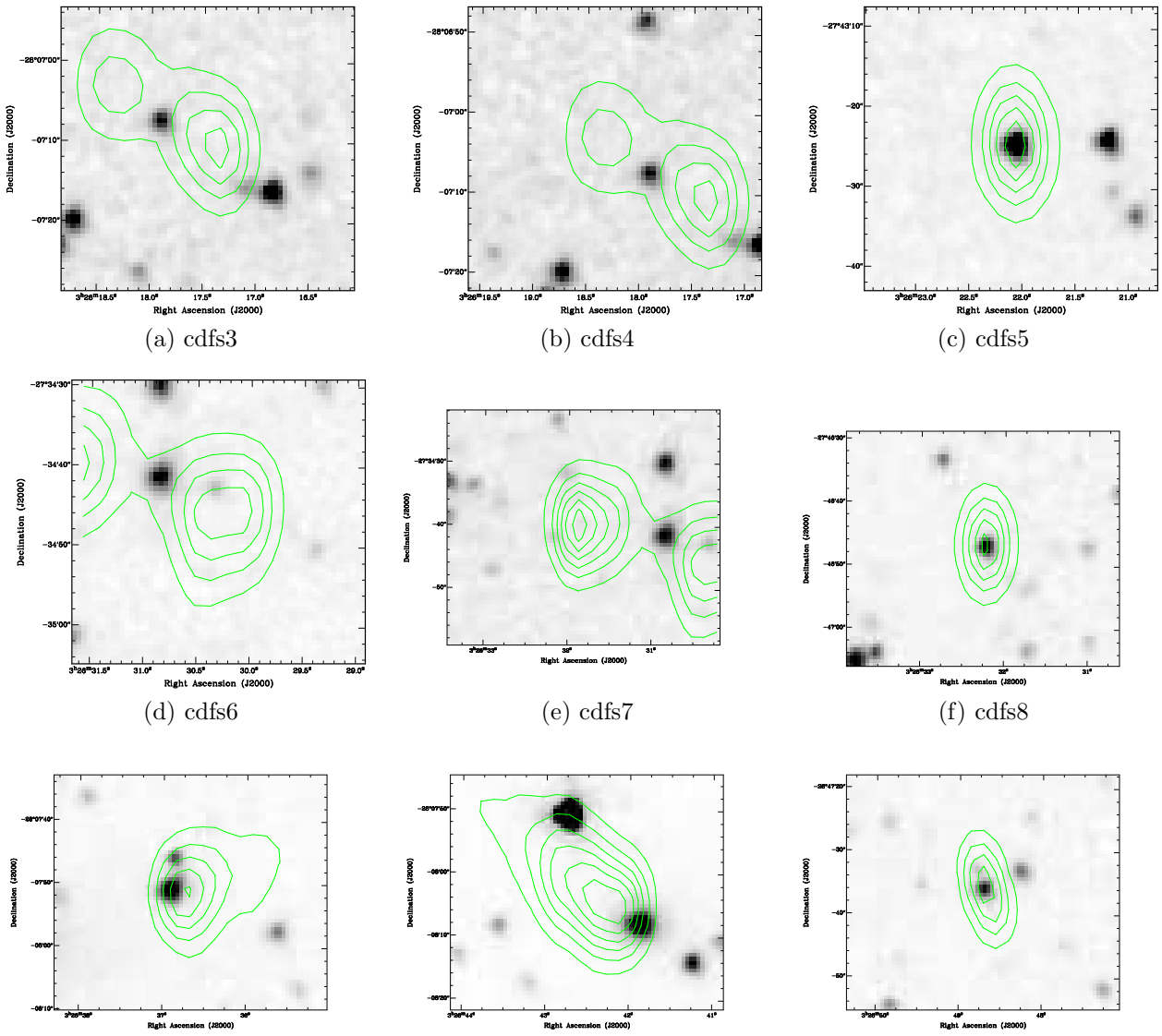

(a) cdfs3 (b) cdfs4 (c) cdfs5

(d) cdfs6 (e) cdfs7 (f) cdfs8

(g) cdfs9 (h) cdfs10 (i) cdfs11

Figure B.47: The IRAC-3.6μm images from SWIRE in the CDFS field, overlaid with the radio image from ATLAS.

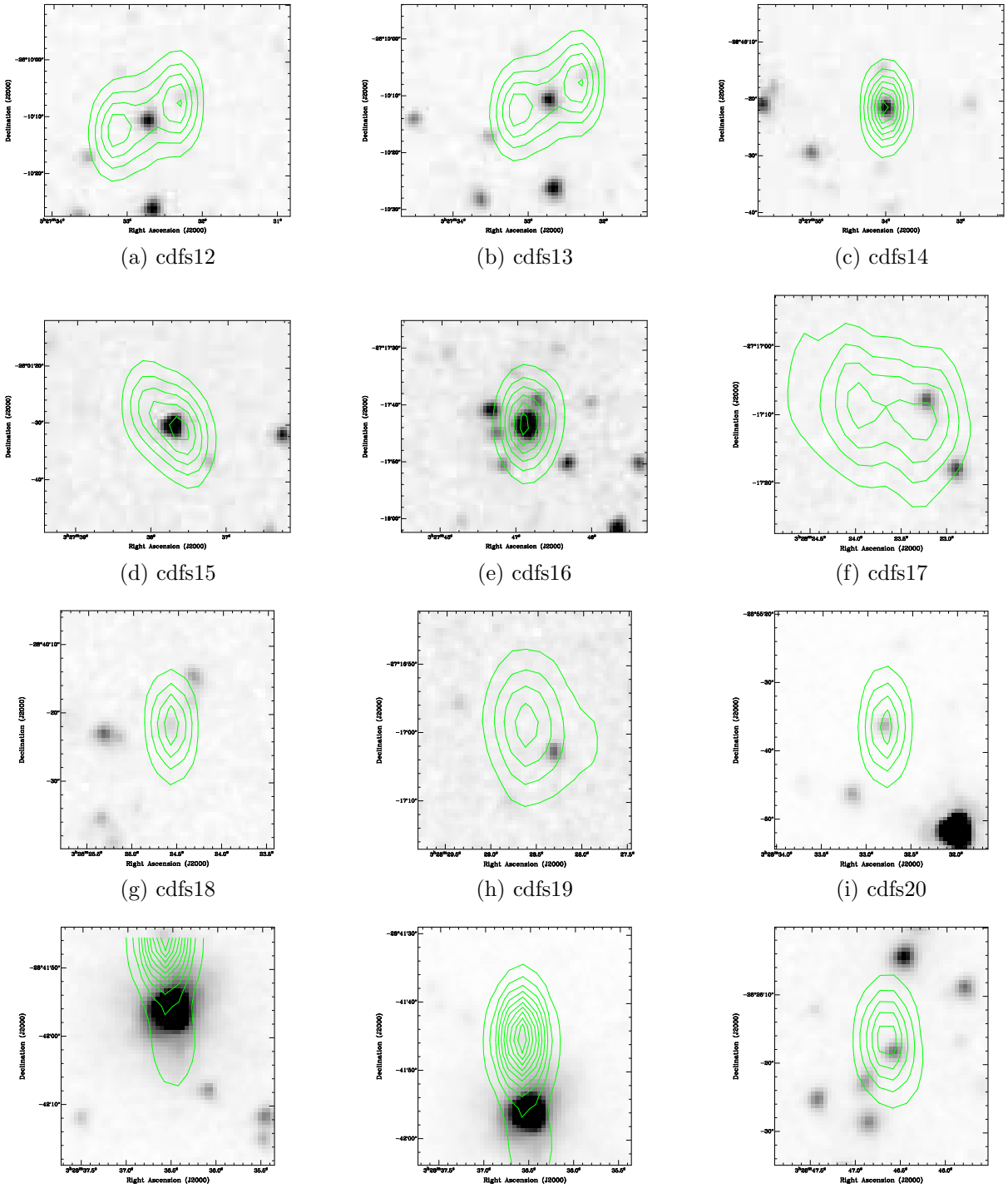

(a) cdfs12 (b) cdfs13 (c) cdfs14

(d) cdfs15 (e) cdfs16 (f) cdfs17

(g) cdfs18 (h) cdfs19 (i) cdfs20

(j) cdfs21 (k) cdfs22 (l) cdfs23

Figure B.48: The IRAC-3.6μm images from SWIRE in the CDFS field, overlaid with the radio image from ATLAS.

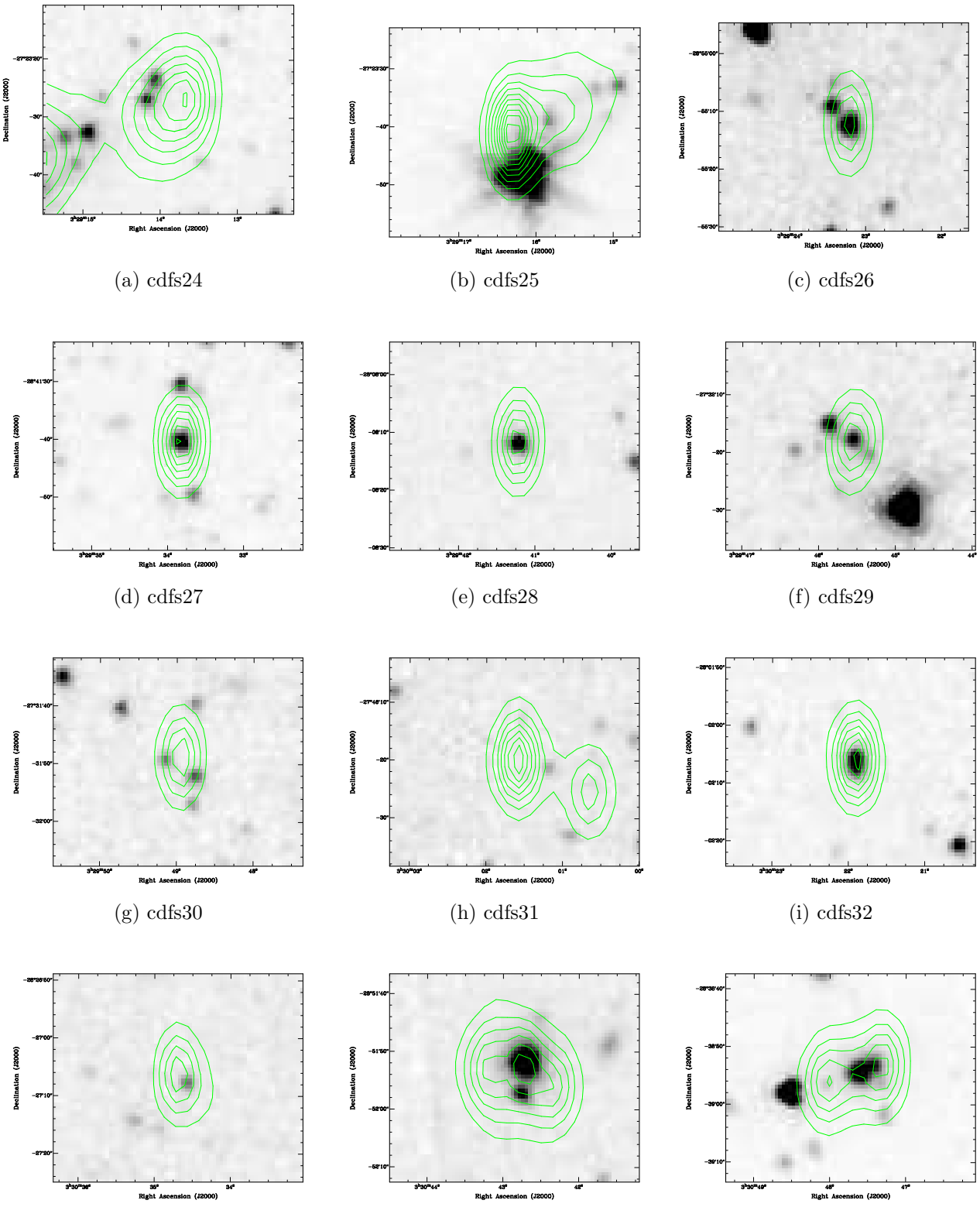

(a) cdfs24 (b) cdfs25 (c) cdfs26

(d) cdfs27 (e) cdfs28 (f) cdfs29

(g) cdfs30 (h) cdfs31 (i) cdfs32

(j) cdfs33 (k) cdfs34 (l) cdfs35

Figure B.49: The IRAC-3.6μm images from SWIRE in the CDFS field, overlaid with the radio image from ATLAS.

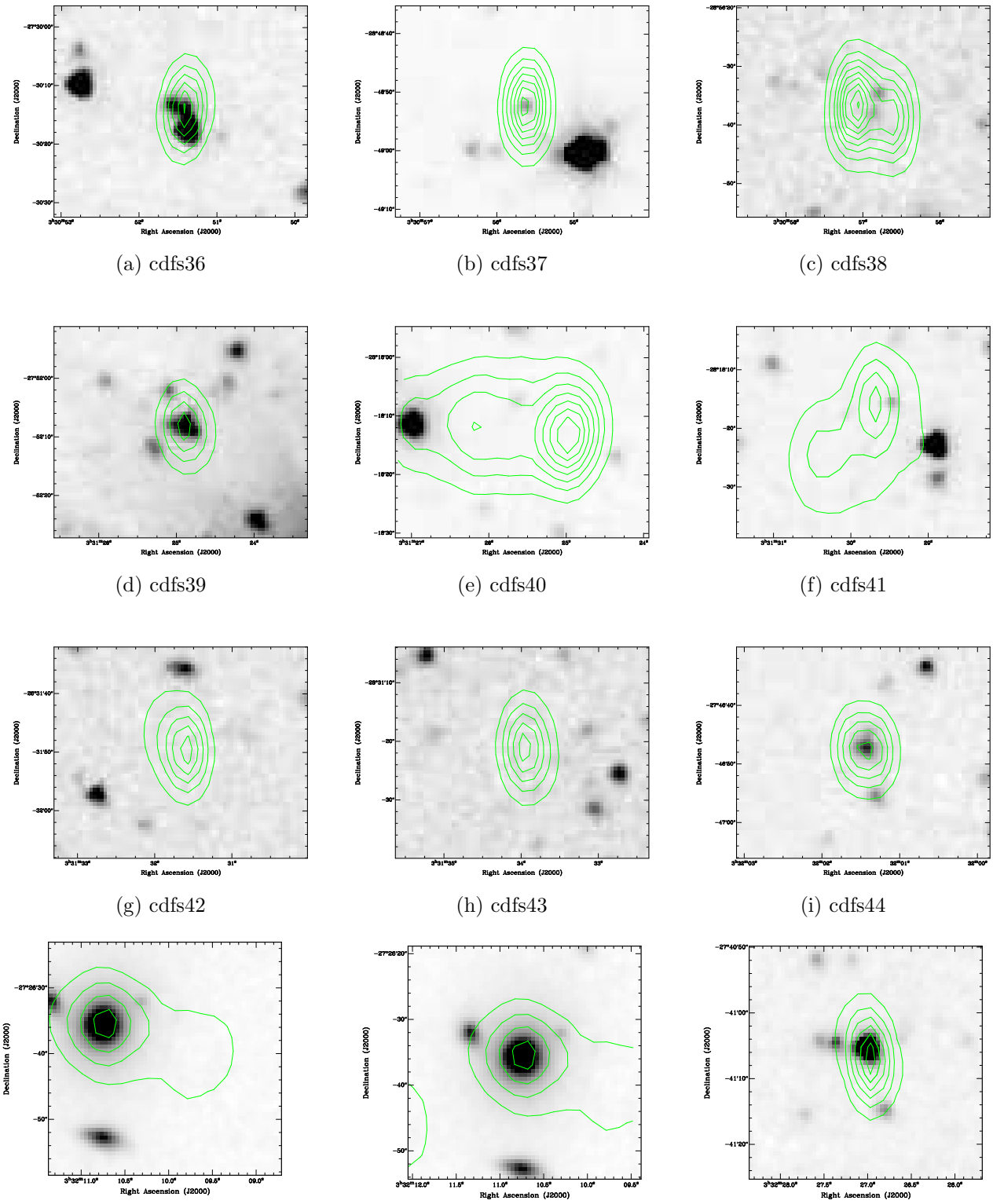

(a) cdfs36 (b) cdfs37 (c) cdfs38

(d) cdfs39 (e) cdfs40 (f) cdfs41

(g) cdfs42 (h) cdfs43 (i) cdfs44

(j) cdfs45 (k) cdfs46 (l) cdfs47

Figure B.50: The IRAC-3.6μm images from SWIRE in the CDFS field, overlaid with the radio image from ATLAS.

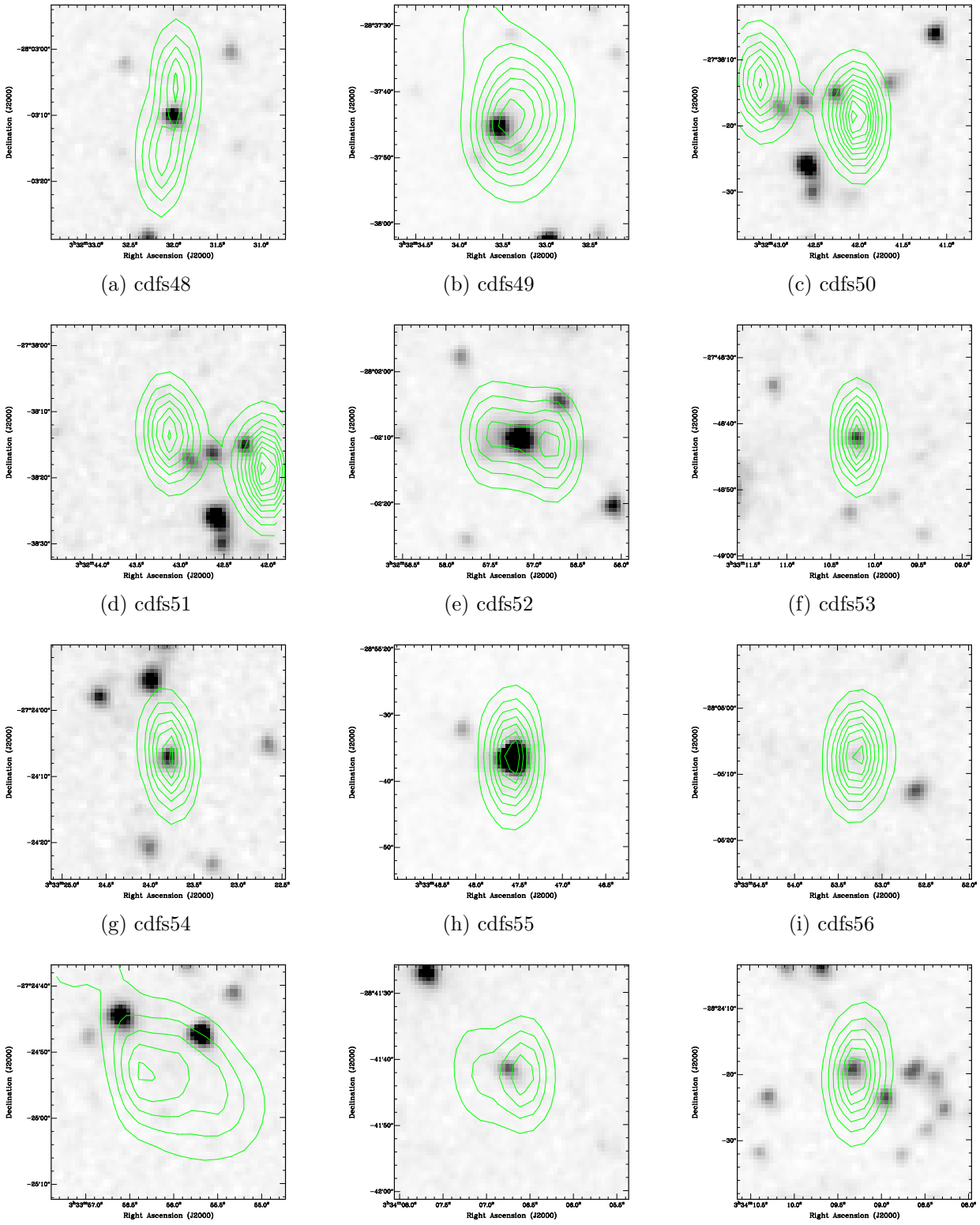

(a) cdfs48 (b) cdfs49 (c) cdfs50

(d) cdfs51 (e) cdfs52 (f) cdfs53

(g) cdfs54 (h) cdfs55 (i) cdfs56

(j) cdfs57 (k) cdfs58 (l) cdfs59

Figure B.51: The IRAC-3.6μm images from SWIRE in the CDFS field, overlaid with the radio image from ATLAS.

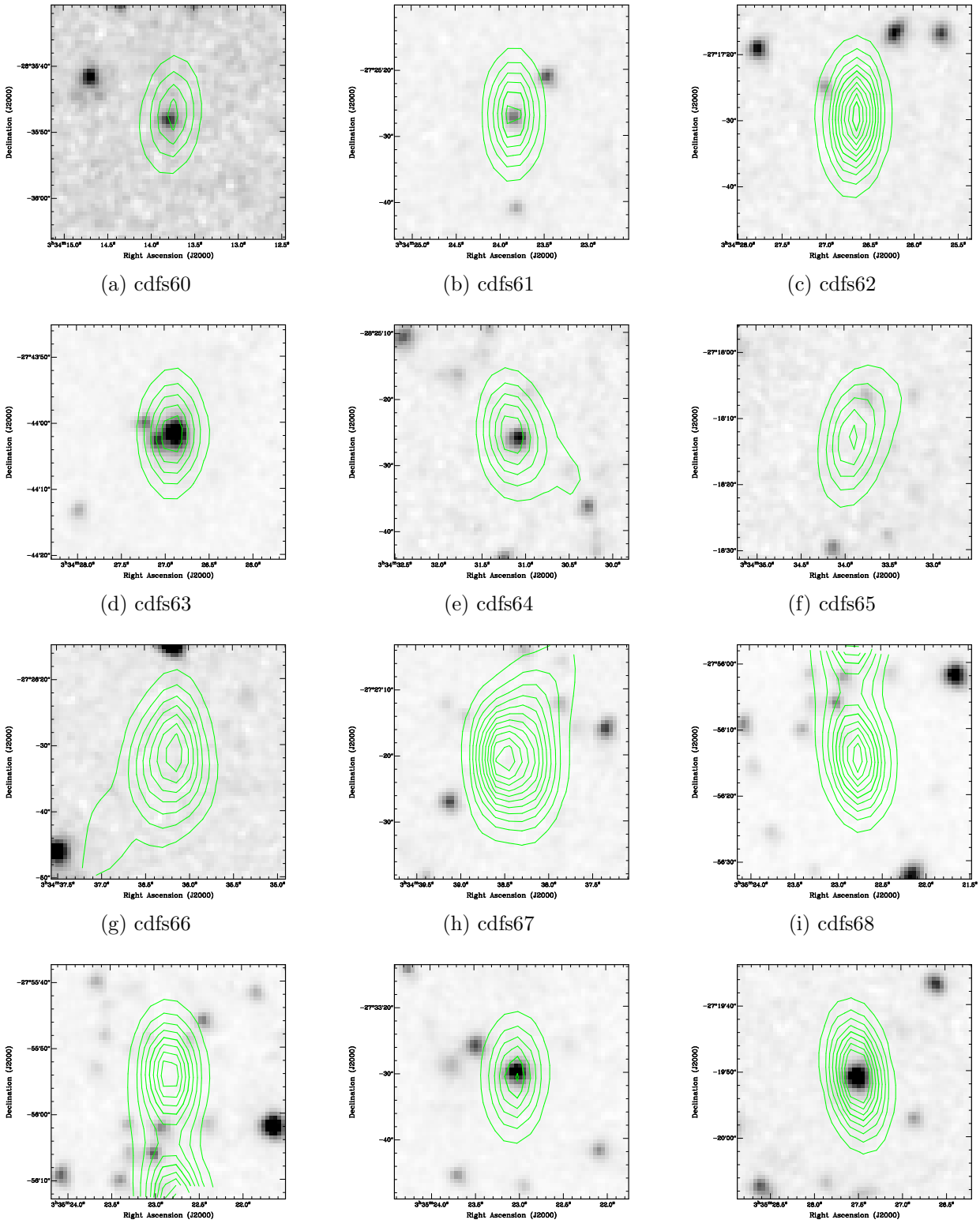

(a) cdfs60 (b) cdfs61 (c) cdfs62

(d) cdfs63 (e) cdfs64 (f) cdfs65

(g) cdfs66 (h) cdfs67 (i) cdfs68

(j) cdfs69 (k) cdfs70 (l) cdfs71

Figure B.52: The IRAC-3.6μm images from SWIRE in the CDFS field, overlaid with the radio image from ATLAS.

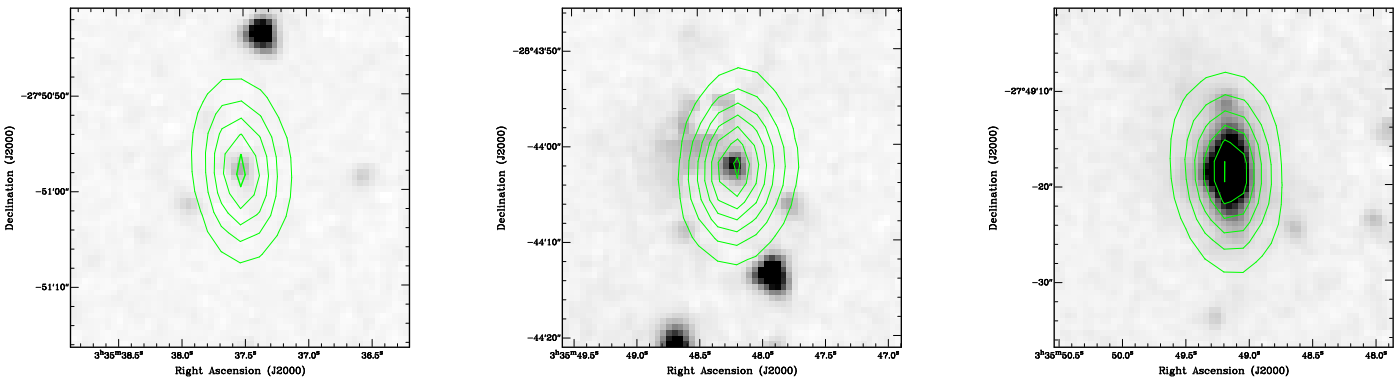

(a) cdfs73 (b) cdfs74 (c) cdfs75

Figure B.53: The IRAC-3.6μm images from SWIRE in the CDFS field, overlaid with the radio image from ATLAS.

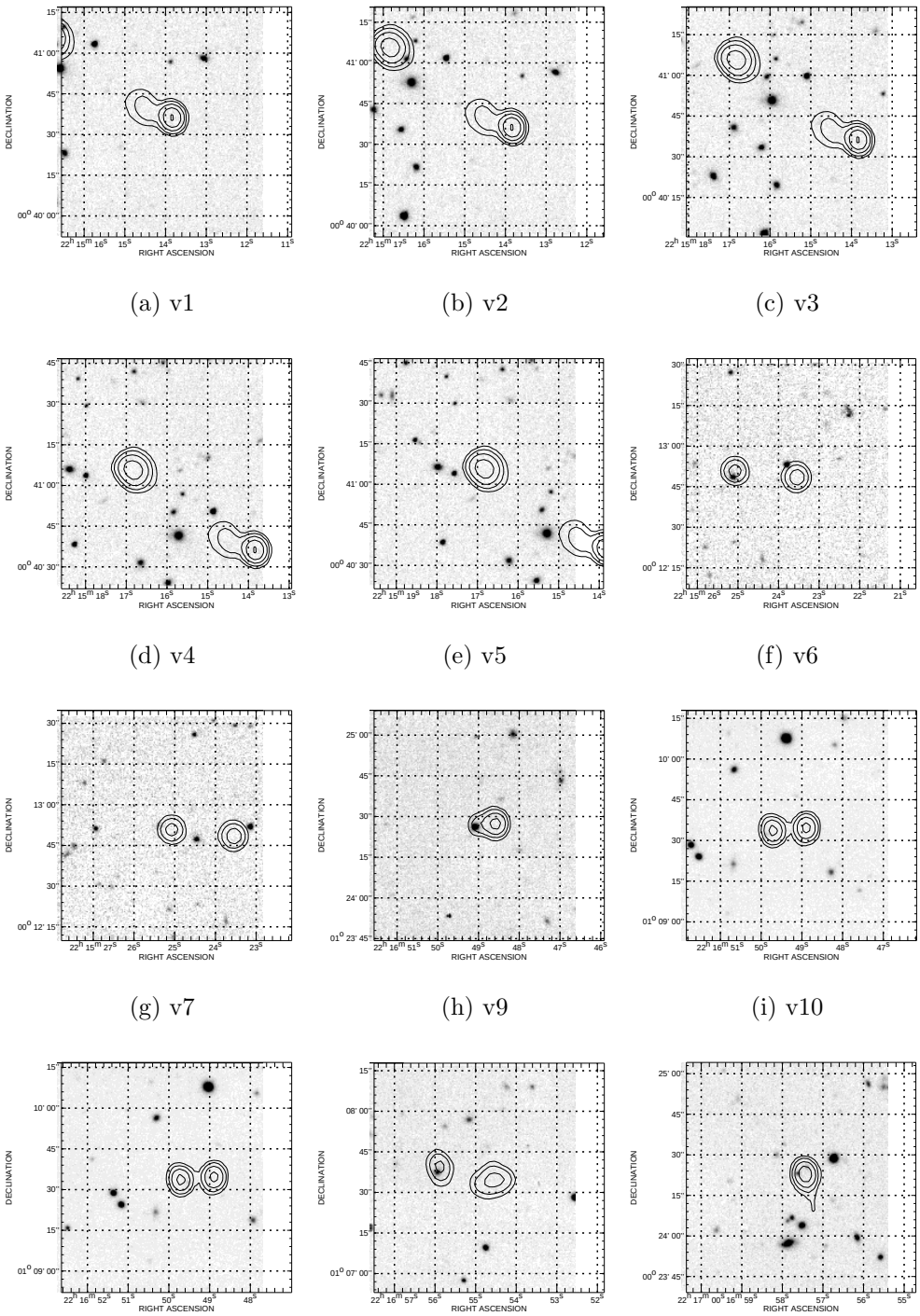

(a) v1 (b) v2 (c) v3

(d) v4 (e) v5 (f) v6

(g) v7 (h) v9 (i) v10

(j) v11 (k) v12 (l) v13

Figure B.54: The K-band images from DXS in the VIMOS field, overlaid with the radio image from FIRST data.

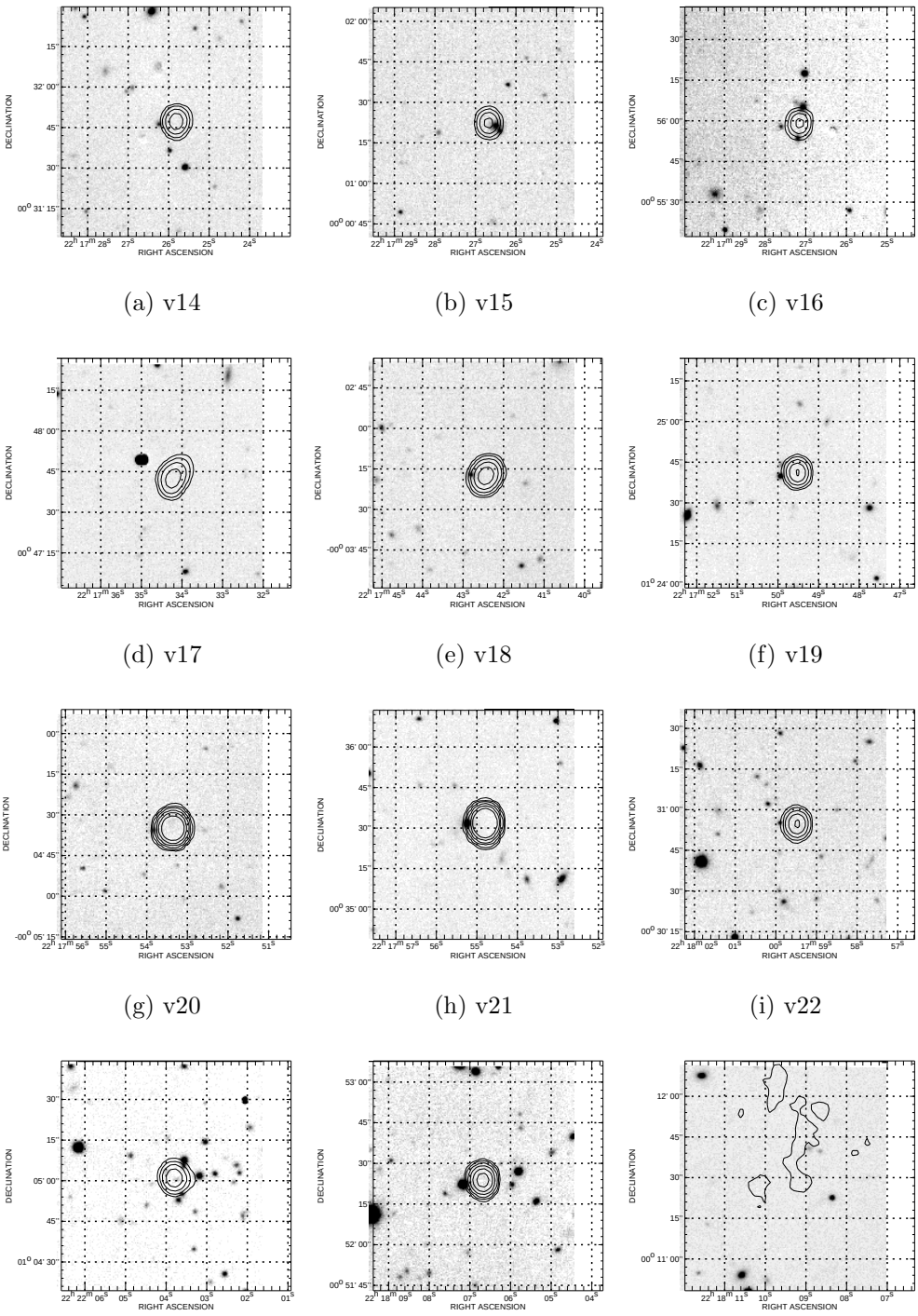

(a) v14 (b) v15 (c) v16

(d) v17 (e) v18 (f) v19

(g) v20 (h) v21 (i) v22

(j) v66 (k) v24 (l) v25

Figure B.55: The K-band images from DXS in the VIMOS field, overlaid with the radio image from FIRST data.

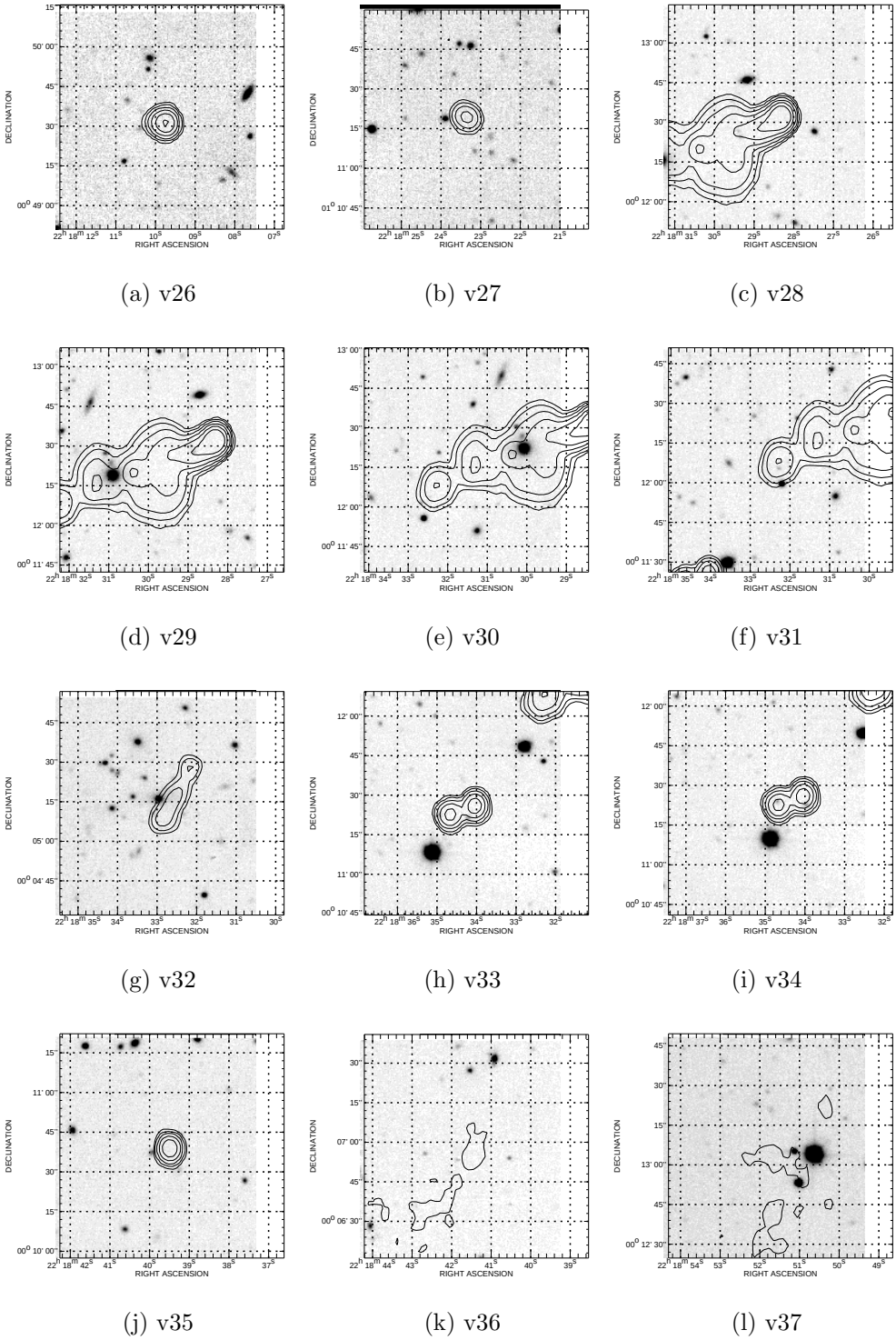

(a) v26 (b) v27 (c) v28

(d) v29 (e) v30 (f) v31

(g) v32 (h) v33 (i) v34

(j) v35 (k) v36 (l) v37

Figure B.56: The K-band images from DXS in the VIMOS field, overlaid with the radio image from FIRST data.

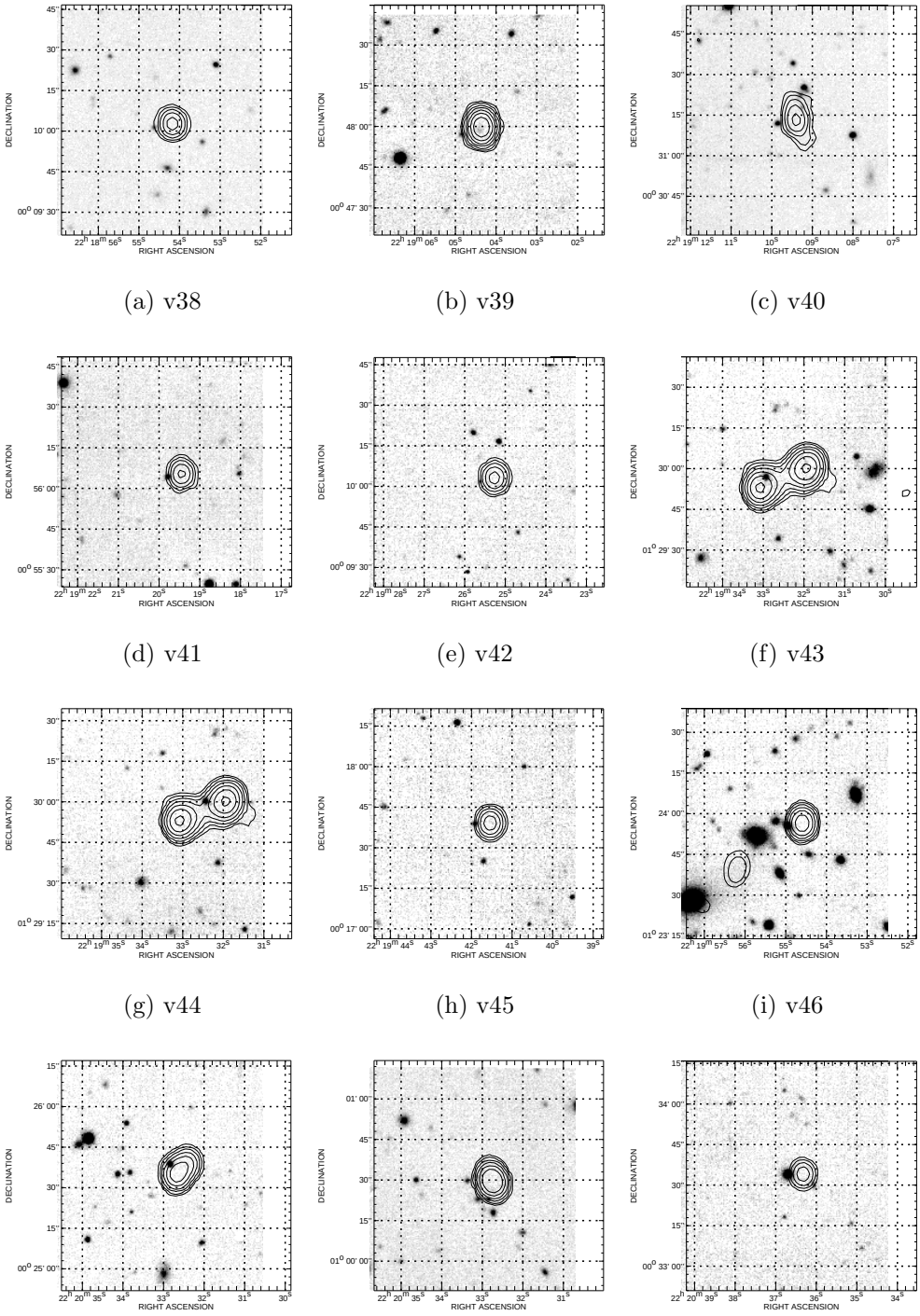

(a) v38 (b) v39 (c) v40

(d) v41 (e) v42 (f) v43

(g) v44 (h) v45 (i) v46

(j) v47 (k) v48 (l) v49

Figure B.57: The K-band images from DXS in the VIMOS field, overlaid with the radio image from FIRST data.

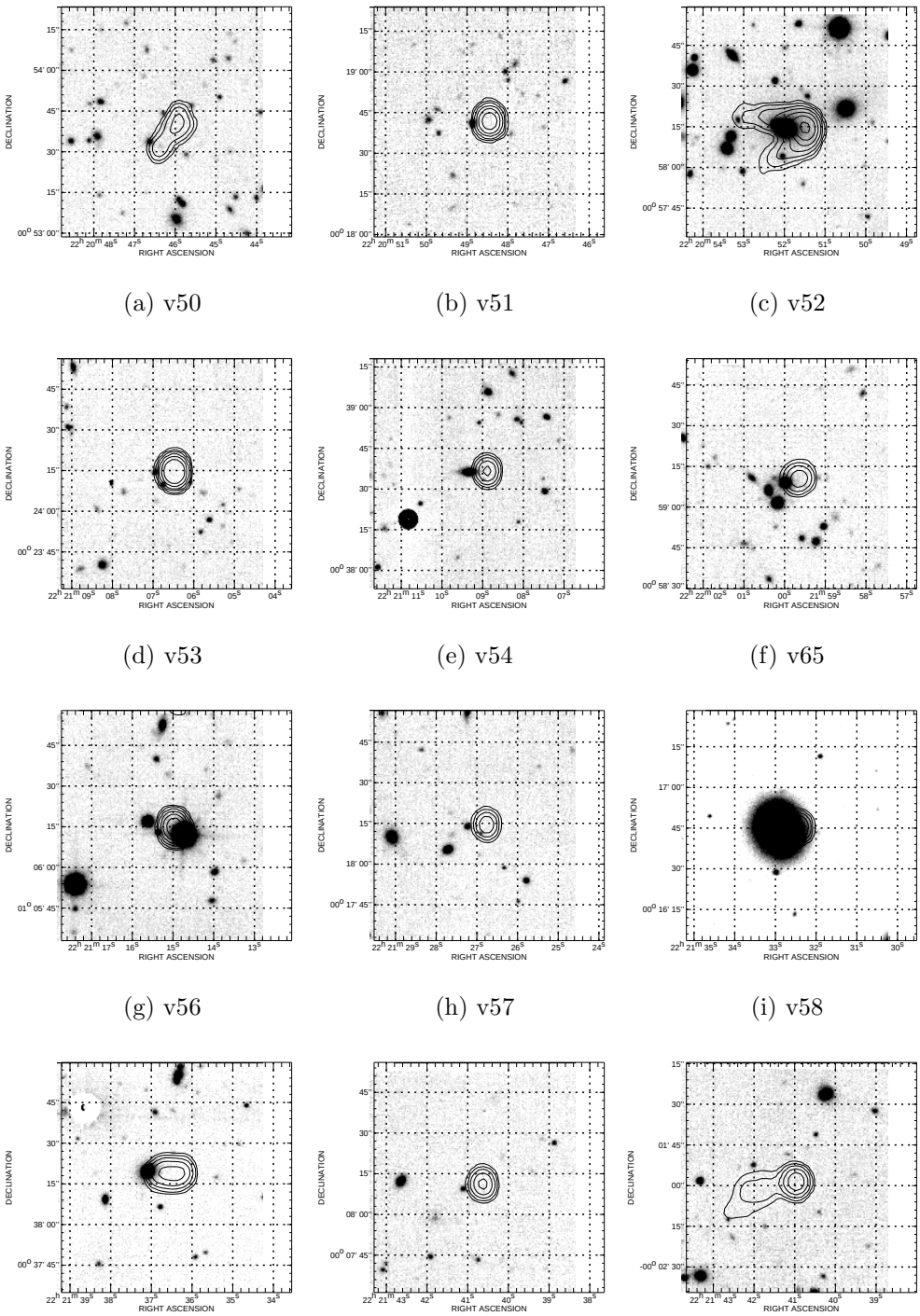

(a) v50 (b) v51 (c) v52

(d) v53 (e) v54 (f) v65

(g) v56 (h) v57 (i) v58

(j) v59 (k) v60 (l) v61

Figure B.58: The K-band images from DXS in the VIMOS field, overlaid with the radio image from FIRST data.

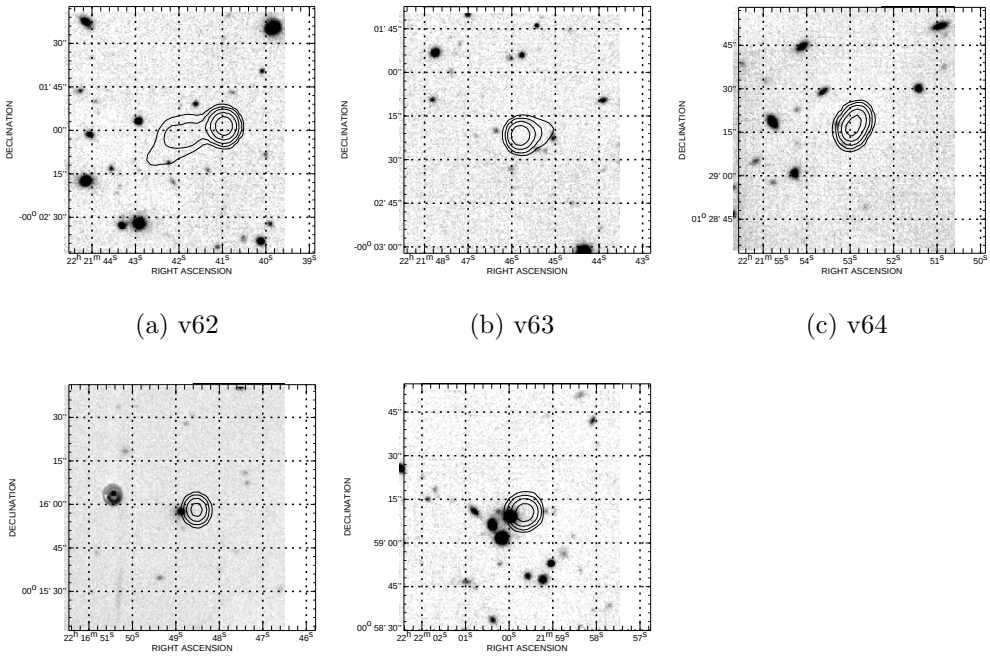

(a) v62 (b) v63 (c) v64

(d) v8 (e) v65

Figure B.59: The K-band images from DXS in the VIMOS field, overlaid with the radio image from FIRST data.

Appendix C

The discovery of a typical radio galaxy at $z = 4.88$

In this appendix I present the work that appeared in the published paper on one of the radio galaxies from my sample. The paper was written by my supervisor Dr. Matt Jarvis, but I contributed significantly. Specifically the sample selection was initially carried out by me as detailed in Chapter 2. I also took part in carrying out the observations and reduced the spectra from this run. I compiled all of the necessary imaging data, but the interpretation was done by Dr. Matt Jarvis, I therefore only present it here in the appendix for completeness.

Abstract

We report the discovery of a $z = 4.88$ radio galaxy discovered with a new technique which does not rely on pre-selection of a sample based on radio properties such as steep-spectral index or small angular size. This radio galaxy was discovered in the Elais-N2 field and has a spectral index of $\alpha = 0.75$, i.e. not ultra-steep spectrum. It also has a luminosity consistent with being drawn from the break of the radio luminosity function and can therefore be considered as a typical radio galaxy. Using the *Spitzer*-SWIRE data over this field we find that the host galaxy is consistent with being similarly massive to the lower redshift powerful radio galaxies ($\sim 1-3L^{\star}$). We note however, that at $z = 4.88$ the Hα line is redshifted into the IRAC 3.6μm filter and some of the flux in this band may be due to this rather than stellar continuum emission. The discovery of such a distant radio source from our initial spectroscopic observations demonstrates the promise of our survey for finding the most distant radio sources.

Introduction

One of the major objectives in extragalactic astronomy today is to pin down the Epoch of Reionization (EoR), where the Dark Ages comes to an end and UV photons are able to propagate throughout the Universe and ionize neutral hydrogen. Although the process of reionization is expected to occur over a relatively short time interval (Gnedin 2000), the HI absorption seen in the spectra of high-redshift quasars (Fan et al. 2006) suggests that $z \sim 6$ marks the threshold of the EoR, while the 5-year WMAP data (Dunkley et al. 2009) suggest that it may have begun at a much earlier time, $z = 11.0 \pm 1.4$.

The first opportunity to make detailed studies of the neutral hydrogen in the EoR is almost upon us with the imminent commissioning of the Low Frequency Array (LOFAR) and the Murchison Widefield Array (MWA). LOFAR and the MWA will be able to detect the neutral hydrogen 21 cm transition line at redshifts beyond $z \sim 6$, predominantly searching for signatures via statistical fluctuations in the power spectrum (e.g. Iliev et al. 2008). However, another avenue for direct measurement of the neutral hydrogen fraction in the early Universe comes from observing the 21 cm forest against a bright distant source. This is also one of the key science questions for the Square Kilometre Array (SKA; see e.g. Carilli et al. 2002).

However, such experiments obviously require a population of $z > 6$ radio-loud sources against which the 21 cm absorption can be viewed and there is still much uncertainty over the number of such sources. There have been many surveys to find very high-redshift radio galaxies (HzRGs; e.g. De Breuck et al. 2000, 2002; Jarvis et al. 2001a,b; Best et al. 2003; De Breuck et al. 2004; Jarvis et al. 2004; Cruz et al. 2006, 2007; Brookes et al. 2008) yet the highest redshift radio galaxy known "only" lies at $z = 5.19$ (van Breugel et al. 1999). See Miley & De Breuck (2008) for a review on the various properties of distant radio galaxies.

This has led to a number of authors proposing that there is a "cut-off" in the radio source population at high redshift (e.g. Dunlop & Peacock 1990; Shaver et al. 1996; Wall et al. 2005). However, analyses by other authors (e.g. Jarvis & Rawlings 2000; Jarvis et al. 2001c) suggest that the sharpest reported declines may be the result of a range of selection effects and/or assumptions about the brightness of radio galaxy hosts (i.e. the $K-z$ relation; Lilly & Longair 1984) holding to redshifts beyond those where there are any constraints.

Tracing the space-density evolution of these powerful sources would have significant implications for the build-up of the relation between the mass of a galaxy bulge and its central supermassive black hole (Magorrian et al. 1998) given the AGN-feedback prescriptions in semi-analytic models of galaxy formation (Bower et al. 2006; Croton et al. 2006). As the quasar nucleus is obscured in radio galaxies they provide us with a clear view of the stellar emission from the host galaxy. With past searches for the HzRGs it has become apparent that powerful radio sources trace the most massive galaxies over the history of the Universe (e.g. Jarvis et al. 2001b).

They have therefore been used as beacons to massive galaxies and (proto-)clusters at early times allowing the build-up of structure to be traced (e.g. Venemans et al. 2005; Miley et al. 2006). Furthermore, the HzRGs themselves may also be crucial in determining the impact that powerful radio activity has on the larger scale environments (Rawlings & Jarvis 2004; Gopal-Krishna & Wiita 2001). Thus, our survey not only aims to produce the first sample of distant radio sources for investigating the EoR but also provide a much larger sample for investigations of the formation and evolution of the most massive galaxies at the highest redshifts.

Here we report the discovery of the second most distant radio galaxy, found in preliminary observations from our new, highly efficient survey to search for the most distant radio sources.

Throughout this letter the AB magnitude system is used (Oke & Gunn, 1983), and a standard cosmology is assumed in which $H_0 = 72$ km s^{-1}, $\Omega_M = 0.26$ and $\Omega_\Lambda = 0.74$ (Dunkley et al. 2009).

Our Survey

HzRGs (by which we mean those at $z > 4$) represent only a very small fraction of all radio

sources at a given flux-density limit and it is necessary to filter out low-redshift contaminants before performing spectroscopy. This has previously been done by applying a filter based on radio properties such as steep spectral index (e.g. Chambers et al. 1996; Blundell et al. 1998; De Breuck et al, 2002; Cohen et al. 2004; Cruz et al. 2006). The next stage has typically been to take K-band images of the targets, since radio galaxies follow an extremely tight locus in the K-band Hubble diagram (Jarvis et al. 2001b; Willott et al; 2003; Bryant et al. 2009) and therefore HzRGs will be faint. However, although K-band imaging is very reliable at identifying radio galaxies, these observations are very expensive, needing to reach $K \sim 20$ to detect sources at the epoch where the AGN density peaks ($z \sim 2$; Jarvis & Rawlings 2000; Willott et al. 2001). Unfortunately, even after filtering on radio source properties, such as angular size and spectral index, the fraction of HzRGs remains low – e.g., 1/68 sources in the 6C** sample of Cruz et al. (2007) lies at $z > 4$ – so most of the follow-up near-infrared imaging simply rules out high-redshift targets. We are now in a position to turn this technique around and use large radio surveys over patches of sky which have relatively deep and wide near-infrared data.

The recent advent of wide-field deep near-infrared surveys has opened up a new path for finding such objects. The *Spitzer*-SWIRE (Lonsdale et al. 2003) and the UKIDSS Deep Extragalactic Survey (DXS; see e.g. Warren et al. 2007) are deep enough to reliably eliminate virtually all $z < 2$ radio galaxies. Therefore by targeting only radio sources which are very faint or not detected in the *Spitzer*-IRAC channels 1 and 2 or the DXS K-band imaging, we are likely to be probing radio sources in the 3 Gyr after the Big Bang.

We have cross-matched the *Spitzer*-SWIRE data with sources at > 10mJy from the 1.4 GHz FIRST survey (Becker et al. 1995) in the Lockman Hole, Elais-N1 and Elais-N2 fields, which together cover a total of $\sim$ 24 square degrees. For our initial search we use a 3.6μm limit of $< 30\mu$Jy in a 1.9 arcsec radius aperture, as given in the SWIRE catalogues. Our choice of radio flux-density limit ensures that all objects at $z > 2$ are above the break in the radio luminosity function and will therefore possess strong emission lines, particularly Lyα which is redshifted into the optical part of the spectrum, allowing redshift identification in much shorter integration times than if signal-to-noise on the continuum is needed.

Simulations (Jarvis & Rawlings 2004; Wilman et al. 2008) predict that $\sim$1 in 15 (adopting the average model; Fig. C.1) of these sources will lie at $z > 4$. This flux-density limit and faint near-infrared magnitude cut also ensures that the number of lower-redshift lower luminosity radio sources are also reduced significantly (see e.g. Fig. C.1) with only ~ 1 in 10 expected at $z > 2$ in 24 square degrees. The survey will be described in more detail in a forthcoming paper (Teimourian et al. in prep.).

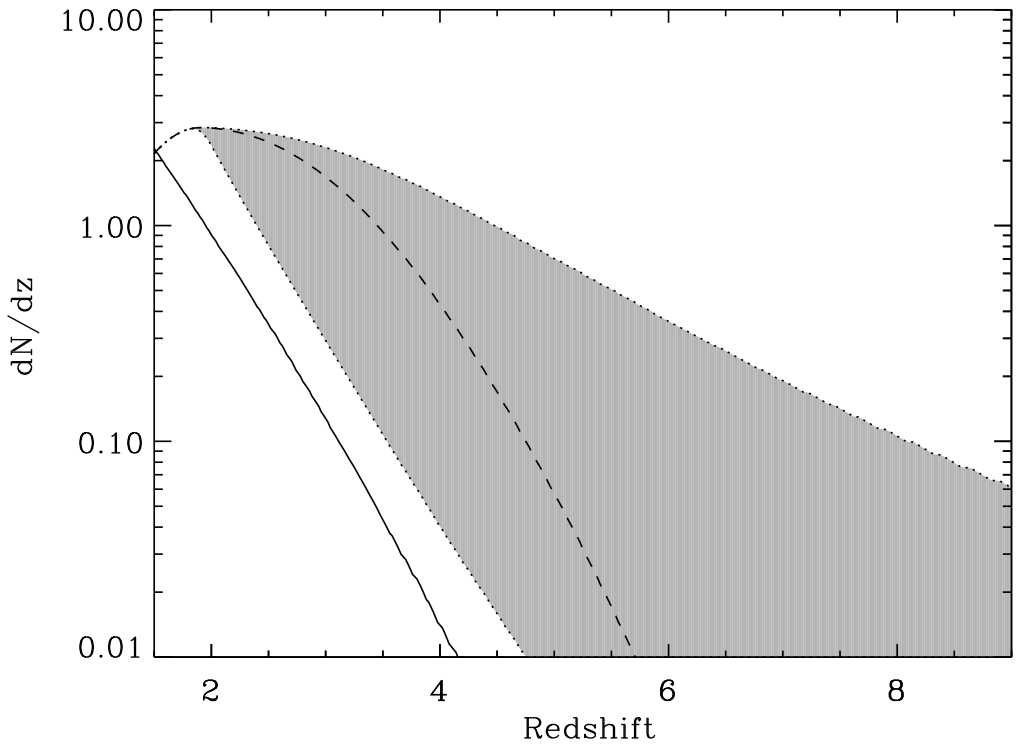

Figure C.1: Expected number of radio sources above 10 mJy as a function of redshift per square degree. The dark solid line is the expected number of low-luminosity radio sources which would have low-luminosity emission lines and be very difficult to obtain redshifts for. The grey banded area shows the degree of uncertainty in the high-redshift evolution of the more powerful, typically FRII sources, from a constant comoving space density and one with a steady decline [see Jarvis & Rawlings (2000) for more details]. The dashed line is the best-fit model C from Willott et al. (2001).

A radio galaxy at $z = 4.88$

J163912.11+405236.5 is detected in the FIRST survey with a flux-density of 22.5 mJy and is unresolved at the 5 arcsec resolution of this survey. This source is also identified in the Northern VLA Sky Survey (NVSS; Condon et al. 1998) with $S_{1.4\mathrm{GHz}} = 21.8 \pm 0.8$ mJy and is therefore consistent with being point like. There is also a source detected in the 325 MHz Westerbork Northern Sky Survey (WENSS; Rengelink et al. 1997) at 16 39 12.17 +40 52 40.3 (J2000) which is 3.6 arcsec away from the FIRST centroid, therefore we associate this source with the FIRST source. The WENSS catalogue gives a flux-density of 67 ± 5 mJy for this source. Assuming a power-law spectral index between 325 MHz and 1.4GHz the spectral index of the source is therefore $\alpha = 0.75 \pm 0.05$[1]. Thus this source would not fall into the category of ultra-steep spectrum sources which have been used to search for high-redshift radio galaxies

[1]We use the convention for spectral index $S_\nu \propto \nu^{-\alpha}$

in recent years. In Fig. C.2 we show the 3.6μm image from the *Spitzer*-SWIRE survey overlaid with the radio image from the FIRST survey. There is a very faint source in the 3.6μm image at the centre of the radio position which we identify as the host galaxy. As this object is on the SWIRE survey area there are also a wealth of imaging data from the INT at optical wavelengths which allow us to constrain the continuum emission from this object. We also use the SWIRE data to constrain the brightness of the source from 3.6-24μm. Photometry of the host galaxy is presented in Table C.1.

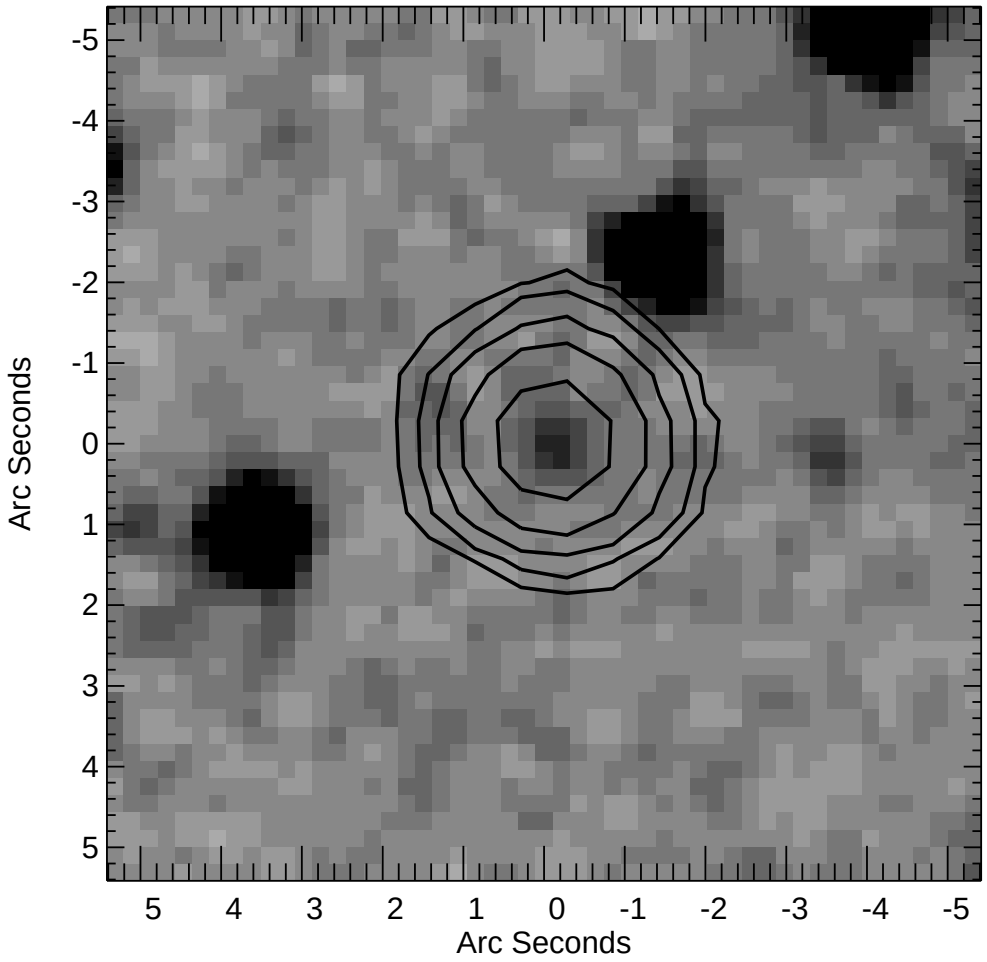

Figure C.2: The *Spitzer*-3.6μm image (greyscale) overlaid with radio contours from the FIRST survey. Contour levels are 0.8, 1.6, 3.2, 6.4 and 12.8 mJy/beam. One can see the faint source at the centre of the radio emission at 16 39 12.11 +40 52 36.5 which we identify as the host galaxy.

The Lyman-α emission

We observed the radio source J163912.11+405236.5 on the 27th April 2009 with the ISIS spectrograph on the William Herschel Telescope. We used the standard 5300Å dichroic to reflect the blue light to an EEV12 4096×2048 pixel^2 CCD using the R300B grism. The red light was dispersed through the R158R grism on to RED+ 4096×2048 pixel^2 CCD. We used a slit width of 2 arcsec which gave a resolution of 8.6Å in the blue arm and 16.5Å in the red arm.

The data were bias subtracted, illumination corrected and flat-fielded using standard IRAF tasks. Wavelength calibration was carried out using CuNe+CuAr lamps and flux-calibration was done using the spectrophotometric standard Feige 34.

In Fig. C.3 we show the 1D-spectrum of the radio galaxy J163912.11+405236.5 which displays a strong emission line at 7149Å, which we identify as Lyman-α due to its blue cut-off and broader red wing, at a redshift of $z = 4.88$. The line has a flux of 1.85×10^{-19} W m^{-2}, which at this redshift corresponds to a luminosity of $L_{\mathrm{Ly}\alpha} = 4.7 \times 10^{36}$ W and a rest-frame full-width half maximum of 1040 km s^{-1}, i.e. a narrow-line AGN. There are no other emission lines in our spectra which also suggest that the line is indeed Lyman-α rather than other common emission lines in radio galaxies. However, one possibility is that the emission line is [OII]λ3727 at $z = 0.92$. If this were indeed [OII] from a narrow-line AGN then we would expect to see the CII]λ2326 and the CIII]λ1909 emission line in the blue end of the spectrum, for which we find no evidence, in addition to a much brighter host galaxy. Another possibility is that it is a starburst galaxy. Using the relation of Kewley, Geller & Jansen (2004) the [OII] luminosity would correspond to a star-formation rate of $SFR \sim 11 \odot$ yr^{-1}. The radio emission one would expect from this starburst galaxy is greater than three orders of magnitudes fainter than what we observe. We are therefore confident that the line is Lyα at $z = 4.88$.

This is the second highest redshift radio galaxy known to date and demonstrates the promise of our new survey in finding high-redshift radio sources. Given the redshift, the radio luminosity of the source at 325 MHz is $\log_{10}(L_{325\mathrm{MHz}}/\ \mathrm{W\ Hz^{-1}\ sr^{-1}}) = 26.94$ and $\log_{10}(L_{1400\mathrm{MHz}}/\ \mathrm{W\ Hz^{-1}\ sr^{-1}}) = 26.47$ at 1.4 GHz. This is very close to the break luminosity in the radio luminosity function of Willott et al (2001) which is where the bulk of the luminosity density arises, and can therefore be classed as a typical radio source at this redshift. We also see hints of associated absorption redward of the line centre. This is reminiscent of the associated absorption found in other powerful radio galaxies (van Ojik et al. 1997; Jarvis et al. 2003; Wilman et al. 2004) and, given the compact nature of the radio source, may also reinforce the idea that small and young HzRGs may be surrounded by a shell of neutral gas which is linked to the fueling of the AGN (e.g. Emonts et al. 2007), although higher resolution spectroscopy is needed to confirm this.

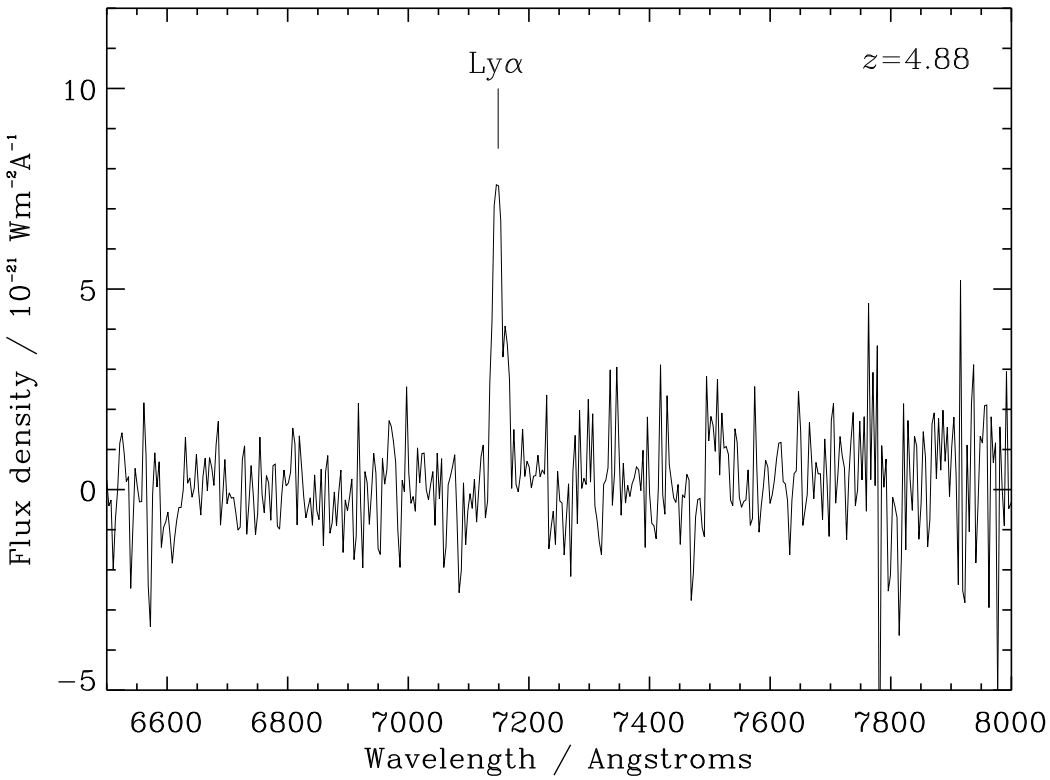

Figure C.3: 1-dimensional spectrum of the radio galaxy J163912.11+405236.5. One can see the bright Lyman-α emission line at $\lambda = 7149$Å, which corresponds to a redshift of $z = 4.88$.

The host galaxy

At $z = 4.88$ the IRAC channels on *Spitzer* sample longward of the 4000Å break and the emission is presumably dominated by an old stellar population. Using the flux-density at 3.6μm and assuming a $K-3.6\mu$m colour of 2.25 from the models of Bruzual & Charlot (2003), we find that the host galaxy would have a $K-$band magnitude of $K_{AB} = 24.2$. Using $K_{AB} - K_{Vega} = 1.9$, we are able to determine where this source would lie on the radio galaxy $K - z$ relation. Using the relation from Willott et al. (2003) for $z = 4.88$, we find that the expected $K-$band magnitude is $K_{Vega} = 20.34$, whereas we find a $K-$band magnitude of $K_{Vega} = 22.3$. Thus this is around 2 magnitudes fainter than the $K - z$ relation determined at low redshift. This is not unexpected as the 4000Å break lies between the K and 3.6μm bands at $z = 4.88$, thus if there is little less ongoing star formation in the host galaxy compared to the assumed evolutionary synthesis model from which the colour correction was determined, it would be extremely difficult to detect at $K-$band even if the host galaxy is relatively massive. If we compare the measured 3.6μm flux with the radio galaxies in the study of Seymour et al. (2007) the only source which is at comparable redshift, and where the 4000Å break would be redshifted beyond the $K-$band, is TN J0924-2201 at $z = 5.195$. This has a reported flux density of 11.3 $\pm$ 1.8μJy at 3.6μm, a factor of two brighter than J163912.11+405236.5. TN J0924-2201 has a radio luminosity that is approximately 1.5 dex brighter than our source, thus this is possibly

Table C.1: Photometric data for the radio galaxy. The quoted limits are 3σ limits for a 2 arcsec diameter aperture for the INT data, 4 arcsec diameter aperture for the channels 1-4 IRAC data and a 10.5 arcsec diameter aperture for the 24μm limit. All are in the AB magnitude system. The radio galaxy is unresolved in both the FIRST and WENSS survey data and as such the radio flux densities are integrated flux over the synthesized beam area.

Photometric Band	AB Magnitude
u'	> 24.8
g'	> 25.5
r'	> 25.1
i'	> 24.1
z'	> 23.2
3.6μm	21.97 ± 0.13
4.5μm	> 21.7
5.8μm	> 20.0
8.0μm	> 19.9
24μm	> 18.1
325 MHz	67 ± 5 mJy
1.4 GHz	22.5 ± 0.4 mJy

related to the fact that the brightest radio galaxies seem to reside in more massive host galaxies (e.g. Eales et al. 1997; Willott et al. 2003; McLure et al. 2004), both of which may be related to the central supermassive black hole. Unfortunately the lack of a detection at the longer wavelength IRAC channels precludes us from carrying out SED fits to estimate the mass of the object. Furthermore, at $z = 4.88$ the Hα line falls within the 3.6μm filter and we cannot be sure whether the emission is indeed due to the stellar continuum emission or a strong emission line. If we assume case B recombination we expect the flux ratio Lyα/H$\alpha = 8.7$ (Brocklehurst 1971) which would then lead to a magnitude in the 3.6μm band of $AB \sim 26$, therefore this does seem unlikely. However, much lower flux ratios have been found in radio galaxies (see e.g. McCarthy et al. 1993) and our measured Lyα flux is possibly an underestimate of the true emission if there is indeed a large amount of associated absorption and/or obscuration by dust. Therefore, we cannot completely rule out significant line emission in the 3.6μm band from Hα.

Although the K-band flux was derived by assuming a colour based on the 3.6μm flux, the model also contains the 4000Å break and as such we would expect the K-band flux to be under luminous compared to lower redshift galaxies where the K-band still sample longward of the 4000Å break. This is therefore suggesting that using the K-z diagram at $z > 4.5$ may only be good for eliminating low-redshift radio galaxies, rather than being useful for estimating redshifts accurately.

Conclusions

We have devised a new survey to find the most distant radio sources with the aim of detecting a source suitable for 21 cm absorption studies with the LOFAR. Initial spectroscopy of this survey has resulted in the discovery of the second most distant radio galaxy known at a redshift

of $z = 4.88$. This source has a spectral index, measured between 325 MHz and 1.4 GHz, of $\alpha = 0.75$ and therefore does not belong to the class of ultra-steep spectrum sources, samples of which have been used to find the majority of the highest redshift radio sources thus far (but see Waddington et al. 1999).

Its luminosity is very close to the break luminosity in the radio luminosity function of Willott et al. (2001) and can therefore be described as a typical radio galaxy at these early epochs. This differs from the other known high-redshift radio galaxies, which are generally towards the extreme luminosities and are thus considerably rarer than the more typical population.

Using the IRAC photometry from the SWIRE survey we are able to determine where this radio galaxy would lie on the $K - z$ relation, and find that it is approximately 2 magnitudes fainter than that inferred from the $K - z$ relation if one uses a simple extrapolation of the relation found by Willott et al. (2003). This can be explained by the fact that the 4000Å break is redshifted beyond the $K-$band and as such is no longer sampling the bulk of the stellar emission from older stars. We therefore conclude that it is possible that this high-redshift radio galaxy is similarly massive to radio galaxies at lower redshifts. We note however that the 3.6μm filter would contain the Hα emission line at this redshift and the detected emission could be at least partially a result of this.

The discovery of such a distant radio source from our initial spectroscopic observations demonstrate the promise of our survey for finding the most distant radio sources. We did not observe all of our candidates HzRGs in this observing run due to poor weather, as a consequence the effective area surveyed was only $\sim$4.5 square degrees. With further observations over the rest of the SWIRE and UKIDSS DXS regions, we will certainly be able to make the most accurate measurements of the space density of radio sources at $z > 3$ and hopefully discover the first radio source appropriate for 21 cm absorption studies within the epoch of reionization. This discovery also shows that samples constructed on the basis of steep-spectral index may miss a significant fraction of high-redshift sources (see also Waddington et al. 1999). Future observations of the rest of the $S_{1.4\mathrm{GHz}} > 10$ mJy sources in the SWIRE/DXS fields will allow us to quantify the distribution of spectral indices for these distant sources and aid in defining the search criteria for distant radio sources with future radio continuum surveys made possible with LOFAR, EVLA and the SKA precursor telescopes. Furthermore, future observations with the VISTA Deep Extragalactic Observations (VIDEO) survey (http://star-www.herts.ac.uk/$\sim$mjarvis/video/) and the Spitzer Representative Volume survey (SERVs; http://www.its.caltech.edu/$\sim$mlacy/servs.html) will not only allow us to make an extremely selective sample of HzRG candidates but also allow us to measure the environmental density around these distant radio sources in the same way that has been attempted around the most distant QSOs (e.g. Willott et al. 2005; Stiavelli et al. 2005).

References

Abazajian, K. N., et al. 2009, ApJS, 182, 543

Abel, T., Bryan, G. L., & Norman, M. L. 2002, Science, 295, 93

Akiyama, M., Ueda, Y., & Ohta, K. 2002, ApJ, 567, 42

Alexander, D. M., et al. 2008, AJ, 135, 1968

Alexander, D. M., Smail, I., Bauer, F. E., Chapman, S. C., Blain, A. W., Brandt, W. N., & Ivison, R. J. 2005, Nature, 434, 738

Alloin, D., Barvainis, R., & Guilloteau, S. 2000, ApJL, 528, L81

Almaini, O., Boyle, B. J., Griffiths, R. E., Shanks, T., Stewart, G. C., & Georgantopoulos, I. 1995, MNRAS, 277, L31

Angel, J. R. P. & Stockman, H. S. 1980, ARA&A, 18, 321

Antonucci, R. 1993, ARA&A, 31, 473

Archibald, E. N., Dunlop, J. S., Hughes, D. H., Rawlings, S., Eales, S. A., & Ivison, R. J. 2001, MNRAS, 323, 417

Arnaboldi, M., Neeser, M. J., Parker, L. C., Rosati, P., Lombardi, M., Dietrich, J. P., & Hummel, W. 2007, The Messenger, 127, 28

Athreya, R. M. & Kapahi, V. K. 1998, Journal of Astrophysics and Astronomy, 19, 63

Babić, A., Miller, L., Jarvis, M. J., Turner, T. J., Alexander, D. M., & Croom, S. M. 2007, A&A, 474, 755

Bahcall, J. N., Kirhakos, S., Saxe, D. H., & Schneider, D. P. 1997, ApJ, 479, 642

Barkana, R. & Loeb, A. 2001, Phys.Rep., 349, 125

Barthel, P. D. 1989, ApJ, 336, 606

Barvainis, R., Lehár, J., Birkinshaw, M., Falcke, H., & Blundell, K. M. 2005, ApJ, 618, 108

Baum, S. A., Heckman, T. M., & van Breugel, W. 1992, ApJ, 389, 208

Becker, R. H., et al. 2001, AJ, 122, 2850

Becker, R. H., White, R. L., & Helfand, D. J. 1995, ApJ, 450, 559

Begelman, M. C., Blandford, R. D., & Rees, M. J. 1984, Reviews of Modern Physics, 56, 255

Bennert, N., Canalizo, G., Jungwiert, B., Stockton, A., Schweizer, F., Peng, C. Y., & Lacy, M. 2008, ApJ, 677, 846

Bennett, A. S. 1962, MNRAS, 125, 75

Best, P. N., Arts, J. N., Röttgering, H. J. A., Rengelink, R., Brookes, M. H., & Wall, J. 2003, MNRAS, 346, 627

Best, P. N. & Heckman, T. M. 2012a, MNRAS, 421, 1569

Best, P. N. & Heckman, T. M. 2012b, MNRAS, 421, 1569

Best, P. N., Kauffmann, G., Heckman, T. M., Brinchmann, J., Charlot, S., Ivezić, Ž., & White, S. D. M. 2005, MNRAS, 362, 25

Best, P. N., Longair, M. S., & Roettgering, H. J. A. 1998, MNRAS, 295, 549

Best, P. N., Longair, M. S., & Rottgering, H. J. A. 1996, MNRAS, 280, L9

Best, P. N., Röttgering, H. J. A., & Longair, M. S. 2000, MNRAS, 311, 23

Bicknell, G. V., Sutherland, R. S., van Breugel, W. J. M., Dopita, M. A., Dey, A., & Miley, G. K. 2000, ApJ, 540, 678

Blumenthal, G. & Miley, G. 1979, A&A, 80, 13

Blundell, K. M., Rawlings, S., Eales, S. A., Taylor, G. B., & Bradley, A. D. 1998, MNRAS, 295, 265

Bolton, J. S., Haehnelt, M. G., Warren, S. J., Hewett, P. C., Mortlock, D. J., Venemans, B. P., McMahon, R. G., & Simpson, C. 2011, MNRAS, 416, L70

Bonning, E. W., Cheng, L., Shields, G. A., Salviander, S., & Gebhardt, K. 2007, ApJ, 659, 211

Bower, R. G., Benson, A. J., Malbon, R., Helly, J. C., Frenk, C. S., Baugh, C. M., Cole, S., & Lacey, C. G. 2006, MNRAS, 370, 645

Bowler, R. A. A., et al. 2012, MNRAS, 426, 2772

Brandt, W. N. & Alexander, D. M. 2010, Proceedings of the National Academy of Science, 107, 7184

Bromm, V. & Larson, R. B. 2004, ARA&A, 42, 79

Brookes, M. H., Best, P. N., Peacock, J. A., Röttgering, H. J. A., & Dunlop, J. S. 2008, MNRAS, 385, 1297

Brookes, M. H., Best, P. N., Rengelink, R., & Röttgering, H. J. A. 2006, MNRAS, 366, 1265

Brooks, A. M., Governato, F., Quinn, T., Brook, C. B., & Wadsley, J. 2009, ApJ, 694, 396

Bruzual, G. & Charlot, S. 2003, MNRAS, 344, 1000

Bryant, J. J., Johnston, H. M., Broderick, J. W., Hunstead, R. W., De Breuck, C., & Gaensler, B. M. 2009, MNRAS, 395, 1099

Bunker, A. J., et al. 2010, MNRAS, 409, 855

Canalizo, G., Bennert, N., Jungwiert, B., Stockton, A., Schweizer, F., Lacy, M., & Peng, C. 2007, ApJ, 669, 801

Canalizo, G. & Stockton, A. 2000, AJ, 120, 1750

Canalizo, G. & Stockton, A. 2001a, ApJ, 555, 719

Canalizo, G. & Stockton, A. 2001b, ApJ, 555, 719

Carilli, C. L. & Barthel, P. D. 1996, A&ARv, 7, 1

Carilli, C. L., Gnedin, N. Y., & Owen, F. 2002, ApJ, 577, 22

Carilli, C. L., Lewis, G. F., Djorgovski, S. G., Mahabal, A., Cox, P., Bertoldi, F., & Omont, A. 2003, Science, 300, 773

Carilli, C. L. & Rawlings, S. 2004, New Astronomy Reviews, 48, 979

Chambers, K. C., Miley, G. K., & van Breugel, W. 1987, Nature, 329, 604

Chambers, K. C., Miley, G. K., & van Breugel, W. J. M. 1990, ApJ, 363, 21

Chambers, K. C., Miley, G. K., van Breugel, W. J. M., & Huang, J.-S. 1996, ApJS, 106, 215

Clavel, J., Wamsteker, W., & Glass, I. S. 1989, ApJ, 337, 236

Clewley, L. & Jarvis, M. J. 2004, MNRAS, 352, 909

Cohen, A. S., Röttgering, H. J. A., Jarvis, M. J., Kassim, N. E., & Lazio, T. J. W. 2004, ApJS, 150, 417

Combes, F., Young, L. M., & Bureau, M. 2007, MNRAS, 377, 1795

Condon, J. J., Cotton, W. D., Greisen, E. W., Yin, Q. F., Perley, R. A., Taylor, G. B., & Broderick, J. J. 1998, AJ, 115, 1693

Cowie, L. L., Songaila, A., Hu, E. M., & Cohen, J. G. 1996, AJ, 112, 839

Croft, S., et al. 2006, ApJ, 647, 1040

Croton, D. J., et al. 2006, MNRAS, 365, 11

Cruz, K. L., et al. 2007, AJ, 133, 439

Cruz, M. J., et al. 2006, MNRAS, 373, 1531

De Breuck, C., Downes, D., Neri, R., van Breugel, W., Reuland, M., Omont, A., & Ivison, R. 2005, A&A, 430, L1

De Breuck, C., Röttgering, H., Miley, G., van Breugel, W., & Best, P. 2000a, A&A, 362, 519

De Breuck, C., Tang, Y., de Bruyn, A. G., Röttgering, H., & van Breugel, W. 2002, A&A, 394, 59

De Breuck, C., van Breugel, W., Röttgering, H. J. A., & Miley, G. 2000b, A&AS, 143, 303

De Breuck, C. A. G. 2000, PhD thesis, Leiden Observatory, Leiden University, P.O. Box 9513, 2300 RA Leiden, The Netherlands

de Oliveira-Costa, A., Tegmark, M., Gaensler, B. M., Jonas, J., Landecker, T. L., & Reich, P. 2008, MNRAS, 388, 247

de Zotti, G., Massardi, M., Negrello, M., & Wall, J. 2010, A&ARv, 18, 1

Dekel, A. & Birnboim, Y. 2008, MNRAS, 383, 119

Dekel, A., Sari, R., & Ceverino, D. 2009, ApJ, 703, 785

Dey, A., van Breugel, W., Vacca, W. D., & Antonucci, R. 1997, ApJ, 490, 698

Di Matteo, T., Springel, V., & Hernquist, L. 2005, Nature, 433, 604

Dijkstra, M. & Loeb, A. 2009, MNRAS, 400, 1109

Donoso, E., Best, P. N., & Kauffmann, G. 2009, MNRAS, 392, 617

Doroshkevich, A. G., Longair, M. S., & Zeldovich, Y. B. 1970, MNRAS, 147, 139

Downes, D., Solomon, P. M., & Radford, S. J. E. 1993, ApJL, 414, L13

Drinkwater, M. J., et al. 1997, MNRAS, 284, 85

Dubinski, J. 1998, ApJ, 502, 141

Dunkley, J., et al. 2009, ApJS, 180, 306

Dunlop, J. S., Hughes, D. H., Rawlings, S., Eales, S. A., & Ward, M. J. 1994, Nature, 370, 347

Dunlop, J. S., McLure, R. J., Kukula, M. J., Baum, S. A., O'Dea, C. P., & Hughes, D. H. 2003, MNRAS, 340, 1095

Dunlop, J. S. & Peacock, J. A. 1990, MNRAS, 247, 19

Eales, S., Rawlings, S., Law-Green, D., Cotter, G., & Lacy, M. 1997, MNRAS, 291, 593

Eales, S. A. & Rawlings, S. 1996, ApJ, 460, 68

Elvis, M., et al. 1994, ApJS, 95, 1

Evans, A. S., Sanders, D. B., Mazzarella, J. M., Solomon, P. M., Downes, D., Kramer, C., & Radford, S. J. E. 1996, ApJ, 457, 658

Fan, X., et al. 2001, AJ, 122, 2833

Fan, X., Narayanan, V. K., Strauss, M. A., White, R. L., Becker, R. H., Pentericci, L., & Rix, H.-W. 2002, AJ, 123, 1247

Fan, X., et al. 2006, AJ, 132, 117

Fan, X., et al. 2000, AJ, 119, 1

Fan, X., et al. 1999, AJ, 118, 1

Fanaroff, B. L. & Riley, J. M. 1974, MNRAS, 167, 31P

Findlay, J. R., Sutherland, W. J., Venemans, B. P., Reylé, C., Robin, A. C., Bonfield, D. G., Bruce, V. A., & Jarvis, M. J. 2012, MNRAS, 419, 3354

Fine, S., Jarvis, M. J., & Mauch, T. 2011, MNRAS, 412, 213

Gao, L., Loeb, A., Peebles, P. J. E., White, S. D. M., & Jenkins, A. 2004, ApJ, 614, 17

Gendre, M. A., Best, P. N., & Wall, J. V. 2010, MNRAS, 404, 1719

Graham, J. A. 1998, ApJ, 502, 245

Granato, G. L., Danese, L., & Franceschini, A. 1997, ApJ, 486, 147

Greenstein, J. L. & Schmidt, M. 1964, ApJ, 140, 1

Greve, T. R., Ivison, R. J., & Papadopoulos, P. P. 2004, A&A, 419, 99

Grimes, J. A., Rawlings, S., & Willott, C. J. 2004, MNRAS, 349, 503

Groves, B. A., Dopita, M. A., & Sutherland, R. S. 2004, ApJS, 153, 9

Gunn, J. E. & Peterson, B. A. 1965, ApJ, 142, 1633

Haiman, Z., Spaans, M., & Quataert, E. 2000, ApJL, 537, L5

Hardcastle, M. J., Kraft, R. P., Worrall, D. M., Croston, J. H., Evans, D. A., Birkinshaw, M., & Murray, S. S. 2007, ApJ, 662, 166

Hardcastle, M. J., et al. 2012, MNRAS, 424, 1774

Hardcastle, M. J., et al. 2010, MNRAS, 409, 122

Harker, G., et al. 2010, MNRAS, 405, 2492

Hasinger, G. 2004, Nuclear Physics B Proceedings Supplements, 132, 86

Hasinger, G., Miyaji, T., & Schmidt, M. 2005, A&A, 441, 417

Heald, G., et al. 2011, Journal of Astrophysics and Astronomy, 32, 589

Heckman, T. M., Smith, E. P., Baum, S. A., van Breugel, W. J. M., Miley, G. K., Illingworth, G. D., Bothun, G. D., & Balick, B. 1986, ApJ, 311, 526

Herbert, P. D., Jarvis, M. J., Willott, C. J., McLure, R. J., Mitchell, E., Rawlings, S., Hill, G. J., & Dunlop, J. S. 2010, MNRAS, 406, 1841

Hill, G. J., Goodrich, R. W., & Depoy, D. L. 1996, ApJ, 462, 163

Hopkins, A. M., Mobasher, B., Cram, L., & Rowan-Robinson, M. 2000, VizieR Online Data Catalog, 729, 60839

Hopkins, P. F., Cox, T. J., Kereš, D., & Hernquist, L. 2008, ApJS, 175, 390

Hoyle, F. & Fowler, W. A. 1963, Nature, 197, 533

Humphrey, A., Villar-Martín, M., Fosbury, R., Vernet, J., & di Serego Alighieri, S. 2006, MNRAS, 369, 1103

Iliev, I. T., Mellema, G., Pen, U.-L., Bond, J. R., & Shapiro, P. R. 2008, MNRAS, 384, 863

Ivezić, Ž., et al. 2002, AJ, 124, 2364

Ivison, R. J. 1995, MNRAS, 275, L33

Jackson, C. A. & Wall, J. V. 1999, MNRAS, 304, 160

Jarvis, M. J., et al. 2012, ArXiv e-prints

Jarvis, M. J., Cruz, M. J., Cohen, A. S., Röttgering, H. J. A., & Kassim, N. E. 2004, MNRAS, 355, 20

Jarvis, M. J. & McLure, R. J. 2002, MNRAS, 336, L38

Jarvis, M. J. & Rawlings, S. 2000, MNRAS, 319, 121

Jarvis, M. J. & Rawlings, S. 2004, New Astronomy Reviews, 48, 1173

Jarvis, M. J., Rawlings, S., Eales, S., Blundell, K. M., Bunker, A. J., Croft, S., McLure, R. J., & Willott, C. J. 2001a, MNRAS, 326, 1585

Jarvis, M. J., et al. 2001b, MNRAS, 326, 1563

Jarvis, M. J., Rawlings, S., Willott, C. J., Blundell, K. M., Eales, S., & Lacy, M. 2001c, MNRAS, 327, 907

Jarvis, M. J., Teimourian, H., Simpson, C., Smith, D. J. B., Rawlings, S., & Bonfield, D. 2009, MNRAS, 398, L83

Jarvis, M. J., van Breukelen, C., & Wilman, R. J. 2005, MNRAS, 358, L11

Jarvis, M. J., Wilman, R. J., Röttgering, H. J. A., & Binette, L. 2003, MNRAS, 338, 263

Jeon, M., Pawlik, A. H., Greif, T. H., Glover, S. C. O., Bromm, V., Milosavljević, M., & Klessen, R. S. 2012, ApJ, 754, 34

Karastergiou, A. & Johnston, S. 2007, MNRAS, 380, 1678

Kaufmann, T., Mayer, L., Wadsley, J., Stadel, J., & Moore, B. 2006, MNRAS, 370, 1612

Kellermann, K. I., Pauliny-Toth, I. I. K., & Williams, P. J. S. 1969, ApJ, 157, 1

Ker, L. M., Best, P. N., Rigby, E. E., Röttgering, H. J. A., & Gendre, M. A. 2012, MNRAS, 420, 2644

Khachikian, E. Y. & Weedman, D. W. 1974, ApJ, 192, 581

Kinney, A. L., Antonucci, R. R. J., Ward, M. J., Wilson, A. S., & Whittle, M. 1991, ApJ, 377, 100

Klamer, I. J., Ekers, R. D., Bryant, J. J., Hunstead, R. W., Sadler, E. M., & De Breuck, C. 2006, MNRAS, 371, 852

Klamer, I. J., Ekers, R. D., Sadler, E. M., & Hunstead, R. W. 2004, ApJL, 612, L97

Kocevski, D. D., et al. 2012, ApJ, 744, 148

Lacy, M., Bunker, A. J., & Ridgway, S. E. 2000, AJ, 120, 68

Lacy, M., Laurent-Muehleisen, S. A., Ridgway, S. E., Becker, R. H., & White, R. L. 2001, ApJL, 551, L17

Lacy, M., et al. 2004, ApJS, 154, 166

Laing, R. A., Riley, J. M., & Longair, M. S. 1983, MNRAS, 204, 151

Lawrence, A. 1991, MNRAS, 252, 586

Lawrence, A. & Elvis, M. 2010, ApJ, 714, 561

Lawrence, A., et al. 2007, MNRAS, 379, 1599

Lilly, S. J. 1988, ApJ, 333, 161

Lilly, S. J. & Longair, M. S. 1984, MNRAS, 211, 833

Lin, D. N. C., Pringle, J. E., & Rees, M. J. 1988, ApJ, 328, 103

Longair, M. S. 1966, MNRAS, 133, 421

Lonsdale, C. J., et al. 2003, PASP, 115, 897

Luo, B., et al. 2011, ApJ, 740, 37

Lynden-Bell, D. 1969, Nature, 223, 690

Magorrian, J., et al. 1998, AJ, 115, 2285

Martínez-Sansigre, A. & Rawlings, S. 2011a, MNRAS, 418, L84

Martínez-Sansigre, A. & Rawlings, S. 2011b, MNRAS, 414, 1937

Martínez-Sansigre, A., Rawlings, S., Lacy, M., Fadda, D., Jarvis, M. J., Marleau, F. R., Simpson, C., & Willott, C. J. 2006, MNRAS, 370, 1479

Martínez-Sansigre, A., Rawlings, S., Lacy, M., Fadda, D., Marleau, F. R., Simpson, C., Willott, C. J., & Jarvis, M. J. 2005, Nature, 436, 666

Martini, P. & Schneider, D. P. 2003, ApJL, 597, L109

Mas-Hesse, J. M., Rodriguez-Pascual, P. M., de Cordoba, L. S. F., & Mirabel, I. F. 1994, ApJS, 92, 599

Matthews, T. A., Morgan, W. W., & Schmidt, M. 1964, ApJ, 140, 35

Matthews, T. A. & Sandage, A. R. 1963, ApJ, 138, 30

McCarthy, P. J. 1993, ARA&A, 31, 639

McCarthy, P. J., Kapahi, V. K., van Breugel, W., Persson, S. E., Athreya, R., & Subrahmanya, C. R. 1996, ApJS, 107, 19

McCarthy, P. J., van Breugel, W., Spinrad, H., & Djorgovski, S. 1987, ApJL, 321, L29

McCracken, H. J., et al. 2012, A&A, 544, A156

McLure, R. J., Dunlop, J. S., Cirasuolo, M., Koekemoer, A. M., Sabbi, E., Stark, D. P., Targett, T. A., & Ellis, R. S. 2010, MNRAS, 403, 960

McLure, R. J. & Jarvis, M. J. 2004, MNRAS, 353, L45

McLure, R. J., Kukula, M. J., Dunlop, J. S., Baum, S. A., O'Dea, C. P., & Hughes, D. H. 1999, MNRAS, 308, 377

McLure, R. J., Willott, C. J., Jarvis, M. J., Rawlings, S., Hill, G. J., Mitchell, E., Dunlop, J. S., & Wold, M. 2004, MNRAS, 351, 347

Middelberg, E., et al. 2007, ArXiv e-prints

Miley, G. 1992, in European Southern Observatory Conference and Workshop Proceedings, Vol. 44, European Southern Observatory Conference and Workshop Proceedings, ed. P. Benvenuti & E. Schreier, 1

Miley, G. & De Breuck, C. 2008, A&ARv, 15, 67

Miller, J. S., French, H. B., & Hawley, S. A. 1978, in BL Lac Objects, ed. A. M. Wolfe, 176–187

Miller, J. S., Goodrich, R. W., & Mathews, W. G. 1991, ApJ, 378, 47

Morales, M. F. & Wyithe, J. S. B. 2010, ARA&A, 48, 127

Morganti, R., et al. 2006, MNRAS, 371, 157

Mortlock, D. J., et al. 2011, Nature, 474, 616

Mullaney, J. R., et al. 2012, MNRAS, 419, 95

Murphy, E. J., Chary, R.-R., Dickinson, M., Pope, A., Frayer, D. T., & Lin, L. 2011, ApJ, 732, 126

Norman, C., et al. 2002, ApJ, 571, 218

Norris, R. P., et al. 2006, AJ, 132, 2409

Obreschkow, D., Heywood, I., Klöckner, H.-R., & Rawlings, S. 2009a, ApJ, 702, 1321

Obreschkow, D., Klöckner, H.-R., Heywood, I., Levrier, F., & Rawlings, S. 2009b, ApJ, 703, 1890

Obreschkow, D. & Rawlings, S. 2009, MNRAS, 394, 1857

Ohta, K., Yamada, T., Nakanishi, K., Ogasaka, Y., Kii, T., & Hayashida, K. 1996, ApJL, 458, L57

Oke, J. B. & Gunn, J. E. 1983, ApJ, 266, 713

Omont, A. 2007, Reports on Progress in Physics, 70, 1099

Osterbrock, D. E. 1978, Proceedings of the National Academy of Science, 75, 540

Osterbrock, D. E. 1981, ApJ, 249, 462

Osterbrock, D. E. 1984, QJRAS, 25, 1

Padovani, P., Miller, N., Kellermann, K. I., Mainieri, V., Rosati, P., & Tozzi, P. 2011, ApJ, 740, 20

Papadopoulos, P. P., Röttgering, H. J. A., van der Werf, P. P., Guilloteau, S., Omont, A., van Breugel, W. J. M., & Tilanus, R. P. J. 2000, ApJ, 528, 626

Pentericci, L., McCarthy, P. J., Röttgering, H. J. A., Miley, G. K., van Breugel, W. J. M., & Fosbury, R. 2001, ApJS, 135, 63

Pentericci, L., Röttgering, H. J. A., Miley, G. K., McCarthy, P., Spinrad, H., van Breugel, W. J. M., & Macchetto, F. 1999, A&A, 341, 329

Péroux, C., Storrie-Lombardi, L. J., McMahon, R. G., Irwin, M., & Hook, I. M. 2001, AJ, 121, 1799

Polletta, M. d. C., et al. 2006, ApJ, 642, 673

Rafferty, D. A., Brandt, W. N., Alexander, D. M., Xue, Y. Q., Bauer, F. E., Lehmer, B. D., Luo, B., & Papovich, C. 2011, ApJ, 742, 3

Rawlings, S., Eales, S., & Lacy, M. 2001, MNRAS, 322, 523

Rawlings, S., Lacy, M., Blundell, K. M., Eales, S. A., Bunker, A. J., & Garrington, S. T. 1996, Nature, 383, 502

Rawlings, S. & Saunders, R. 1991, Nature, 349, 138

Rees, M. J. 1984, ARA&A, 22, 471

Rengelink, R. B., Tang, Y., de Bruyn, A. G., Miley, G. K., Bremer, M. N., Roettgering, H. J. A., & Bremer, M. A. R. 1997, A&AS, 124, 259

Reuland, M., Röttgering, H., van Breugel, W., & De Breuck, C. 2004, MNRAS, 353, 377

Reuland, M., et al. 2007, AJ, 133, 2607

Richards, G. T., et al. 2005, MNRAS, 360, 839

Rigby, E. E., Best, P. N., Brookes, M. H., Peacock, J. A., Dunlop, J. S., Röttgering, H. J. A., Wall, J. V., & Ker, L. 2011, MNRAS, 416, 1900

Rigby, E. E., Snellen, I. A. G., & Best, P. N. 2007, MNRAS, 380, 1449

Rocca-Volmerange, B., Le Borgne, D., De Breuck, C., Fioc, M., & Moy, E. 2004, A&A, 415, 931

Rocca-Volmerange, B. & Remazeilles, M. 2005, A&A, 433, 73

Roche, N. & Eales, S. A. 2000, MNRAS, 317, 120

Roy, A. L., Norris, R. P., Kesteven, M. J., Troup, E. R., & Reynolds, J. E. 1994, ApJ, 432, 496

Sadler, E. M., et al. 2007, MNRAS, 381, 211

Sanders, D. B. & Mirabel, I. F. 1996, ARA&A, 34, 749

Sanders, D. B., Soifer, B. T., Elias, J. H., Madore, B. F., Matthews, K., Neugebauer, G., & Scoville, N. Z. 1988, ApJ, 325, 74

Santos, M. G., Amblard, A., Pritchard, J., Trac, H., Cen, R., & Cooray, A. 2008, ApJ, 689, 1

Schinnerer, E., Böker, T., Emsellem, E., & Downes, D. 2007, A&A, 462, L27

Schmidt, M. 1962, ApJ, 136, 684

Schmidt, M. 1963, Nature, 197, 1040

Scoville, N., et al. 2007, ApJS, 172, 38

Scoville, N. Z., Yun, M. S., Windhorst, R. A., Keel, W. C., & Armus, L. 1997, ApJL, 485, L21

Seyfert, C. K. 1943, ApJ, 97, 28

Seymour, N., et al. 2007, ApJS, 171, 353

Seymour, N., Symeonidis, M., Page, M. J., Huynh, M., Dwelly, T., McHardy, I. M., & Rieke, G. 2010, MNRAS, 402, 2666

Shaver, P. A., Wall, J. V., Kellermann, K. I., Jackson, C. A., & Hawkins, M. R. S. 1996, Nature, 384, 439

Shlosman, I., Frank, J., & Begelman, M. C. 1989, Nature, 338, 45

Simpson, C. 2005, MNRAS, 360, 565

Simpson, C. & Eisenhardt, P. 1999, PASP, 111, 691

Simpson, C., et al. 2006, MNRAS, 372, 741

Simpson, C. & Rawlings, S. 2000, MNRAS, 317, 1023

Simpson, C., Rawlings, S., & Lacy, M. 1999, MNRAS, 306, 828

Simpson, J. M., et al. 2012, MNRAS, 426, 3201

Skrutskie, M. F., et al. 2006, AJ, 131, 1163

Smith, D. J. B. & Jarvis, M. J. 2007, MNRAS, 378, L49

Smolčić, V., et al. 2009, ApJ, 696, 24

Snellen, I. A. G. & Best, P. N. 2001, MNRAS, 328, 897

Solomon, P. M. & Vanden Bout, P. A. 2005, ARA&A, 43, 677

Springel, V., et al. 2005, Nature, 435, 629

Steffen, A. T., Barger, A. J., Cowie, L. L., Mushotzky, R. F., & Yang, Y. 2003, ApJL, 596, L23

Steidel, C. C. & Hamilton, D. 1992, AJ, 104, 941

Stern, D., et al. 2005, ApJ, 631, 163

Stern, D., Holden, B., Stanford, S. A., & Spinrad, H. 2003, AJ, 125, 2759

Stevens, J. A., et al. 2003, Nature, 425, 264

Strazzullo, V., Pannella, M., Owen, F. N., Bender, R., Morrison, G. E., Wang, W.-H., & Shupe, D. L. 2010, ApJ, 714, 1305

Surace, J. A. & Sanders, D. B. 1999, ApJ, 512, 162

Surace, J. A., Sanders, D. B., Vacca, W. D., Veilleux, S., & Mazzarella, J. M. 1998, ApJ, 492, 116

Tasse, C., Best, P. N., Röttgering, H., & Le Borgne, D. 2008, A&A, 490, 893

Tasse, C., et al. 2006, A&A, 456, 791

Tasse, C., Roettgering, H. J. A., Best, P. N., Cohen, A. S., Pierre, M., & Wilman, R. 2007, VizieR Online Data Catalog, 347, 11105

Tielens, A. G. G. M., Miley, G. K., & Willis, A. G. 1979, A&AS, 35, 153

Treister, E., Krolik, J. H., & Dullemond, C. 2008, ApJ, 679, 140

Ueda, Y., Akiyama, M., Ohta, K., & Miyaji, T. 2003, ApJ, 598, 886

Urry, C. M. & Padovani, P. 1995, PASP, 107, 803

van Breugel, W., De Breuck, C., Stanford, S. A., Stern, D., Röttgering, H., & Miley, G. 1999, ApJL, 518, L61

van Breugel, W. J. M. & Dey, A. 1993, ApJ, 414, 563

van Breugel, W. J. M. & McCarthy, P. J. 1990, in Astronomical Society of the Pacific Conference Series, Vol. 10, Evolution of the Universe of Galaxies, ed. R. G. Kron, 359–370

van Breugel, W. J. M., Stanford, S. A., Spinrad, H., Stern, D., & Graham, J. R. 1998, ApJ, 502, 614

van Gorkom, J. H., Knapp, G. R., Ekers, R. D., Ekers, D. D., Laing, R. A., & Polk, K. S. 1989, AJ, 97, 708

van Ojik, R., Roettgering, H. J. A., Miley, G. K., & Hunstead, R. W. 1997, A&A, 317, 358

Vanden Berk, D. E., et al. 2001, AJ, 122, 549

Venemans, B. P., et al. 2007, A&A, 461, 823

Vernet, J., Fosbury, R. A. E., Villar-Martín, M., Cohen, M. H., Cimatti, A., di Serego Alighieri, S., & Goodrich, R. W. 2001, A&A, 366, 7

Villar-Martin, M. & Binette, L. 1996, A&A, 309, 97

Villar-Martín, M., Humphrey, A., De Breuck, C., Fosbury, R., Binette, L., & Vernet, J. 2007a, MNRAS, 375, 1299

Villar-Martín, M., Humphrey, A., De Breuck, C., Fosbury, R., Binette, L., & Vernet, J. 2007b, MNRAS, 375, 1299

Villar-Martin, M., Tadhunter, C., & Clark, N. 1997, A&A, 323, 21

Villar-Martín, M., Tadhunter, C., Humphrey, A., Encina, R. F., Delgado, R. G., Torres, M. P., & Martínez-Sansigre, A. 2011, MNRAS, 416, 262

Waddington, I., Dunlop, J. S., Peacock, J. A., & Windhorst, R. A. 2001, MNRAS, 328, 882

Waddington, I., et al. 2002, MNRAS, 336, 1342

Wall, J. 2008, ArXiv e-prints

Wall, J. V., Jackson, C. A., Shaver, P. A., Hook, I. M., & Kellermann, K. I. 2005, A&A, 434, 133

Weedman, D. W. 1977, ARA&A, 15, 69

Williams, C. L., et al. 2012, ApJ, 755, 47

Willott, C. 2001, in HST Proposal, 9045

Willott, C. J., et al. 2013, AJ, 145, 4

Willott, C. J., Rawlings, S., Blundell, K. M., & Lacy, M. 1999, MNRAS, 309, 1017

Willott, C. J., Rawlings, S., Blundell, K. M., & Lacy, M. 2000, MNRAS, 316, 449

Willott, C. J., Rawlings, S., Blundell, K. M., Lacy, M., & Eales, S. A. 2001, MNRAS, 322, 536

Willott, C. J., Rawlings, S., Jarvis, M. J., & Blundell, K. M. 2003, MNRAS, 339, 173

Wilman, R. J., Jarvis, M. J., Mauch, T., Rawlings, S., & Hickey, S. 2010, MNRAS, 405, 447

Wilman, R. J., Jarvis, M. J., Röttgering, H. J. A., & Binette, L. 2004, MNRAS, 351, 1109

Wilman, R. J., et al. 2008, MNRAS, 388, 1335

Windhorst, R. A. 2003, New Astronomy Reviews, 47, 357

Woltjer, L. 1959, ApJ, 130, 38

Ye, Y.-C. & Wang, D.-X. 2005, MNRAS, 357, 1155

Yun, M. S., Reddy, N. A., & Condon, J. J. 2001, ApJ, 554, 803

Zakamska, N. L., et al. 2003, AJ, 126, 2125

Zirm, A. W., Dickinson, M., & Dey, A. 2003, ApJ, 585, 90

Zirm, A. W., et al. 2005, ApJ, 630, 68